Promoters **Prof. Dr. Ir. Marc Van Meirvenne**
Department of Soil Management
Faculty of Bioscience Engineering
Ghent University

Prof. Dr. Ir. Piet Seuntjens
Department of Soil Management
Faculty of Bioscience Engineering
Ghent University

Dean **Prof. Dr. Ir. Marc Van Meirvenne**
Rector **Prof. Dr. Anne De Paepe**

Ellen Van De Vijver

Proximal soil sensing in the context of urban (re)development: an evaluation of multi-receiver electromagnetic induction and stepped-frequency ground penetrating radar at landfills and industrial sites

Thesis submitted in fulfilment of the requirements
for the degree of Doctor (PhD) in Applied Biological Sciences

Dutch translation of the title:
De toepassing van proximale bodemsensoren in de context van stedelijke (her)ontwikkeling: een evaluatie van meerspoelige elektromagnetische inductie en stapfrequentie grondradar op stortplaatsen en industriële sites.

Illustration on the cover:
Electromagnetic induction survey for landfill detection in the context of a nature redevelopment project (see case study I in Chapter 5).

Citation of this thesis:
Van De Vijver, E. (2017). *Proximal soil sensing in the context of urban (re)development: an evaluation of multi-receiver electromagnetic induction and stepped-frequency ground penetrating radar at landfills and industrial sites* (Doctoral dissertation). Ghent University, Ghent, Belgium.

ISBN-number: 978-94-6357-025-1

Table of contents

Abbreviations

AGC	Automatic gain control
AGIV	Agentschap Geografische Informatie Vlaanderen (Flanders Geographical Information Agency)
CDW	Construction and demolition waste
CEC	Cation exchange capacity
CV	Coefficient of variation
DC	Direct current
dGNSS	Differential global navigation satellite system
DOE	Depth of exploration
DOV	Databank Ondergrond Vlaanderen (Database of the Subsoil of Flanders)
DTM	Digital terrain model
EC_a	Apparent electrical conductivity
EC_p	Probe electrical conductivity
ELFM	Enhanced landfill mining
EM	Electromagnetic
EMI	Electromagnetic induction
EU	European Union
EURELCO	European Enhanced Landfill Mining Consortium
FAO	Food and Agriculture Organization of the United Nations
GPR	Ground penetrating radar
HCP	Horizontal coplanar
HM	Heavy metal
IP	In-phase
ITPS	Intergovernmental Technical Panel on Soils
IUSS	International Union of Soil Science
IW	Industrial waste
LRD	Large-scale Reference Database
MS_a	Apparent magnetic susceptibility
MSW	Municipal solid waste

OM	Organic matter
OVAM	Openbare Vlaamse Afvalstoffenmaatschappij (Public Waste Agency of Flanders)
PAH	Polycyclic aromatic hydrocarbon
PRP	Perpendicular
PVC	Polyvinyl chloride
QP	Quadrature-phase
RDP	Relative dielectric permittivity
RTK	Real-time kinematic correction
SEC	Spherical and exponential compensation
SFCW	Stepped-frequency continuous wave
SNR	Signal-to-noise ratio
TDS	Total dissolved solids
TOC	Total organic carbon
TPH	Total petroleum hydrocarbon
UN	United Nations
US EPA	United States Environmental Protection Agency
UXO	Unexploded ordnance
WRB	World reference base for soil resources
3D	Three-dimensional

Samenvatting

Menselijke populaties hebben doorheen hun geschiedenis onuitwisbare sporen nagelaten in hun leefomgevingen en in de bodem waarop ze gefundeerd zijn. Vooral vanaf de Industriële Revolutie nam de urbanisatie en industrialisatie van onze leefomgevingen sterk toe en werden steeds grotere oppervlaktes aan land in beslag genomen door menselijke activiteiten. De bodem vormt een essentiële component van urbane ecosystemen en in de recente jaren groeide het besef dat inzicht in en gepast beheer van deze bodem cruciaal is om te kunnen dienen als duurzame basis voor verdere ontwikkeling. Omwille van zijn onderschikt belang voor landbouwproductie, werd aan de ondergrond in urbane en industriële gebieden door de klassieke bodemkunde echter slechts een minderwaardige bodemstatus toegeschreven. Mede onder druk van zijn toenemende alomtegenwoordigheid, verkreeg deze bodem inmiddels herkenning in de wetenschappelijke wereld en wordt doorgaans aangeduid als *urban soil*. Desondanks de letterlijke vertaling als 'stadsbodem', wordt *urban soil* hier ruimer gedefinieerd als bodem waarvan de vorming sterk werd beïnvloed door menselijke activiteiten geassocieerd met processen van urbanisatie en/of industrialisatie, met uitzondering van activiteiten gerelateerd met landbouw, bosbouw en tuinbouw. Omwille van verschillende menselijke invloeden vertoont *urban soil* vaak een sterke ruimtelijke heterogeniteit. De conventionele methodes voor bodeminventarisatie zijn algemeen gebaseerd op het maken van een beperkt aantal puntobservaties verkregen via boringen of proefsleuven. Deze zijn echter vaak onvoldoende om de kleinschalige ruimtelijke variaties in *urban soil* te kunnen reconstrueren. Proximale geofysische bodemsensoren laten toe om fysische eigenschappen van de bodem te meten op een niet-invasieve manier en bieden zo een efficiënt alternatief voor het verzamelen van ruimtelijk gebiedsdekkende bodeminformatie. Deze sensoren hebben reeds een gevestigde reputatie in toepassingen op het gebied van landbouw en (geo)archeologie. Hun inzet voor het karakteriseren van bodem in urbane en industriële omgevingen is tot nog toe echter beperkt.

De algemene doelstelling van dit doctoraatsonderzoek is het evalueren van het potentieel van proximale geofysische sensoren voor bodemonderzoek in urbane en industriële gebieden. In deze gebieden wordt bodemonderzoek vaak uitgevoerd naar aanleiding van de aanwezigheid van bodemverontreiniging en sluit

landherontwikkeling veelal aan bij een noodzaak tot sanering. In dit onderzoek wordt specifiek gefocust op stortplaatsen en industriële en commerciële sites, aangezien deze types van landgebruik overeenstemmen met de belangrijkste oorzaken van bodemverontreiniging. Daarnaast werd in de laatste jaren toenemende aandacht gevestigd op de herontwikkeling van stortplaatsen in het kader van de uitbouw van het concept van *Enhanced Landfill Mining* (ELFM). Dit concept beoogt de duurzame integratie van het beheer van stortplaatsen en de valorisatie van de grondstoffen die ze omvatten, inclusief materialen, energie en land. De toepassing van proximale bodemsensoren wordt algemeen beoordeeld vanuit een pragmatisch perspectief, met het oog op hun gebruik in de dagdagelijkse praktijk van bodemonderzoek in de context van land(her)ontwikkeling.

Twee types van geofysische sensoren worden beschouwd waarvan de werking voor beiden gebaseerd is op de principes van elektromagnetisme: elektromagnetische inductie (EMI) en grondradar (*ground penetrating radar*, GPR). Via EMI kunnen de elektrische geleidbaarheid en de magnetische gevoeligheid van de bodem worden gemeten. Er wordt gebruik gemaakt van een instrument met meerdere spoelconfiguraties waardoor tegelijkertijd meerdere signalen met een verschillende dieptegevoeligheid kunnen worden geregistreerd. Via GPR kunnen contrasten in de diëlektrische permittiviteit van de bodem in kaart worden gebracht. Het toegepaste GPR-systeem is een zogenaamd stap-frequentie systeem waarbij metingen worden gemaakt in het frequentiedomein over een breed frequentiebereik. In vergelijking met conventionele tijdsdomein GPR-systemen heeft dit het voordeel dat er geen compromis moet worden gemaakt tussen meetresolutie en meetdiepte: het brede frequentiebereik biedt de optimale resolutie voor elke bereikbare meetdiepe. Zowel EMI als GPR worden geïmplementeerd in een mobiele meetconfiguratie wat zorgt voor een verder efficiëntieverhoging voor de gebiedsdekkende verzameling van data met een hoge staalnamedichtheid.

De toepassing van EMI voor de karakterisering van stortplaatsen werd beoordeeld aan de hand van vier casestudies. De beschouwde stortplaatsen waren verschillend in aanleg, grootte en type van gestort afval. Via het uitvoeren van een hoge-resolutie EMI-survey werden ondergrondse variaties in elektrische geleidbaarheid en magnetische gevoeligheid gedetailleerd in kaart gebracht. Dit liet toe om een accurate bepaling te maken van de locatie en de laterale dimensies van de stortplaats. Daarnaast kon op basis van de meetwaarden, en hun ruimtelijke heterogeniteit, een indicatie worden gegeven van het type gestort afval. De verticale afbakening van een

gestorte afvalmassa werd bemoeilijkt door de talrijke, oppervlakkige aanwezigheid van metalen objecten in combinatie met de gereduceerde resolutie van de meetsignalen op grotere diepte, of was überhaupt onmogelijk omwille van een te beperkte meetdiepte van de EMI signalen (maximum ongeveer 6.4 m).

De combinatie van EMI en GPR werd eerst geëvalueerd op een site van een voormalige garage met een tankstation waarbij via eerder conventioneel bodemonderzoek een verontreiniging met minerale olie werd vastgesteld. Op basis van de geofysische data werden restanten van voormalige bebouwing in kaart gebracht, alsook de bovengrens van een bodemlaag met een hogere dichtheid die vermoedelijk overeenstemde met een vroeger leefoppervlak. Daarnaast werd een overeenkomst gevonden tussen een zone met een lagere elektrische geleidbaarheid en verhoogde concentraties aan minerale olie.

Ten laatste werden EMI en GPR metingen gecombineerd voor bodemonderzoek op de site van een voormalige gasfabriek. Verschillende lokale structuren/fenomenen konden worden gedetecteerd en geïdentificeerd, waaronder nutsvoorzieningen zoals een elektriciteitskabel, restanten van voormalige funderingen en een vermoedelijke verontreiniging met zouten.

Algemeen wordt geconcludeerd dat proximale geofysische bodemsensoren ideale tools zijn voor het uitvoeren van verkennend bodemonderzoek. Op basis van de in kaart gebrachte bodemvariaties kan verder onderzoek via conventionele, invasieve methodes meer gericht en, dus efficiënter, worden uitgevoerd. Bovendien zorgt een afstemming van de staalnamegrootte en –locaties op de waargenomen geofysische contrasten voor een hogere betrouwbaarheid en representativiteit. De voorgestelde methodologie voor het uivoeren van hoge-resolutie EMI en GPR metingen biedt daarom een veelbelovende uitbreiding voor bodemonderzoek in stedelijke en industriële gebieden.

Summary

The historical development of human populations has left indelible traces in their habitat landscapes and the soil they rest upon. Particularly from the Industrial Revolution onwards, significant areas of land have been affected by human activities related to urbanization and industrialization. Soil is an essential component of urban ecosystems and in the recent years it has been realized that proper understanding and management of the soil in urban and industrial environments is crucial to provide a sustainable basis for future human development. Because of its subordinate importance for agricultural production, the subsurface in urban and industrial areas was largely ignored in early pedology. Under pressure of its growing omnipresence, *urban soil* has become an established concept in modern soil science. In this work, *urban soil* is defined as soil that has been profoundly affected by activities that support the modern-day process of urbanization and/or industrialization, with the exception of activities related to agriculture, sylviculture and horticulture. Due to diverse anthropogenic influences, urban soil typically shows strongly heterogeneous properties. Conventional methods for soil survey, which commonly rely on a limited number of discrete observations from borehole drillings and excavations, are often insufficient to capture the full extent of the spatial heterogeneity. Proximal geophysical sensors enable measuring physical soil properties in a non-invasive way, providing an efficient alternative to collect spatially comprehensive soil data. These sensors have an established reputation in the application fields of precision agriculture and (geo)archaeology, but their use for characterizing soil in urban and industrial environments remains largely unexplored.

The general objective of this doctoral research is to evaluate the potential of proximal geophysical sensors for soil investigation in urban and industrial areas. In these areas, soil investigation often is motivated by the presence of soil contamination and land redevelopment mostly follows from the need for soil remediation. As waste disposal and industrial and commercial activities are two main causes of local soil contamination, this research focuses on landfills and industrial/commercial sites. In addition, in the recent few years intensified attention has been addressed to the reclamation of landfills due to the establishment of the concept of enhanced landfill

mining (ELFM). This concept aims at the sustainable integration of landfill management and the valorization of its accompanied resources of materials, energy and land. The application of proximal sensing is evaluated from a pragmatic perspective, in view of their use in the daily practice of soil investigation as conducted in the environmental consultancy and land redevelopment industry.

Two types of geophysical sensors are considered, the operation of which relies on the principles of electromagnetic induction: electromagnetic induction (EMI) and ground penetrating radar (GPR). The method of EMI allows measuring the electrical conductivity (EC) and the magnetic susceptibility (MS) of the soil. A multi-receiver instrument is used that enables the simultaneous sensing of multiple soil volumes extending to different depths. Through GPR, contrasts in the soil dielectric permittivity can be mapped. The specific GPR system used is a stepped-frequency system, recording measurements in the frequency-domain over a wide frequency bandwidth. As compared to conventional time-domain GPR systems, this has the advantage of overcoming the trade-off between measurement resolution and depth of exploration: an optimal resolution is offered for each achievable measurement depth. Both EMI and GPR are implemented into a mobile survey configuration which further expedites the collection of spatially comprehensive data with a high sampling density.

The performance of EMI for the characterization of landfills was evaluated based on four case studies, in which the considered landfills varied in construction setting, size and the type of waste that was disposed. High-resolution EMI surveying allowed to produce detailed maps of subsurface variations in electrical conductivity. This enabled accurate determination of the landfill's location and lateral dimensions. The measurement values, and their spatial heterogeneity, also provided an indication of the nature of the disposed waste materials. The vertical delineation of the disposed waste generally proved to be difficult due to various reasons. The interface between waste and host materials was below the measurement depth of the sensor (maximum 6.4 m), or could not be unambiguously resolved because of the interference of numerous shallow metal objects in combination with the reduced vertical resolution of the measurement signals at larger depth.

The combination of EMI and GPR was first tested at a former garage with petrol station, at which previous soil investigation had indicated contamination with petroleum hydrocarbons. The sensor combination demonstrated the ability to identify and accurate locate building remains and the upper boundary of a high-density soil layer, which likely represented a former living surface. Furthermore, a correspondence

was found between an area of lower electrical conductivity and elevated concentrations of petroleum hydrocarbons.

Finally, EMI and GPR were combined for soil investigation at a former manufactured gas plant. Different localized structures/phenomena could be successfully detected and identified, including utility infrastructure such as an electric cable, remains of foundations and a presumed contamination with salts.

Generally, it is concluded that proximal geophysical sensors are ideally suited for reconnaissance surveying in the initial stage of site investigation. The spatially exhaustive data provided by EMI and GPR surveys can guide the design of invasive sampling campaigns. The sample size and locations can be targeted to actual contrasts in subsurface properties, which not only improves sampling efficiency but also increases the reliability and representativeness of the results. Therefore, the proposed methodology for high-resolution surveying with EMI and GPR presents a promising tool to enhance soil investigation in urban and industrial environments.

Chapter 1
Introduction

1.1 Urban soil: omnipresent yet misconceived?

The historical development of human populations has left indelible traces in their habitat landscapes and the soil they rest upon. Particularly from the Industrial Revolution onwards, significant areas of land have been affected by human activities related to urbanization and industrialization. Urban soil has become a non-negligible part of our modern living environments and is still continuously "winning ground" as urbanization further evolves. It has been agreed upon that proper understanding and management of soil in urban and industrial environments is pivotal to provide a sustainable basis for future human development (e.g. Lehmann & Stahr, 2007). Despite its omnipresence, our knowledge of urban soil remains fragmented. Because of its inferior importance for agricultural production, the subsurface in urban and industrial environments was largely ignored in early soil science. Legacy soil maps are a poor source of information as these areas commonly correspond to grey zones. Furthermore, due to various anthropogenic influences, urban soil typically has properties that are distinct from natural and agricultural soil, which makes it is hardly compatible with the constitutive concepts of classical soil science. The extreme spatial heterogeneity of urban soil is a key example (e.g. Greinert, 2015). Small-scale spatial variations are recalcitrant to reconstruction from conventional soil survey campaigns, which generally consist in a sparse number of discrete observations from borehole drillings and excavations. Despite that the scientific literature of recent decades testifies to an increased attention devoted to urban soil in general, and on the assessment of its functionality in particular, there is currently no universal consensus

on how to tune the traditional pedological toolbox to the specific characteristics of soil in urban and industrial environments. Furthermore, these environments are the main operating base for land development and reclamation activities. The acquisition of reliable and representative information about the subsurface is a prerequisite for success. However, in such projects, soil investigation mostly is orchestrated under stringent economic constraints of available time and budget. Hence, in addition to the scientific interest in improving our understanding of urban soil dynamics, the environmental consultant and land (re)development industry provides an incentive to search for new tools allowing to tackle urban soil investigation in a more efficient way. This research explores the potential of proximal geophysical sensing to support soil investigation in view of urban soil assessment and management.

1.2 Investigating urban soil via proximal geophysical sensing

Soil sensing essentially refers to the measuring of soil properties in a non-invasive way. As compared to conventional soil survey methods, sensing techniques have the competitive advantage of being inexpensive and fast, and therefore are ideally suited for high-resolution soil mapping or to cover large areas in a relative short period of time. Particularly the first is of interest for investigating soil with highly heterogeneous properties as is commonly the case in urban and industrial environments. In a proximal set-up, the sensor is in contact with the soil, within the soil body or at its surface, or in its direct vicinity, i.e. within 2 m distance (Viscarra Rossel et al., 2010, 2011). Geophysical sensors are those concerned with measuring physical properties of the earth. The application of proximal geophysical sensors can be situated at the interface of two disciplines, *proximal soil sensing* and *near-surface applied geophysics* (Figure 1.1). Within these disciplines, what is the perspective on urban soil?

In its elementary sense, proximal soil sensing is the oldest activity in soil science. More specifically, the term *proximal soil sensing* indicates a particular area of soil science in which the human senses have been supplemented with modern technology to unravel the secrets of the subsurface. Despite having been mainly developed in the latest decades, proximal soil sensing strongly adheres to its roots in the more traditional soil science and it is primarily associated with agricultural applications (e.g. Adamchuk et al., 2004). In recent years, proximal sensing techniques also have made their mark in the field of (geo)archaeology, demonstrating their value for the investigation of soil which developed in interaction with human activity (e.g. De Smedt,

Saey, et al., 2013; De Smedt, Van Meirvenne, et al. 2013, De Smedt, Van Meirvenne, et al., 2014; Saey et al., 2013). A few hot-of-the-press publications aside (e.g. Howard et al., 2016), the practice of proximal soil sensing seems to be shunning urban environments, in which the complexity of anthropogenic soil interference is taken to an even higher level.

The longer standing discipline of *near-surface geophysics*, evolved from a geological background, per definition applies physics to the investigation of 'the very outermost part of the earth's crust' (Butler, 2005, p. 1). In most near-surface investigations the depths of interest are less than 10 m, but there are also investigations to depths of 300 m or more (Butler, 2005; Everett, 2013). Although the vertical extent of the near-surface may not be sharply delineated, it is clear that soil as the epiderm of the earth (Nachtergaele, 2005) is included. Furthermore, environmental and engineering site investigations form one of the most important applications of near-surface geophysics, in which many of the targeted subsurface phenomena have been induced by human activities associated with urbanization and industrialization, for example, contaminant mapping, locating buried metal containers, characterization of the foundation beneath building structures (Reynolds, 2011; Teixidó, 2011). In the beginning of the 1990s, the term *urban geophysics* was coined capturing applications of geophysical techniques 'to solving special problems in urban environments' (Henderson, 1992, p. 531). This acknowledged the challenges involved in mastering these environments, such as logistical, operational and regulatory – and possibly also social and political – constraints, the higher level of ambient noise, and the high heterogeneity of the shallow subsurface requiring improved resolution and precision. About twenty years later, relaunches of the subject re-emphasized the relevance of tweaking conventional geophysical survey protocols to be successfully implemented in urban settings in view of supporting urban planning and development (Liu & Chan, 2007; Miller, 2013; Verma & Sharma, 2011). However, the subdiscipline has remained low-profile and, despite the heterogeneity of the shallow, soil part of the near-surface is a point of special interest, the majority of research contributions originates from geotechnical studies for construction activities and investigations associated with geological hazard evaluation, which commonly relate to deeper targets. In general, in geophysical literature an explicit link to urban and industrial landscapes – let alone to urban soil – is only occasionally made (e.g. Boudreault et al., 2010; Kulessa, et al., 2006; Vaudelet et al., 2011; Pazzi et al., 2016). This is probably also due to the relatively recent establishment of the concept of urban soil. However, that the

complexity of the uppermost near-surface layer has led to its designation as a mere 'zone of cultural noise' (Everett, 2013, p. 72; referring to the study of Rucker et al., 2010) betrays there is more involved than just semantics.

For both proximal soil sensing and near-surface geophysics the application to urban soil seems to be beyond the comfort zone. However, the common ground between the disciplines, complemented with knowledge from related, more established application areas, holds an underestimated potential to advance the investigation of urban soil, which is the central research objective of this work (Figure 1.1).

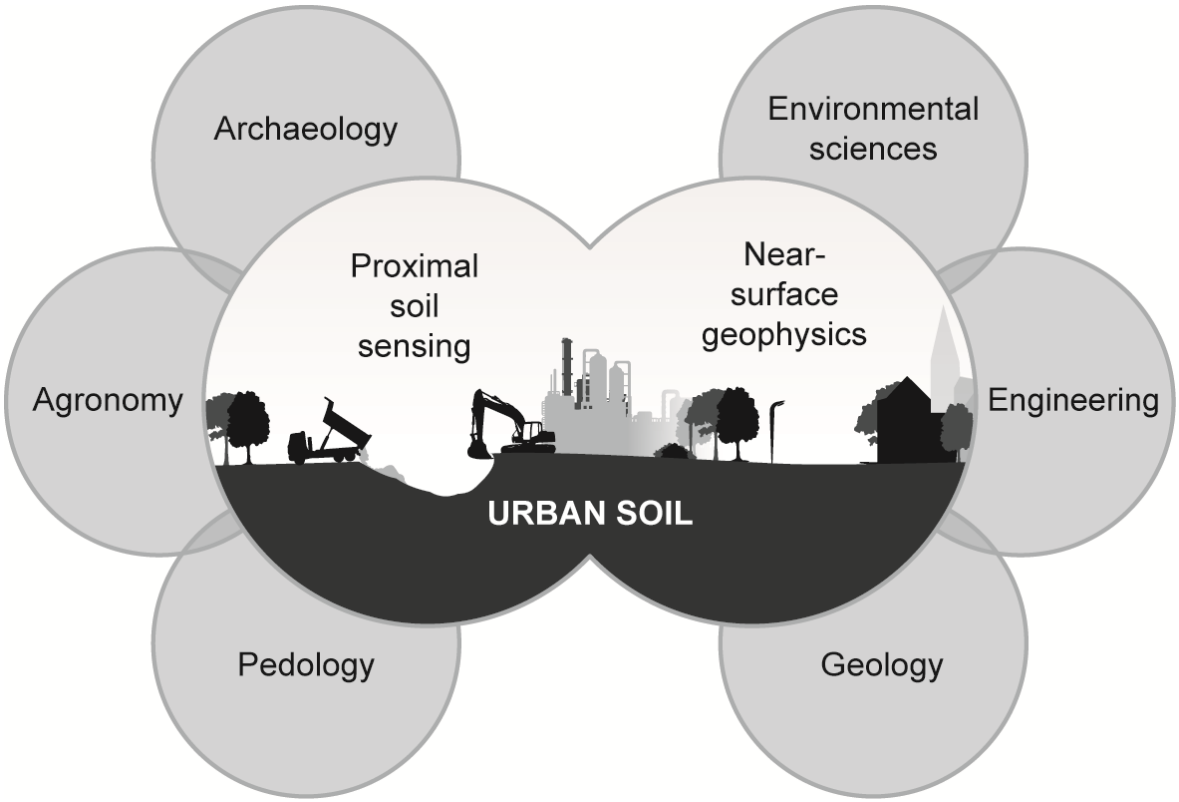

Figure 1.1 Proximal geophysical sensing: a multidisciplinary approach to investigating urban soil.

1.3 Research scope and objectives

The overall objective of this work is to evaluate the application of proximal geophysical sensors to the investigation of urban soil. The research scope is further narrowed down according to the following aspects.

Geographically – Flanders, Belgium. The research question will be addressed by conducting a series of case studies, each of which are situated in the region of Flanders, the northern part of Belgium. In this respect, the results reflect to the

Flemish context of urbanization and industrialization. Belgium belongs to the top ten most urbanized countries in the world, with nearly 98% of its population living in urbanized area (United Nations [UN], 2014). Considering the population distribution over the three different regions of Belgium, namely Brussels, Flanders and Wallonia, the degree of urbanization in Flanders is anticipated to be even higher than that of the country average (see Chapter 2 for more details). Flanders is characterized by a fragmented landscape of urban sprawl; the region has been described as one large diffuse city (De Decker, 2011; De Vos, 2015). This provides a wealth of opportunities to advance the investigation of urban soil. Yet, it is noted that while the geographical research domain of this work is limited to Flanders, the local environments considered in the different case studies are deemed exemplary of urban and industrial settings found in all parts of the world, at least in those with a similar level of development. Hence, the conclusions of this work can be generalized well beyond the boundaries of Flanders.

Urban land use – Landfills and industrial/commercial sites. Particularly in urban and industrial areas, soil contamination is a widespread problem, which poses a key threat to the soil ecosystems functions (Jones et al., 2012). The (suspicion of the) presence of soil contamination can be considered a primary driver for the examination of urban soil, in both an academic and industrial context. Soil examination at these sites generally aims at assessing the risk posed to human health and the environment in order to devise a proper management strategy, with respect to the future land use destination and current legal requirements. Therefore, the necessity of remediation measures is a common trigger for land redevelopment. Two main causes of local soil contamination are past and present industrial or commercial activities, and the inadequate or unauthorized disposal of waste (Panagos et al., 2013). This research focuses at urban soil associated with a (former) land use as industrial/commercial site or as landfill, as these sites are characterized by a more insistent tendency towards redevelopment in the near future. Furthermore, in the recent few years intensified attention has been paid to the redevelopment of landfill sites due to the establishment of the concept of enhanced landfill mining (ELFM, Jones et al., 2013). This concept aims at the sustainable integration of landfill management and valorization of the its accompanied resources of materials, energy and land. The region of Flanders was the cradle of ELFM and, under coordination of the Public Waste Agency of Flanders (Openbare Vlaamse Afvalstoffenmaatschappij, OVAM), committed efforts are being

made to support the further research, implementation and policy development on the topic.

A few figures are given to substantiate the relevance of studying these sites. From data collected through the European Environment Information and Observation Network, it has been estimated that Europe hosts more than 2.5 million potentially contaminated sites, of which about 14% are confirmed to be contaminated and are likely to require remediation. Waste disposal and treatment contributes most to soil contamination (37%), in which municipal and industrial wastes have similar shares. Industrial and commercial activities take the second place with a contribution of 33%. In the production sector, metal industries are the most frequently reported sources of contamination (15%), while in the service sector, gasoline and car service stations are the most important sources (21%). This is consistent with heavy metals and mineral oils being the most frequently occurring contaminants (Panagos et al., 2013; van Liedekerke et al., 2014). For Flanders, records on potentially contaminated sites are gathered in the Land Information Register which is managed by the OVAM. The register is not yet completed, but the number of sites in Flanders with a high risk of contamination is currently estimated at 85 000 (OVAM, 2017a).

In 2015, the European Enhanced Landfill Mining Consortium (EURELCO) organized a dedicated data collection on the landfill situation in Europe through a bottom-up inventory (EURELCO, 2015). The total number of landfills is estimated at more than 500 000, of which 90% have been constructed without environmental protection technologies and are likely heading for a remediation scenario. Around 80% of the landfills chiefly contain municipal solid waste (MSW), the remaining 20% consist of industrial waste (IW). Comparison with the abovementioned data on Europe's contaminated sites suggests the bottom-up inventory underestimates the total number of landfills. Furthermore, there seems to be a discrepancy in the relative distribution of municipal and industrial waste landfills. The number of landfill sites in Flanders is rated at more than 2000, covering a total area of nearly 90 km² (OVAM, 2015; see also Wille, 2016).

Methodologically – High-resolution electromagnetic induction and ground penetrating radar surveying. Among the geophysical methods, electric and electromagnetic methods have been the most popular for environmental and engineering site investigation, because the majority of relevant targets in this context result in changes of the soil electrical properties (Pellerin, 2002; Tezkan, 1999). In practice, however, electromagnetic methods are far underrepresented as compared to

electric methods. This is likely partly due to the more established processing routines available for electric methods. Yet, the principle of electromagnetic induction has a major advantage in that direct contact with the ground is not required and, consequently, the speed with which electromagnetic surveys can be made is much greater than for their electric counterparts. Furthermore, more flexibility is offered for application on rough terrain or on surfaces that are covered with hard, technogenic material such as asphalt or concrete, which is particularly pertinent in urban and industrial environments. In this work, the focus is on the two electromagnetic methods of electromagnetic induction (EMI) and ground penetrating radar (GPR). Consistent with a sustained striving for more efficient data collection, both techniques in recent years have witnessed significant technological improvements facilitating high-resolution surveying (Auken et al., 2006). For EMI, the state-of-the-art sensors are multi-receiver (e.g. Saey, Simpson, et al., 2009; Simpson et al., 2010; Triantafilis et al., 2011) or multi-frequency (e.g. Marchetti & Settimi, 2011; Martinelli & Osella, 2010) instruments that enable – or in the case of the latter at least have been claimed to enable –the simultaneous sensing of multiple soil volumes extending to different depths. The GPR technology has developed towards more effective coverage of three-dimensional (3D) space with the introduction of antenna arrays (Novo et al., 2012) and multi-frequency systems (Eide & Hjelmstad, 2002). In addition, these latest sensor designs allow for integration with real-time geo-referencing and implementation in a mobile survey platform, supporting horizontal sampling resolutions in the decimetre to centimetre range. The luxuriant data sets obtained with these sensing systems open up new prospects for analyses of soil volumes featuring complex, small-scale variability. In this work, a multi-receiver EMI sensor and a stepped-frequency GPR system with motorized conveyance are put to the test.

The performance of these proximal geophysical sensors is evaluated according to the following criteria:

- the practical implementation of the proposed mobile survey platforms,
- the stand-alone interpretation of the acquired sensor data,
- the integration of the sensor data with conventional soil information, and
- the relevance of gained information to support remediation and/or redevelopment of the site.

Considering the majority of urban soil investigations is developer-driven, the research objectives will be dealt with from a pragmatic point of view, in the sense that it is examined how geophysical surveys can be of assistance to the daily practice of

soil investigation as conducted in the environmental consultancy and land redevelopment industry. While some authors of scientific literature give the impression that these surveys are a well-established practice outside the academic context (e.g. Wang et al., 2015), this is certainly not a general truth. In most legal protocols for site investigation and assessment the integration of information from non-conventional survey methods also remains unaddressed or a subject of discussion. Conventional approaches are primarily geared towards data collection in view of human and ecotoxicological risk assessment, to which non-convential data as from geophysical sensors mostly only contribute indirect information. An exception is the so-called Triad approach developed by the United States Environmental Protection Agency (US EPA): next to systematic project planning and dynamic work plan strategies, innovative technologies providing for "real-time" data collection and analysis in the field are recognized as a key element in an advanced approach to hazardous waste site characterization and remediation (United States Environmental Protection Agency [US EPA], Office of Solid Waste and Emergency Response, 2003). While the standard procedure for descriptive soil examination (OVAM, 2017b), a quality reference for soil investigations conducted in the framework of the Soil Decree (VLAREBO, 2008), recommends geophysical investigations as useful alternative tools to complement conventional soil investigations, their application is far from standard practice in Flanders. Land developers may not be familiar with geophysical techniques or may have some reservations about their results. In a commercial survey, any investigation technique applied is expected to contribute concrete information as direct input to the planning of remediation and reclamation actions. Yet, few geophysical methods specify a unique solution to a specific multivariate distribution of subsurface properties and, in general, the interpretation of geophysical data can only be successful when tested against the constraints of the physical reality, which is all the more relevant in intricate survey environments as those associated with urban soil. Therefore, this work aims to formulate some boundary conditions for the proper application of proximal geophysical sensing tools in an urban setting and to elucidate the quality and usefulness of the data that can be acquired, in order to clear up some misunderstandings on the information that can be gained.

1.4 **Structure of the thesis**

The structure of the thesis is visualized in Figure 1.2. After – almost literally – having been confronted with the question "Do you still consider it *soil* that you are investigating?", Chapter 2 of this dissertation has decidedly been devoted to the concept of *urban soil*. Some background is given on the historical struggle of the urban subsurface to be recognized as soil, but it is also argued why the answer to the aforementioned question is a resolute "Yes". A working definition for urban soil is composed, which then serves as a basis for further analysis of the significance of this soil for the example of Flanders. Ample consideration is given to the challenges involved in investigating urban soil, which motivate the exploration of the alternative provided by proximal sensing techniques. Chapter 3 enlarges on the specific sensor technology and survey methodology that will be evaluated. For both the electromagnetic methods of EMI and GPR, the operating principle, instrumentation, survey design and data processing are discussed. The interpolation of the survey data is addressed in a separate section. In the last section of this chapter, the factors influencing the electromagnetic response of soil are reviewed, providing some basic guidelines for data interpretation. In preparation of Chapter 5, Chapter 4 sketches the theory behind the practice of geophysical surveying of landfills: how do geophysical sensor data relate to the structure of the landfill and the types of waste disposed? In Chapter 5 follows the presentation of four case studies in which the application of high-resolution EMI surveying is evaluated for landfill characterization to support the development of an appropriate land reclamation scenario. The landfills considered vary in construction setting, size and the type of waste disposed. In Chapters 6 and 7, the value of combining EMI and GPR is researched for the characterization of contaminated commercial/industrial sites. In the first, a former garage and gasoline station is considered; the latter involves a former manufactured gas plant. In the final chapter, the most important conclusions on the application of the proposed geophysical sensing methods to urban soil are highlighted and some prospects for future research are suggested.

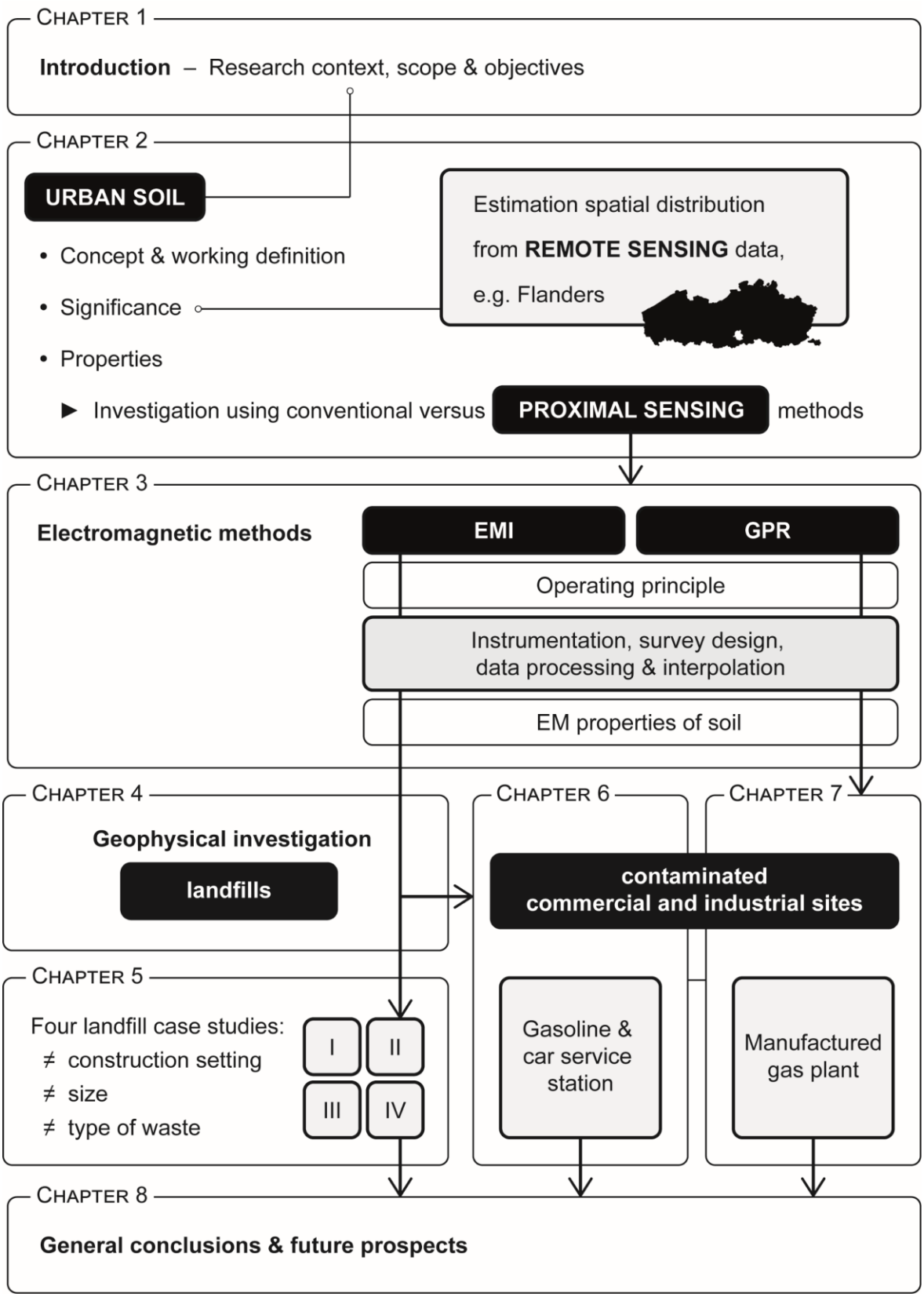

Figure 1.2 Structure of the thesis

Chapter 2
The challenge of urban soil

2.1 Soil versus urban soil

'The menu is not the meal.' – Alan Watts

2.1.1 The classical "profile" of soil

Many works of soil science literature open with an attempt to define the central concept under study: what is *soil*? Hans Jenny honours this custom in his 'Factors of soil formation' by devoting the first chapter on definitions and concepts. Yet, he immediately puts the question into perspective: 'As a science grows, its underlying concepts change, although the words remain the same' (Jenny, 1994, p. 4). The author agrees with Jenny in that there is no timeless definition of soil and, even more importantly, that there also is no need to establish one, in the conviction that soil science can only benefit from a dynamic and multi-perspective approach. The motive behind these introductory paragraphs is not to break new ground in the quest for a universal soil definition, but to accentuate the particularities of soil in urban and industrial areas against the background of the classical concept of soil in general.

The definition formulated by Joffe (1936) serves as a good reference of the concept of soil in early pedology:

> The soil is a natural body, differentiated into horizons of mineral and organic constituents, usually unconsolidated, of variable depth, which differs from the parent material below in morphology, physical properties and constitution, chemical properties and composition, and biological characteristics. (p. 37)

With his definition, Joffe (1936) meant to emphasize the change in properties induced

by the transformation of "rock" or parent material into soil, by processes of soil formation. Soil at the time was exclusively studied in natural or agricultural contexts and, in classical pedology, formation of soil was attributed to five factors: time, parent material, topography, climate and organisms. The crux of the soil formation concept proposed by Jenny (1994) is that each of these factors possesses the properties of an independent variable, i.e. it can be made to vary independently of other variables. From the perspective of urban environments, special attention deserves to be directed to man as a soil-forming factor, who in principle is subsumed under the factor of organisms or the biotic factor. Whereas the influence of man on soil originally may have been unconscious and inconsiderable, through history man developed the ability to consciously and intentionally shape land and, by extension, soil. This ability makes the independence of man as biotic soil-forming factor of a different order than the role microorganisms, plants and animals can play. Dudal (2005) considers this an important argument advocating the recognition of man as a separate, sixth soil formation factor. The effect of human activities on soil formation often is indirect, occurring through modification of other soil-forming factors. Modern urbanization and industrialization activities almost routinely include excavations, transport of (soil) materials and levelling, raising or sealing of the surface, entailing the introduction of new parent materials (Dudal, 2005), changes in local topography and modifications of soil climate and biology. Other than soil sealing, irrigation and drainage are typical examples of human intervention in climatic conditions. Crop cultivation is the most prominent example of man controlling the vegetational soil cover (Jenny, 1994). Generally, one could say that the independent behaviour of parent material, topography, climate and non-human organisms has become conditional to the behaviour of man. Man's ability to control the remaining factor of time, to the author's knowledge, has not yet escaped the limits of science-fiction. Nevertheless, human-induced soil changes occur on a wide range of time scales, which can be much shorter than those associated with natural pedogenic processes. Supported by technological tools, soil operations are usually concentrated in short, economic time intervals, such as the installation of new soil material for building and construction purposes. Man can also indirectly accelerate soil formation processes, for instance, by introducing technogenic materials that are highly reactive (Rossiter, 2007). According to Jenny (1994), any change in one of the soil-forming factors starts a new cycle of soil formation and, hence, any soil subjected to such a change, by definition, is reset to parent material. In urban areas, where the subsurface intensely and recurrently is

modified by human interventions, the possible lack of time for actual pedogenesis to occur, gives rise to the question whether the subsurface in these areas is still to be considered as soil (Rossiter, 2007; Dudal, 2005). Apart from this soil-formation issue, the subsurface in urban areas commonly conflicts with the definition of soil morphology as prescribed by the classical soil concept. Soil horizons often cannot, or can no longer, be discriminated because the original soil profile has been truncated, physically, chemically or biologically altered, or buried beneath new parent material. Exploitation of earth materials and land disposal of wastes have basically been practiced since the dawn of man. However, the amounts of materials being transported to become new parent material have shown ever-increasing trends, and, particularly from the Industrial Revolution onwards, a significant part can consist of technogenic materials – i. e. materials created by involvement of human technology. The properties of these can fundamentally differ from the mineral and organic constituents of natural soil and within themselves can be extremely heterogeneous (Greinert, 2015, Lehmann & Stahr, 2007). An illustration of the prominence of technogenic materials in the subsurface of built-up land and a former landfill is given in Figure 2.1. In addition, technogenic parent materials can lead to divergent pedogenetic processes (Huot et al., 2014, 2015). Similar to natural deposits, deposits of anthropogenic origin usually are initially unconsolidated, but the processes of subsequent settlement can be different, as, for example, has been observed in landfills of MSW (e.g. El-Fadel et al., 1999). Furthermore, a parallel can be drawn between MSW decomposition processes and weathering of geological materials (e.g. Meju, 2000). Whereas our understanding of soil formation processes in urban and industrial areas remains fragmented, these processes do obey general physical, mechanical and pedological principles. The study of management of materials in the present and the past can be a good lead for further research on urban soil formation (Lehmann & Stahr, 2007).

2.1.2 **A track record of *urban soil* in soil science**

Notwithstanding the recognition of *urban soil* has long been debated, soil in urban and industrial areas has been considered since the rise of modern soil science. According to Lehmann & Stahr (2007), anthropogenic urban soil was first mentioned in the soil science book of Ferdinand Senft (1847), discussing its reduced fertility due to contamination and thereby corroborating the initially predominantly agricultural interest in soil. However, the focus of soil studies conducted in urban environments

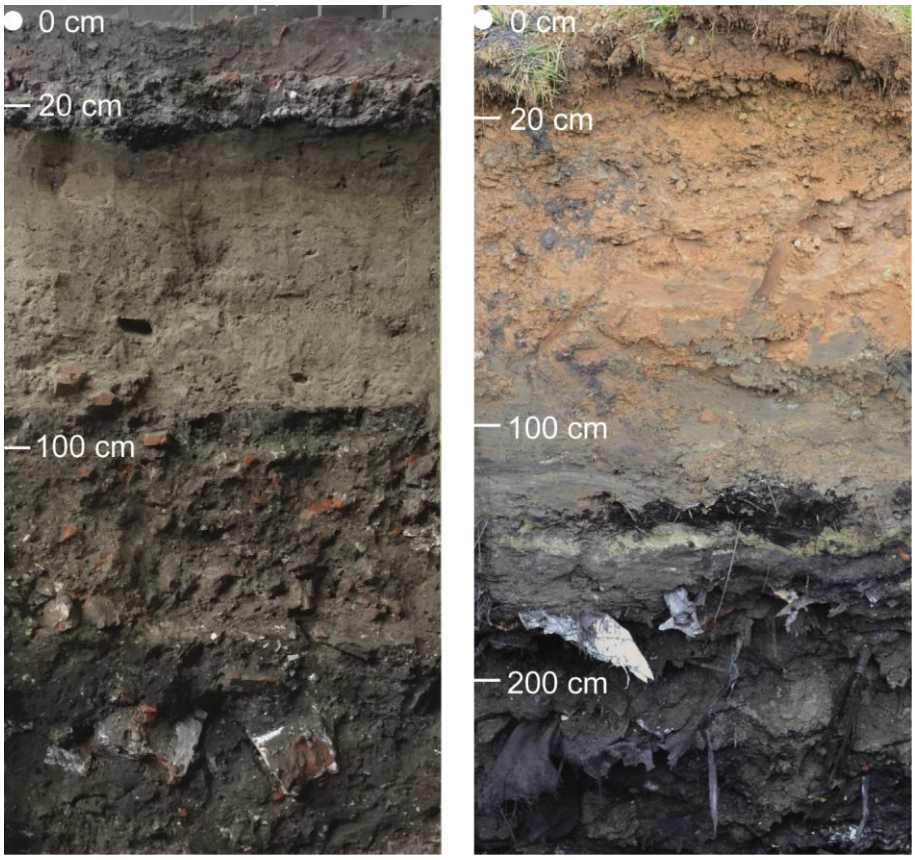

Figure 2.1 Two example profiles of anthropogenically changed soil in Flanders, Belgium: (left) built-up soil in the inner city of Ghent, the present building originates from the construction of a "stone circus" at the end of the 19th century, which was converted to a garage shortly after World War II (Source: Department of Soil Management, Ghent University, Delbecque, N., 2015); (right) former landfill from MSW covered with relocated soil material, recently used as grassland, located in a village near the Brussels-Capital Region (not localized any closer because of guaranteed anonymity). Note the perspective in depth in the photograph on the right.

was soon diverted to the hazards that soil pollution pose to human health (e.g. Purves, 1967), which has remained an important research topic until today (e.g. Bavec & Gosar, 2016; Delbecque & Verdoodt, 2016). Starting from the 1950s, local initiatives were launched to study soil from the perspective of urban development and spatial planning, recognizing the importance of soil functions other than agricultural production (e.g. Pettry & Coleman, 1973; Lindsay et al., 1973). These studies emphasized the use of soil information to evaluate the land suitability for the construction of buildings and roads, and for the installation of drainage and sewage systems, and sanitary landfills. Hence, they were among the first to touch upon two soil functions that later were identified as key functions of soil for society and the environment: (1) soil serves as a physical basis for human activities (e.g. for the development of infrastructure for housing, industrial premises, transport and

recreation), and (2) soil protects humans and the environment against contamination (e.g. from sewage and solid waste disposal; Blum, 2005).

As the general interest in ecology started to grow, the ecological functions of soil were highlighted. According to Lehmann & Stahr (2007), the significance of urban soil in urban ecology already received attention in the 1970s. However, this is only poorly reflected in scientific literature, which situates the burgeoning of the topic of urban ecosystems a few decades later (e.g. Grimm et al., 2000). Around the turn of the millennium, global change was the ecological topic in the limelight and, as soil plays a key role in the carbon cycle, this promoted research on soil organic matter (OM). Appreciating the significant contribution of urbanization to carbon cycle changes, also the study of carbon storage and dynamics in urban environments has gained increasing interest in recent years (e.g. Beyer et al., 2001; Dorendorf et al., 2015; Lal, 2007; Pataki et al., 2006; Pouyat et al., 2006). Besides the contribution of urban soil dynamics to climate change, the reverse causal connection is a new research topic, for instance, Rawlins et al. (2015) review the possible impacts of climate change on urban soil functions.

Today, there is a common consent on that, whether in a natural, agricultural or urban environment, soil essentially performs the same basic functions (De Kimpe & Morel, 2000). Although in some cities urban agriculture is strongly growing, the major weight of provisioning food, fresh water and raw materials stays on soil in rural areas. Yet, other imperative environmental and socio-economic functions of soil are concentrated in urban environments, such as carrying infrastructure, protecting against pollution of groundwater and the food chain, and preserving our cultural heritage. Furthermore, the interaction and competition between soil functions in these environments is more intense (Blum, 2005; Lehmann & Stahr, 2007; Rawlins et al., 2015). In recent years, awareness has grown that sustaining the functionality of urban soil is crucial to human development and it is increasingly recognized that urban soil is part of our natural capital requiring proper protection and development (e.g. Lehmann & Stahr, 2007; Rawlins et al., 2015). In 2014, 54% of the world's population lived in urban areas and this percentage is expected to increase up to 66% by 2050 (UN, Department of Economic and Social Affairs, Population Division, 2015). As a consequence, it can be assumed that the use of urban soil, within its current territory, will be further intensified and, at the same time, its territory will expand. In spite of the significant research progress made in the latest years, knowledge of urban soil in general and of the soil processes governing its functions in particular remains largely

incomplete. Hence, researchers advocate urgent attention to these issues, to be able to anticipate effects of proceeding urbanization in the near future.

Being confronted with the emerging omnipresence of urban soil, in the real world and as research concept, at the end of the 1980s, pedological societies started to set up more committed research efforts, aspiring to introduce the concept of urban soil into the conventional pedological framework (Lehmann & Stahr, 2007). It should not be surprising that soil scientists shared many different visions on the issue and particularly the adoption of urban soil into existing soil taxonomic systems became the subject of protracted controversy. Over the past decades, a multitude of proposals has been made. A milestone was reached in 2006, when anthropogenic urban soil was acknowledged in the world reference base for soil resources (WRB) with the inauguration of the soil group 'Technosols' (International Union of Soil Science [IUSS] Working Group WRB, 2006), following the suggestion of Andreas Lehmann (Lehmann, 2006). Some soil classifications still assign only a dubious status on soil developing from substrates of anthropogenic origin, e.g. the Russian soil classification system excludes technogenic surface formations (Prokof'eva et al., 2014), and even the fathers of the WRB still associate Technosols with *non-soils* (e.g. Food and Agriculture Organization of the United Nations [FAO] & Intergovernmental Technical Panel on Soils [ITPS], 2015). Nevertheless, it is safe to say that *urban soil* today is an established concept in soil science.

2.1.3 **Defining urban soil**

Along with the pedological attempts to “profile” urban soil, several definitions of the concept have been provided. Urban soil can be considered in a broad sense, as soil 'profoundly affected by urbanization' (Lehmann & Stahr, 2007, p. 248), which automatically redirects to a definition of *urbanization.* Lehmann and Stahr (2007) hold to the general dictionary definition indicating urbanization is the process of becoming more like a town or city. Urbanization can also be expressed in terms of population, as in the information provided by the UN (e.g. UN, 2014). Similarly, Meuser (2010) defines urbanization as 'the increase in share of urban population in relation to the total population in the area of concern' (p. 6). Some specific examples of man’s manipulation of soil have already been given above, but to achieve a more comprehensive and concrete interpretation of urbanization with respect to its effects on soil, it is adequate to consider the different types of human activities involved. Housing, trading, traffic, non-agricultural production and disposing of accompanying

wastes usually are concentrated in urban and suburban areas, i.e. in city centres and their surrounding residential and industrial suburbs. Mining and agricultural production, on the other hand, are mostly situated outside city boundaries. The long-term submission of soil to agricultural practices such as ploughing, terracing and flooding can also have significant, cumulative, effects on the soil's properties (Norra & Stüben, 2003; Lehmann & Stahr, 2007). It is noticed that, in contrast to soil in urban areas, the anthropogenic nature of such agricultural soil has never jeopardized its standing of *soil*, because this soil served the common good of food production. Lehmann (2006) points out that there is no agreement on whether all soil within the boundaries of cities and conurbations is urban soil. He defines urban soil in 'a more pedological' way, as soil that is 'strongly influenced by human activities such as construction, transportation, manufacturing processes, industry, mining, rural housing and similar activities' (p. 130). The definition of Meuser (2010) lists influential human activities and related side effects in a more concrete form, yet again includes a geographical restriction: 'Urban soils are soils in urban and suburban areas consisting of anthropogenic deposits with natural (mineral, organic) and technogenic materials, formed and modified by cutting, filling, mixing, intrusion of liquids and gases, sealing and contamination' (p. 5).

Working definition

In this work, urban soil identifies soil that has been profoundly affected by activities that support or have supported the modern-day process of urbanization and/or industrialization, with the exception of activities related to agriculture, sylviculture and horticulture. This definition essentially conforms to the one given by Lehmann (2006). The strict connection to urban and suburban areas is omitted as the (administrative) boundaries defining them are arbitrary and therefore are regarded as a poor indicator of human influence on soil. For instance, the soil at mining and waste disposal sites, the location of which can be more remote, is also considered to be urban soil. On the other hand, it is possible for natural soil to occur within the boundaries of a city. This soil is outside the postulated definition of urban soil and will simply be termed ‘natural soil’ instead of ‘natural urban soil’, the latter of which, for example, is used by Lehmann & Stahr (2007). The same principle can be applied to agricultural soil, assuming agricultural soil refers to soil that has been altered exclusively by agricultural activities. In practice, natural and agricultural soil within city limits is rare, especially in developed countries. Even when a city soil is used for urban green space or urban agriculture, it is often man-made or influenced by urban or industrial activities

in the neighbourhood, such as by atmospheric depositions from traffic emissions. Furthermore, there is no restriction imposed on the thickness, nor on the depth, of the soil layer that evidences the influence of urbanization. For example, the soil classification system for England and Wales requires a layer of artificially displaced material of at least 40 cm thickness for soil to be considered disturbed (Avery, 1980). The author prefers to approach the significance of urbanization effects in a qualitative way. Soil with a layer of technogenic nature at or near the surface is deemed urban soil, irrespective of the layer thickness. However, the focus is on effects of recent human activities that are presumed to occur within the first few meters below the soil surface – hence the reference to modern-day urbanization and industrialization – and not on archaeological artefacts that, over millennia of time, have been buried more deeply under influence of natural soil formation processes.

Also for soil in general an inclusive definition is favoured. For the subsurface to be considered as soil, it is not an absolute prerequisite for a minimum degree of "natural" soil development to have occurred. Urban soil in particular is mostly still young soil (e.g. Lehmann, 2006) and the role of classical soil formation processes often is subsidiary to human-induced transport and accumulation of material (De Kimpe & Morel, 2000).

As a final remark, it is explicitly mentioned that throughout this work soil is in singular form. Soil is viewed as a continuum of which the properties vary in space and time and not as a set of individual soil units with distinct properties, as is the rationale underlying soil classification systems. Specifically for urban soil, the spatial and temporal heterogeneity of soil properties can be large. Without wanting to undermine the value of comprehensive soil classification systems to improve our understanding of urban soil, one should mind that severe heterogeneity defies the soil classification logic. In addition, by using soil in singular, the author wants to emphasize the soil identity of urban soil: urban soil has properties that may be markedly different from those of natural of agricultural soil, but it still is soil. It would be mistaken to represent the subsurface in urban and industrial areas as outlying soil units in the soil population distribution. The main aim of this work is to investigate alternative means to study urban soil properties. Despite much of the terminology used in this chapter is drawn from literature on soil taxonomy, addressing unresolved controversies in urban soil classification goes beyond the scope of this work.

2.2 The urban soil information gap

'The map is not the territory.' – Alfred Korzybski

2.2.1 Conventional soil survey and legacy soil maps

The general purpose of a soil map is to enable more accurate and more meaningful predictions of specific soil properties to be made than could have been made without location-specific information about the soil, i.e. without a soil map. In the traditional approach to soil mapping, land area is subdivided into polygons resulting in the creation of a choropleth map. Soil survey for the purpose of producing such a soil map follows a three-step procedure:

1. Creating a map legend. The legend should consist in relatively homogeneous units with comparable within-unit variability. This process can be supported by ancillary information such as observations of soil cover, aerial photography and geology. Each legend unit then represents a soil type; this step expresses the strong link between soil mapping and soil classification.
2. Identifying and mapping the spatial distribution of the legend units or soil types.
3. Characterizing the soil types through representative soil profiles or other means of soil sampling, so that soil types can be related to their potential for specific land use or land management (FAO, 2016).

For the description of urban soil in the field, in principle, the same methods can be used as for natural and agricultural soil (e.g. Lehmann & Stahr, 2007). However, their application in urban and industrial environments often poses both practical and conceptual problems. First, it is evident that the subsurface in these environments can be difficult to access, due to aboveground obstacles, such as buildings or other infrastructure, or surface sealing by technic hard material. In these circumstances, manual tools mostly are no longer sufficient and mechanical equipment is needed for soil profile excavations or other invasive ways of soil investigation. A related aspect that requires extra attention in urban and industrial environments is safety. The possible presence of subsurface utility infrastructure, e.g. cables for electricity supply or telecommunication, water and sewer pipes, pipes for conveyance of (heating) gas and oil, has to be verified prior to invasive soil investigations. Also other structures such as underground storage tanks and buried basements, contaminants and unexploded ordnance (UXO) can pose significant danger. Careful terrain observation is a primary precaution. It also is strongly recommended to consult available

documents of utility infrastructure and historical land use, although this documentation often is incomplete or out-of-date (Lehmann & Stahr, 2007). Second, the actual description of an urban soil profile can be rather complicated. As argued in the first section of this chapter, urban soil morphology can strongly differ from the classical archetype and an extreme variety of artefacts[1] can be found. Whereas some artefacts, such as pottery, bricks and glass, are easy to identify, this can be difficult for substances of a more specific origin, such as products or waste from industrial processing. Particularly inexperienced urban soil surveyors, who are not familiar with the broad spectrum of technogenic materials, may struggle with the recognition of these materials in different environmental conditions (Meuser, 2010). In addition, if soil horizons can be discriminated, soil properties can show considerable variation within one horizon. In the most recent version of the FAO guidelines for soil description (FAO, 2006) specific attention is devoted to human-made and human-transported materials, providing clear instructions in case there is a suspicion of these materials in the field. Nevertheless, the level of detail of the description will depend on the surveyor, while it can be generally questioned which level of detail is truly relevant. The high spatial heterogeneity is where impracticality of urban soil description also becomes a conceptual problem, which is manifested in each of the steps of the conventional soil survey procedure:

1. How to define useful soil types if large soil variability is expected yet difficult to be estimated due to a poor correlation with the natural geology and topography of the environment?
2. How to identify and map the spatial distribution of predefined soil types if the soil surface is poorly representative of subsurface soil properties?
3. How to define a representative soil sample in case of extreme variability (e.g. De Kimpe & Morel, 2000; Howard & Orlicki, 2015), and how to relate soil types with potential land uses in environments with a dynamic multifunctionality?

[1] IUSS Working Group WRB (2006) defines *artefacts* as follows:

> Artefacts (from Latin *ars*, art, and *facere*, to make) are solid or liquid substances that are:
>
> 1. one or both of the following:
>   a. created or substantially modified by humans as part of an industrial or artisanal manufacturing process; ***or***
>   b. brought to the surface by human activity from a depth where they were not influenced by surface processes, with properties substantially different from the environment where they are placed, ***and***
> 2. have substantially the same properties as when first manufactured, modified or excavated. (p. 60)

The intensity of a soil survey campaign is constrained by the time and money that can be invested. This has direct consequences for the number of different soil types that can be identified and the size of the representative sample to be taken for each of them. Lehmann and Stahr (2007) state that the costs for urban soil mapping are roughly the same as those for mapping natural or agricultural soil, considering the extra time needed per individual soil profile description is compensated for by the smaller number of descriptions that has to be carried out when sealed areas are excluded. Although sealed soil has a reduced functionality, estimates have shown that sealed surfaces can take up about half of the urban area (Rawlins et al., 2015). Neglecting these areas in urban soil survey campaign could lead to strongly biased maps. In addition, characterization of soil with presumably higher variability based on a lowered number of soil profiles is at odds with the statistical theory prescribing an increase in sample size with increasing variability, if the same level of estimation reliability is to be achieved (Webster & Lark, 2013).

When considering the legacy soil maps, it is important not to overlook the time spirit in which these maps were created. The initial drivers for soil surveying and mapping were to assess the potential for agricultural production and to develop suitable strategies for maximizing the yield. Because urban and industrial areas were ascribed little significance in contributing to this purpose, its soil was, possibly obliviously, ignored. On the other hand, the subordinate importance of urban soil may have been convenient for the "classical" pedologist who struggled with the reconciliation of urban soil with conventional soil survey and classification, due to the lack of clear-cut guidelines to investigate such soil (e.g. De Kimpe & Morel, 2000; Lehmann & Stahr, 2007). In either way, in traditional soil maps – many of which are still the first tool at hand for soil investigations today – urban and industrial areas are blind spots. The subsurface of these areas was not surveyed; at best, there is an indication of the reason why. For instance, in the legacy soil map of Belgium, representing data that were collected during the national soil survey taking place between the late 1940s and the middle 1970s (Dudal et al., 2005), artificial soil or non-surveyed area has one of the following specifications: 'built-up area', 'formerly built-up area', 'elevated terrain', 'levelled terrain', 'quarry' or 'landfill' (Dondeyne et al., 2014). Furthermore, because of rapid urban development in recent decades, even in only "middle-aged" soil maps the data on non-surveyed areas are likely to be already out-of-date. In general, legacy soil maps leave us with a lack of information on the present urban soil status.

The urban soil information gap can be considered to be dual: (1) the current extent and spatial distribution of urban soil is vaguely detailed, and (2) its actual local properties are usually unknown. Both aspects are pivotal in soil studies in the perspective of land evaluation, land use planning and environmental protection and thereby can relate to different spatial scales. The poor knowledge of the extent and spatial distribution of urban soil can not only complicate studies of urban soil itself, but can also have severe implications when natural or agricultural soil are in focus. Particularly when soil-related phenomena are studied on a regional or higher scale (e.g. habitat availability; Mücher et al., 2009), calculations of the contributing surface area can become inaccurate and, in addition, the connectivity between the areas of interest can be seriously misjudged. The next section gives an illustration of this problem for the region of Flanders, Belgium.

Regardless of the distinct drawbacks of outdated soil maps, some objections can be made to the relevance of updating these maps. As discussed above, application of the conventional survey approach to urban soil involves both practical and conceptual difficulties and a considerable investment of resources would be necessary if new data need to be collected with the same level of detail. In addition, the level of detail is a relative concept. Soil maps created in the context of basic data inventory will always have limitations with respect to spatial resolution, map scale and pertinence of the soil properties considered depending on the purpose they are to serve, which can be manifold in the case of urban environments (e.g. De Kimpe & Morel, 2000; Lindsay et al., 1973). Last but maybe foremost, for areas with rapidly developing urbanization a new soil map is likely to expire soon again.

Conventional soil survey for soil mapping that heavily relies on soil profile descriptions and soil sample analysis, both of which can only be achieved by investigating the soil in an invasive way, tends to be inefficient in an urban or industrial context. In such a context, sources of information other than direct observations may provide valuable alternatives. In the following sections, the use of secondary information for urban soil characterization is further introduced in relation to the two aspects of the urban soil information gap defined above.

2.2.2 Scaling the challenge for the region of Flanders, Belgium

As the case studies discussed in the later chapters are all situated in the northern part of Belgium, Flanders, this introductory section provides a broader view on the urbanization situation of the region. According to the UN's prospects on world

urbanization, in 2014, Belgium was the 7th most urbanized country in the world, with 97.8% of the population living in urban areas (UN, 2014). Besides, FAO and ITPS (2015) mention Belgium, together with the United Kingdom, as ultimate example of the area of Technosol as compared to country total area. However, considerable differences exist between the different regions of Belgium, as illustrated by the population statistics given in Table 2.1. According to the most recent census data (1st of January 2015), Belgium counts over 11.2 million inhabitants, 6.4 million (57.5%) of which living in the Flemish Region, 3.6 million (32.0%) in the Walloon Region, and 1.2 million (10.5%) in the Brussels-Capital Region (FPS Economy, SMEs, Self-employed and Energy, 2016b). Regional differences are even more clear when considering the population density. The average population density of the country approaches 370 inhabitants per km². Yet, this number is considerable higher Flanders, approximately 480 inhabitants per km², whereas for Wallonia the average population density is only about 210 inhabitants per km². For the Brussels-Capital Region, the population density is as high as nearly 7300 inhabitants per km² (FPS Economy, SMEs, Self-employed and Energy, 2016a, 2016b; see also Antrop, 2004). The regions of Flanders and Brussels are outstanding examples of highly urbanized areas; from here onwards, we focus on the first.

Table 2.1 Population in Belgium in 2015

	Population (inhabitants)[a]	Area (km²)[b]	Average population density (inhabitants per km²)
Belgium	11 209 044	30 527.93	367
Flemish Region	6 444 127	13 522.25	477
Walloon Region	3 589 744	16 844.29	213
Brussels-Capital Region	1 175 173	161.38	7282

[a] FPS Economy, SMEs, Self-employed and Energy (2016b)

[b] FPS Economy, SMEs, Self-employed and Energy (2016a)

What does the high urbanization degree of Flanders mean in terms of its soil? To formulate a quantitative answer to this question, in this section it is aimed to estimate the current extent and spatial distribution of urban soil in Flanders. In a first attempt, the legacy soil map of Belgium is used as information source, as this is still one of the

most, if not the most, commonly used reference document for routine soil investigation. Second, the occurrence of urban soil will be derived from more recently acquired land cover data.

Technosol in the legacy soil map of Belgium

A detailed description of the history behind the Belgian soil map and the methodology of data collection can be found in Dudal et al. (2005). Only the most relevant aspects are presented here. During the field work, map units were drafted using copies of cadastral plans at scale 1:5000. These units were then generalised on 1:10 000 topographic base maps, which were published at a reduced scale of 1:20 000. Each of the map sheets published covered an area of 80 km². During the 1990s, this series of map sheets was digitized and, finally, all data from soil profile descriptions and sample analysis, together with available metadata, were organized in a relational database named AARDEWERK (Van Orshoven et al., 1988). In the following years, the database received several updates, including both revisions and additions of data. The most recent version for the regions of Flanders and Brussels is the AARDEWERK-Vlaanderen-2010 database (Van De Vreken et al., 2011), which can be consulted through internet applications.

The motivation for a systematic soil survey on the national level was fostered by the demand for information on the country's soil resources to enhance agricultural production, the initiative having been introduced shortly after the end of World War II. The agricultural interest is reflected in the definition of the legend of the Belgian soil map: soil texture, natural drainage conditions and the nature of profile development outline the fundamental criteria to differentiate between soil types, each of which are morphogenetic properties that – at least for natural and agricultural soil – are easily identifiable in the field. Because each soil type defined in the Belgian soil classification system can be traced to a combination of these three properties, the system is open and flexible (Dondeyne et al., 2012). The impressive data set collected during the national soil survey has been serving numerous applications, also outside an agricultural context, such as environmental impact assessment of different types of land use and assessment of soil OM stocks and fluxes with respect to global change (e.g. Sleutel et al., 2011). However, soil surveys in other European countries were conducted independently, fitting own custom-made soil map legends, which hampers the use and exchange of soil data from different countries. Matching the background of an increased commitment to harmonize agricultural policies among the countries of the European Union, the Flemish and Walloon governments recently commissioned to

convert the legend of the Belgian soil map to the WRB system (Dondeyne et al., 2012, 2013, 2014). The WRB classification is based on diagnostic features determined by morphological, physical and chemical soil properties and is now the official reference soil nomenclature and soil classification system recognized by the European Commission. For Flanders, the WRB translation of the soil map is currently available at scales 1:40 000 and 1:250 000.[2] To derive an estimation of the occurrence of urban soil in Flanders, the most detailed one will be used (Databank Ondergrond Vlaanderen [DOV], 2015).

In the WRB, urban soil is represented primarily by the reference soil group Technosols, as is evident from the definition of the last. Technosol refers to soil consisting of at least 20% artefacts or having a (quasi-)impermeable geomembrane or technic hard material near the soil surface (IUSS Working Group WRB, 2015). It is the most dominant soil classification in urban and industrial environments (e.g. Rawlins et al., 2015). However, the interpretation of urban soil adopted in this work is broader than just Technosols. A more detailed delineation of urban soil in the WRB could be achieved by additionally accounting for non-Technosol units with qualifiers indicating anthropogenic influence. Qualifiers as *technic*, *relocatic* and *transportic* also point to soil affected by human activities that often are related to the present process of urbanization (IUSS Working Group WRB, 2015). Nevertheless, a perfectionist translation of urban soil into WRB terminology is out of the scope of this work and including only Technosol is here deemed sufficient to give a fair impression of the spatial significance of urban soil in Flanders. On the other hand, Technosol was not actually determined in the Belgian soil survey. In fact, urban and industrial areas were generally not surveyed, because (resultants of recent) human activity restricted soil investigation to be carried out. This explains the use of the expanded label of 'Technosols/Not Surveyed' in the WRB soil map for Belgium. As mentioned before, the Belgian soil map gives an indication of the specific activity responsible. Although the odds are in favour, such indications are no guarantee for the presence of

[2] Both versions can be consulted through the internet application of Databank Ondergrond Vlaanderen (DOV, Database of the Subsoil of Flanders, www.dov.vlaanderen.be). DOV is a cooperation between the Flemish Government, Department of the Environment, Nature and Energy, Division of Land and Soil Protection, Subsoil, and Natural Resources, the Department of Mobility and Public Works, and the Flemish Environment Agency. In addition, the data are available at Geopunt Vlaanderen, the central portal for public geographic information of Flanders (www.geopunt.be).

Technosol, neither at the time, nor now. Cities were entirely assigned to built-up area, including area occupied by water, as illustrated by the ports of Ghent and Antwerp.

For reasons of consistency, the soil map was here corrected to the administrative boundary of Flanders as of 2003 (Agentschap voor Geografische Informatie Vlaanderen [AGIV, Flanders Geographical Information Agency], 2003). Area within the administrative boundary that is not covered by the Belgian soil map was considered as additional non-surveyed area. The soil map generally only slightly deviates from the adopted administrative boundary and the corresponding expansion of 'Technosols/Not Surveyed' area was small. The only local exception worthy of mention is the part of the Flemish boundary at the North Sea. Along the entire coastline of nearly 70 km long, there is a strip of at least about 300 m wide that is additionally included within the administrative boundary of Flanders. This resulted in a supplemental non-surveyed area of over 35 km². The man-made nature of the Belgian beaches and the stony seafront plead in favour of this alteration, although part of this area is mostly under water and it can be questioned if this part is still to be considered as soil.

The estimate of urban soil in Flanders as derived from the corrected 'Technosols/Not Surveyed' area in the WRB soil map is presented in Figure 2.3b. Henceforth, the combined Technosol and not surveyed area is more briefly referred to as Technosol area. As a reference for interpretation, Figure 2.3a indicates the 20 municipalities of Flanders with the largest population according to the census of 2015 (FPS Economy, SMEs, Self-employed and Energy, 2016b). These include each of the capitals of the five Flemish provinces. Following this approach, the area of urban soil in Flanders amounts to 1870 km², nearly 14% of the total area. Urban soil is scattered over the region, with large, saturated areas centred around the largest cities. Antwerp and Ghent (indicated with their Dutch names, *Antwerpen* and *Gent*, in Figure 2.3a) are clear hot spots. Another prominent area can be seen directly north-east of Beringen. This represents the military domain of Leopoldsburg, which was classified as built-up area during the Belgian soil survey. Furthermore, a close look at the urban soil map in Figure 2.3b reveals that the level of detail with which Technosol-representing areas were recorded was not the same everywhere. Differences can be seen between different 80-km² map sheets of the originally published soil map. These can be explained by a change of the data collection protocol over the different phases of the national survey campaign (Dudal et al., 2005).

Reclassification of the land cover map

While spatially comprehensive, up-to-date information of the Flemish soil is not available, it is for its surface. Images from satellites and aerial photography provide informative displays of land use patterns, on a broad range of spatial scales. Image acquisition technology and digital image processing have progressively developed in the recent decades and, today, remote sensing implies an established tool set for producing high-resolution plan views of the land surface in a time-efficient way (Campbell & Wynne, 2011). For large parts of the world, aerial imagery is frequently renewed. In Flanders, AGIV is responsible for the generation of a new orthophoto mosaic every three years (AGIV, 2013). These data are readily available for the broad public through different internet applications. In addition to remote sensing images, exhaustive information on land use, and its history, can be supplied by cadastral databases. Most countries have developed legal systems relying on cadastral data and, hence, these data are constantly updated. In Belgium, part of the cadastral information also is publicly available and, since 2013, cadastral plans can be consulted online.[3] Although data of land cover and land use do not provide direct information of the soil, they give clear clues on the nature of human activity it is being exposed to. As an illustration of the use of this type of "ground-plan" information to study the underlying soil, the spatial distribution of urban soil in Flanders is here derived from the land cover map dating from 2012 (AGIV, 2016a).

The land cover map of Flanders of 2012 is compiled from three supporting data sets:

1. vegetation map of Flanders – a raster file derived from multispectral aerial imagery recorded during the summer of 2012, with a resolution of 1 m;
2. agricultural parcel database – vector database of parcels in agricultural use, brought up to date yearly for regulations related to European agricultural subsidies and the Flemish manure policy;
3. Large-scale Reference Database (LRD) – vector-based geographic information serving as topographic reference for Flanders, updated continuously.

The land cover map of Flanders was produced at a resolution of both 1 m and 5 m. For the estimation of urban soil presented here, the highest resolution was used. Similar to the soil map, the land cover map was first corrected to the administrative

[3] The cadastral plan of Belgium can be consulted through an internet application of the Federal Public Service Finance, at http://ccff02.minfin.fgov.be/cadgisweb/?local=nl_BE.

boundaries of Flanders as of 2003. Land cover data were not available for an area of no more than 5 ha. Since this only represents ~0.0003% of the total administrative area of Flanders, this no-data area was neglected in the following calculations. The 14 classes identified in the land cover map of Flanders are listed in Table 2.2 and Figure 2.2a shows their relative distribution.

The land cover map was translated in an urban soil probability map by reclassification into three categories according to the likelihood of a specific land cover to correspond to urban soil, respecting the working definition of urban soil described above. The categories cluster land covers that (1) definitely or at least very probably correspond to urban soil, (2) possibly or probably correspond to urban soil, i.e. in a considerable part of cases, and (3) probably or definitely do not correspond to urban soil. The reclassification logic is further detailed in Table 2.2. The aim was to estimate the occurrence of urban soil based on simple reasoning, so that the reclassification rules could easily be transposed to related sources of land information. Attention has been given to possible shortcomings of the reclassification and a few suggestions for further improvement are included. The urban soil likelihood level assigned to each land cover also is indicated by the rim colour of the pie slices in Figure 2.2a (black, grey or white). The resulting urban soil probability map is shown in Figure 2.3c. In total, 2215 km² (16.3% of the area of Flanders) was reclassified to the category with a high likelihood of urban soil (black area in Figure 2.3c). A slightly larger area of 2272 km² (16.7%) was converted to grey zone, with an intermediate likelihood of urban soil. A major part of Flanders, 9135 km² (67.0%), remained for a low urban soil likelihood. Buildings, roads and other sealed surfaces are the major contributors to the first category, which is in line with the expectations. Of these three land covers, the last has the largest area, representing undefined non-green, and therefore assumed sealed, areas. The intermediate category chiefly consists of area covered by grass and shrubs that is not connected to a road and is not in agricultural use. Essentially, this is the low green in residential areas, supplemented with pasture and (half-standard) orchards in private use. This type of grass and shrubs cover often is spatially associated with the equivalent tree cover class (class 9 in Table 2.2). In spite of this, the latter was not reclassified to possible urban soil, for the main reason of not wanting to include more extensive forest areas as well. Distinguishing between a single or a small group of trees and a forest could be achieved by adding a condition on the size of individual tree patches. The large area with a low urban soil likelihood is explained by the large area in agricultural use. The attribution of a low likelihood is

Table 2.2 Reclassification of the land cover map of Flanders of 2012 into an urban soil map

	Land cover	Urban soil[a]	Reclassification rationale
1	Buildings	Y	Soil has man-made surface layer of technic material, largely sealed surface, corresponds to Technosol in WRB
2	Roads	Y	
3	Other sealed surfaces	Y	
4	Railroads	Y	
5	Water	N	Not considered as soil
6	Other unsealed surfaces	P	Correspond to non-green areas in vegetation map, include but are not limited to unmetalled roads, sports fields, undeveloped non-agricultural land, brownfields and quarries. The soil of many of these has been formed under influence of human activities related to urbanization.
7	Arable land	N	Corresponds to agricultural soil
8	Grass, shrubs	P	Largely consist of low green in gardens and parks, the soil of which often is man-changed.
9	Trees	N	Include discrete groups of trees (e.g. in gardens) as well as (relatively) extensive forests. Notwithstanding most forests in Flanders are cultivated ecosystems, recent direct human influence on the soil is assumed to be minimal.
10	Grass, shrubs – agricultural use	N	Corresponds to agricultural soil
11	Grass, shrubs – roads	Y	Soil probably has been disturbed by road (construction) works and its surface is a primary receiver for deposits from traffic emissions.
12	Trees – roads	Y	
13	Grass, shrubs – water	P	Correspondence to urban soil depends on nature of watercourse, additional information is required to discriminate between natural and artificial banks.
14	Trees – water	P	

[a] Level of likelihood for land cover to correspond to urban soil: Y = very probably or definitely, P = possibly or probably, and N = probably not or definitely not.

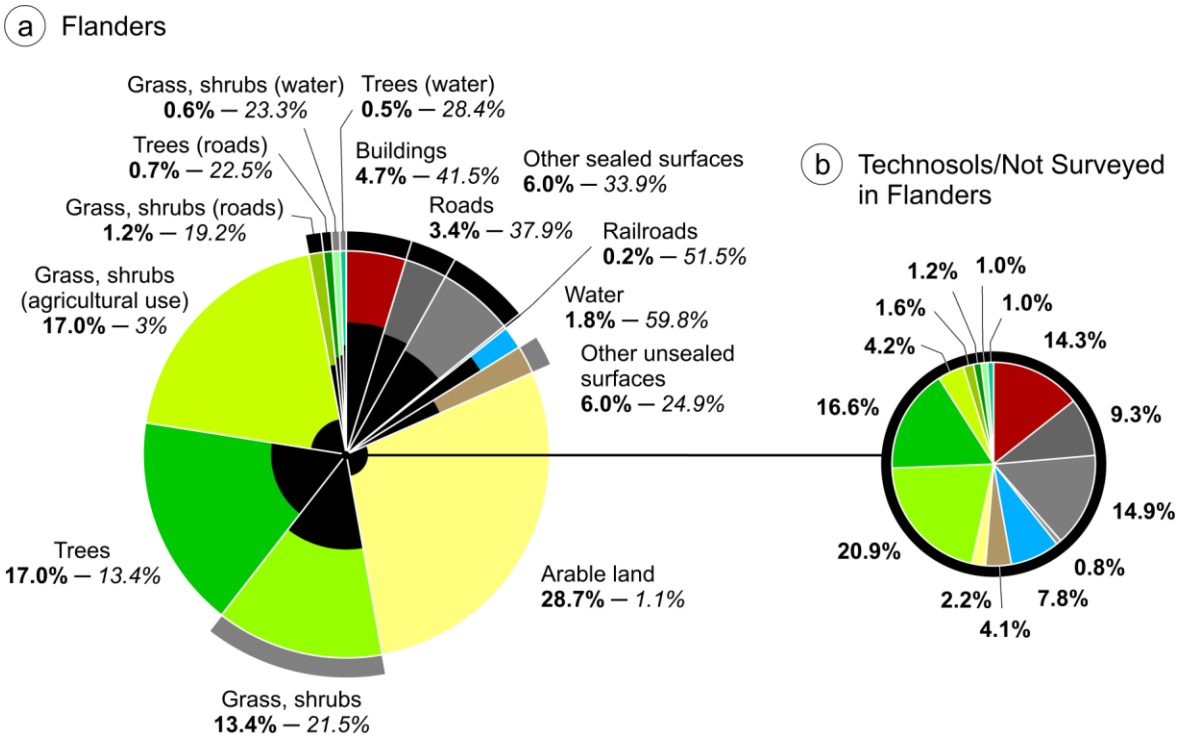

Figure 2.2 (a) Pie chart of the land cover in Flanders in 2012. The proportional areas of Flanders occupied by the 14 land covers is indicated by the labelled percentages in **bold**. The rim colour of the pie slices indicates the reclassification category of the land covers in the urban soil probability map, corresponding to Tabel 2.1. The black part of the pie slices indicates the proportion of the land cover areas that coincide with Technosol area in the WRB soil map, the corresponding figure is given by the labelled percentage in *italics*. (b) Distribution of the land covers only within 'Technosols/Not Surveyed' area in the WRB soil map.

based on the assumption that current agricultural land use points to soil that only has been affected by agricultural activities and, hence, represents agricultural soil. Particularly for meadowland and pasture, encompassed by the land cover class 'Grass, shrubs – agricultural use', this assumption might not be valid. For instance, former illegal or uncontrolled waste disposal sites were typically covered by a layer of natural soil material and afterwards used as grassland, a considerable part of which is expected to be registered as agricultural land (see also the case studies presented in Chapter 5).

To evaluate the reclassification of the land cover map with respect to actual soil data, a cross-analysis was made between land cover in 2012 and Technosol area in the WRB soil map. For each land cover it was determined how much of its area coincides with Technosol; the proportionate area is visualized in the black part of the respective pie slice in Figure 2.2a. The pie chart in Figure 2.2b shows the complementary land cover distribution within the Technosol area of the soil map. Particularly the last is useful to appraise the validity of the reclassification. Each of the

land covers with a high probability of urban soil have a larger share in the Technosol area of Flanders than in Flanders as a whole, which confirms their reclassification into this category. For example, 4.7% of Flanders is covered by buildings, for the Technosol area alone this percentage is 14.3%, more than three times as high. The same holds for the land covers allocated to the intermediate probability category, except for the class of 'Other unsealed surfaces'. For the trees land cover the percentage is approximately the same. This can be related to the above-mentioned issue on the reclassification of this land cover. In the Belgian soil survey, trees in areas of residential concentrations were incorporated in non-surveyed built-up area, while in forests the conventional survey routine was applied. The two land covers associated with agricultural activity both only have a small portion in the Technosol area. The area of water is four times as high with respect to the Technosol area as to entire Flanders. A relatively extensive area of land covered with water has the label of 'not surveyed' in the legacy soil map, without a necessary involvement of human activities, which in the Technosol approach has contributed to an overestimation of the urban soil area. In the reclassification of the The area of Flanders with a high likelihood of urban soil as estimated by the land cover approach (16.3%) is already larger than the Technosol area in the soil map (13.7%). Additionally accounting for the area with a moderate likelihood of urban soil (16.7%), the land cover approach estimates the incidence of urban soil significantly higher than the Technosol approach. This is clearly illustrated in Figure 2.3. The reclassified land cover map shows that an elaborate network of urban soil is omnipresent. Whereas the most part of the Flemish surface area (67.0%) was assigned only a low likelihood of urban soil, no bright white areas are visible in this map. The most plausible explanation is that the territory of urban soil has been significantly expanded over the last few decades. However, the difference in resolution of the two source maps is expected to have had an appreciable contribution as well. In the land cover approach every single discrete 1 m² area of which the surface suggested urban soil has increased the total urban soil area, while in the soil map such small local anomalies were not registered. The higher resolution of the

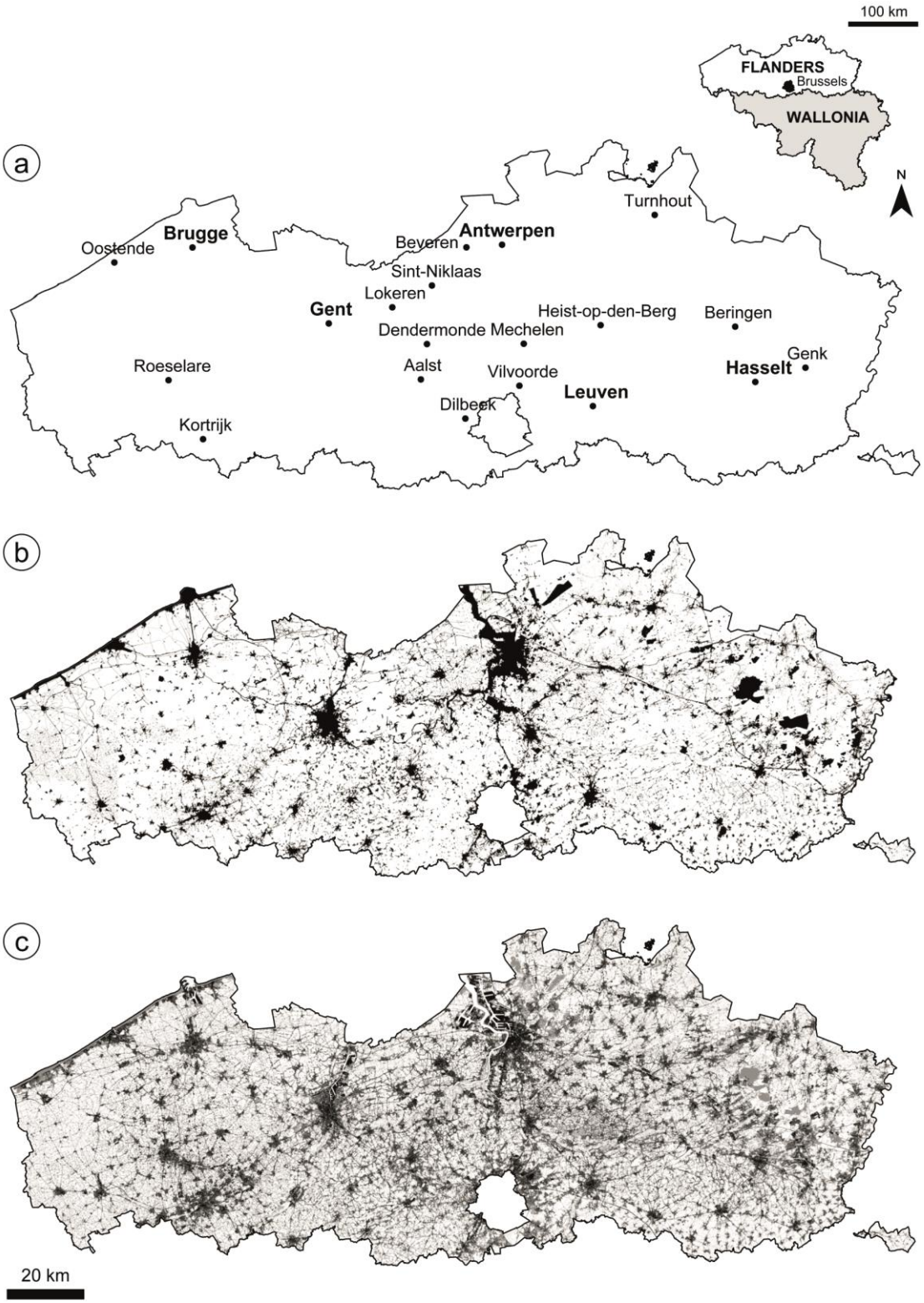

Figure 2.3 The significance of urban soil in Flanders, the northern region of Belgium. (a) Location map of the 20 municipalities with the largest population in 2015. Provincial capitals are indicated in **bold**. (b) From the legacy soil map it is estimated Flanders contains 1870 km² of Technosol (black), 13.7% of its total area. (c) Reclassification of the land cover map of 2012 results in an area of 2215 km² (16.3%) that very probably or definitely corresponds to urban soil (black) and 2272 km² (16.7%) for which urban soil is possible or probable (grey).

urban soil map derived from the land cover approach is evident in Figure 2.3c and is particularly demonstrated by the extra detail within large Technosol areas. In this respect, it is also interesting to consider the common part between the different land covers and Technosol area (Figure 2.2a). Railroads, buildings, roads and other sealed surfaces, all land covers assumed to have a high likelihood of urban soil, have the highest proportions coinciding with Technosol. Yet, except for railroads, these proportions are below 50%. The relatively high Technosol part of land covered by grass and shrubs subscribes to the Technosol saturation of residential areas applied in the creation of the soil map.

Remote sensing: bridging the gap?

The presented reclassification of the land cover map exemplifies how remote sensing data can be used to make a valid estimation of the spatial distribution of urban soil. A similar exercise could be made using related land information data sets, such as the land use map of Flanders, the most recent version of which dates from 2001 (AGIV, 2002), and the CORINE Land Cover 2012 data set (European Environment Agency, 2016). The absolute estimates will differ depending on the data considered, the definition of the class units involved (either predefined or custom created), the scale and resolution at which data are available, and the definition of urban soil that is applied. The relative message, however, is anticipated to be the same: in the quintessential urban landscape of Flanders, urban soil is a vital part of the modern human living environment.

Can remote sensing overcome the urban soil information gap? The data sets derived from aerial photography that are referred to above comprise only a segment of the data that can be offered by remote sensing, as clarified by the definition given by Campbell and Wynne (2011):

> Remote sensing is the practice of deriving information about the Earth's land and water surfaces using images acquired from an overhead perspective, using electromagnetic radiation in one or more regions of the electromagnetic spectrum, reflected or omitted from the Earth's surface. (p. 6)

Remote sensing operates far beyond the visible part of the electromagnetic spectrum catering for a broad range of techniques which inclusively support the investigation of properties that may not always be directly observable from, visible, aerial photographs. For instance, apart from visible data, soil moisture content is also examined from infrared, thermal and microwave data (Ahmad et al., 2011). The synoptic view that remote sensing data supply makes them particularly suited for

mapping and monitoring properties on large spatial scales. However, the focus is on the soil surface. The majority of remote sensing techniques provide data that are only informative of the upper few centimetres or, at most, upper few decimetres of soil (Campbell & Wynne, 2011; see also Ahmad et al., 2011). Remote sensing is not suited to investigate the deeper soil profile, leaving the second aspect of the urban soil information gap – unknown local urban soil properties – largely unaddressed.

2.3 Investigating urban soil properties

The challenges involved in urban soil investigation for soil mapping were discussed in the previous section. Nevertheless, in the recent decades a considerable amount of research has been dedicated to the study of urban soil properties on a more local scale. Table 2.3 presents an illustrative, non-comprehensive, overview of common urban soil characteristics together with the artefacts or human activities they can be related to. The summary provided by Lehmann & Stahr (2007) was used as a starting point and was supplemented with information from other publications. Note that for each of the properties mentioned urban soil can depart from the standard, as represented by natural or agricultural soil, in both "increasing" and "decreasing" directions, depending on the originating human interference. Apart from the type of the human impact which is directly related to the urban land use, many studies mark the importance of time as influencing factor. For example, Scharenbroch et al. (2005), who focused on the investigation of residential gardens and green elements in the public urban landscape (mulched plant beds, street tree plantings, and parks), emphasize changes in soil bulk density, microbial biomass and activity, and OM content as a function of the age of the urban soil, referred to as the time passed since disturbance by anthropogenic activity (assuming a single event). After an initial drop of the microbial biomass, disturbance induces an increase in the metabolic active portion of the microbial community (metabolic quotient), yet afterwards metabolic activity decreases rapidly with time. The metabolic quotient can be considered a measure for the recovery efficiency after disturbance. Furthermore, the trend in metabolic activity is inversely related to OM accumulation. In general, microbial biomass and activity increases as urban soil develops. Similar observations have been made for depositions with a higher content of technogenic materials such as construction debris, slag and ashes, and MSW (Meuser, 2010). The physical, chemical and biological properties of urban soil are unique to its age and human impact intensity,

Table 2.3 Some typical characteristics of urban soil, adapted from (a) Lehmann & Stahr (2007), with additions from (b) Meuser (2010), (c) Scharenbroch et al. (2005), (d) Jodeiri Shokri et al. (2016), (e) Rawlins et al. (2015), and (f) Howard & Orlicki (2015). Abbreviation: TOC, total organic carbon content.

Property	Explanatory artefact or human activity	
Dominant particle size	**Coarse**	**Fine**
	– coarse fragments from construction and demolition debris (e.g. bricks, pottery, glass, crushed stone)[a] → high hydraulic conductivity	– high sludge content[a] – high ash content[a] – → low hydraulic conductivity
Bulk density	**High**	**Low**
	– compaction by mechanical forces on the surface (topsoil) or through construction activities (subsoil)[a] – surface layers of hard technic material to increase load-bearing capacity (e.g. roads and sports fields)[b, c]	– mechanical loosening[a] – high OM content (e.g. from organic waste)[a, b] – high ash content[a, b]
pH	**High** ALKALINE	**Low** ACIDIC
	– construction and demolition debris such as brick, cement, plaster, mortar and concrete[a, b, f] – application of slaked lime ($Ca(OH)_2$) – application of calcium or sodium chloride (e.g. roads and sidewalks)	– sulphur from coal or technically produced sulphuric acid[a] (e.g. manufactured gas plants) – acid mine drainage from oxidation of pyrite in coal mine or coal washing wastes[b, d]
TOC content	**High**	**Low**
	– application of compost or manure (e.g. gardens)[b] – accumulation of organic waste and coal combustion residues[a, b] – subsoil consisting in former topsoil material[a]	– regularly swept soil to prevent vegetation (e.g. sidewalks)[a] – accumulation of construction debris[b] – removal of topsoil in preparation for construction activities[c]

Table 2.3 (continued) Some typical characteristics of urban soil, adapted from (a) Lehmann & Stahr (2007), with additions from (b) Meuser (2010), (c) Scharenbroch et al. (2005), (d) Jodeiri Shokri et al. (2016), (e) Rawlins et al. (2015), and (f) Howard & Orlicki (2015). Abbreviation: TOC, total organic carbon content.

Property	Explanatory artefact or human activity	
Temperature	**High**	**Low**
	– high air temperature (e.g. urban heat islands)[a, e]	
	– biodegradation of organic waste (aerobic conditions)[b]	
	– heating infrastructure[a]	– cooling infrastructure[a]

including the deposition of technogenic materials and the form of land use, in which age can be considered a diversifying factor for impact intensity. The typically strong horizontal and vertical heterogeneity in urban soil properties results from differentiation in the combination of these factors. Yet, the perception of spatial variability of urban soil also depends on the variable considered (Greinert, 2015).

As evidenced by Table 2.3, there is a consensus on the trend of change of soil properties in response to certain human impacts. However, quantitative comparison of data from different studies is far more complicated. The actual origin of reported data generally requires critical consideration, including sample collection, preparation and analysis methodology (see Johnson et al., 2011, for a detailed discussion in view of chemical analysis). The field sampling protocol and sample preparation can have important implications for the reliability and representativeness of the analysis results, specifically when concerning urban soil with a high proportion of coarse technogenic artefacts. Soil sampling is mostly restricted to the fine fractions (clay, silt and sand) and, if more coarse (gravel or stone) fragments are included, classical soil analysis procedures usually prescribe them to be removed or to be reduced in size during sample preparation (Meuser, 2010). The results obtained can therefore disregard an important part of the actual soil constituents or can be modified as a consequence of sample preparation. Analysis results further differentiate according to the analysis protocol applied. Unfortunately, detailed descriptions of the followed analytical procedure are not always provided, making interrelation between different data sources impossible. For some properties, mainly chemical contaminants, a solution to standardization may be found in the legal framework on the assessment of soil contamination, in which standard sampling and analysis methods are specified for

data quality control. These protocols could serve as a regional or national reference. However, these protocols do not necessarily comply with the scientific state-of-the-art and may not match with specific academic research objectives. It is clear that, due to the various purposes of urban soil investigation, the design of a universal protocol is likely to overreach itself. Yet, it could be worth investing in the development of a flexible framework in order to facilitate data exchange and integration.

While clarity on the sampling protocol in the field and the subsequent sample preparation and analysis in the laboratory are indispensable, the uncertainty involved with sample analysis needs to be put into perspective with the field spatial variability. Greinert (2015) argued that some soil properties tend to be relatively homogeneous under conditions of similar land use. Yet, a complex land use history, which is often not known in detail, can make it particularly difficult to reconstruct such zones of presumed homogeneity. The investigation of urban soil on a local scale is confronted with the same problems as soil surveying on a regional scale. How to select sample size and locations? What is the validity of the obtained results in space and time? These problems raise the need for alternative tools that can measure local urban soil properties in a more time-efficient and spatially-comprehensive way.

The alternative of proximal soil sensing

Proximal soil sensors can measure soil properties in a non-invasive way and therefore provide efficient tools for high-resolution soil mapping. Some techniques have a depth of penetration limited to a few centimetres or decimetres, such as visible or near- or mid-infrared reflectance spectroscopy, while others provide measurement depths of several metres, such as EMI sensors. In agricultural applications, the soil electrical conductivity, which can be measured using electric and electromagnetic methods, is a frequently used proxy for soil salinity, texture, OM and moisture content, bulk density or compaction, and pH (e.g. Adamchuk et al., 2004; Doolittle & Brevik, 2014; Islam et al., 2014a, 2014b). Note that these are properties that have been demonstrated to change under influence of human impact (see Table 2.3). In recent years, the use of proximal soil sensors, and EMI sensors in particular, has significantly expanded in the field of (geo)archaeology as well (e.g. De Smedt, Saey, et al., 2013; De Smedt, Van Meirvenne, et al., 2013, De Smedt, Van Meirvenne, et al., 2014; Saey et al., 2013). Apart from the measurements of electrical conductivity which also have proven useful for palaeo-landscape reconstruction, measurements of magnetic susceptibility have been successfully used to map traces of human activity. For example, fire pits and the presence of brick typically produce distinct magnetic

anomalies (e.g. Schmidt, 2007). This evidences the potential of these sensing techniques to support the investigation of human soil interference and the presence of technogenic substrates. Furthermore, a few studies have analyzed the electric and magnetic properties of urban soil and of specific technogenic materials in laboratory conditions. Howard and Orlicki (2015) found significant differences in electrical conductivity and magnetic susceptibility between parkland and farmland soil on the one hand, and urban soil on the other. The latter showed unique properties in function of its former land use, concurring with the conclusions of studies focusing on standard soil properties such as Scharenbroch et al. (2015). Moreover, analysis of artificially created mixtures of sand and particular technogenic substrates indicated that even a small concentration of anthropogenic particles had a measurable effect on the electric and magnetic properties. Although it has to be kept in mind that these results respond to a specific sample preparation and analysis protocol, they provide an additional, sound argument to further explore the use of proximal soil sensors to study the properties of urban soil on a local scale. The following chapters elaborate on the application of two electromagnetic sensors, EMI and GPR, to investigate urban soil associated with a (former) land use as landfill or industrial/commercial site.

Chapter 3
EMI and GPR survey methodology

'The real voyage of discovery consists not in seeking new landscapes, but in having new eyes.' – Marcel Proust

As outlined in the introduction, this research focuses on soil sensors measuring physical properties and, more particularly, on two sensors the operating principle of which relies on the principles of electromagnetism. The first sections of this chapter briefly summarize the electromagnetic theory underlying EMI and GPR. Afterwards, for each technique, a dedicated section details the specific instrumentation, survey methodology and data processing applied in the conducted case studies presented in Chapters 5, 6 and 7. The prediction methods used for visualisation of the survey data in interpolated maps are addressed in a separate section. Finally, the meaning of EMI and GRP data in terms of their related soil properties is discussed, drawing from knowledge acquired in more established application fields such as pedology, precision agriculture and (geo)archaeology.

3.1 The spectrum of electromagnetic methods

Electromagnetic (EM) methods provide information on the physical properties of the subsurface by investigation of their influence on the propagation of electromagnetic waves. These methods can be passive, relying on the detection of natural fields (e.g. magnetotellurics), or active, where an artificial signal is generated and transmitted into the ground (e.g. EMI and GPR). Electromagnetic waves have a very broad frequency range and, correspondingly, EM techniques encompass the widest variety of instrumental systems among all geophysical methods. Also due to

the geographical diversity in their development, a plethora of terms is used and the techniques are organized differently in different reference works. While each of these classification may be equally relevant, this makes it difficult to compile a universal overview. Figure 3.1 presents an overview of the most common EM methods with respect to the frequency range of EM waves they cover, assembled from Everett (2013), Reynolds (2011), and Tezkan (1999). Electrical resistivity and magnetic methods allow measuring physical properties that are closely connected to the output of EM methods, which is why they are included in the overview as well.[4] A detailed discussion of the complete spectrum of EM methods is out of the scope of this work and the remainder of this chapter will focus on the methods under consideration in the next chapters, EMI and GPR. For further reading on EM methods the following references are recommended. Reynolds (2011) presents an easy-to-read comprehensive overview of EM methods, approached from a pragmatic perspective. Everett (2013) for each method gives a dense description of the fundamental theory, followed by a variety of illustrated applications. A more theoretical discussion of EM methods, with the exception of GPR, can be found in Nabighian (1987, 1991). Jol (2009) presents a dedicated discussion on the theory, data-processing and applications of GPR.

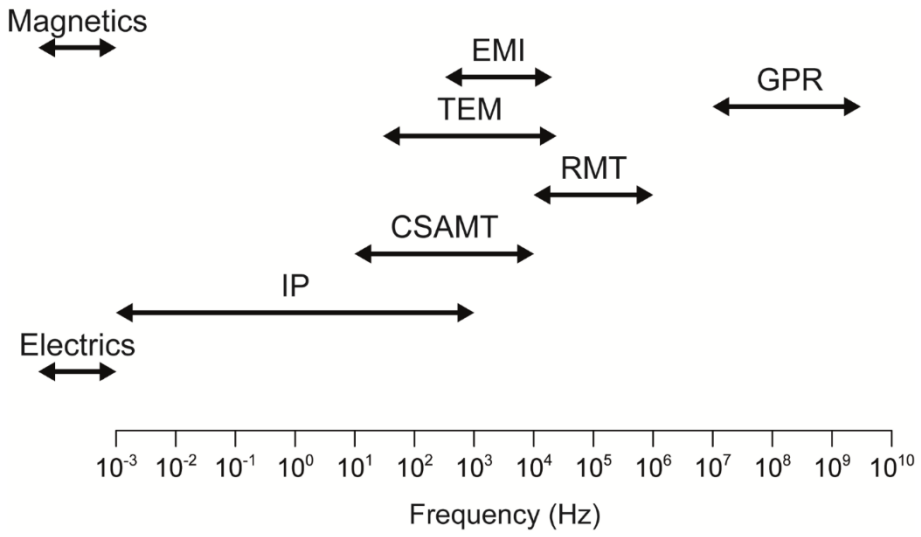

Figure 3.1 Operation frequency range of a few common EM methods. Abbreviations: EMI, (frequency-domain) electromagnetic induction; GPR, ground penetrating radar; TEM, transient or time-domain electromagnetic induction; RMT, radiomagnetotellurics; CSAMT, controlled-source audio-frequency magnetotellurics; IP, induced polarization.

[4] Electrical resistivity makes use of stationary fields which can be considered special cases of EM fields at zero frequency. In these cases, the magnetic field decouples from the electric field (Tezkan, 1999).

3.2 Electromagnetic waves

Electromagnetic waves are made up of two orthogonal vector components, the electric and magnetic fields, in a plane perpendicular to the direction of travel (Figure 3.2). The two fields can be described in terms of the field intensity vectors $\boldsymbol{E}$ (V m^{-1}) and $\boldsymbol{H}$ (A m^{-1}) or the flux density vectors $\boldsymbol{D}$ (C m^{-2}) and $\boldsymbol{B}$ (Wb m^{-2} = T). If either one of the components of the field is lost (attenuated, absorbed, or conducted away), the wave will cease propagating and die. The behaviour of propagating EM waves is fully described by the Maxwell's equations.

Gauss' theorem in electrostatics – The electric flux through a surface is proportional to the charge enclosed by the surface:

$$\nabla \cdot \boldsymbol{D} = \rho \tag{3.1}$$

Gauss' theorem in magnetostatics – The total magnetic flux through a closed surface is zero; magnetic monopoles do not exist:

$$\nabla \cdot \boldsymbol{B} = 0 \tag{3.2}$$

Faraday's Law of Induction – A time-varying magnetic flux density gives rise to an electric field circulating around it:

$$\nabla \times \boldsymbol{E} = -\frac{\partial \boldsymbol{B}}{\partial t} \tag{3.3}$$

Ampère's circuital Law with Maxwell's correction – A magnetic field arises from the sum of a time-varying electric flux density (displacement current) and a flowing electric current ($\boldsymbol{J}$, conduction current):

$$\nabla \times \boldsymbol{H} = \frac{\partial \boldsymbol{D}}{\partial t} + \boldsymbol{J} \tag{3.4}$$

The associated constitutive relationships make the link to the material properties that are relevant to a material's response to an EM field.

The *electric conductivity* (σ), expressed in siemens per meter (S m^{-1}), describes the ability of a material to pass free electric charges under the influence of an applied EM field and is defined by Ohm's Law:

$$\boldsymbol{J} = \sigma \boldsymbol{E} \tag{3.5}$$

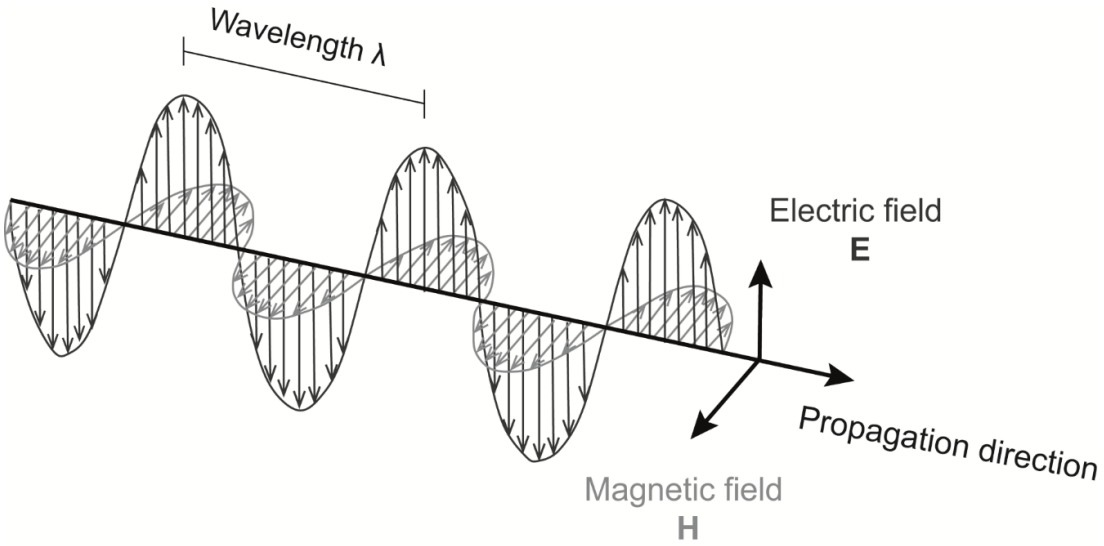

Figure 3.2 Schematic of an EM wave, existing in two orthogonal components, the electric (**E**) and magnetic (**H**) fields, in a plane perpendicular to the propagation direction.

The *dielectric permittivity* (ε), expressed in Farad per meter (F m^{-1}), describes the ability of a material to restrict the flow of free electric charges or the degree of electric polarization under the influence of an applied field:

$$\boldsymbol{D} = \varepsilon \boldsymbol{E} \tag{3.6}$$

The *magnetic permeability* (μ), expressed in henrys per meter (H m^{-1}) or in newtons per ampere squared (N A^{-2}) describes the ability of a material to support the formation of a magnetic field within itself, due to intrinsic atomic and molecular magnetic moments:

$$\boldsymbol{B} = \mu \boldsymbol{H} \tag{3.7}$$

The magnetic permeability of free space ($\mu_0 = 4\pi \times 10^{-7}$), also referred to as the magnetic constant, is a measure for the resistance encountered when establishing a magnetic field in free space. A closely related property is the *magnetic susceptibility* (κ) which is a measure for the degree of magnetization that a material undergoes in response to an applied magnetic field:

$$\boldsymbol{M} = \kappa \boldsymbol{H} \tag{3.8}$$

where ***M*** is the magnetic polarization vector. As ***M*** and ***H*** have the same units, κ is dimensionless and is usually expressed as the magnetic susceptibility per unit volume. Values of magnetic susceptibility are often labelled with 'msu SI' to indicate they are defined according to the International System of Units. The

magnetic field ***B*** quantifies the strength of the force on an elementary dipole embedded in a material with permeability μ, including both externally applied currents and the equivalent surface and volume currents that are intrinsic to the magnetic material. This can be expressed as follows:

$$\boldsymbol{B} = \mu_0 (\boldsymbol{H} + \boldsymbol{M}), \tag{3.9}$$

hence, the magnetic permeability μ and the magnetic susceptibility κ are related through:

$$\mu = \mu_0 (1 + \kappa). \tag{3.10}$$

It is noted that in the equations above, the properties are given as simple constants, which theoretically only holds for uniform, homogeneous material with no losses, anisotropy, or frequency dependence. In reality, this assumption is seldom – if ever – valid, yet for practical applications this simplification usually suffices.

3.2.1 **EMI versus GPR: diffusive versus wave propagation**

As illustrated in Figure 3.1, EMI and GPR operate in distinct frequency ranges, corresponding to a disparate character of the EM fields applied. When the energy loss, associated with conductivity, is much larger than the energy storage, associated with dielectric permittivity, diffusion is the dominant energy transport mechanism. This conforms to the requirement that $\sigma >> \omega\varepsilon$ where ω is the angular frequency (= $2\pi f$). At the low frequencies deployed in EMI, the EM field is quasi-stationary and propagation is diffuse, hence, the representation of the EM energy as an actual field (see Figure 3.3). On the other hand, the EM field shows wave-like propagation at the high-frequency regime utilized in GPR. The EM energy transmitted in GPR therefore is commonly represented as a ray (see Figure 3.8). The propagation character can be derived from the Maxwell's equations by rewriting them as to eliminate either the electric of the magnetic field. However, the difference between EMI and GPR can also be easily seen in the Ampère-Maxwell law (Equation 3.4). In EMI, the contribution of the displacement current (the first term in the right-hand side of Equation 3.4) is negligible and the response almost entirely relates to free-charge movement expressed by the electrical conductivity (included in the second term in the right-hand side of Equation 3.4, corresponding to the Ohmic conduction current). For GPR, conduction can play an important role in signal attenuation, but bound-charge

displacement, or polarization, represented by the dielectric permittivity is the dominant mechanism.

3.3 EMI

'It ain't what they call you, it's what you answer to.' – W. C. Fields

First, it is important to be clear about terminology. Essentially, the physical phenomenon electromagnetic induction relates to all electromagnetic methods. Here, the term *electromagnetic induction* (EMI) is used for a specific EM method, the configuration of which in other works often is referred to as *terrain conductivity meters* (e.g. Everett, 2013) or *ground conductivity meters* (e.g. Reynolds, 2011). The individuality of EMI lies in both its instrumental configuration and its modus operandi. In literature, EMI has been classified under the following subgroups of EM methods:

- *active methods*, an artificial signal is generated and transmitted into the ground;
- *continuous-wave / frequency-domain systems*, the generated EM wave is applied in a continuous way and the system response is analysed in frequency domain;
- *near-field / small-loop / horizontal-loop / slingram systems*, the transmitter and receiver exist in small loops that are at a constant, relatively short distance of each other in a horizontal plane;
- *moving-source systems*, in common survey practice measurements at different sampling locations (stations) are made by moving both the transmitter (source) and receiver. The midpoint between transmitter and receiver is conventionally taken as point of reference for the measurements.

For an extensive theoretical background on the method of EMI, the reader is referred to Keller and Frischknecht (1966), and Frischknecht et al. (1991). Here, only a brief description of the operating principle is given to serve as background for the discussion of the survey results presented in the next chapters.

3.3.1 Operating principle

The operating principle of EMI sensors follows the general theory of electromagnetic induction and is illustrated in Figure 3.3. The basic configuration of an EMI sensor is a combination of two coils of wire, one a transmitter and the other a receiver. By application of Ampère's law (Equation 3.4), an alternating current is

passed through the transmitter coil to generate a primary magnetic field ($\boldsymbol{H}_p$). The current has the form of time-harmonic wave: $I = I_0 \sin(\omega t)$. The primary field is in-phase with the current flowing through the transmitter and consequently can be formulated as

$$\boldsymbol{H}_p = \boldsymbol{H}_0 \sin(\omega t), \tag{3.11}$$

where H_0 is the peak amplitude of the magnetic field. In a conductive medium, the incident time-varying magnetic field induces eddy currents, according to Faraday's law (Equation 3.3). The strength of the induced currents is governed by Ohm's law (Equation 3.5) and hence depends on the electrical conductivity of the medium. The eddy currents then generate their own magnetic field, which is organized such that it tends to oppose the primary field. In general, this secondary magnetic field ($\boldsymbol{H}_s$) is delayed and attenuated due to the dissipation of energy:

$$\boldsymbol{H}_s = \boldsymbol{H}_1 \sin(\omega t + \varphi), \tag{3.12}$$

in which $\boldsymbol{H}_1 << \boldsymbol{H}_0$, and φ the phase lag. Both the primary magnetic field, travelling through the air, and the secondary magnetic field, modified by the conductive medium it is travelling through, will induce current in the receiver coil. The receiver thus registers the voltage induced by the overall, combined effect of the primary and the secondary magnetic fields. The sensor response is quantified in the ratio of the secondary to the primary field ($\boldsymbol{H}_s/\boldsymbol{H}_p$). This ratio is complex and comprises two orthogonal components, the real or in-phase (IP) component and the imaginary or out-of-phase, or quadrature (QP) component, which can be linked to the properties of the conductive medium. More specifically, the QP response has been demonstrated to pertain to the electrical conductivity of the medium, while the IP response can be interpreted in terms of its magnetic susceptibility.

Operation at low induction numbers

The conversion of the sensor output, the QP and IP components, into the soil properties of electrical conductivity and magnetic susceptibility relies on the adoption of conditions of low induction numbers (LIN; Keller & Frischknecht, 1966; McNeill, 1980). To define the induction number (B), we first need to introduce the concept of skin depth (δ). The skin depth is a common measure for the depth of penetration of EM waves and is defined as the depth at which the amplitude of an incident plane wave has decreased to $1/e$ or ~37% of its initial amplitude:

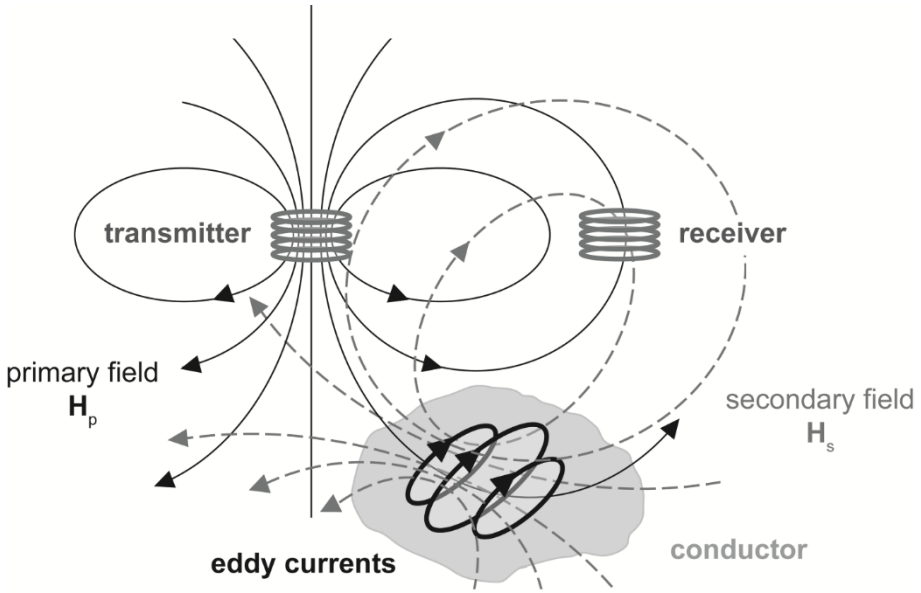

Figure 3.3 Schematic representation of the EMI operating principle. After Reynolds (2011).

$$\delta = \sqrt{\frac{2}{\mu\sigma\omega}} \tag{3.13}$$

where ω = 2π*f* expressed in radians s^{-1}, and *f* is the frequency in Hz, σ is the electrical conductivity in S m^{-1}, and μ is the magnetic permeability. In the application of EM methods, the magnetic permeability is generally assumed to equal its free space value. This shows that the depth of penetration of EM waves is largely determined by the frequency of the transmitted wave and the conductivity of the media through which it travels. The induction number is then determined by:

$$B = \sqrt{\frac{s}{\delta}} \tag{3.14}$$

with *s* the separation between the transmitter and receiver coil. Under conditions of LIN, i.e. *B* << 1, the measured QP response of the EMI sensor is directly proportional to apparent electrical conductivity (σ_a, or abbreviated as EC_a in the following chapters) according to:

$$\sigma_a = \frac{4}{\omega\mu_0 s^2}\left(\frac{\mathbf{H}_s}{\mathbf{H}_p}\right)_{QP}. \tag{3.15}$$

The apparent electrical conductivity relates to the conductivity of a half-space under influence of the propagated EM field. If the affected soil volume is entirely homogeneous, a measure of its true electrical conductivity is obtained. In reality,

however, soil mostly consists in different constituents with different intrinsic electrical conductivity. The apparent electrical conductivity then should be interpreted as the bulk electrical conductivity of the soil volume under influence. Similarly, if the LIN conditions are met, the apparent magnetic susceptibility (κ_a, or MS_a in the next chapters) can be derived simply by multiplying the IP response with a factor of two, to account for the measuring a half-space of soil:

$$\kappa_a = 2\left(\frac{\mathbf{H}_s}{\mathbf{H}_p}\right)_{\text{IP}}. \tag{3.16}$$

Whereas not explicitly expressed in Equations 3.15 and 3.16, the sensor response also depends on the orientation of the coils. The three most commonly used dual-coil configurations are horizontal coplanar (HCP, vertical dipoles), vertical coplanar (VCP, horizontal dipoles), and perpendicular (PRP). For each of these orientations, the sensitivity distribution of the sensor response in depth has been approximated in function of the coil separation, providing an alternative means to define the depth of exploration (DOE) specific of a certain coil configuration. In the next section on sensor instrumentation, these functions will be discussed in more detail for the HCP and PRP coil configurations that are incorporated in the EMI instruments used in this research. It is remarked that any definition of DOE always will involve some arbitrary decisions, yet, the longing for a universal measure of DOE, and the associated sample volume of EMI measurements, continues to live on (e.g. Callegary et al., 2012; Christiansen & Auken, 2012).

The conditions of LIN are translated into the sensor design through the selection of the operation frequency (*f*) and the inter-coil spacing (*s*) and orientation. However, if these conditions are actually fulfilled also depends on the properties of the soil to which the EM field is applied, which – as targets of the EMI survey – are usually unknown. Mostly, the caveat is in the soil's true electrical conductivity. The effective conductivity limit that has to respected to fulfill LIN depends on the criterion used. An often suggested guide value is 100 mS m^{-1}, yet the LIN limit generally decreases with increasing coil separation. Different manufacturers include practical LIN limits in the instruments' user's manuals. For example, Dualem Inc. (2013) mentions LIN limits of 240 mS m^{-1} and 15 mS m^{-1} for HCP coil configuration with respective separations of 1 m and 4 m. For legitimate data interpretation, it is important to be aware of the possible consequences of violation of the LIN conditions (Beamish, 2011; and Callegary et al., 2007, see also Delefortrie, Saey, et al., 2014):

- The σ_a measurements can become underestimates of the true conductivity due to departure from the linear relationship between the σ_a and the QP response.
- The depth of penetration of the EM field can be reduced and, correspondingly, the soil volume of which the measurements can be considered representative can become smaller.
- The interpretation of σ_a and κ_a measurements can no longer be performed independently, because the IP response also tends to increase with increasing electrical conductivity.

On a related note, some other situations can be responsible for the derivation of the σ_a and κ_a as presented above to become invalid:

- As opposed to high conductivities causing the LIN limit the be exceeded, sensor measurements also can show erratic behaviour if the conductivity is too low; in highly resistive media induced currents can become insufficient to obtain reliable measurements of the QP response; i.e. the QP response is below the system noise level. This may lead to the display of negative σ_a values.
- In very low conductive environments, the presence of magnetic material can influence the QP response and thereby interfere with accurate readings of the σ_a (Tabbagh, 1986a).
- Finally, the assumption of the magnetic permeability $\mu = \mu_0$ that is usually made in the practical calculation of the skin depth is invalid if ferrous metal objects/structures are present, such as pipelines, steel drums, or UXO (Everett, 2013). The magnetic permeability may be a factor of 50 higher in these cases, causing a severe reduction of the skin depth, which propagates into a proportional increase of the induction number.

3.3.2 **Sensor instrumentation**

The specific EMI instruments applied in this research are two multi-receiver EMI sensors manufactured by Dualem Inc. (Milton, ON, Canada). Both operate at a fixed frequency of 9 kHz. The DUALEM-21S incorporates four transmitter-receiver coil combinations: one transmitter coil paired with four receiver coils at separation distances of 1 m, 1.1 m, 2 m and 2.1 m. The 1 m and 2 m pairs have a HCP orientation, while the 1.1 m and 2.1 m pairs have a PRP configuration. The DUALEM-421S has an additional HCP and PRP coil combination with a transmitter-receiver

separation of respectively 4 m and 4.1 m. A schematic representation of these two sensors is shown in Figure 3.4. Both sensors allow for simultaneous measurement of the QP and IP response, in contrast to many previous generation instruments such as the pioneer, dual-coil EM38 sensor (Geonics Limited, Mississauga, ON, Canada). The sensor provides a direct reading of the QP response as the apparent electrical conductivity (σ_a), expressed in millisiemens per meter (mS m^{-1}), by assumption of operation under conditions of LIN. The IP response is outputted as the raw secondary to primary field ratio, expressed in parts per thousand (ppt). As evidenced by Equation 3.16, the IP response can be easily converted to the apparent magnetic susceptibility (κ_a), by multiplication of the measured values with 0.002 (Simpson et al., 2010).

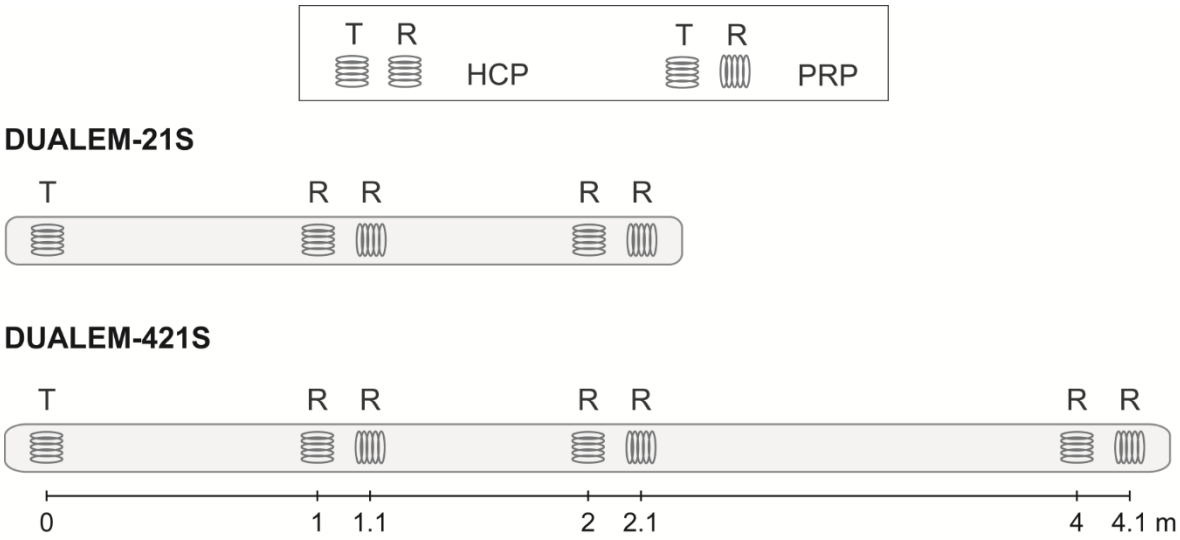

Figure 3.4 General scheme of the coil configurations included in the DUALEM-21S and DUALEM-421S EMI instruments.

DOE

As mentioned above, functions have been constructed that express the sensitivity of the EMI response in depth (McNeill, 1980; Wait, 1962). Assuming the instrument is operated at LIN and considering a homogeneous half-space, the impulse response functions (ϕ) describe the relative contribution of a thin semi-infinite horizontal layer to the secondary magnetic field ($\boldsymbol{H}_s$) in function of the depth of the layer. The dependence on the depth is normalized to the inter-coil separation *s*. Figure 3.5a shows the impulse response functions of the QP component – or apparent electrical conductivity σ_a – for the coil configurations included in the DUALEM instruments that will be used in this research. For the PRP configurations, the relative response is maximum at the surface and decreases with depth. In contrast, in the HCP responses there is little contribution from shallow depths and maximum sensitivity is reached

around a depth of 40% of the coil separation. In general, the measurement depth increases with an increasing coil separation and, for the same coil separation, is larger for a HCP orientation than for a PRP orientation. The impulse response functions can be integrated to calculate the contribution of the soil volume above a certain depth, creating the so-called cumulative response functions (*R*). Based on these curves, the DOE characteristic of a specific coil configuration has been defined as the depth at which 70% of the response is obtained from the soil volume above this depth (e.g. Abdu et al., 2007; Callegary et al., 2007; Saey, Simpson, et al., 2009). According to this convention, the DUALEM-21S provides measurements of the σ_a that are representative of soil volumes reaching down to depths of 0.5 m (1.1 m PRP), 1.0 m (2.1 m PRP), 1.6 m (1 m HCP), and 3.2 m (2 m HCP). The additional 4.1 m PRP and 4 m HCP configurations included in the DUALEM-421S have a DOE of respectively 2.0 m and 6.4 m. Note that these values are custom to an instrument elevation of zero, i.e. the coil centres are on the ground surface.

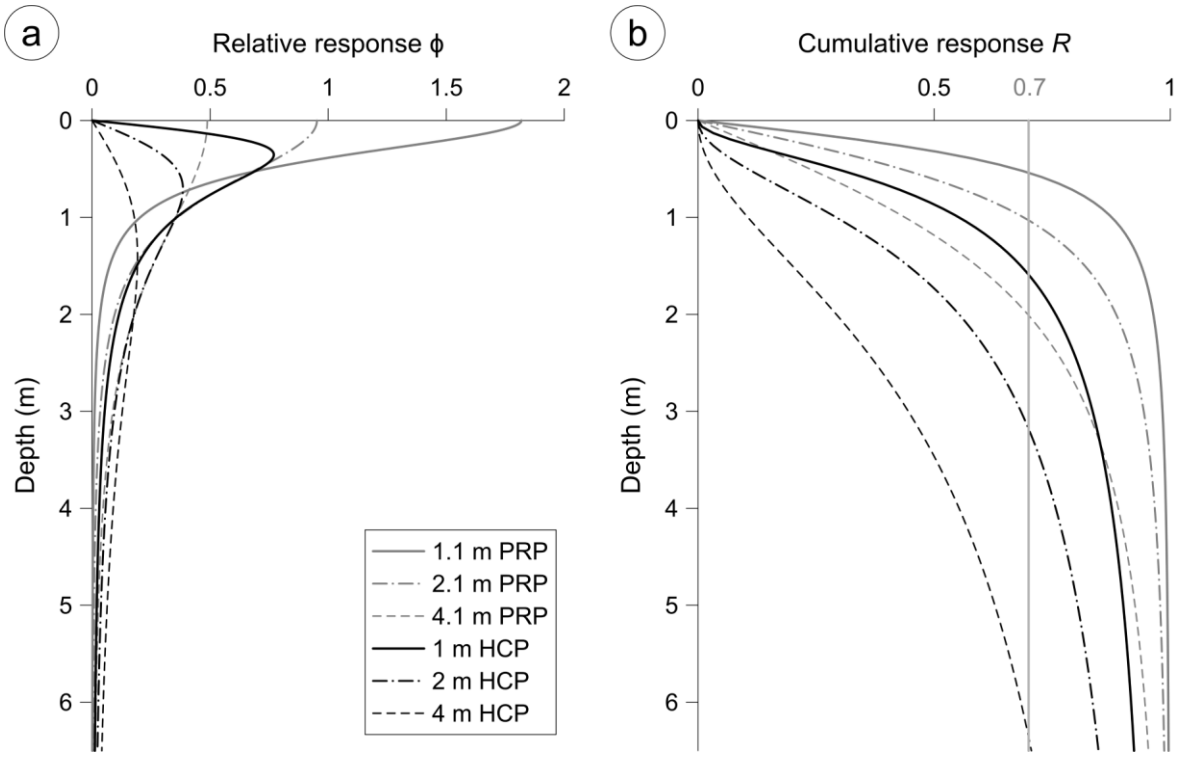

Figure 3.5 Impulse or relative response functions (a) and cumulative response functions (b) of the σ_a response as a function of depth for the transmitter-receiver coil combinations comprised in the DUALEM-21S and DUALEM-421S sensors. The threshold cumulative response *R* of 70% is indicated allowing to derive the DOE of the different coil configurations.

Similarly, depth sensitivity functions have been derived for the IP response – or apparent magnetic susceptibility κ_a, yet these functions have a more complex form: the relative response functions have negative parts so that the cumulative responses

are non-monotonically increasing with depth (McNeill & Bosnar, 1999; Simpson et al., 2010; Tabbagh, 1986b). The interpretation of the IP depth sensitivity is fraught with intricacy. De Smedt, Saey, et al. (2014) introduced the concept of critical depth, i.e. the depth at which the cumulative response function reaches its maximum. For the 1 m and 2 m HCP configurations the critical depth is 0.6 m and 1.2 m, respectively. Only when a magnetic structure occurs above the critical depth of a coil configuration, it will produce a pure positive anomaly in the corresponding signal. Generally, the IP responses of the different coil configurations are assumed to have the same order of DOE as the corresponding QP responses, but the IP depth sensitivity is consistently shallower.

It is emphasized the presented depth sensitivity curves comply with a homogeneous or horizontally stratified soil and therefore are theoretically incompatible with lateral inhomogeneity. Considering the lateral extent of the soil volume contributing to the response of a certain coil configuration is approximately the same the same as its vertical depth, as postulated by McNeill (1980), the requirement of lateral uniformity can be relaxed to a radius of one or a few metres around the instrument. Note that this also implies that there is a trade-off between measurement depth and measurement resolution. Furthermore, the sensitivity distribution is not necessarily symmetrical in the lateral plane. While this is indeed the case for symmetric coil configurations such as the HCP configurations, asymmetric configurations such as the PRP configurations are known to produce asymmetric responses along the transmitter-receiver line. When alternate survey lines are collected in opposite directions (see the following paragraph on survey design), elongated conductors perpendicular to the alternating survey line direction can result in a so-called herringbone pattern (Frischknecht et al., 1991; Reynolds, 2011). An in-depth discussion of the 3D sensitivity distributions of EMI responses is out of the scope of this work. Yet, it can be useful to consult the publications of Callegary et al. (2012) and Tølbøll and Christensen (2007) to get an idea of the general patterns of the 3D sensitivity distributions for the different coil configurations here considered. The first group of authors visualizes the local sensitivity of the HCP and VCP coil orientations, conforming with operation under conditions of LIN. The second provides comprehensive illustrations of the sensitivity distribution of both the QP and IP components for HCP, VCP, PRP and vertical co-axial orientations. The work addresses airborne EM frequency-domain systems, but the essence can easily be downscaled to land-based surveys.

Summarizing, the presented multi-receiver EMI instruments allow for the simultaneous collection of multiple σ_a and κ_a data sets that are representative of different soil volumes. The maximum DOE of the DUALEM-21S and DUALEM-421S is 3.2 m and 6.4 m, respectively. Textbook operation of the instruments and interpretation of the acquired data is amply constrained. The question is to which extent these constraints will be provoked by the typically heterogeneous conditions of urban soil.

3.3.3 **Survey design**

Mobile survey configuration

For each of the case studies presented in the following chapters, EMI surveying was performed using a mobile survey platform as shown in Figure 3.6. The EMI sensor was fixed in a polyethylene sled which was towed by a quad bike. In the case of the DUALEM-21S, the sled completely enclosed the instrument; in the case of the DUALEM-421S, the instrument extends approximately 1.2 m outside of the sled casing. For both, the instrument elevation, defined as the height of the inter-coil centre line above the ground surface, was 0.16 m. The sled was tied to the quad by means of two ropes, providing a flexible connection. The distance between the front of the sensor and the back of the quad was 3.0–3.5 m, to prevent the (metal parts of the) quad from interfering with the sensor measurements. During surveying, this distance varies due to variable tension on the ropes and possible inertia of the sensor when taking turns. The sled ran parallel to the driving line, so the inter-coil centre line was in-line with the moving direction. Moving the instruments perpendicular to the driving direction could provide better spatial resolution and a higher signal-to-noise ratio (SNR), and would allow to scan a larger area in a single run (Frischknecht et al., 1991). For multi-receiver sensors, however, this would cause the midpoints of the different transmitter-receiver coil pairs to be on separate parallel survey lines, which might complicate the data processing and the interpretation of vertical variability from comparison of signals with a different DOE. Furthermore, dragging along a 2.5-m/4.5-m broad sled would strongly hamper smooth manoeuvring on uneven terrain.

The position of the mobile survey platform was recorded in real-time by use of a differential global navigation satellite system (dGNSS). Two specific systems are used: a Trimble AgGPS 332 with OmniSTAR differential correction (Trimble Navigation Ltd., Sunnyvale, CA, USA), which provides a positional accuracy of 10 cm, and a Leica Viva GNSS-G15 system (Leica Geosystems, Heerbrugg, Switzerland)

Figure 3.6 Mobile EMI survey configuration illustrated for the DUALEM-421S sensor; the photograph was taken at the landfill site discussed in case study IV in Chapter 5, more specifically in survey zone 5.

with real-time kinematic (RTK) correction, which further improves the accuracy to 2 cm. Detailed reviews of dGNSS and RTK geo-referencing solutions can be found in Grejner-Brzezinska (2008) and Landau et al. (2009). The dGNSS receiver antenna is mounted at the back of the quad instead of on top of the carrier sled to avoid interference with the EM signals of the sensor (e.g. Corwin & Lesch, 2005b) and to provide a more stable base to intercept changes in the tilt of the antenna due to terrain unevenness. Furthermore, the real-time positioning data were used as input for navigation guidance, which also benefited from the installation of the antenna on the quad. Sensor and position data are synchronously logged to a field computer (Allegro model, Juniper Systems, Inc., North Logan, UT, USA) with HGIS software (Starpal, Inc., Fort Collins, CO, USA). Position data are commonly recorded at a frequency of 1 Hz. A lightbar guidance system (Trimble EZ-Guide 150 System), affixed in front of the driver's seat, facilitates surveying along parallel lines (see next paragraph) and simultaneously offers rudimentary real-time visualization of the positioning data.

Survey pattern and sampling intervals

By default, a survey area is scanned by driving along parallel lines, in which alternate lines are collected in an opposite sense. Such a bidirectional pattern is commonly used thanks to its high time-efficiency: there a no dead ends; successive survey lines can be taken in a continuous way, without requiring intermediate reorientation of the survey platform (e.g. Wilson et al., 2005). The main driving line direction is aligned with the longest dimension of the survey area in order to minimize the number of turns. In case the straight-line driving length was too short, with a minimum length of about 45 m, the standard zigzagging was left for block driving. In

Figure 3.7 the two survey patterns are illustrated in a plot of the raw position data of the EMI survey that will be discussed in Chapter 5, case study II.

To decide on sampling intervals it is generally recommended to be mindful of the phenomenon of spatial aliasing (Reynolds, 2011). However, this requires having an *a priori* idea of the nature and size of the targeted subsurface phenomena. As discussed in Chapter 2, urban soil is typically characterized by a high variability which already manifests at small spatial scales, hence, the general motivation for high-resolution surveying. The horizontal survey resolution is determined by the distance between successive survey lines (cross-line sampling interval) and the distance between two consecutive measurements within the survey line (in-line sampling interval). The cross-line interval in most cases is chosen in the order of 1–1.5 m, to correspond with the minimum lateral extent of the soil volume that can be "intrinsically" resolved by the sensor's transmitter-receiver coil pair with the smallest separation distance. In this way, literally the entire area is sensed. In case study I presented in Chapter 5, the objectives require less detailed surveying and a larger cross-line distance was

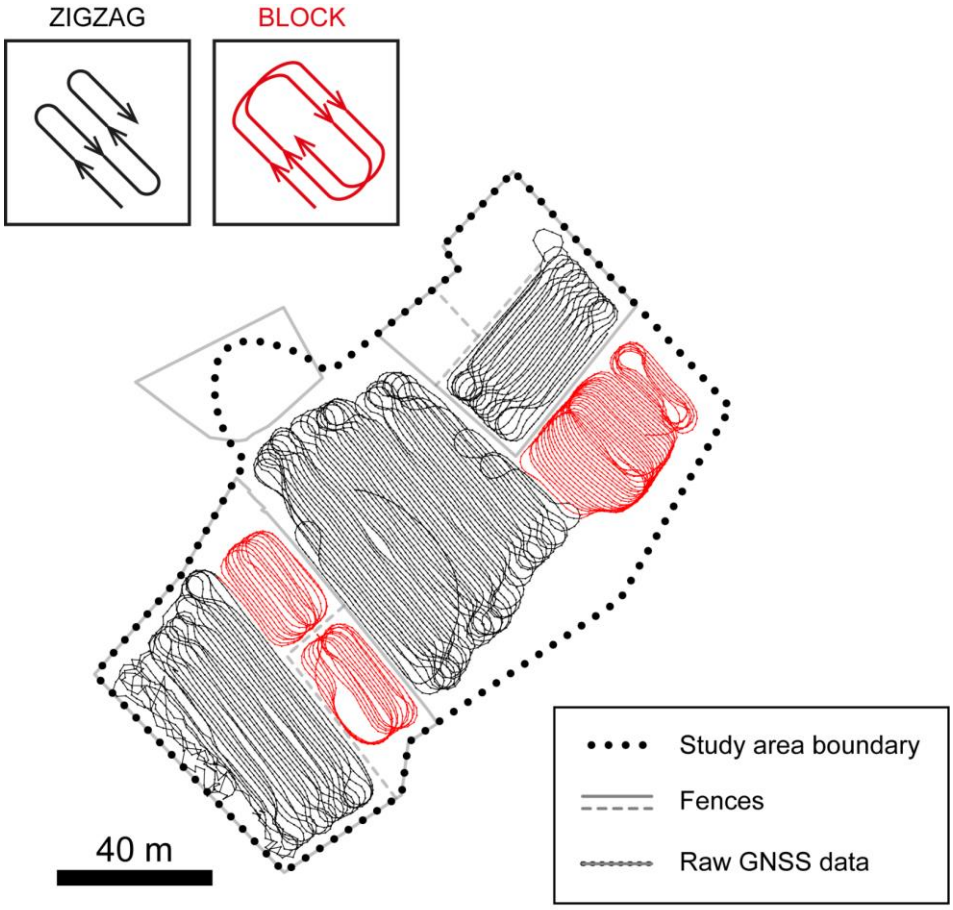

Figure 3.7 Outline map of the landfill site under consideration in Chapter 5, case study II, with connected raw position data illustrating the default zigzag and block survey patterns.

experimented with in order to evaluate the effect on survey efficiency. The selection of the in-line sampling interval is less straightforward because it is indirectly determined by the combination of sampling rate and driving speed. For mobile surveying, a sampling rate in the 4–10 Hz range has been recommended (Beamish, 2011; Delefortrie, De Smedt, et al., 2014). Lower sampling rates are advantageous to data quality, which is of increasing relevance for increasing soil volumes being measured. This means that the DUALEM-421S could be better off with a lower data rate; a sampling rate of 4 Hz as well as 8 Hz is tested. In previous studies deploying the same survey configuration, the majority of which performed on agricultural land, the achievable driving speed usually was between 5 km h^{-1} and 10 km h^{-1} (e.g. Saey et al., 2013; 2015). In combination with the applied sampling rates, the in-line sampling interval is anticipated to be roughly between 0.2 m and 0.7 m.

3.3.4 **Data processing**

The optimization of EMI survey data processing was a main objective of the doctoral research of Samuël Delefortrie (Delefortrie, 2017); hence, for a comprehensive discussion on this topic, supported with explanatory figures, the reader is directed to this reference. Here only the most important aspects are summarized. All data processing was done in MATLAB (The MathWorks Inc., Natick, MA, USA), except for final data interpolation.

Data cleaning

Before starting any actual data crunching, the collected data sets need to be checked for possible survey errors. These include but are not limited to incorrect data positioning due to GNSS signal loss, deviating data measurements caused by turning over of the sensor sled in sharp turns, operational noise induced by rough surface conditions, and inference with above-ground (metallic) structures/objects. An illustration of the first can be seen in the westernmost survey lines plotted in Figure 3.7. In general, erroneous data points are manually removed. An exception is made when removal of all affected data would lead to a spatially disconnected data set and/or when disturbing effects can be easily accounted for in interpretation. For example, interference with metal fences typically manifests at the edges of a survey area and has a clearly recognizable signature. The affected data points are then deliberately disregarded in the interpretation of the measurements in terms of subsurface properties. While data errors may not always ask for categorical

measures, it is crucial that they are adequately recognized. This is often easier if the data positions are first shift-corrected.

Shift correction

The presented survey configuration requires the recorded position data to be corrected for the spatial offset between the GNSS receiver, positioned at the back of the quad, and the midpoints of the transmitter-receiver coil combinations. This correction will be henceforth referred to as *shift correction*. It is clear that the objective of a high-resolution survey is overreached if accurate data positioning cannot be guaranteed. Considering the typically large heterogeneity of urban soil, accurate spatial referencing in this context likely is an even more pressing issue than in agricultural studies (e.g. Gottfried et al., 2012). Correcting for spatial shift of position data might seem straightforward at first glance, yet several non-singular sources of positional inaccuracy are involved. Besides the spatial offset resulting from the distance between the GNSS receiver and the sensor, and the differential midpoints of the different transmitter-receiver coil, temporal offsets arise from communication delays between the GNSS receiver and the EMI instrument on the one hand, and the data logger on the other. Furthermore, the sensor measurements are non-instantaneous. Although these time discrepancies are small, they can propagate into significant positional offsets at relatively high survey speeds as proclaimed by motorized surveys (see also Corwin & Lesch, 2005b).

Correction for the horizontal offset between position and sensor data is performed using the methods scrutinized in Delefortrie et al. (2016), which can be consulted for a more detailed description of the applied procedures and information on their implementation. The crux of the shift correction concept is summarized here. The offset is essentially approached as the sum of the offset due to physical distance and the offset to a time lag between the registration of sensor and position data points. The first in its turn is split up in two parts, according to the two pivot points along the connection between the quad and the transmitter-receiver midpoints: (1) the offset between the position of the GNSS receiver, which is also the point of attachment of the towing ropes, and the front end of the sled – corresponding to a flexible connection, and (2) the offset between the front end of the sled and the transmitter-receiver midpoints – corresponding to a rigid connection. Three different methods are considered to derive the position of a connection tail from the position of the corresponding connection head, the latter of which coinciding with a pivot point.

1. *Direction vector shift* – Position data points are corrected by shifting them backwards along the instantaneous driving direction, which is determined from comparison with a previous (or subsequent) position data point in time, over a constant distance fixed from the survey configuration (see also Simpson et al., 2008).
2. *Constrained shift* – Position data points are corrected by shifting them backwards, over a constant distant fixed from the survey configuration; the allocation of the corrected coordinates is restricted to the course of the survey track as determined by the pivot point (see also Delefortrie, De Smedt, et al., 2014).
3. *Kinematic correction* – Position data points are corrected by application of a kinematic model (tractrix equation) accounting for the mechanisms acting on a sled or cart being towed at a constant distance of a drawing vehicle (see also Gottfried et al., 2012).

In most cases presented in this research, a combination method is used: the location of the GNSS receiver is transposed into the location of the front of the sled through a kinematic correction and, subsequently, the transmitter-receiver midpoints are obtained from a constrained shift along the sled. Delefortrie et al. (2016) proved this to be best practice for the adopted survey configuration. Equal performance was achieved when using the direction vector method to compensate for the offset along the sled. However, here the constraint method is preferred by virtue of its robustness. An additional temporal offset due to a communication delay between the devices can be easily reckoned with by selecting an earlier GNSS data points as starting point for the spatial offset correction.

In practice, shift correction is implemented by addressing the spatial offset based on the (assumed) constant distance spanned by the towing ropes and the separation between the front of the sensor and the coil pair midpoints, followed by optimization of a time lag. The selection of the time lag is usually evaluated by plotting the corrected sensor data points, for different time lag values and then, based on visual inspection, choosing the time lag which best succeeds in producing a spatially continuous pattern in the direction perpendicular to the main driving direction. In the case of bidirectional surveying along parallel lines, a time lag typically reflects in a striped pattern, as adjacent measurement lines, corresponding to opposite driving directions, are shifted with respect to each other. Shift correction is considered optimal if the striped pattern has disappeared. However, this can be difficult to perfect for the PRP coil

configurations displaying an asymmetric response. Finally, it is remarked that under- or overcorrection of the spatial offset may be (partly) compensated for by the correction of the temporal offset and vice versa. Yet, correction for the spatial offset between position and sensor data should as much as possible rely on knowledge of the applied survey set-up.

Drift correction

The response of EMI sensors is well-known to be prone to drift. In Delefortrie, De Smedt, et al. (2014), drift is defined as a systematic variation of the response over time that exceeds the signal noise level, without appreciable changes above or underneath the surface. Drift can be responsible of global trends or abrupt changes in the collected data that are not related to changes in soil properties and, hence, can strongly affect the data reliability, although the importance of the effect is relative to the SNR (Abdu et al., 2007). While many authors have addressed the issue, the causes of drift have not been unambiguously resolved. Changes in ambient temperature have been indicated as an important external factor contributing to drift, however, their influence has been proven inconsistent (Sudduth et al., 2001). Also instrumental aspects such as circuit design and coil performance under heating have been reported to contribute to data instability. Some of the recent EMI instruments, as the DUALEM sensors, have been provided with internal calibration, yet, this generally is incapable to eliminate drift completely, so that additional correction measures are recommended. Several methods have been proposed, most of which consisting in a "relative" calibration to the prevailing field circumstances, including a sufficiently long sensor warm-up time prior to the survey (Robinson et al., 2004) and repeated measurements at one or more fixed locations or transects for drift assessment and correction (e.g. Sudduth et al., 2001; Pedrera-Parilla, 2016). Another type of methods relies on the use of more robust ancillary data, such as from other geophysical methods as electrical resistivity (e.g. Minsley et al., 2012).

In this work, the drift correction procedure as proposed by Delefortrie, De Smedt, et al. (2014) is followed, or the procedure at its cradle (summarily) described in Simpson, Lehouck, et al. (2009). The first is briefly summarized here. Essentially, this procedure is founded on the same principle as the collection of repeated measurements. Calibration data are aquired along a line crossing the entire survey, usually in the shape of the letter W, within a short time span (less than ten minutes). A calibration line is collected at the end of a separate survey zone, meaning that the procedure applied only corrects for drift within this zone. In does not account for drift

over different survey zones, for instance, due to different weather conditions on different survey days.

The correction for drift is generally performed after correction for the spatial offset between the recorded position and sensor data. Any remaining errors in the corrected measurement positions will propagate in the comparison of survey and calibration data for drift correction; hence, proper shift correction is a prerequisite for the meaningful evaluation of drift. On the other hand, severe drift may be problematic for an accurate shift correction, in the case of which iteration between these two processing steps may be recommended. The comparison pairs of calibration and survey data are determined by combining each calibration point with the survey points in its direct vicinity (within a radius smaller than 1 m). It is underlined that, apart from drift, small-scale subsurface heterogeneities and the difference in sensor orientation can contribute to the difference between calibration and survey comparison data. Drift modelling is performed through spline-fitting of the residuals – the differences between corresponding calibration and survey data points – plotted in function of survey time. Prior to the actual modelling, outlying residuals are removed by application of a Hampel filter. The drift corrected survey data are obtained from summation of the original survey data and the estimated drift at that time. The reader is referred to Delefortrie, De Smedt, et al. (2014) for more details.

Temperature correction

The difference in ambient conditions between different survey zones can be (partly) compensated for by standardizing the measured σ_a values to a reference temperature. If terrain conditions permitted for measurement of the subsurface temperature, the σ_a data were converted to a temperature of 25°C according to the equation presented by Sheets and Hendrickx (1995):

$$\sigma_{25} = \sigma_a \left(0.4470 + 1.4034\, e^{T/26.815}\right), \qquad (3.17)$$

where σ_{25} is the standardized σ_a and T is the soil temperature in degrees Celsius. The soil temperature was measured at a shallow depth (~10 cm) near the centre of the survey zone, during collection of the calibration line.

Data visualization

For final visualization, the processed EMI data are interpolated through ordinary kriging (Goovaerts, 1997). This will be separately discussed in section 3.5.

3.4 GPR

As mentioned above, a comprehensive review of GPR is provided by Jol (2009). Conyers (2004) gives an approachable introduction to the method with focus on archaeological applications. As for EMI, only the basic principles of GPR are summarized here to support interpretation of the data presented in Chapters 6 and 7.

3.4.1 Operating principle

A GPR system essentially consists of a signal generator, one or more transmitting and receiving antennae, and a console to control the signal generation and recording. A train of EM waves with fixed frequencies is transmitted into the ground, propagating away from the transmitter antenna in a broad beam. The receiver antenna detects reflected and scattered EM waves. Reflections are generally generated from contrasts in the dielectric permittivity of the media through which the EM wave travels, as these correspond to changes in the wave propagation velocity (see below). The strength of the reflection, represented by the amplitude or magnitude of the GPR signal, is proportional to the degree of contrast encountered. The time delay between the transmission of the signal and the detection of a returning reflection, indicated as the *two-way travel time*, is determined by the depth at which the contrast occurs and the velocity of the wave in the above-lying medium. The transmitted high-frequency waves travel at high speeds and the two-way travel time is usually in the order of a few tens of nanoseconds (1 ns = 10^{-9} s). Figure 3.8 schematically illustrates the operating principle of GPR and the construction of a reflection from a series of wavelets generated at different interfaces between contrasting layers of dielectric permittivity. Note that the transition between the air and the ground surface also produces a reflection, which corresponds to the so-called direct ground wave. In common survey practice the GPR transmitter-receiver combination is moved along a transect and the output is displayed as a sequence of traces, representing the received signal at a certain point along the survey line plotted in function of their two-way travel time, in the form of a so-called radargram. The amplitude of the signals is usually visualized according to a grey-scale.

Wave velocity, energy loss and attenuation

To properly analyse data provided by GPR, two aspects of EM wave propagation need to be understood: the speed of propagation and the attenuation of the waves. An

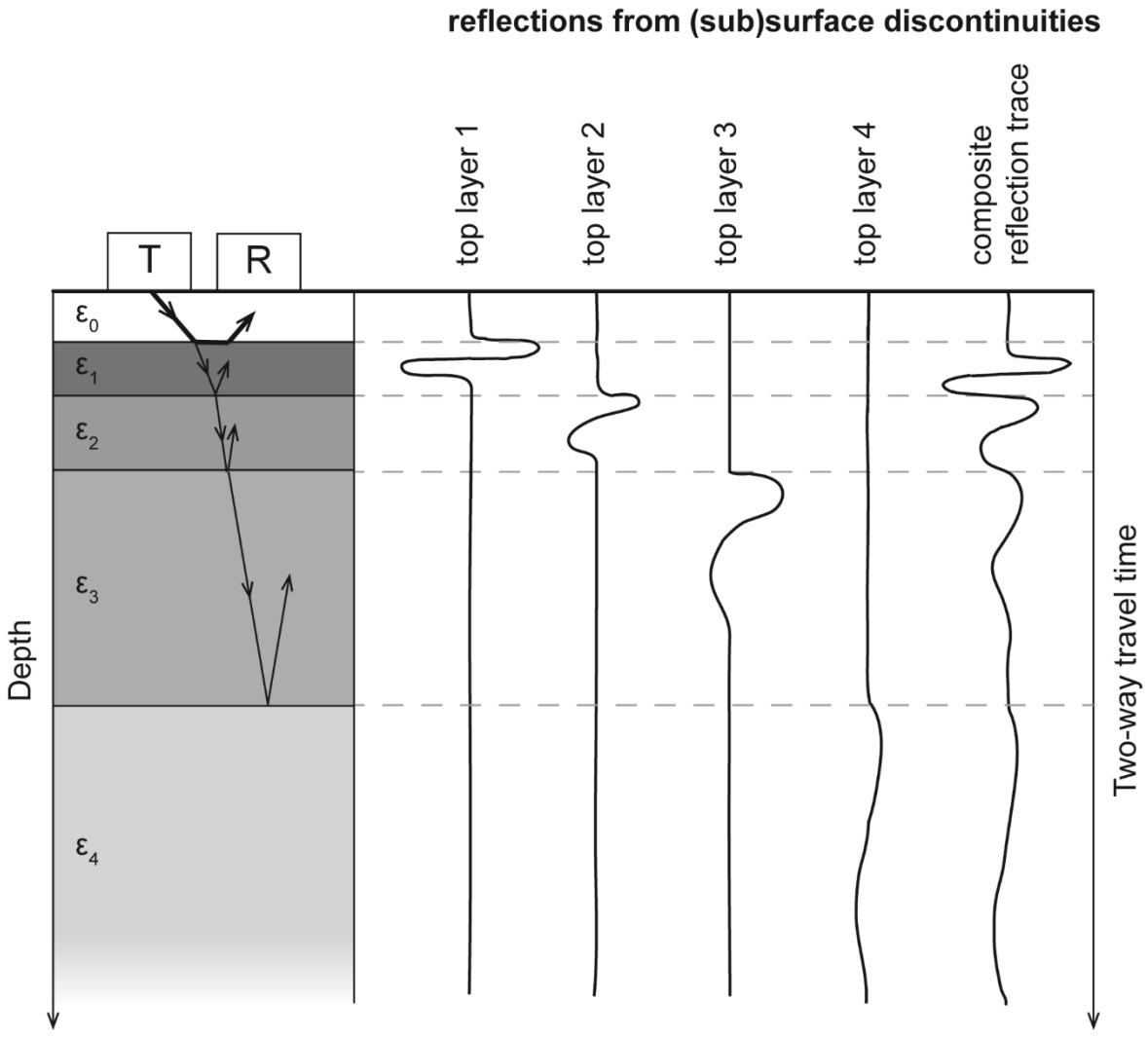

Figure 3.8 Schematic representation of the operation principle of GPR. The transmitter antenna (T) generates an EM wave which propagates into the ground. At the interface between layers with contrasting dielectric permittivity, a part of the wave is reflected and a part is transmitted to deeper layers. Also the interface between the air (ε_0) and the top soil layer (ε_1) produces a reflection, corresponding to the so-called direct wave travelling along the soil surface. The returning reflection recorded at the receiver antenna (R) is a complex wave shape consisting of different wavelets generated at different layer boundaries. After Annan (2009) and Conyers (2004).

approximation of the speed of EM waves can be made under the condition of a low loss factor (*P*), which is expressed by:

$$P = \frac{\sigma}{\omega\varepsilon} \approx 0 \qquad (3.18)$$

where σ is the electrical conductivity, $\omega = 2\pi f$ where *f* is the frequency, and ε is the dielectric permittivity of the medium through which the wave propagates. This is mirrored into the operational design of GPR in that, within the typical radar frequency range of 10 MHz to 2 GHz, the velocity is independent of the frequency and the

conductivity of the medium. Thus, for low-loss, non-magnetic media (media with a magnetic permeability equal to that of free space, $\mu = \mu_0$), the EM wave velocity can be simplified to

$$v = \frac{c}{\sqrt{\varepsilon_r}} \tag{3.19}$$

where $c = 3 \times 10^8$ m s^{-1} = 0.3 m ns^{-1} is the speed of light in vacuum and $\varepsilon_r = \varepsilon/\varepsilon_0$ is the relative dielectric permittivity (abbreviated as RDP in the following chapters) or the dielectric constant, with ε_0 the permittivity of free space with an approximate value of 8.85×10^{-12} F m^{-1}. In general, propagation velocity is inversely related to the relative dielectric constant of the medium, with air and water representing the two extremes (see also Table 3.2). Air has a relative dielectric constant $\varepsilon_r = 1$ so that in air EM waves travel at the speed of light. Due to the high polarizability of the water molecule in the presence of an applied electric field, water has an anomalously high dielectric constant of $\varepsilon_r \sim 81$, causing EM waves to travel nine times slower as compared to in air. Consequently, the relative dielectric constant of soil is largely controlled by its water content; dry sand has a relative dielectric constant $\varepsilon_r \sim 3$, for wet clay the relative dielectric constant $\varepsilon_r \sim 40$ (see also paragraph 3.6.2).

The amplitude of a transmitted radar wave decreases as it propagates through subsurface media, which is caused by several factors. First, energy loss occurs when the EM wave passes through the interface of two dielectrically contrasting media, due to partial reflection and transmission of the wave. A particular type of reflection/transmission losses results from objects of which the dimensions are of the same order of the wavelength of the signal. Such small-scale heterogeneities scatter an incident radar beam in all directions and introduce clutter noise in the signal reflected back to the receiver. This phenomenon is indicated as scattering attenuation. Energy is also lost by absorption, the conversion of EM energy into heat. Furthermore, reflected signals weaken with depth due to geometric spreading of the energy. The transmitted signal can be represented as a cone-shaped beam: the incidence area increases with the distance from the transmitter, resulting in a reduction of energy per unit area. Finally, attenuation is a fundamental cause of energy loss, which is a complex function of the electric, magnetic and dielectric properties of the media though which the radar signal travels, as well as frequency of the signal itself. The attenuation coefficient (α) has been defined as the reciprocal of skin depth (δ), which,

as explained above, serves as a universal measure for the depth of penetration of an EM field:

$$\alpha = \frac{1}{\delta}. \tag{3.20}$$

For a full mathematical expression of the attenuation coefficient the reader is directed to the above-mentioned specialized literature. In the case of propagation without dispersion, i.e. under low-loss conditions ($P << 1$), the attenuation coefficient can be considered frequency-independent:

$$\alpha = \sqrt{\frac{\mu}{\varepsilon}} \cdot \frac{\sigma}{2}. \tag{3.21}$$

Usually non-magnetic media are assumed, so that the electrical conductivity and the dielectric permittivity are the decisive factors in the attenuation: the larger the conductivity, the stronger the attenuation and the smaller the depth of penetration; the opposite applies for the dielectric permittivity, although the effect of the last is mitigated by the square root. In a frequency-dependent regime, the attenuation is directly proportional to the frequency. Higher frequencies are preferentially attenuated and result in smaller depths of penetration. Signal attenuation generally has an exponential signature in depth. Note that the skin depth here only relates to the phenomenon of attenuation and does not account for other causes of energy loss such as antenna losses, transmission losses at the air-ground interface and geometric spreading of the transmitted energy; hence, the real depth of penetration will be consistently smaller than indicated by the skin depth. Due to the strong dependency on a variety of soil properties as well as on instrumental settings, the *a priori* estimation of depth of penetration is far from straightforward.

Vertical and horizontal resolution

The vertical or range resolution corresponds to the ability to discriminate between two reflection-generating contrasts succeeding each other in time, and thus in depth. Fundamentally, the vertical resolution is the inverse of the bandwidth of incident signal. Conventional GPR instruments consist in impulse systems in which a time-domain pulse of EM waves is generated, the peak power of which occurs at the nominal centre-frequency of the antenna being used. The bandwidth in this case is directly related to the centre-frequency (for most systems, the bandwidth is approximately equal to the centre-frequency), which explains why the vertical

resolution often has been expressed in terms of frequency. As a general rule the vertical resolution can be taken as one-quarter of the wavelength of the incident radiation, in which the wavelength $\lambda = v/f$. Table 3.1 gives an example of the theoretical vertical resolution according to this rule for three materials with different relative dielectric permittivity at three different frequencies. It is important to realize that the waveform transmitted in air will not be reproduced when being transmitted into the ground. Mostly, the bandwidth of the signal decreases as it propagates through the ground due to preferential attenuation of the higher frequencies. Hence, the resolution becomes coarser with depth. Note that the decrease in bandwidth also corresponds to a reduction in the SNR, as the noise bandwidth remains constant.

The horizontal resolution of radar reflections is determined by the size of the footprint of the transmitted beam, which enlarges with depth because of geometrical spreading. This also can affect the vertical resolution, for instance, for interfaces with steep slopes or high-amplitude roughness. Besides, the horizontal resolution is related to the attenuation: finer resolution is achieved when the attenuation is higher, which, intuitively contradictory, means that resolution is better for high-loss materials. The horizontal resolution is generally much poorer than the vertical resolution, roughly by a factor of ten. Both the vertical and horizontal resolution deteriorates with depth.

Table 3.1 Theoretical vertical resolution in three materials with different εr at three frequencies.

	Frequency (MHz)		
	100	500	1000
$\varepsilon_r = 5$, $v = 0.13$ m ns^{-1}			
λ (m)	1.34	0.27	0.13
resolution (m)	0.34	0.07	0.03
$\varepsilon_r = 15$, $v = 0.077$ m ns^{-1}			
λ (m)	0.77	0.15	0.08
resolution (m)	0.19	0.04	0.02
$\varepsilon_r = 25$, $v = 0.06$ m ns^{-1}			
λ (m)	0.60	0.12	0.06
resolution (m)	0.15	0.03	0.02

3.4.2 **Sensor instrumentation**

As mentioned above, the most commonly used GPR systems are impulse radar techniques, where a time-domain pulse is transmitted and the reflected signals are recorded as a function of time. In this work, however, a GPR system operating in the frequency-domain is used. The specific instrument is a GeoScope-GS3F system, a stepped-frequency continuous wave (SFCW) radar manufactured by 3d-Radar AS, Trondheim, Norway. This SFCW system transmits continuously, producing a waveform that consists in a sequence of sine waves with step-wise, linearly increasing frequency over a bandwidth of 50–3000 MHz. Because of this wide bandwidth, the system has also been denominated an ultra-wideband system. The reflected energy is received as a function of frequency and indicates the energy scattered from subsurface objects. The received signal is mixed with a portion of the transmitted one and sampled at each discrete frequency step. Data are recorded in complex form, in the real and imaginary components of the returned signal. In the following, the amplitude of the signal refers to either the real or the imaginary part of the signal; the magnitude of the signal is the absolute value of the complex signal, defined as the square root of the sum of the squared real and imaginary parts. For conventional visualisation of the data, transformation to time domain is required resulting in so-called synthetic pulses. The wide bandwidth overcomes having to compromise between penetration depth and vertical resolution as in the selection of an appropriate centre-frequency for impulse GPRs; an optimal resolution is offered for each achievable penetration depth. In addition, the system theoretically provides more efficient energy transmission into the ground, because energy is focused in one single frequency at a time. This anticipates an improved SNR as well as a greater depth of penetration (Koppenjan, 2009).

The SFCW system operates with a an electronically scanned array of air-coupled antennae, allowing for quasi-simultaneous data collection along multiple survey lines (channels), which strongly expedites the full spatial coverage of a survey area. The array consists of bow-tie, monopole pairs representing a quasi-monostatic antenna configuration with practically zero-offset distance. Here, a VX1213 antenna array was used, which includes seven transmitting and receiving antennae that are iteratively combined to supply 13 channels (Figure 3.9). The channels are at a uniform spacing of 7.5 cm so that the antenna array covers a total scan width of 97.5 cm. Although the system also provides for common-midpoints measurements (see De Pue et al., 2016), in the presented case studies only fixed-offset measurements are made. The air-

coupling of the antennae facilitates the use of motorized conveyance (see next paragraph), but is at the expense of a part of the potential gain in SNR of the SFCW technology as a higher proportion of the energy will be reflected at the air-ground interface. Furthermore, while the antenna array is shielded, it is sensitive to interference from above-ground reflections due its open sides (see Figure 3.10).

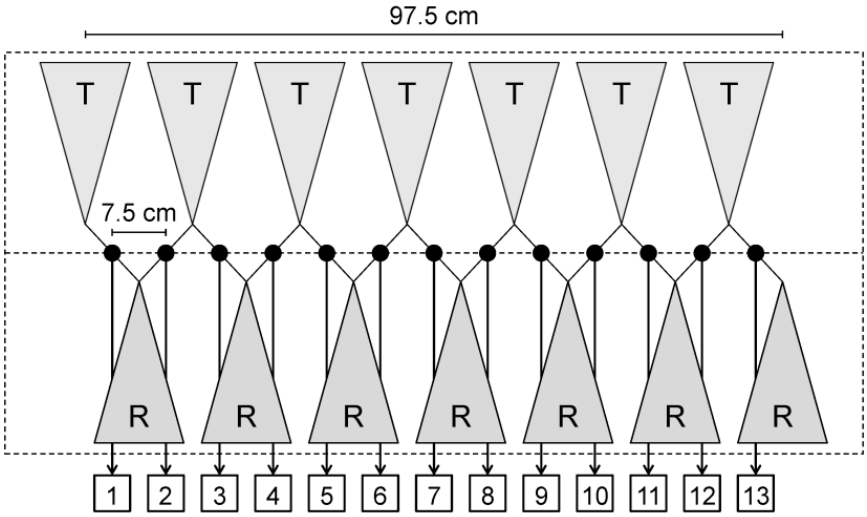

Figure 3.9 Schematic of the VX1213 antenna array used in combination with the GeoScope-GS3F SFCW system (3d-Radar AS, Trondheim, Norway). Seven transmitting (T) and seven receiving (R) antennae are included combining into 13 parallel data collection channels.

3.4.3 **Survey design**

Mobile survey configuration

Similar to the EMI survey set-up, the SFCW GPR system is integrated into a mobile survey configuration as shown in Figure 3.10. The GeoScope is installed at the back of a quad bike and is controlled from a rugged notebook (Panasonic Toughbook, Panasonic Corporation, Osaka, Japan) in the front, which also serves for real-time data visualization and quality control during data acquisition. The antenna array is mounted on a trailer with its lowest point around 5 cm above the ground surface. Position data are recorded with the same dGNSS systems as used for EMI surveying. Here, the GNSS receiver was mounted on the top of the centre of the GPR antenna array so that a spatial offset between position and GPR data in the in-line direction was avoided. The cross-line offset between the centre of the antenna array and the midpoints of the transmitter-receiver antenna combinations was automatically accounted for in the data recording by the GeoScope system. The survey speed was dictated by the time necessary to send the entire frequency range for a single trace, defined as the integration time, multiplied by the number of channels to be scanned at

a single sampling point along the driving direction. The driving speed usually was around 6 km h^{-1}.

Figure 3.10 Mobile survey configuration of the 3d-Radar GeoScope GS3F SFCW system in combination with a VX1213 antenna array; the photograph was taken at the industrial site discussed in Chapter 7.

Survey pattern and data recording

Parallel GPR scans are collected by following a block driving pattern (see Figure 3.7) as the rigidity of the trailer does not allow making sharp turns. To achieve complete coverage of the survey area, a minimum overlap of 10 cm between adjacent scans is ensured. The distance between two measurements in the driving line direction is controlled by an odometer integrated in one of the trailer wheels. Note that, while the survey path is traversed in a continuous way, data recording is regularly stopped and restarted so that the total data set consists in a series of successive sections stored in separate files. The main reason is to avoid too large data files and to minimize the damage if a file becomes compromised. In both case studies presented in Chapters 6 and 7, the in-line sampling interval is fixed at 5 cm, so that within an individual scan track – defined as the 3D data volume combined from the sections of the 13 parallel channels – a horizontal sampling resolution of 7.5 cm × 5 cm is obtained. The acquisition frequency bandwidth of the SFCW system was adjusted to 50–1500 MHz. The higher frequency range is not used as very-high resolution measurements of the upper few centimetres are deemed irrelevant in view of the research scope and including this higher frequency range would significantly increase the integration time required at a single sampling point and, correspondingly,

limit the survey speed. The frequency bandwidth is stepped in intervals of 2 MHz with a dwell time of 2 µs at each step. Previous field experiments (not further discussed in this work, see also Van De Vijver, De Pue, et al., 2015) had indicated these settings provided a good balance between data quality and survey speed.

3.4.4 **Data processing**

Literature provides a large number of publications devoted to the processing of GPR data (e.g. Annan, 1999, 2001; and Cassidy, 2009b). The majority of these focus on the processing of time-domain GPR data, yet many processing steps are applicable to frequency-domain data as well. Sala and Linford (2012) give a detailed discussion of the specific processing steps required for SFCW GPR data in the context of archaeological surveying.

The processing of GPR data can range from basic data clean-up to very complex dedicated processing, the latter of which is often focused on the extraction of information on specific well-defined targets (e.g. UXO and utilities). In this work, GPR surveying serves the integral characterization of a site where a complex history of human activities is expected to have resulted in a high subsurface heterogeneity. The specific subsurface structures and phenomena to be encountered are difficult to assess in advance. To avoid possible preferential highlighting of some contrasts at the cost of eliminating others, the processing is kept to a rather basic level. A brief overview is given of the data processing workflow applied, for more details on the specific steps the reader is directed to the included references. Data processing and analysis for the most part was performed in 3d-Radar's proprietary 3DR-Examiner software. For final visualization, the data were gained in MATLAB and gridded in Surfer (Golden Software Inc., Golden, CO, USA).

Data editing

Scans or scan segments that were redundant or inaccurately positioned due to GNSS signal loss were removed. If the outer channels of the antenna channels showed remarkably more interference from extraneous reflections, also these data were discarded. This should not affect the spatial coverage of the survey area as the survey pattern anticipated some overlap between adjoining scans.

Frequency-domain filtering

The recording of the data in frequency-domain makes that frequency-domain filtering can be readily applied. This type of filtering is suited to remove interference

from extraneous sources at distinct frequencies, such as from mobile phone networks (in Belgium operating at 900 MHz and 1800 MHz). The 3DR-Examiner software offers a function for interference removal, which essentially consists in low-pass filter: for each sampling location, the frequency spectrum of the received signal is analysed and frequencies with outlying power are suppressed. Together with the conversion to time-domain, a band-pass filter can be implemented to reduce both low- and high-frequency noise.

Conversion to time domain

To allow for conventional visualization and analysis of the GPR data, a conversion to time-domain is required. An inverse fast Fourier transform (Cooley & Tukey, 1965) is applied, using a Kaiser window with a beta value of 6 (Harris, 1978). As mentioned above, the input frequency bandwidth can be limited. Note that this can contribute to an improved resolution in depth: the reflected bandwidth is already reduced for signals derived from larger depth, so reduction of the bandwidth before transformation into time domain will only reduce the noise bandwidth (Våland, n.d.).

Time zero correction

Variations in the height of the antenna array above the ground surface, due to terrain roughness, in combination with instrumental drift can cause abrupt changes in the arrival time of the air-ground reflection wavelet indicated as the time zero. As a result, the position of the ground surface, and of deeper reflection interfaces, can be different for different traces within and between scan lines, which can compromise the use of spatial filters. Therefore, the collected traces require correction to a common time-zero position. In 3DR-Examiner, time zero can be traced manually or the average time zero per scan track can be estimated, using the highest magnitude of the signal as detection criterion. The detection of time zero is best performed on non-filtered traces, so after inverse Fourier transformation including the full frequency bandwidth.

Spatial filtering

Contrary to the frequency-domain filters operating within individual traces, spatial filters operate across the traces in distance, along the transects of different scan channels. Background removal based on high-pass filtering is used to reduce horizontal banding in the profiles. This function in 3DR-Examiner allows to retain a proportion of the background signal so that flat-lying reflectors are not removed completely. The SNR can be further improved by a horizontal filter the window size of which increases with depth.

Data subsampling

Mainly to facilitate visualization of the data, the total GPR data consisting in (partially) overlapping scans is merged and subsampled so that the remaining sampling locations correspond to a square grid (in both case studies presented in Chapters 6 and 7 to a 10 cm × 10 cm grid). In 3DR-Examiner this function is indicated as 'stitching': individual scan tracks are stitched together so that one large 3D data cube is created. The subsampling essentially is a nearest-neighbour interpolation (see below) in which the selection priority of the nearest neighbour is determined by the centrality of the corresponding transmitting-receiving antennae combination in the antenna array. This procedure thus suppresses the sampling of GPR traces from outer antenna pairs that are more susceptible to interference.

Gain correction

Because of signal attenuation and geometrical losses, a temporal gain is applied to enhance the appearance of deeper reflections. All gain functions operate by applying a multiplying factor to successive regions of the traces in time with a certain. The width of the region is indicated as the time window. The multiplying factor depends on the type of gain function applied. In 3DR-Examiner, gain can be applied through a user-defined function (a combination of constant, linear and exponential components) or through spreading and exponential correction (spherical and exponential compensation, SEC). Spreading losses are automatically accounted for by SEC, possibly supplemented with a compensation for material losses. Yet, the latter requires an accurate estimate of the attenuation to be effective. An advantage of SEC is that the relative amplitude of the reflections in time is retained. However, here preference is given to a gain function that is not available in the 3DR-Examiner software: automatic gain correction or control (AGC). With this function, the median magnitude of the signal in a particular time window is equalized over the entire trace. Hence, in the gained profiles all two-way travel times have the same median reflection amplitude. Differences in reflection strength are eliminated and the profiles are no longer informative of differences in attenuation in depth. However, the (average) attenuation can be visualized by plotting the applied gain factor in function of the time window midpoints. The AGC function was implemented in MATLAB.

Velocity analysis and depth conversion

So far, the processing steps have operated in the time domain and 'depth' referred to relative depth expressed in two-way travel time. For realistic interpretation, it is

desirable the convert the two-way travel time into an actual depth expressed in distance units. This conversion requires an estimate of the time zero and of the average GPR wave velocity:

$$t = t_0 + \frac{2z}{v}, \qquad (3.22)$$

where t is the two-way travel time, t_0 is time-zero and z is the depth. The velocity v is directly related to the relative dielectric permittivity ε_r of the soil (Equation 3.19). The estimation of the time zero has been addressed above. The wave velocity in this work is either derived from typical values of the dielectric permittivity of the observed soil material provided in literature, or estimated from observations of the depth of reflection-generating contrasts through borehole drilling.

Data visualization

The processed and gained 3D volume of GPR data is visualized in a selection of relevant vertical and horizontal slices. In the vertical slices the amplitude, or the real part, of the GPR signal is displayed; the horizontal slices express the absolute signal strength, or the magnitude of the GPR signal. The horizontal slices can be averaged over a certain time or depth interval, which further reduces high-frequency noise. The slices are visualized as grids in Surfer.

3.5 Data interpolation

'Maps are a way of organizing wonder.' – Peter Steinhart

Whereas both EMI and GPR surveying according to the methodology presented above already provide quasi-exhaustive measurements, a spatially continuous surface of a measured property is usually preferred above a map of colour-coded discrete point observations for interpretation, as this better represents the continuity of soil variations (e.g. Scull et al., 2003). Interpolating spatially discrete point observations to a continuous surface is conventionally performed by using the observed values of a certain variable to predict its value at unvisited locations that are organized according to a regular grid nodes, hence the use of the term *gridding* as synonym to interpolation. A wide variety of methods is available, reaching from pretty straightforward deterministic methods to more sophisticated probabilistic algorithms. This section explains the principles of the specific interpolation methods applied in this

research. For a comprehensive overview of spatial prediction methods focusing on environmental applications, the reader is referred to Webster and Oliver (2007).

3.5.1 Local prediction methods

Motivated by the high density of available sensor measurements, the interpolation methods considered are local methods, meaning they use only a subset of the observations selected within a neighbourhood centred at a prediction location. Generally, a local prediction is made by calculating a weighted average of the observations within the local neighbourhood:

$$Z^*(\boldsymbol{x}_0) = \sum_{i=1}^{n(\boldsymbol{x}_0)} \lambda_i \, z(\boldsymbol{x}_i) \qquad \text{with} \qquad \sum_{i=1}^{n(\boldsymbol{x}_0)} \lambda_i = 1 \qquad (3.23)$$

where $Z^*(\mathbf{x}_0)$ is the predicted value of a variable Z at location $\mathbf{x}_0$, $z(\mathbf{x}_i)$ with $i = 1,\ldots,$ $n(\mathbf{x}_0)$ are the observed values of Z at the $n(\mathbf{x}_0)$ locations within the neighbourhood of $\mathbf{x}_0$, and λ_i the weight assigned to the respective observation $z(\mathbf{x}_i)$. To neutralize the overall influence of multiplying the observations with a weight factor, the sum of the weights has to equal 1. The difference between interpolation methods is in the determination of the interpolation weights.

3.5.2 Nearest-neighbour interpolation

The simplest local interpolation method is nearest-neighbour interpolation, which, as the name implies, consists in deriving the prediction from the single nearest observation. Expressed in terms of Equation 3.23, the observation closest to $\mathbf{x}_0$ receives of weight $\lambda_\alpha = 1$ and all other observation within the neighbourhood are assigned zero weight. The predicted value $Z^*(\mathbf{x}_0)$ is copied from the nearest observation: the prediction is deterministic and there is no account of possible uncertainty. In this work, this method is used to subsample the GPR data that are originally recorded at horizontal sampling resolution of 7.5 cm × 5 cm, or even denser in the overlap between different scan tracks, to facilitate the visualization of (primarily horizontal) slices in a regular grid. Note that instead of enhancing the spatial continuity, the method is here used to equalize the sampling density, to a slightly coarser resolution (10 cm × 10 cm).

3.5.3 Kriging

In EMI surveying the resolution is up to an order of magnitude coarser than for GPR, and there is a larger discrepancy between the in-line and cross-line sampling

intervals. The EMI data are therefore interpolated using the more advanced geostatistical method of kriging, named after Daniel G. Krige, the father of geostatistics (e.g. Webster, 2015). For a dedicated description of kriging and all of its variants, the work of Goovaerts (1997) is recommended. In this method, the weights attributed to the neighbour observations also depends on their distance to the prediction location, but the distance influence is modified by accounting for the spatial structure in a data set modelled by the variogram.

The experimental variogram

The experimental variogram is a second order data statistic that quantifies the variance between observation points in function of their separation distance. To this day, the variogram (γ) is most commonly calculated according to the formula that was originally provided by Georges Matheron, who's PhD couched the empirical work of Daniel G. Krige in the theoretical discipline of geostatistics (Matheron, 1965):

$$\gamma_M(\mathbf{h}) = \frac{1}{2n(\mathbf{h})} \sum_{i=1}^{n(\mathbf{h})} \{z(\mathbf{x}_i + \mathbf{h}) - z(\mathbf{x}_i)\}^2, \qquad (3.24)$$

where γ(***h***) is the mean variogram for all pairs of observation points $n(\boldsymbol{h})$ that are separated by a distance vector or lag ***h***, and $z(\boldsymbol{x}_i)$ and $z(\boldsymbol{x}_i + \boldsymbol{h})$ are the actual values of Z at these observation points. The factor 2 in the denominator is a correction for the fact that two data points are involved in the variance calculation and is the reason why the variogram also is termed semi-variance. Because the classical Matheron estimator consists in the calculation of an arithmetic mean, it is sensitive to outlying variances between observations or, more concretely, to outlying measurement values resulting in extreme squared differences with other measurements, which can lead to unreliable variogram estimations. If the number of extreme values is limited, this issue can be resolved by eliminating these values from the data set – although this should not be done rashly, particularly if the extreme values are part of the target population – or by disregarding them in the calculation the variogram. Alternative, robust variogram estimators can be used, such as that proposed by Dowd (1984) which takes the median of the absolute differences between observations as basis:

$$2\,\gamma_D(\boldsymbol{h}) = 2.198\,\{\text{median}|z(\boldsymbol{x}_i + \boldsymbol{h}) - z(\mathbf{x}_i)|\}^2. \qquad (3.25)$$

The constant 2.198 is a correction factor that scales the median absolute pair difference to the standard deviation of a normally distributed population.

Variogram modelling

To use the spatial structure as represented by the variogram in interpolation, a variogram model, i.e. a continuous function of γ(***h***) versus ***h***, needs to be fitted to the experimental variogram. A variogram function typically increases with increasing lag distance (Figure 3.11), which agrees with the common observation of spatial autocorrelation: a variable is more likely to show similar values at points close together than at points far apart. Mostly, the variogram levels off at a certain distance indicating the disappearance of a spatial relation between the observations. The maximum variogram value is termed the *sill*, the lag distance at which the sill is reached is indicated as the *range* (*a*). Theoretically, the variogram equals zero at a lag distance of zero. In practice, however, there mostly is a minimal distance between observations and even if two observations can made be at exactly the same location – which is not that inconceivable in the case of non-invasive measurements such as EMI – there can be some difference between the observed values due to noise inherent to the measurement technique. This non-structured of the spatial variation, including random noise as well as micro-variability, is quantified in the so-called *nugget effect* (C_0) and corresponds to the (apparent) intercept of the variogram model with the vertical axis. The variance of a variable thus exists in the sum of a non-structured part and a structured part, the latter of which, at its maximum, is indicated as the *sill contribution* (C_1). Furthermore, the pattern of the increase of the variogram at lag distances smaller than the range can conform to different functions. Due to restrictions implied by the matrix algebra of the kriging system (see below), not all mathematical functions are permissible variogram models. In Figure 3.11, three

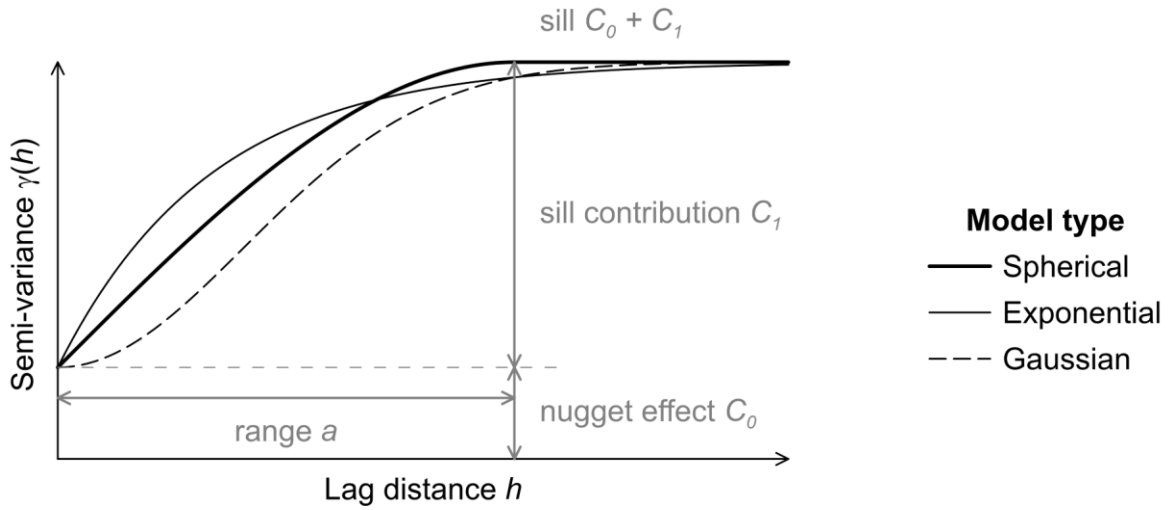

Figure 3.11 Behaviour of three variogram models having the same nugget effect (C_0), range (a) and sill ($C_0 + C_1$).

commonly used models are plotted for the same values of the nugget effect, sill and range: a spherical, an exponential and a Gaussian model, each with a distinct behaviour near the origin. Note that for exponential and Gaussian models the sill is approached asymptotically and, therefore, the range is practically defined as the lag value at which 95% of the sill is reached. A variogram model can have a nested structure consisting in a linear combination of simple models, which is characteristic of spatial variation resulting from the interaction of different phenomena acting at different spatial scales. Finally it is remarked that fitting a model to the experimental variogram should not be considered a mathematical minimization of the misfit. Although statistical goodness-of-fit parameters can provide some guidance, insight in the spatial behaviour of a variable is of much more relevance to creating an appropriate model for the structure of spatial variation.

Ordinary kriging

The kriging algorithm is designed so to provide unbiased predictions and a minimal prediction error. Ordinary kriging is the default kriging variant derived under the conditions that the mean is locally stationary and unknown. The general formula of a local predictor as given in Equation 3.23 applies, in which the weights are obtained from solving the following system of equations:

$$\begin{cases} \sum_{j=1}^{n(\boldsymbol{x}_0)} \lambda_j \gamma(\boldsymbol{x}_i - \boldsymbol{x}_j) + \Psi = \gamma(\boldsymbol{x}_i - \boldsymbol{x}_0) \\ \sum_{j=1}^{n(\boldsymbol{x}_0)} \lambda_j = 1 \end{cases} \tag{3.26}$$

where $\gamma(\boldsymbol{x}_i - \boldsymbol{x}_j)$ represents the variogram values between all pairs of observations in the local search neighbourhood and $\gamma(\boldsymbol{x}_i - \boldsymbol{x}_0)$ the variogram values between the observations and the prediction locations. Both are derived from the adopted variogram model. The Lagrange multiplier Ψ is introduced to include the restriction that the sum of the weights must equal 1. Because the kriging systems incorporates the variogram between the observation points, it accounts for their relative spatial positions and kriging has an inherent declustering effect. This explains its suitability to interpolate data sets with a different sampling density in different directions.

3.6 Electromagnetic properties of soil

'There are no facts, only interpretations.' – Friedrich Nietzsche

In the final section of this chapter, some guidelines for interpretation of the EMI and GPR data are given. Therefore, we return to the constitutive relationships that linked a medium's response to an incident electromagnetic signal to the medium's properties, which were defined in Equations 3.5–3.8. More specifically, the meaning of electrical conductivity, dielectric permittivity and magnetic susceptibility is discussed with respect to the medium of soil. The focus is here on soil consisting of natural aggregates, the properties of depositions of technogenic materials is elaborated on in the next chapter. It is emphasized that the geophysical response obtained from both EMI and GPR generally relates to a certain soil volume and, hence, the *bulk* properties of soil have to be considered. These depend on the intrinsic properties of the soil constituents and their relative proportions, although the dependence is seldom genuinely straightforward.

3.6.1 Electrical conductivity

Soil basically is a three-phase system with the solid, liquid and gaseous phases as main components. As illustrated in Figure 3.12, the electrical conductivity of soil can be conceptually approached by considering three pathways of electrical current flow (Corwin & Lesch, 2005a; Rhoades, 1999):

1. a continuous liquid phase pathway via dissolved anions and cations (e.g. Na^+, Ca^{2+}, Cl^-, CO_3^{2-}) contained in the soil fluid occupying the larger pores;
2. a pathway through alternating solid particles and their surrounding soil solution primarily via exchange of cations associated with clay minerals and OM, corresponding to so-called surface conduction;
3. a solid pathway via soil particles that are in direct and continuous contact with one another.

Because of the insulating capacity of air, the contribution of the gaseous phase is usually negligible. Also most soil minerals are insulators, so the first two pathways involving the liquid component are predominant for electrical conduction. The exchange of cations actually takes places in the water films associated with the solid surfaces, explaining the dependence of surface conduction on the soil moisture level. Extremely dry conditions impedes will impede current flow along both the liquid and

liquid-solid phase pathways. Surface conduction is generally smaller than that of the pore solution because in the former the electrolytes are limited in amount and mobility. The relative contribution of the different pathways depends on the volumetric proportions of the different phases, the solute concentration in the liquid phase relative to pore size and the nature of the solid phase. The soil electrical conductivity increases with increasing salinity. In non-saline soil, the content and type of clay and OM are the main controlling factors through determination of the soil cation exchange capacity (CEC). The soil moisture content has an obvious influence and in itself depends on the nature of the solid phase as soil with a higher clay and OM content generally has a higher water holding capacity (see also Pedrera-Parilla et al., 2016). The effect of an increasing saturation with pure water, however, is subordinate to that of an increasing salinity or a, increasing clay and/or OM content. Soil bulk density, which also is directly influenced by clay and OM content, is another property determining the soil electrical conductivity. In non-saline conditions, soil compaction increases the soil electrical conductivity through enhancement of surface conduction (e.g. Islam et al., 2014a, 2014b). Note that the positive correlation between bulk density and electrical conductivity only applies for porous substrates. For instance, massive concrete has a higher bulk density due to a higher intrinsic density of the material and is non-porous, hence its low electrical conductivity. The electrical conductivity of some typical subsurface materials is listed in Table 3.2.

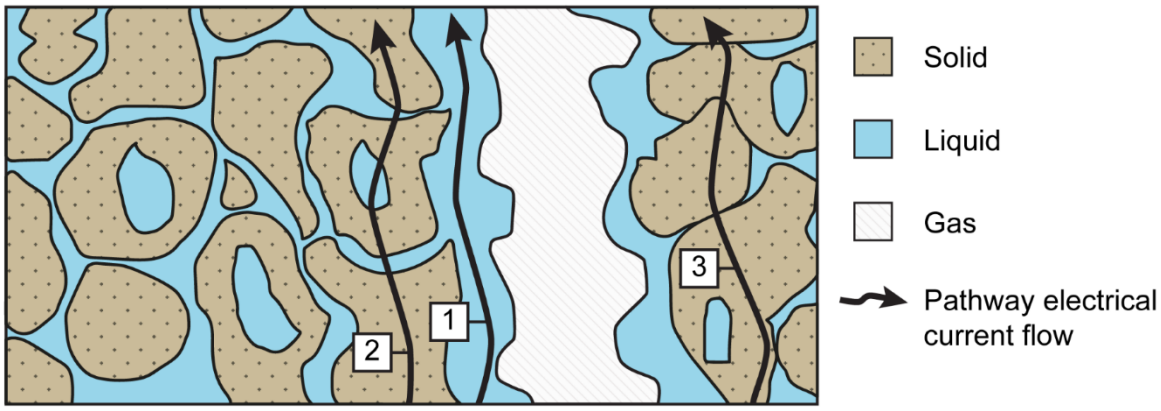

Figure 3.12 Three pathways of electrical current flow in soil. After Corwin and Lesch (2005a).

3.6.2 **Dielectric permittivity**

As an alternative definition to the one given above, the dielectric permittivity quantifies the capacity of a material to store and release EM energy in the form of electric charge. It is usually a complex, frequency-dependent property with its real and imaginary components respectively corresponding to storage and loss of energy.

However, the latter component is often ignored so that the permittivity values is simplified to its constant real component at low frequencies. The adoption of this simplification can be justified by the fact that GPR is ineffective in high-conductive – and, hence, high-loss – environments anyway. As mentioned above, air and liquid water represent the extremes of dielectric permittivity (Table 3.2). The relative dielectric permittivity of an aqueous solution further increases with its ion concentration. Natural soil minerals typically are good dielectric insulators corresponding to a relative dielectric permittivity in the range of 3–8. For granular soil media, the bulk dielectric permittivity the contribution of a saturating fluid will dominate over the solid phase properties and will be a direct function of the degree of saturation. As such, the soil dielectric permittivity essentially relates to the same

Table 3.2 Typical values of electrical conductivity (σ or EC) and relative dielectric permittivity (ε_r or RDP, real component) of common subsurface materials at an antenna frequency of 100 MHz. Taken from Cassidy (2009a).

Material	σ or EC (mS m^{-1})	ε_r or RDP (-)
Air	0	1
Freshwater	0.1–10	78–88
Freshwater ice	0.000001–1	3
Seawater	4000	81–88
Seawater ice	10–100	4–8
Permafrost	0.1–10	2–8
Limestone – dry	0.0000001–0.001	4–8
Limestone – wet	10–100	6–15
Sand – dry	0.0001–1	3–6
Sand– wet	0.1–10	10–30
Clay – dry	1–100	2–20
Clay – wet	100–1000	15–40
Concrete – dry	1–10	4–10
Concrete – wet	10–100	10–20

physical soil properties as the electrical conductivity and these dielectric properties are generally positively correlated, as demonstrated for the materials included in Table 3.2 (Annan, 2009; Cassidy, 2009a).

3.6.3 **Magnetic susceptibility**

Before describing the magnetic susceptibility of soil, it is necessary to first introduce some additional terminology with respect to magnetisation. The discussion of the constitutive relationships given in the beginning of this chapter referred to the application of an external magnetic field. The magnetisation a material shows in response to an external field is termed induced magnetisation. However, materials can also have permanent or remanent magnetisation which remains after an applied field is removed, due to permanently magnetic particles. For instance, igneous rocks acquire remanent magnetisation by cooling from a temperature greater than their characteristic, composition-dependent Curie temperature. This type of remanent magnetisation is indicated as thermal remanent magnetisation.

To explain the magnetisation of materials, it is required to zoom in on the origin of magnetism at the atomic scale. All atoms possess a magnetic moment, due to the orbital motion of electrons around the nucleus and their spin around their own axis. If two electrons are paired in the same orbital, they have an opposite spin so that their magnetic moments are cancelled out. Unbalanced magnetic moments give rise to a net magnetic moment. Based on the overall magnetic dipole moment, materials can show three different types of magnetism. *Diamagnetic* materials have no unpaired electrons and, when submitted to an external magnetic, only a weak magnetic field is induced that opposes the applied field. These materials are characterized by a weak, negative magnetic susceptibility and are generally considered non-magnetic. Examples of diamagnetic minerals are quartz and calcite (Table 3.3). *Paramagnetic* materials have a permanent or remanent magnetic moment – due to the presence of unpaired electrons, although this is usually weak because of the random orientations of individual magnetic moments (Figure 3.13). Under influence of an external magnetic field, the magnetic moments align themselves in the same direction. This corresponds to a weak, positive magnetic susceptibility, which is at least an order of magnitude larger than the susceptibility of diamagnetic materials. Most clay minerals, excepting kaolinite, along with pyrite and biotite are paramagnetic. *Ferromagnetic* materials contain unpaired electrons the spin moments of which are aligned because of overlapping electron orbitals of adjacent atoms in the crystal lattice. The magnetic

coupling between spin moments can cause these materials to have a relatively strong remanent magnetisation and a large susceptibility. Three different subtypes of ferromagnetism can be distinguished. In ferromagnetic materials sensu stricto, the magnetic moments of individual atoms are equally large and have the same direction, as illustrated in Figure 3.13. Examples of ferromagnetic materials are iron, nickel and cobalt. In *anti-ferromagnetic* materials, such as the mineral haematite, magnetic moments are aligned parallel within a sublattice but anti-parallel on different sublattices: the net magnetic moment is zero and the susceptibility is generally low, similar to that of paramagnetic materials. However, magnetisation can be enhanced by defects in the crystal lattice. Finally, in *ferrimagnetic* materials, the sublattices are anti-parallel and unequal attributing these materials high magnetic susceptibilities. Magnetite, titanomagnetite and ilmenite are prime examples. Ferromagnetic materials lose their spontaneous magnetisation when they are heated above their Curie temperature to become paramagnetic. Finally, it is noted that for many materials the intensity of magnetisation is dependent on the applied magnetic field and, hence, no unique value of susceptibility exists. The values cited in literature are usually are for a weak applied field (Clark, 1997; Evans & Heller, 2003).

Table 3.3 Type of magnetism and magnetic susceptibility (κ or MS) of some common minerals. Compiled from Clark (1997) and Reynolds (2011).

Mineral	Type of magnetism	*κ or MS* (msu SI $\times 10^5$)
Quartz	Diamagnetism	−1.5
Calcite	Diamagnetism	−1.3
Gypsum	Diamagnetism	−2.9
Haematite	Anti-ferromagnetism	42–3 800
Magnetite	Ferrimagnetic	7 000–2 000 000

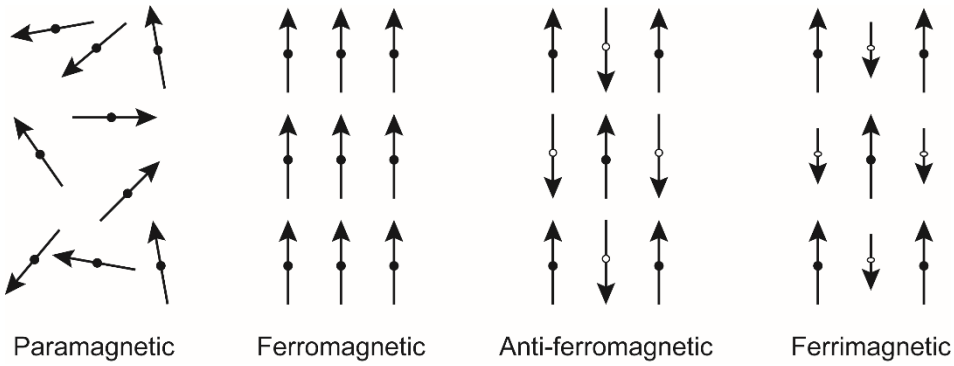

Figure 3.13 Schematic of magnetic moments in paramagnetic, ferromagnetic, anti-ferromagnetic and ferrimagnetic materials.

Most common soil minerals are diamagnetic or paramagnetic and are nominally non-magnetic. The magnetic susceptibility of natural soil is mostly dominated by the ferrimagnetic minerals they contain, of which magnetite and maghaemite are two of the most prominent ones. Several processes can contribute to the formation of ferrimagnetic minerals. Many processes involve bacterial activity and require the presence of OM, which explains why the magnetic enhancement of soil is often concentrated in the upper, humus-rich layers. Also the heating of soil in the presence of OM, during natural or man-made fires, can introduce reducing conditions leading to the thermal conversion of anti-ferromagnetic haematite to ferrimagnetic magnetite, corresponding to a strong increase in magnetic susceptibility (e.g. Schmidt, 2007). Furthermore, in the case of magnetic parent material, magnetic particles can be distributed throughout the soil via natural soil formation processes. It is noted that ferrimagnetic minerals such as magnetite are resistant to weathering and therefore tend to accumulate (Evans & Heller, 2003). If soil contains magnetic materials, it has the capacity of showing both remanent and induced magnetisation, and it is the resultant of both that will be measured with EMI.

Chapter 4
Geophysical investigation of landfills

4.1 Introduction

'Obsession with the hidden.' – Rene Magritte

As discussed in Chapter 2, urban soil can pose severe challenges to the conventional investigation methods, consisting in soil drilling or excavation followed by profile description and sample collection for laboratory analysis. Challenges of practical nature are mainly related to substrates urban soil can contain, for example, layers of technic, hard materials hampering the accessibility of the subsurface. The principal conceptual challenge exists in the high heterogeneity of urban soil properties. Site characterization based on a limited sample – in terms of the number of discrete locations visited as well as the volume selected for the sample support – can raise legitimate questions on the reliability and representativeness the results. With respect to both types of challenges, landfill soil presents a high-end example. Practical difficulties concerning invasive investigation of landfills are supplemented with risks for the environment and human health. Additional safety measures are required when hazardous waste is involved. Soil drilling can perforate existing landfill liners and create new pathways for contaminant migration (e.g. De Carlo et al., 2013; Yamanaka et al., 2015). Furthermore, the migration of landfill gas can be induced which can pose fire and explosion hazards, both on- and off-site (e.g. Çinar et al., 2016). Particularly non-sanitary landfills can be expected to contain complex combinations of both natural and technogenic materials resulting in extreme heterogeneity. As for urban soil

investigation in general, it is highly recommended that the actual site investigation is preceded by a thorough study of available historical information, such as land register data, records of the landfill owner and business administration documents. However, uncontrolled landfill activities mostly are poorly documented and for controlled landfills, even when licensed, available documents do not necessarily provide a truthful account of the activities actually performed (e.g. Meju, 2000).

As a landfill soil is anticipated to show distinct physical (and chemical) properties, geophysical sensing techniques can offer a valuable alternative to produce complementary subsurface data. These techniques collect data in a non-destructive or even fully non-invasive way and thereby overcome important practical problems inherent to the conventional, intrusive, investigation of landfills. Furthermore, their operation mode gives them the competitive advantage of being relatively inexpensive and fast. Especially non-invasive geophysical techniques are ideally suited to provide spatially comprehensive datasets, with the prospect of improving the representation of the spatial heterogeneity (e.g. Boudreault et al., 2010). The earliest recognition of the potential of geophysical sensing to support the characterization of landfill sites goes back to the late 1960s (e.g. Cartwright & McComas, 1968) and since then numerous studies have reported on their application (Meju, 2000). In most previous studies, the interest in landfill investigation related to the assessment of associated environmental pollution problems, primarily the contamination of groundwater by landfill leachate. Leachate formation is generally attended by a strong change in the subsurface electrical conductivity (EC), which explains why electrical and electromagnetic methods have been the most popular in this context (e.g. De Carlo et al., 2013; Meju, 2000). However, there are several other factors that influence the geophysical response of a landfill, which is the topic addressed in the next section.

4.2 The geophysical signature of landfills

'The whole is other than the sum of its parts.' – Kurt Koffka

As for man-made soil in general, the properties of newborn landfills are largely inherited from the substrates of which they are created. Each substrate is unique by its origin and therefore has unique properties. Yet, the main types of waste considered in this work, construction and demolition waste (CDW), MSW and IW, can be represented by distinct groups of similar substrates. As the production processes of

technogenic substrates are identical worldwide, their properties appear to be quite universal (Meuser, 2010). Nevertheless, particularly non-sanitary landfills are typically composed of complex mixtures of monosubstrates, causing their physical and chemical properties to be highly spatially heterogeneous (e.g. Meju, 2000). The complexity of the waste mixture can be expected to be reflected in its geophysical response, to an extent depending on the specific geophysical method applied and the survey parameters selected. However, the bulk properties of landfilled waste can depart strongly from weighted averages of the substrates' intrinsic properties, under influence of locally prevailing conditions. These conditions result from a combined effect of different types of processes, which, in their turn, can be highly variable in space and time.

In the following paragraphs an overview is given of the main types of waste considered in this work, CDW, slag and ashes, and MSW; mining waste and sludges are left out of consideration. Their origin and general "raw" characteristics are discussed, with focus on those characteristics that are expected to be determinant of the geophysical response. If available, experimental data from previous waste or landfill characterization studies are included. Afterwards, the processes that play a key role in the evolution of a landfill's geophysical (and geochemical) signature over time are discussed. The geophysical signature here primarily refers to the output provided by EMI, namely the subsurface electrical conductivity (EC) and magnetic susceptibility (MS), as landfill exploration through high-resolution EMI surveying is the specific research topic addressed in the next chapter. In addition, it is noted that waste (or similar anthropogenic) depositions are commonly found on historical commercial/industrial sites, so the exposition of fill properties given below also serves as a handle for interpretation of the electromagnetic anomalies encountered in the case studies presented in Chapters 6 and 7.

4.2.1 **Waste type**

Construction and demolition waste

As the name implies, CDW originates from the construction or demolition of civil or industrial infrastructure. This type of waste is principally identified as construction debris or rubble, which mainly consists of inert materials as brick, mortar, concrete, ceramic, gypsum and tarred products as asphalt. As per definition, CDW also comprises waste materials produced from construction operations, such as wood, plastics, glass, metals and isolation material. It is noted hazardous materials can be

included, for instance, asbestos and lead-based paints. Furthermore, construction works often involve excavation and terrain levelling, and the excess soil then forms type of waste *in se* (Meuser, 2010). Its properties obviously will be highly variable, depending on the land use history of the site in question. Especially before the establishment of waste management and earth-moving regulations, CDW was commonly – conceivably oblivious of any harm – recycled in new constructions, for example, in foundations of roads and car parks, or for landscaping. It can be accepted that this has contributed to dispersion of the hazardous materials associated with CDW into the wider environment (Meuser, 2010).

In this paragraph, the discussion of the properties of CDW is restricted to the prime substrates encompassed by construction rubble. Concrete and mortar are mixtures of lime cement and, respectively, gravel- and sand-sized aggregates (Howard & Orlicki, 2015). As compared to mortar, concrete mostly shows a higher density and weathering resistance (Meuser, 2010). To provide concrete with tensile strength, it is frequently embedded with reinforcement bars (rebar), which are usually made of steel. Hence, reinforced concrete is a composite waste material; the properties of its components are here considered separately. The term concrete refers to the non-reinforced material. In addition, it has become an established practice in concrete production industry to partially replace cement with fly ash derived from coal combustion in electric power station (e.g. Lou et al., 2008; Ondova et al., 2012). However, a detailed discussion of the influence of the use of fly ash on the properties of the produced concrete is out of the scope of this work. Wall and roof tile bricks form the main constituents of masonry rubble. Brick is created from loamy or clayey parent material. Modern, fired or ceramic, brick is produced from firing clay at a temperature of 900–1100°C, which causes the phyllosilicate clay minerals to decompose into glass (Howard & Orlicki, 2015). Brick generally has a lower density than concrete and mortar, and due to a high-percentage of micropores it demonstrates an enhanced water-holding capacity (Meuser, 2010). Gypsum – the natural mineral corresponding to the formula $CaSO_4 \cdot 2H_2O$, typically occurs in CDW in the form of plaster and drywall. This material has a white to yellowish colour and is characterized by a low specific gravity, which is in accordance with its mineral constituent. In a soil environment, plaster shows a low stability because of its relatively high water solubility. Asphalt consists in a cement of bituminous hydrocarbons that is intermixed with natural aggregates like sand, limestone and dolostone, and/or with technogenic

aggregates like bottom and fly ash, and blast furnace slag. Its density is comparable to that of concrete (Howard & Orlicki, 2015; Meuser, 2010).

Calcareous building materials as concrete and mortar typically result in an elevated soil pH (see also Table 2.3). Calcium is permanently released during the weathering of these materials causing the pH to increase. Meuser (2010) reports the pH ($CaCl_2$) value to be around 8 for construction rubble in general, as well as for the specific materials of mortar and concrete. Howard and Orlicki (2015) also found the highest values of abrasion pH for these calcareous substrates, relating to the very high abrasion pH of around 12.4 for lime and portlandite. For brick, consistently lower pH values were observed. Asphalt and plaster displayed the lowest pH amongst specific construction rubble substrates. Despite its high calcium content and high pH, construction rubble exhibits a relatively low CEC. Investigation of soil horizons of deposited construction debris revealed a CEC between 2 and 25 $cmol_c\ kg^{-1}$, with a mean of 9.1 $cmol_c\ kg^{-1}$. These low values are suggested to be associated with the coarse texture of construction rubble and its low total organic carbon (TOC) content. Fresh deposits of construction debris also show low microbial activity, yet the microbial biomass has been observed to increase over time (Meuser, 2010).

Meuser (2010) states technogenic substrates are generally characterized by relatively high values of EC, although many also show a large variation. For construction rubble, it is indicated the EC ranges between 10 and 230 mS m^{-1}, with a mean value of 78 mS m^{-1}. Howard and Orlicki (2015) measured even higher values for specific types of calcareous building materials: for mortar the mean EC varied between about 210 mS m^{-1} and 520 mS m^{-1} and for concrete between about 320 and 1030 mS m^{-1}. Also for drywall a relatively high EC was found, with a mean around 230 mS m^{-1}. This can be explained by the ready solubility of calcium and sulphate ions from abraded gypsum particles. Brick demonstrated values that were about an order of magnitude lower, with the mean EC varying between 18 and 88 mS m^{-1}. Old brick from the 19th century (orange brick) had an exceptionally high mean EC of 508 mS m^{-1}, which was attributed to its production from lower temperature firing, leaving the parent clay minerals relatively intact. The mean EC of asphalt was near 340 mS m^{-1}. Particularly with respect to the high EC observed for the calcareous CDW substrates, it is emphasized that the results of Howard and Orlicki (2015) respond to laboratory analysis of an artefact-water extract (1:2 extraction ratio), the artefact specimen preparation of which included crushing and wet sieving. The representativeness of these analysis conditions for the bulk EC in the field can be questioned. In their raw

form, most technogenic substrates show a coarse to very coarse texture. Construction debris may, for instance, contain massive blocks of concrete or still-intact structures of masonry, the size of which can reach up to several decimetres or even metres. When deposited in a landfill, this incidentally results in a subsurface matrix with a high porosity, and a correspondingly enhanced hydraulic conductivity and reduced bulk density (see also Table 2.3). As a result, construction rubble tends to demonstrate a limited water retention capacity. To explain the significance of the structure of rubble depositions for the bulk EC in the field, we go back to the three pathways of electrical current flow as described by Corwin and Lesch (2005a). The contribution of the solid pathway is restricted by the low intrinsic EC of building materials, for example, dry concrete has an EC of 1–10 mS m^{-1} (Cassidy, 2009a; see also Table 3.2). The current flow along the liquid phase and solid-liquid phase pathways depends on the soil water content and the available ions in solution, both of which have been procedurally enhanced in the analysis method used by Howard and Orlicki (2015). Especially for unsaturated conditions, the values reported by these authors likely will substantially overestimate the bulk EC of a landfilled construction rubble substrate. This conclusion is supported by previous geophysical investigations (e.g. Boudreault et al., 2010). Whether measurements of EC of a substrate-water solution are representative of the bulk EC in the field – the EC_a measured by EMI sensors, depends on the solution's resemblance to the actual field conditions – within the volume under influence of the applied electromagnetic field.

Lime and gypsum based building materials are non-magnetic; their prime constituents calcite and gypsum are diamagnetic minerals (Clark, 1997, see paragraph 3.6.3). Brick forms an exception as their production process provides a typical example of the magnetic effect of thermoremanent magnetization. Thermoremanence is acquired when materials that are rich in iron-oxides are heated above their Curie temperature and then cool down in the ambient earth's magnetic field. The parent clay material commonly contains magnetite and maghaemite, the Curie temperatures of which (578°C and 578–675°C, respectively) are exceeded during firing of the bricks. Furthermore, the heating and cooling cycles of the brick production process may cause weakly magnetic minerals such as haematite and goethite to convert into ferrimagnetic iron-oxides (Schmidt, 2007). In archaeological investigations, brick artefacts are commonly detected as magnetic anomalies (e.g. De Smedt, Van Meirvenne, et al., 2013). However, if the orientation of the remanent magnetization vectors of individual bricks (or brick fragments) is randomized, the

overall magnetic response can be reduced. This phenomenon has been frequently observed in archaeological surveys aiming at the detection of buried walls (Schmidt, 2007; see also Simpson, Lehouck, et al., 2009). A similar effect can be excepted when examining landfilled brick substrates.

Slag and ashes

Slag and ashes are residues that mainly stem from industrial combustion processes. The first are produced from an ore smelting process, while the second relate to combustion processes in power stations or MSW incinerators.

Slag is the waste product remaining from the separation of a desired metal from its raw ore. Depending on the wanted end-product of a smelting process, slag is defined by different, metalliferous and non-metalliferous, impurities which will result in different properties of the slag. In iron (and steel) making, iron ore (and scrap metal) and coked coal are combined with a flux of a calcareous aggregate (mostly limestone). The blast furnace slag produced from iron smelting has a texture which is determined by its cooling conditions. Slow cooling results in gravel-like, crystalline, grey slag, whereas faster cooling in the presence of water produces blast furnace sand. Porous blast furnace pumice is created when fresh air is added. Steelworks slag generally has a crystalline, dense structure and a very high specific gravity. For example, the density of lead slag can reach values up to 4000 kg m^{-3}. Slag from ferrous smelting mainly consist in oxides of calcium, silicon, magnesium and aluminium. The smelting processes of specific heavy metals (HMs) such as copper, lead, zinc and nickel, are designed to remove impurities of iron and silica and, consequently, these dominate the composition of the slag produced. Slag from non-ferrous smelting has a structure resembling steelworks slag, but shows different colours depending on the metal it originates from (Meuser, 2010).

Residues derived from coal combustion can be discriminated into ashes and cinders. Bottom ash consists of gravelly textured and porous components when retrieved from low temperature combustion (1200–1500°C); at higher temperatures (1400–1700°C) ash with a sandy to gravelly texture and glassy surfaces is derived from quick cooling in the presence of water. Fly ash is collected through filtering of the boiler flue gas and, hence, has a fine, silty texture. Cinders is the general term for what remains after incomplete combustion of coal or wood. They also are produced in domestic stoves. In coal-fired power stations, cinders are recovered from raking out the boilers. These several types of residues are produced irrespective of the kind of coal fuel combusted, although their properties may (slightly) differ. For instance,

anthracite coal results in light grey coloured ashes, while lignite coal gives a more brownish colour. Similar to coal combustion processes, MSW incinerators give rise to the production of fly and bottom ash. These can easily be distinguished from coal ashes as, besides ashes, they typically contain glass and metal residues (Meuser, 2010).

Slag tends to have a high pH, in response to the addition of calcareous aggregates in metal smelting processes. Meuser (2010) indicates the pH ($CaCl_2$) value of slag ranges between 9 and 11. This is backed by the findings of Howard and Orlicki (2015). The CEC of slag is reported to easily exceed the standard values of natural soil: for monosubstrate soil horizons of slag a mean CEC of 47.4 $cmol_c\ kg^{-1}$ was found, derived from a range of values between 14 and 111 $cmol_c\ kg^{-1}$. The EC of slag generally varies between 10 and 50 $mS\ m^{-1}$, with a mean value of 43 $mS\ m^{-1}$. However, for particular types of slag the EC can be much higher, for instance, for salt slag derived from aluminium smelting an EC of approximately 12 000 $mS\ m^{-1}$ was found (Meuser, 2010). Howard and Orlicki (2015) more generally discriminate between metalliferous and glass slag; the first is described as ferruginous and crystalline to non-crystalline, while the second per definition is non-crystalline. For metalliferous slag, these authors found a mean EC of around 175 $mS\ m^{-1}$, with a standard deviation of 30 $mS\ m^{-1}$. This high value is ascribed to electron transfer reactions involving elemental iron and iron oxides. For glass slag, the EC was considerably lower: a mean value of 10 $mS\ m^{-1}$ and a standard deviation of 2 $mS\ m^{-1}$ was observed. The EC_a of slag depositions in the field is expected to be largely determined by the metal and salt content of the slag, which both have an enhancing effect. Furthermore, supported by the evidenced high CEC, a positive correlation is expected with the moisture content of the deposited substrate. Yet, due to the generally coarse texture of slag and the resulting low bulk density (500–1300 $kg\ m^{-3}$ according to Meuser [2010]), its water retention capacity is anticipated to be rather low, which can mitigate high bulk EC. Metalliferous slag is characterized by a high MS: at the high temperatures reached during metal smelting haematite is converted into magnetite. Howard and Orlicki (2015) found the MS of metalliferous slag to be nearly as high as for corroded iron. If blast furnace slag is used as substitute for natural aggregates in the production of concrete or asphalt, these construction materials correspondingly inherit the slag's magnetic properties.

Like slag, ash is characterized by an alkaline pH, although the values seem to be more variable in function of the type and origin of the ash. Fly ash derived from hard

coal combustion has a pH ($CaCl_2$) of nearly 11, while for lignite coal combustion the pH merely approaches 7. For fly and bottom ash produced in MSW incinerators, the pH is in the range of 9 to 10. This high pH is attributed to the often calcareous waste input and the high processing temperatures, which cause calcium, sodium, potassium and sulphate ions to be readily soluble from the ash particles (Meuser, 2010; Howard & Orlicki, 2015). Ash and ash-soil mixtures typically show a high total carbon content, which is almost completely accounted for by technogenic TOC. Together with the fine texture of ash – as is particularly the case for fly ash, the high TOC content is assumed to be responsible for the high CEC observed for this substrate. The data cited in Meuser (2010) show that the average CEC for ashes is 36.9 $cmol_c\ kg^{-1}$, however, with a range of 5–142 $cmol_c\ kg^{-1}$ the value also appears to be highly variable.

Meuser (2010) indicates the EC of ashes generally ranges from below 10 to 70 $mS\ m^{-1}$, with a mean value of 32 $mS\ m^{-1}$. Yet, for fly ash in specific, a range of 110–400 $mS\ m^{-1}$ is mentioned. For bottom and fly ash from MSW incinerators respective ranges of 60–220 $mS\ m^{-1}$ and 105–202 $mS\ m^{-1}$ are given. In the study of Howard and Orlicki (2015), the mean EC for coal ash varied between around 50 to 90 $mS\ m^{-1}$. For coal cinders, a considerably lower EC of approximately 15 $mS\ m^{-1}$ was identified. A high TOC content and CEC give depositions of ashes a higher potential to meet the high extract EC values observed for this type of substrate. The high bulk EC of ash depositions also has been proven by previous geophysical surveys (Bernstone et al., 2000; Boudreault et al., 2010). Ashes also feature a high MS. For coal ashes this is explained by the formation of magnetite as by-product of coal combustion. Coal often contains pyrite which at high temperatures decomposes into haematite and magnetite (Howard & Orlicki, 2015).

MSW

MSW is the waste type consisting in the broadest variety of distinct components, including but not limited to plastics, glass, ceramics, textiles and metals. Bulky waste which is built up out of a combination of this single components is also encompassed. Furthermore, a significant proportion of MSW is constituted by organic and biodegradable waste such as food and garden waste, and paper and cardboard, and wood. Finally, MSW can contain toxic substances, such as those incorporated in batteries or colourant residues (Meuser, 2010).

The overall composition of MSW has varied considerably over time, with the standard of living of the population at its origin (Meuser, 2010). Apart from actual

variations in waste generation, composition data available in literature are troublesome to compare as there is no standard methodology for solid waste component analysis, inclusive of the number, type and definition of the separate waste components that are discriminated (Dahlén & Lagerkvist, 2008; Edjabou et al., 2015). In view of assessing the properties of waste depositions, a distinction has to be made between the waste generated and the (part of) MSW that is landfilled, which evolves from the waste management and landfill regulations in place. Whereas the amount of MSW produced in the European Union (EU) is still growing, the proportion that is landfilled has significantly decreased over the recent decades. In 1995 still 63.8% of the MSW was landfilled; in 2015 this figure had dropped to 25.3% (Eurostat, 2017; see also Fischer, 2011). These changes can be attributed to the implementation of more stringent EU legislation on landfilling on the one hand, and on alternative waste management options such as recycling, composting and incineration on the other. For instance, the separate collection and recycling of packaging waste has markedly increased under influence of the European Parliament and Council Directive 94/62/EC on packaging and packaging waste; by the end of 2008 EU Member States had to recover a minimum of 60% of all packaging put on the market. The Council Directive on 1999/31/EC on the landfill of waste, hereinafter denoted as the Landfill Directive, included restrictions on the amount of biodegradable municipal waste going to landfills, by July 2016 this amount had to be reduced to 35% (by mass) of the total amount of biodegradable municipal waste produced in 1995. The adoption of these waste management regulations has indubitably also affected the composition of the MSW deposited in landfills, yet, supporting composition data seem to be scarce – compilation of these data also may prove difficult due to pronounced differences between countries in the systematic collection of such data and the analysis methods they respond to.

Nevertheless, this work focuses on the investigation of landfills that have been closed or abandoned. Considering the majority of these landfills stems from before the establishment of the current waste and landfill legislation, recent MSW generation data may not be representative to this end anyway. An alternative source of information is provided by the literature on landfill mining. The characterization of deposited waste is performed in function of the assessment of resource recovery, in which material composition analysis has priority. The general types of recoverable materials in MSW are metals, waste fuel and possibly soil. Component analysis frequently is performed after dividing the waste into different particle size categories

(e.g. Prechthai et al., 2008; Kaartinen et al., 2013). A key – merely surprising – conclusion of previous research is that the waste composition varies between and within sites. Similar to the compositional analysis of fresh MSW, the absolute proportional composition determined is subordinate to the methods used for separating the different fractions (Kaartinen et al., 2013; see also Quaghebeur et al., 2013). However, Krook et al. (2012) argue there is a persistent pattern in the composition of landfilled MSW over different parts of the world. So-called soil-type material – sometimes more generally indicated as the fine fraction,[5] including cover material and heavily degraded waste, typically compose more than half of the MSW substrate, about 50–60% of the total MSW mass. Combustible materials, such as plastics, paper and cardboard, textiles, and wood, form the second main component, corresponding to 20–30%. Inorganic materials, such as concrete, stones and glass, generally count for 10%, and the remaining few percentages are made up by metals (mainly ferrous). This four-component classification likely derives part of its universal character from the fact that variations in the fractions of subordinate waste components counterbalance each other, especially within the combustible fraction. Still, Quaghebeur et al. (2013) inferred broader variations of these components' fractions based on comparison of excavated MSW from a landfill in Belgium, Sweden and Thailand. Fine, soil-like, material contributed for 34–60%, combustibles for 21–50%, inerts for 10–17%, and, finally, metals for 3–6%. The variations in composition were connected to the period during which the MWS was landfilled.

The mass fractions of individual waste materials demonstrated changes over time. These changes result from processes of waste degradation, evolving with the age of the landfill, as well as from differences in the composition of the fresh MSW that was deposited. The latter pertains to trends in both production and consumption of materials, and the waste management strategies being practiced. Quaghebeur et al.

[5] No explicit definition is provided for what is meant by *soil*, or *soil-type material*. In many studies, *soil* seems to used interchangeably with the *fine fraction* or simply *fines*, as *soil-type material* usually is the dominant component of the *fine fraction*. Kaartinen et al. (2013) explicitly identify *soil* also is a separate waste material contained in the fine fraction. Yet, the definition of the fine fraction is equivocal as it corresponds to a particle size category of which the upper boundary depends on the separation method used. For instance, in Quaghebeur et al. (2013) and Hull et al. (2005) the fine fraction is the fraction <10 mm and <25.4 mm, respectively. In Kaartinen et al. (2013), the fine fraction separated from mechanical pre-treatment had a particle size <30 mm. This fine fraction should also not be confused with fine textured material in the sense of soil science terminology. In soil science, *fine* refers to particle sizes that are a few orders of magnitude smaller. Very fine to fine sand has a particle size between 63 and 200 μm, clay has particle size <2 μm (FAO, 2006).

(2013) observed the mass fraction of plastic in landfilled MSW to increase from 10% to 25% over the period between 1980 and 2000. A corresponding increase in the plastic content of fresh household waste served as a logical explanation. Complementarily, the landfilled MSW content of glass and ceramics decreased from 1.7% to 0.5% and that of metal from 4.3% to 2.2%, which was also reflected in a change of fresh MSW composition over time. The mass fraction of paper and cardboard, like plastic a type of material belonging to the combustible fraction, was 10% higher in the most recently landfilled MSW (14% as compared to 4%). This difference was presumed to be the outcome of degradation of the material, particularly because the fresh MSW showed a decrease in paper and cardboard over the period between 1995 and 2000. Organic waste, mainly kitchen and garden waste, could no longer be recognized after a storage time of 15 years in a landfill, as the material degrades to become part of the fine fraction. As a consequence, the proportion of soil-type material increases with the age of the MSW landfill (see also Hogland et al., 2004, and Krook et al., 2012). The results of Quaghebeur et al. (2013) are consistent with the findings of other studies. Kaartinen et al. (2013) observed a plastic content between 20–25% for MSW landfilled between 2000 and 2009. The increase in plastic as compared to the study of Huller et al. (2005) on MSW landfilled between 1989 and 1999, was suggested to be linked with an increased use of plastics since the 1980s and increased source separation of other MSW components, causing the relative proportion of plastics to increase. The manual sorting performed by Kaartinen et al. (2013) revealed similar mass fractions of metals as observed in other studies (3.4–4.4%); the full-scale trials runs with mechanical pre-treatment machinery provided additional information on the magnetic metal content, which amounted to approximately 1%.

From the above, it should be clear that a monosubstrate of MSW is a *contradictio in terminis* and, consequently, the definition of a universal set of properties for this type of waste is problematic. Moreover, available data on the physical and chemical properties of MSW and its components, particularly under landfill conditions, are rather limited. A few landfill mining studies included investigation of properties related to possiblevalorization options for the recovered waste fractions. To evaluate the energy recovery potential from anaerobic digestion or incineration, OM content and calorific value are of interest. For the fine soil-type fraction, the concentration of contaminants (primarily HMs), and leachate generation and quality have been investigated in view of the reuse of this fraction as soil or construction material, or as

soil fertilizer or compost in the case of high TOC contents (e.g. Hogland et al., 2004; Hull et al., 2005; Quaghebeur et al., 2013). Kaartinen et al. (2013) also examined the moisture content of excavated waste to assess its effect on processability by mechanical pre-treatment machinery. Furthermore, the estimation of bulk properties of MSW substrates based on composition data and properties of individual waste components is hampered by the fact that composition data are commonly expressed in mass percentages whereas MSW bulk properties may relate to volumetric contributions of the different components, as is often the case for measurements from geophysical sensors such as EMI. Nonetheless, in the following some general characteristics of the principal MSW materials are given, supplemented with data from landfill literature, if available.

The material type of plastics exists in a broad group of synthetic or semi-synthetic organic compounds. Polyethylene, polypropylene and polyethylene terephthalate are the most common (Meuser, 2010; Pichtel, 2014). Plastics are biochemically inert and resistant to degradation (e.g. Shah et al., 2008). They have been observed to dominate the coarse MSW fractions: in Prechthai et al. (2008) plastics accounted for a mass fraction of 34% in the particle size distribution category of >50 mm; in Kaartinen et al. (2013) they made up nearly 50% of the particle size distribution category of >100 mm. Plastics are well-known electrical insulators, for example, polyvinyl chloride (PVC) is typically used for electrical wire insulation (Shah et al., 2008). Their direct contribution to the bulk EC of MSW substrates can be assumed to be negligible. They can, however, have an indirect influence on bulk MSW properties, e.g., due to their impervious character, plastics can cause local accumulations of soil water. Hogland et al. (2004) observed a practically constant bulk moisture content of nearly 30% (m/m) for excavated MSW which had been landfilled between 1975 and 1980. Yet, the moisture content of waste contained in a plastic bag rose up to 66%. Plastic polymers are diamagnetic materials: if subjected to an external magnetic field, a magnetic field will be produced which is opposite to the applied field (e.g. Wapler et al., 2014). However, the response is generally weak and plastics can be considered to have an insignificant contribution to the bulk MS of landfilled substrates.

The electrical properties of inert materials such as glass and ceramics is comparable to that of plastics. Glass and ceramics are classified as insulators, the EC of which is considered to be 0.1 mS m^{-1} or lower (Fackler, 2002). This is confirmed by the results of Howard and Orlicki (2015). The absolute values of EC they determined, from extracts of crushed and sieved artefact specimens, were still relatively high: for

bottle glass the average EC was 66.1 mS m^{-1}, with a standard deviation of 22.5 mS m^{-1}; for glazed ceramic pipe the average value was 17.7 mS m^{-1}, with a standard deviation of 1.4 mS m^{-1}. Yet, these values were low in comparison with the other technogenic investigated, such as calcareous building materials and metalliferous slag. With respect to magnetic properties, glass and ceramics are different types of materials. Glass exists in amorphous silica and can be considered magnetically inert. As the production process of ceramics is similar to that of brick, ceramics may exhibit an enhanced magnetic response due to thermally induced remanent magnetization and enrichment in ferrimagnetic minerals. Nevertheless, these inert materials usually take up only a few mass percentages of MSW substrates and the contribution of ceramics is unlikely to be responsible for substantial bulk MS values.

The metals found in MSW are mainly derived from packaging, electrical appliances and furniture. More than 75% (w/w) of the metal fraction exists in ferrous metals (iron and steel). In the non-ferrous part, aluminium is predominant (>90%, Quaghebeur et al., 2013). For the most part of scrap metal in MSW, both an electric and magnetic anomaly can be expected. However, other frequently occurring non-ferrous metals such as copper, zinc and lead, are non-magnetic, so that metal fragments of this nature will only result in increased electrical conductivity.

The organic waste fraction is anticipated to mirror the properties of soil OM. As explained in Chapter 3, according to its chemical composition, soil OM in itself is electrically and magnetically neutral, but its presence can have a significant indirect effect on bulk properties due to interactions with other soil components. Soil OM is a key factor determining water saturation and, through its high CEC, can be pivotal to electric current flow along the soil-liquid phase pathway (Corwin & Lesch, 2005a). Organic matter also was attributed a role in the soil's magnetization potential because of its capacity for complexation of iron. Furthermore, organic materials may provide a substrate for bacterial reduction of haematite into magnetite under anaerobic conditions (Schmidt, 2007). Howard and Orlicki (2015) measured the pH, EC and MS of a specimen of wood (peat). In contrast to the majority of reference artefacts investigated, wood showed an acidic abrasion pH. The dissociation of carboxyl or other organic functional groups was raised as potential explanation. A relatively low extract EC was observed (56 mS m^{-1} on average) and a slightly negative MS value was obtained, confirming the obvious non-magnetic character of wood. The high water-holding potential of organic waste was illustrated in the study of Hogland et al. (2014): samples of wood and newspapers had moisture contents of 42% and 72%,

respectively, whereas the overall MSW moisture content was 30% – a typical average value for MSW (Williams, 2005). As organic waste is the MSW fraction liable to biological degradation, its content decreases with storage time in the landfill. This generally has been observed to lead to a corresponding increase in the fine soil type content.

The fine fraction, recovered from screening wet or dry waste samples over a sieve with mesh size varying between 10 mm and 30 mm, generally covers the largest mass fraction of MSW (e.g. Kaartinen et al., 2013; Quaghebeur et al., 2013). From this respect, investigation of deposited waste substrates through samples that exclude the coarser fractions could yet be considered an acceptable solution. Nevertheless, characterization data of the fine fraction are scarce, presumably also because its valorization potential is deemed inferior to that of other waste fractions such as combustibles and metals (e.g Kaartinen et al., 2013). The properties of the fine soil type fraction largely depend on the degradation and leachate status of the material (see the paragraph on biophysicochemical landfill processes below). Quaghebeur et al. (2013) observed the TOC content of the fine fraction to increase with decreasing age of the waste: values of 7.6% and 12.4% were found for MSW landfilled in the periods 1980–1985 and 1995–2000, respectively. A similar trend was seen in the calorific value (2.2–4.8 MJ kg^{-1}). The loss of organic carbon over time was ascribed to the production (and recovery) of landfill gas. The concentration of arsenic, cadmium, chromium, copper, mercury, nickel and zinc in the fine fraction decreased for more recently landfilled MSW, but this was suggested to relate to a change in quality of the fresh MSW. A percentage of 0.5–5.3% of the fine fraction mass was magnetic. Also in Kaartinen et al. (2013) an increase of the TOC content with decreasing MSW age was evidenced. The fraction <20 mm retrieved from manual sorting had a slightly lower TOC content (4.7–5.8%) than the fraction <30mm derived from mechanical pre-treatment (6.8–11%). Furthermore, in this study, the pH and EC of fine fraction eluates (~ 1:10 soil:water extracts) were measured as part of a one-stage batch leaching test (EN 12457-4, European Committee for Standardization [CEN], 2002). Each of the samples showed a pH around 8, the values were slightly lower for the middle layers as compared to the bottom layers of the landfill (8.1–8.3 for manual sorting and 7.8–8.2 for mechanical pre-treatment samples). The EC, on the other hand, was considerably higher for the middle-layer samples than for those from the bottom layers: 280 mS m^{-1} versus 170 mS m^{-1} and 360 mS m^{-1} versus 160 mS m^{-1} for the manual sorting and mechanical pre-treatment samples, respectively. The same trend

was observed for the chloride (Cl^-), sulphate (SO_4^{2-}) and dissolved organic carbon concentrations of the eluates, which were identified as the primary leaching substances. This is consistent with the established relationships between EC, on the one hand, and Cl^- and SO_4^{2-} as major dissolved inorganic solutes, on the other, applied in soil salinity assessment (Rhoades et al., 1999). The lower values for the bottom waste layers were explained by higher amounts of these substances that were lost through leaching (and landfill gas formation), during the longer storage time in the landfill. Prechthai et al. (2008) found values of the same order of magnitude for the pH (7.7 ± 0.3) and EC (260 ± 80 mS m^{-1}) for the fine fraction (<25 mm) of MSW with age between 3 and 5 years.

Finally, a few overall characteristics of MSW are given. The density of raw MSW is in a low range of 115–180 kg m^{-3}. The density will increase under influence of compaction during emplacement of the waste in the landfill and/or any size-reduction (for example, shredding) during pre-landfill processing (Pichtel, 2014). The density of deposited MSW varies between a broad range of between 275–1300 kg m^{-3} (see also the paragraph on mechanical waste alterations below). Corresponding to the bulk density, a broad range in hydraulic conductivity values have been observed. According to Meuser (2010), the hydraulic conductivity of household waste is in the range of approximately 0.07–0.48 m s^{-1}. Also the field capacity of MSW generally is relatively high, but it varies with the degree of compaction and the state of decomposition (Pichtel, 2014). For uncompacted waste, the field capacity can amount to 50–60% of the dry waste mass. Williams (2005) and Pichtel (2014) mention that the overall moisture content of MSW typically is within a range of 15–40%, being 30% on average. Hogland et al. (2004) corroborate this average value for excavated waste, yet several other studies revealed higher values. For instance, in Prechthai et al. (2008) the moisture content increased with depth from approximately 37% to 54%. Quaghebeur et al. (2013) found values between 48 and 66% (w/w) and stresses the severe heterogeneity of landfill moisture conditions, due to the presence of poorly-draining or impermeable materials or substrates. For landfills in Europe, the TOC content of fresh MSW appears to be constant around 43–44% (w/w) (Quaghebeur et al., 2013). The CEC of MSW depositions varies between 3 and 67 $cmol_c$ kg^{-1}, with an average around 21 $cmol_c$ kg^{-1}. This average value is comparable to that of a loamy to clayey soil (Rowell, 1994); it is twice as high that of construction debris, but only nearly half of that of slag and ashes (Meuser, 2010). Fresh MSW depositions are anticipated to show an electric conductivity and magnetic susceptibility considerable

higher than (mostly inert) CDW, yet well below the values expected for metalliferous slag.

The properties of fresh MSW set the baseline for the specific geophysical response that can be expected for the deposited substrate. However, to a greater extent than the other waste types considered, the properties of MSW depositions are apt to evolve over time as effect of the processes of waste settlement, leachate generation and landfill gas production which are more extensively discussed in the following paragraphs.

4.2.2 **Mechanical waste alterations**

During the deposition of waste into the landfill, an initial change in properties of the waste substrate occurs as a result of the mechanical forces it is subjected to. Modern landfill practice includes compaction of the waste to minimize landfilled volumes and systematic addition of a cover layer to prevent airborne pollution. Also due to the development of improved landfill machinery, new landfills tend to show higher bulk densities and correspondingly lower permeabilities. The bulk density of fresh waste deposits is determined by the type and proportions of waste and cover materials, and the degree of compaction. Bulk density can be expected to change over time with settlement of the waste, which is affected by transient loads such as from precipitation or additional waste disposal, and processes of decomposition and consolidation. The initial heterogeneity of waste deposits is likely to reflect in non-uniform settlement, which can lead to fracturing of the landfill cover. Preferential infiltration routes for rainwater and snow-melts created from cracks in the capping layer can, in their turn, propagate divergent settlement conditions (Bernstone et al., 2000; El-Fadel et al., 1999; Meju, 2000; Whiteley & Jewell, 1992). Yet, the increase in bulk density due to settlement is tempered by the effect of landfill gas production and, according to Bernstone et al. (2000), the overall change in bulk density over time can be expected to be minimal.

The bulk density of MSW deposits has been observed to vary between 275 kg m^{-3} and 1300 kg m^{-3} (Meju, 2000; Pichtel, 2014; Whiteley & Jewell, 1992; see also Prechthai et al., 2008). Intermixtures of MSW with construction debris or important fractions of metals likely produce higher values. However, the bulk density of waste deposits is generally well below that of natural geological materials. This serves as a basis for landfill depth or volume determinations using geophysical methods that are sensitive to density contrasts such as seismic refraction (Meju, 2000; Whiteley &

Jewell, 1992). If compaction or settlement of the waste results in smaller pore volumes, it can contribute to higher bulk EC of waste substrates by enhancing the electric current flow through the solid-liquid phase pathway (e.g. Islam et al., 2014a; 2014b).

4.2.3 **Biophysicochemical landfill processes**

Next to – and mostly superior to – waste settlement, the evolution of a landfill's geophysical signature in time is shaped by processes related to leachate generation and landfill gas production. Both processes are commonly associated with the microbial decomposition of biodegradable waste fractions and therefore are particularly relevant to MSW landfills. Referring to the definition of leachate provided by the EU Landfill Directive (p. 4) – 'any liquid percolating through the deposited waste and emitted from or contained within a landfill', biodegradation is not a prerequisite for leaching to occur. Yet, inert waste, as representing a major constituent of CDW, by definition 'does not undergo any significant physical, chemical or biological transformations' (EU Landfill Directive, p. 3). Consequently, it should also not produce any significant quantities of leachate or landfill gas, in a way that may pose risks to the environment or human health (see also Williams, 2005).

Even if the landfill has been provided with a capping layer, serving as impermeable barrier to the infiltration of precipitation, there is still some ingress of water taking place during landfilling or through possible cracks in the capping layer. If the landfill is unlined, infiltration can also occur at the interface between fill and host material. Percolating water, or other liquids disposed of within the waste, will cause soluble constituents to dissolve allowing them to leach to deeper landfill layers – under the condition that the fluid content exceeds the fill's field capacity, which usually is higher for more compacted waste layers. On the other hand, leachate expulsion may by facilitated by compression of waste, particularly if it has a high inherent moisture content. Leaching may lead to the removal of the mineral elements calcium, magnesium, potassium, nitrogen and phosphorus and of small soil particles such as clay. Supplemented by ion exchange reactions, this can induce changes in the structure and composition of the solid-fluid phase system. The leachate liquid produced is typically rich in fungi and bacteria, inorganic salts and OM. Its composition will vary in function of the type of solvent and solutes that are present, which also depend on the ongoing degradation processes. The quantity and the concentration of the leachate generated is primarily governed by the water infiltration rate and the

permeability of the fill (Meju, 2000), but also the progress of biodegradation plays a role, considering water is a reaction product (Williams, 2005).

To go more deeply into the change of the leachate composition over time and to explain the production of landfill gas, it is necessary to amplify on the decomposition processes of biodegradable wastes. For a comprehensive discussion and elucidative diagrams, we refer to Williams (2005) and Pichtel (2014); only a summary is presented here. The degradation of bioreactive solid wastes consists in five main stages.

I. The first *hydrolysis stage* occurs under *aerobic conditions*, i.e. during landfilling and the short period (usually only a few days or weeks) thereafter, depending on the initial amount of air trapped in the waste and the degree of compaction. Aerobic microorganisms metabolise oxygen and organic waste to produce simpler hydrocarbons, carbon dioxide (CO_2), water (H_2O) and heat. These exothermic reactions can raise the temperature in the landfill up to 70−90°C (see also Quaghebeur et al., 2013). Carbon dioxide is emitted as gas or reacts with water to form carbonic acid, which reduces the leachate pH.
II. The second stage of *hydrolysis and fermentation*, also termed the *acidogenic* stage, takes off as depletion of oxygen sets in and *anaerobic conditions* are created. Facultative anaerobic bacteria become dominant and induce the formation of CO_2, hydrogen (H_2), ammonia (NH_3) and organic acids (mainly acetic acid). The leachate is enriched with NH_3-N and organic acids. The corresponding decrease in pH stimulates the mobility of HMs such as Iron, Chromium and Manganese. The landfill gas generated in this stage mainly consists in CO_2 (up to 80%), supplemented with H_2. The temperature drops to between 30°C and 50°C.
III. During the *acetogenesis* stage, acetogen microorganisms are responsible for the further conversion of the organic acids formed in stage II to acetic acid, CO_2 and H_2. At the same time, CO_2 and H_2 are used by another type of microorganisms to convert carbohydrates directly to acetic acid. The high concentration of organic acids causes the pH to decrease to a value of 4 or even less. Because of these strongly acidic conditions and the complexation of metals with other organic and inorganic ions in the leachate solution (e.g. NH_4^+ and Cl^-), the mobilisation of HMs is further enhanced. With decrease of the H_2 concentration, methane-generating microorganisms are promoted and the landfill evolves into the next degradation stage.

IV. In the *methanogenesis* stage, the anaerobic conditions of stage II and III persist. Methanogen microorganisms turn the organic acids and their derivatives generated in the previous stages into CO_2 and CH_4. In addition, CH_4 is produced from the reaction of CO_2 and H_2. The consumption of organic acids causes the pH to increase to about 7–8. Stage IV is the main landfill gas generation stage; landfill gas primarily consists in CH_4 (~60%) and CO_2 (~40%) with other minor components and water vapour. The optimum conditions for landfill gas generation are at a soil moisture content between 60% and 80%, a temperature between 30 and 45°C and a pH between 6.8 and 7.5. Because the average landfill moisture content is well below the optimum (15%–40%), the reactions involved are relatively slow and the methanogenesis is the longest stage of waste degradation. Depending on the water content, methanogenesis begins after a period of six months to a few years after deposition of the waste and will continue over the next 15 to 30 years, although landfill gas generation has been observed to last up to 100 years (see also Clément et al., 2010).

V. The final stage of *oxidation* evolves from the complete depletion of organic acids for the production of CO_2 and CH_4. As methane-generating microorganisms are slowly replaced by methane-oxidising microorganisms, *aerobic conditions* are reinstalled. Residual CH_4 may be converted into CO_2 and H_2O.

Because of the heterogeneous nature of waste deposits and the heterogeneous conditions of moisture content and temperature, the progress of biodegradation can vary significantly within a landfill and all the different stages may be take place simultaneously. In surface waste layers the availability of oxygen is expected to prosper rapid aerobic degradation, while in deeper layers degradation is mainly anaerobic. It can take several decades for all the waste to complete the full process and to reach stabilization of the landfill (Meju, 2000; Williams, 2005).

Many studies only discriminate between an acetogenic and a methanogenic stage, probably because the most substantial changes in leachate and gas production occur at the transition between these stages. The relatively short duration of the first aerobic hydrolysis stage and that the final stage of oxidation has mostly not yet been reached may provide additional explanation. Acetogenic leachate, produced from young waste depositions, is characterized by very levels of organic acids, ammonia and total dissolved solids (TDS). As degradation evolves into the methanogenic stage, the concentrations of these solutes decreases. Correspondingly, the TOC content, the

chemical oxygen demand (COD) and biological oxygen demand (BOD) will decrease with the age of the waste deposition. Components with high ionic mobility (e.g., Cl^-, SO_4^{2-} and DOC) generally show the highest concentrations in leachates. The leachate composition is determined by the type and age of the waste deposition, the water infiltration rate and the prevailing pH. The rate and quantity of leachate and landfill gas production varies with the depth in the landfill, regional climate conditions, local hydrogeology, and the degree of fluid in- and outflow control (e.g. presence of capping and/or lining layers) (Meju, 2000; see also Abdulrahman et al., 2016; and Wijesekara et al., 2014).

Chapter 5
Landfill investigation through high-resolution multi-receiver EMI surveying

'Of all the paths you take in life, make sure a few of them are dirt' – John Muir

5.1 Introduction

The general rationale behind using geophysical methods as an alternative to conventional invasive methods for landfill site investigation was already explained in Chapter 4: to obtain more spatially comprehensive information in a more efficient way. In the vast majority of previous studies, the motivation for geophysical investigations is to support the assessment of the environmental risks posed by groundwater contamination with landfill leachate. Also in the literature of the most recent years the focus remains on the detection and delineation of leachate in the waste masses and of leachate plumes (e.g. Abdulrahman et al., 2016; Abudeif, 2015; Ayolabi, Epelle, et al., 2015, Ayolabi, Oluwatosin, et al., 2015; Bellezoni et al., 2014; Belmonte-Jiménez et al., 2014; Çinar et al., 2016; Rehman et al., 2016). It is remarked that in these types of studies the landfill itself is sometimes even left out of consideration (e.g. Wijesekara et al., 2014). In geophysical studies that were conducted in more direct support of planning remediation or reclamation activities, landfill geometry and internal structure are recurrent research targets (Vargemezis et al., 2015; Xin et al., 2015; Yin et al., 2015). While remediation usually involves excavation of the disposed wastes, in which

part of the excavated materials can be recycled, only a few studies have made an explicit link to landfill mining (e.g. Bernstone et al., 2000; Zanetti & Godio, 2006).

According to Krook et al. (2012), landfill mining can be defined as 'a process for extracting minerals or other solid natural resources from waste materials that previously have been disposed of by burying them in the ground' (p. 513). While the first landfill mining initiative has been traced back to Israel in 1953, which was motivated by the recovery of fertilizers for orchards (Savage et al., 1993), notable interest only emerged in the 1990s. Changes in waste and landfill legislation, landfill management problems such as local pollution and a lack of landfill space, and the reclamation of land to allow for urban expansion have been the main drivers for landfill mining. Resource recovery was mostly limited to the recycling of natural soil material used for (intermediate) waste covering and of part of the metal fraction, and the extraction of methane as secondary energy source (Jones et al., 2013; Krook et al., 2012). In 2013, the concept of ELFM was launched: 'the safe conditioning, excavation and integrated valorization of (historic and/or future) landfilled waste streams as both materials (Waste-to-Material, WtM) and energy (Waste-to-Energy, WtE), using innovative transformation technologies and respecting the most stringent social and ecological criteria' (Jones et al., 2013, p. 48). Since then, concerted efforts have been made to advance waste processing technology and the development of ELFM decision support systems, for instance, based on life cycle analysis. Also considerable attention has been addressed to the societal and legal aspects involved in order to create a broader public support for ELFM activities. An important stimulus was provided by the results of the bottom-up inventory organized by the European Enhanced Landfill Mining Consortium (EURELCO) to gain insight in the current landfill situation in Europe. The total number of landfills in Europe was estimated at more than 500 000 (EURELCO, 2015). About 90% of the landfill sites are considered to be non-sanitary, meaning they have been constructed without implementation of environmental protection technology as currently imposed by the Landfill Directive (1999). It is likely a similar tendency occurs in other parts of the world, for example, Wijesekara et al. (2014) cites an equal proportion of non-engineered landfills for South and Southeast Asia. Envisioning the costs associated with the remediation of these non-sanitary landfills, ELFM could be even considered a necessity rather than an opportunity. Acknowledging the need for more proactive management of landfills and the secondary resources they conceal, in March 2017 the European Parliament voted the adaption of four EU Directives, including the Landfill Directive, in order to include a

so-called 'Waste Package'. Hereby, the European Commission commited to further examine the feasibility of proposing a regulatory framework for ELFM.

Up to now, scientific research efforts in view of ELFM have been mainly concentrated on the development of new technologies and processes to improve thevalorization of excavated materials (e.g. Bosmans et al., 2013). Yet, it is clear there also is an incentive to enhance the stage of landfill exploration, which is the very start of the ELFM value chain and, hence, crucial to the design of a valid ELFM scenario. This involves accurate estimation of the landfill location and dimensions, and characterization of the contained waste. The latter encompasses characterization of the material in terms of its recycling or upcycling potential as well as its mineability, which results from the ease of excavation and the extractability of fractions of interest (Hull et al., 2005; Kaartinen et al., 2013; Quaghebeur et al., 2013). Furthermore, the results of the landfill exploration stage should allow for an *a priori* evaluation of the relevance of an ELFM scenario as a whole, as compared to a do-nothing or a classic remediation scenario (Jones et al., 2013). Regarding the considerable variations in waste composition between and within individual landfills, previous landfill mining studies have emphasized the importance of site-specific investigations (Krook et al., 2012). Nevertheless, it has been recognized that intensive sampling campaigns, set up to adequately address the heterogeneity of landfills, may become unfeasible in large scale landfill mining projects, advocating the need for more economic tools to characterize the mining potential of landfill sites (Kaartinen et al., 2013). This provides a new impetus to advance the exploration of landfills using geophysical sensors.

The currently established practice of geophysical landfill investigation leaves room for technological improvement. As for environmental and engineering geophysics in general, electric methods have dominated the landfill scene. Electrical resistivity imaging or electrical resistivity tomography (ERT) is the technique most commonly applied, in which electrical sounding and electrical profiling is combined to producing transects of electrical resistivity – the reciprocal of electrical conductivity. While this is a generally robust technique for which well-established data processing routines are available, there are also some drawbacks involved in its application on landfills. The operation principle of ERT relies on the introduction of a direct current into the subsurface through two electrodes (current electrodes) and then measuring the resultant potential difference between two additional electrodes (potential electrodes). Using Ohm's law, the output voltage is converted into a resistance reading for the soil volume between the potential electrodes. The latter is in its turn related to the soil

volume's apparent electrical resistivity, according to the specific electrode configurations applied. The introduction of electric current requires good galvanic contact between the electrodes and the ground, which can be problematic when the electrodes are implanted into surface material consisting of dry sand or gravel. Also the superficial presence of construction debris can give rise to high contact resistance. This may be overcome by wetting the current electrodes with water or saline solution, or by application of bentonite, yet, such additional interventions strongly slow down the data acquisition in the field (Reynolds, 2011). Apart from possible practical complications, the landfill subsurface can pose some challenges to the standard processing of ERT data, particularly to the inversion of the collected apparent electrical resistivity data into a distribution of true electrical resistivity. If a highly conductive waste layer, such as leachate-saturated MSW, or a highly conductive, relatively large, lateral anomaly, such as an underground storage tank, is present at shallow depth, the actual electrical current flow in the subsurface can strongly deviate from the theoretical distribution assumed for inversion, which generally causes the electrical resistivity of the material underneath the conductive layer/structure to be underestimated. This phenomenon is known as a 'shadow effect' (e.g. Wang et al., 2015). Furthermore, the deepest measurement signals can be unreliable because of 3D distorting effects due to a complex landfill geometry (e.g. Meju, 2000). These issues with the accurate reconstruction of the deeper electrical resistivity distribution counter the advertised advantage of ERT to offer a larger measurement depth and an improved depth resolution as compared to EMI. In addition, the derivation of lateral resistivity maps has been demonstrated to suffer from surveying along discrete lines. Different survey lines usually have a parallel orientation, but the distance between the lines is typically much larger than the in-line sampling interval. Lateral interpolations are usually made with simple deterministic methods that are poorly suited to cope with different sampling densities in different directions and therefore often introduce a pattern of spatial stretching. In Bernstone et al. (2000), for example, this effect is clearly visible in resistivity depth slices extracted from a 3D-model created from merging individual inverted sections through triangulation with linear interpolation. Mathematical functions and geostatistical interpolation methods are available allowing to remove or at least reduce this effect, yet they are rarely called upon. The main reason for this probably is the absence of more sophisticated interpolation methods in most of the commercially available ERT data processing software. Interpolation artefacts could also be avoided by adapting the survey design, but for the

conventional electrode configurations (Wenner, Schlumberger and dipole-dipole arrays) a perfect balance in the cross-line and in-line ERT survey resolution is unseen. Usually, the minimum electrode spacing is in the range of one to a few metres, while the distance between survey lines varies from a few to a few tens of metres. Vargemezis et al. (2015) provide an example of a landfill survey with a pole-dipole array, in which the distance between the potential electrodes as well as the distance between survey lines equals 3 m. High lateral survey resolutions remain difficult to achieve with ERT, due to the extensive extra field time required. Bernstone et al. (2000) experimented with an increased data density, i.e. a between-line distance of 10 m and a minimum electrode spacing of 2 m, but they concluded this was still not enough to solve the complex landfill structure.

While ERT and EMI measure directly related subsurface properties, they come with opposite survey strategies: ERT is intended to produce profiles of electrical resistivity along discrete transects, but has limited lateral mapping capacity; EMI is ideally suited to map lateral variations in electrical conductivity, but provides limited depth resolution due to relatively small inter-coil separations. Can EMI provide a worthy alternative to conventional ERT surveying? The method of EMI has been used for landfill investigation before (e.g. Triantafilis et al., 2011, 2013; Wang et al., 2015), but its application is generally limited and the integration with motorized conveyance, offering improved survey efficiency, has not yet been evaluated in this context.

The next four sections each present a case study on the application of the mobile multi-receiver EMI survey system described in Chapter 3 on a specific landfill. All sites considered are non-sanitary landfills located in Flanders, Belgium. In three of the four cases, investigation of the landfill was (indirectly) commissioned by OVAM. However, the exact landfill locations are not specified to avoid traceability of the private parties involved, particularly the landfill site owners and the people living in the direct neighbourhood of the landfills. The landfills considered vary in construction setting, size and the type of waste that was disposed. A general overview is given in Table 5.1. In line with the overall aim of this thesis, in this series of case studies it is intended to evaluate (1) the practical implementation of the proposed survey methodology in a landfill environment, (2) the application of the standard data processing, (3) the stand-alone interpretation of the acquired EMI data, (4) the integration with conventional, invasive, investigation methods, and (5) the value of the results for supporting the design of a redevelopment scenario. It is noted that with respect to the first two, the application of this type of survey in natural or agricultural

environments is used as benchmark. More specific objectives related to the particular context of the landfill investigation are mentioned in the introductory subsections of the individual case studies.

Table 5.1 General description of the selected landfill sites

Case study	Size of study area (ha)	Waste disposal	Construction setting	Type of waste[a]
I	20.1	Uncontrolled	Old tidal channel or wetland[b]	?
II	1.4	Licensed	River wetland	IW, CDW
III	1.6	Licensed	March, land-raise	MSW, IW
IV	9.9	Controlled, yet not licensed	Former sand quarry	CDW

[a] According to historical documentation

[b] Assumed from the environmental context and from investigation results

5.2 CASE STUDY I: Landfill detection in nature redevelopment project

5.2.1 Site description and research objectives

This case study concerns an agricultural area comprised in a nature development project situated in one of the polder areas in the north of the province of East-Flanders. The specific area considered covers 20.1 ha and is located alongside a creek that is a remainder of a former branch of a main tidal channel (Figure 5.1). The shallow creek has fresh to light brackish water. From a practical organizational perspective, it is worth mentioning that more than 60 unique cadastral parcels were included and, as a consequence, a hotchpotch of land owners and land users was involved in the planning of the soil investigation activities. About 80% of the study area is currently used as pasture; the remaining part in the south is arable land. According to the Belgian soil map, the soil texture varies from light sandloam in the north, over loamy sand, to sand in the south. A corresponding trend exists in the natural drainage, with extremely wet soil in the north, over very wet and wet soil in the major, middle, part of the study area, to moderately wet and moderately dry soil in the south. The uttermost north-eastern parcels, visible as an area with dark green vegetation in

Figure 5.1a, are covered with reed (and therefore were excluded from the EMI survey, see Figure 5.1b).

During the exploratory investigations conducted by the environmental consultant assigned to the project, several indications were found advocating that in the past waste had been disposed in the area:

- Elevation data suggest that part of the terrain has been raised. The local digital terrain model (DTM) is shown in Figure 5.1b.
- Local residents confirm that waste used to be dumped along the riverside.
- In certain parcels, waste materials such as plastic, brick and pieces of metal came to the surface when the land was ploughed. This is illustrated in the photograph given in Figure 5.2C.

The principal objectives of the EMI survey in this case study were (1) to detect the presence of any landfill(s) and, (2) if this was the case, to delineate its (their) lateral extent.

5.2.2 **EMI survey and data processing**

The EMI survey was performed using a DUALEM-21S sensor (Dualem Inc., Milton, ON, Canada), which was mounted in a mobile survey configuration as described in Chapter 3. Considering the superficial traces of waste observed on the terrain suggested waste depositions were likely to occur at shallow depth, the measurement depth of this sensor (maximum theoretical DOE of 3.2 m) was deemed sufficient to be able to meet the survey objectives of detection and lateral delineation of possible buried waste masses. Furthermore, from a practical perspective this sensor is usually preferred above a DUALEM-421S sensor because the dimensions of the corresponding mobile survey set-up are considerably smaller (approximately 7.5 m versus 9.5 m in length), which allows easier manoeuvring in the field. Data locations were measured using a Leica Viva GNSS-G15 differential GPS (Leica Geosystems, Heerbrugg, Switzerland).

The EMI survey was conducted on the 18th and 20th of January 2016, during a cold winter period after a few days of heavy rainfall. This timing was the main reason why the study area could be only partly surveyed. The southernmost parcels were excluded to avoid damaging recently sown winter wheat and grass. The adjacent parcel had previously been cropped with maize and had remained unworked after the harvest. In combination with the frosty weather at the time of the survey, surface conditions were too rough to guarantee the safeguarding of the sensing system

equipment in the proposed mobile survey configuration (Figure 5.2A). In the middle part of the study area, the northern parcels were largely under water (Figure 5.2B). The tight schedule of the project did not allow for a supplemental survey to be carried out on a later time, when weather and terrain conditions were more opportune. Conditioned by the land use organisation, the survey was comprised of 13 separate

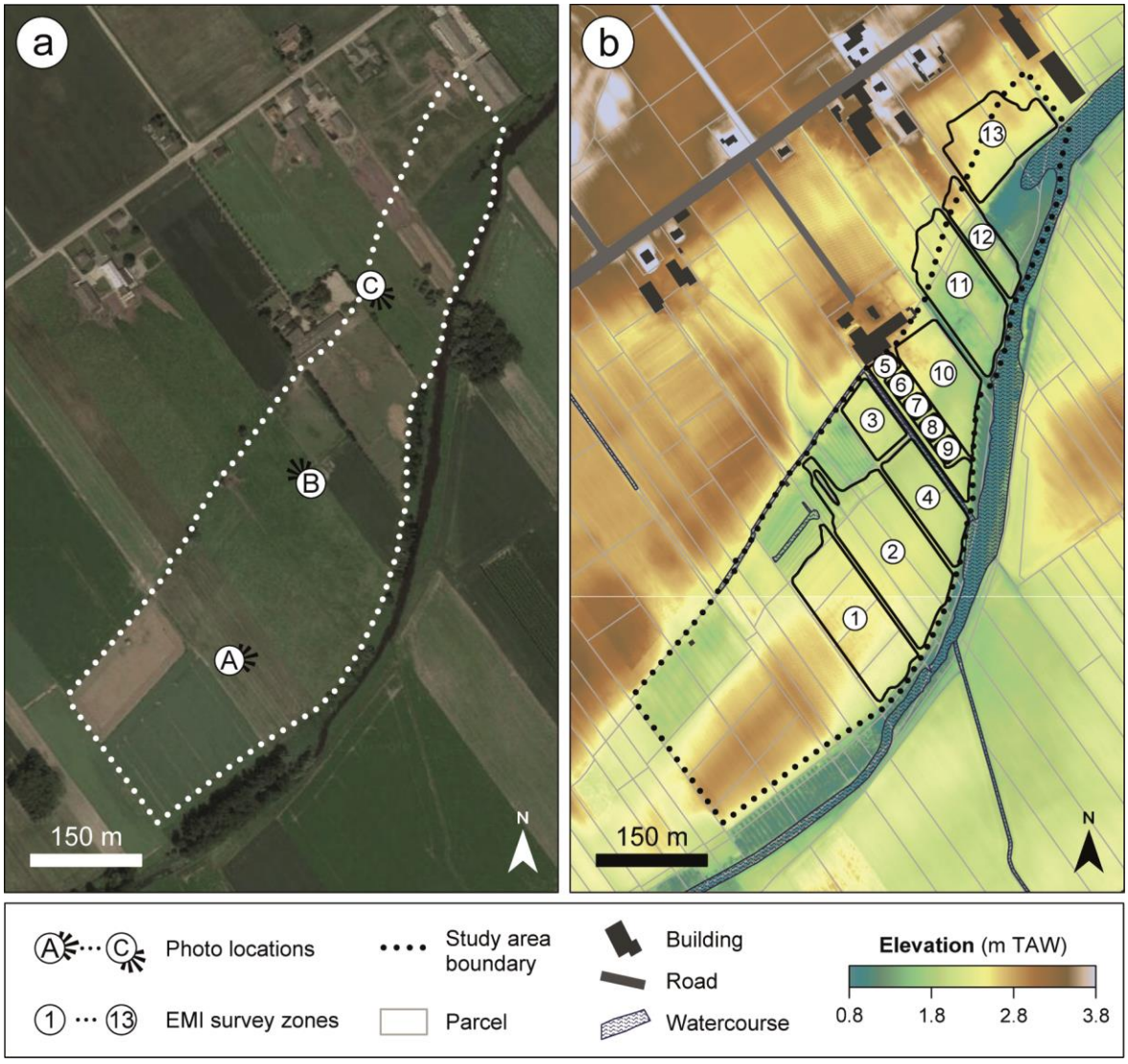

Figure 5.1 (a) Satellite image of the study area considered in landfill case I (source: Google Maps, Imagery ©2016, Aerodata International Surveys, Cnes/Spot Image, DigitalGlobe) with indication of the locations and points of view from which the photographs shown in Figure 5.2 were taken; and (b) local DTM with the elevation expressed in m TAW[6] (AGIV, 2014), overlaid by the cadastral parcel boundaries, buildings, roads and watercourses included in the LRD (AGIV, 2016b). The 13 separate survey zones are outlined by black contours.

[6] TAW is a Dutch abbreviation for "Tweede Algemene Waterpassing", the reference level for elevation measurements in Belgium. An elevation of 0 m TAW corresponds to the average low spring tide level at Ostend.

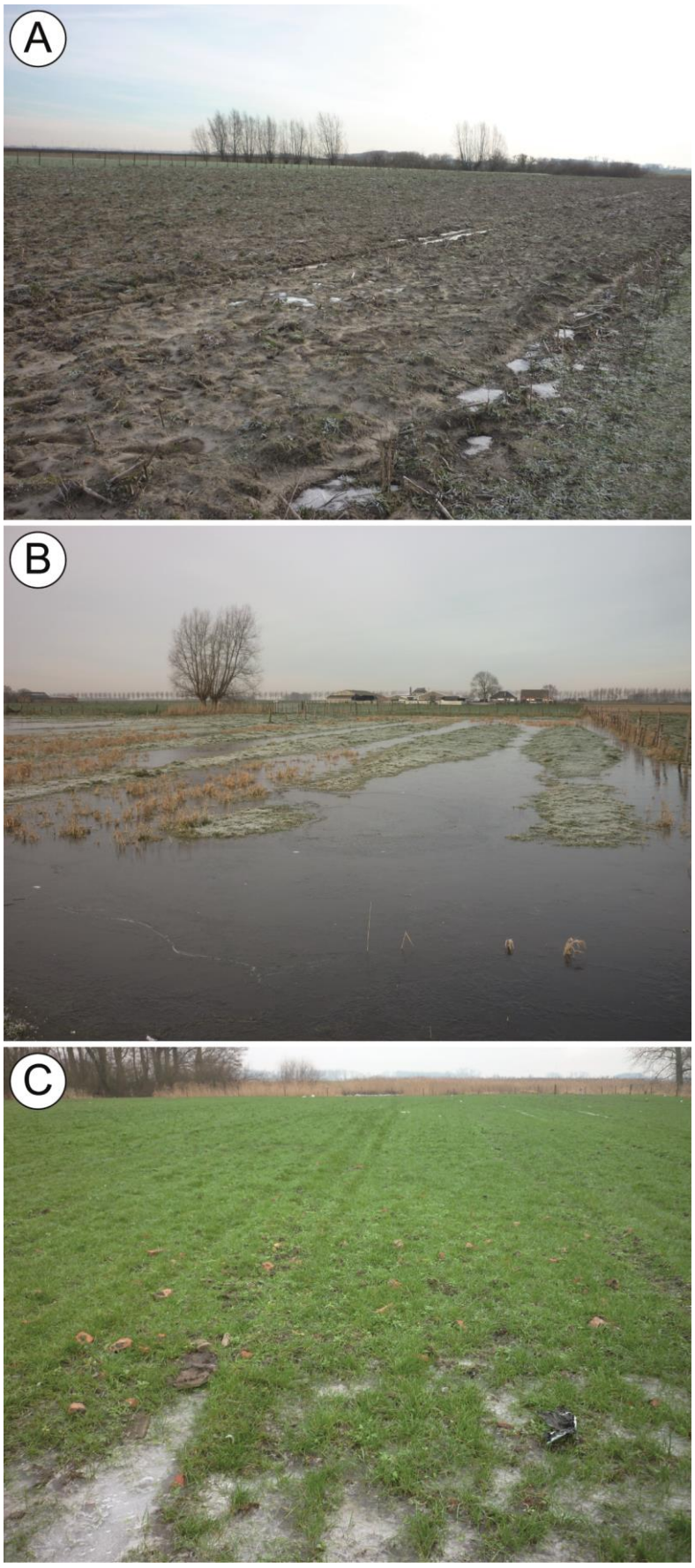

Figure 5.2 Photographs of the study area taken during the EMI survey campaign; the location and viewpoint direction of each photograph is indicated in Figure 5.1a.

survey zones. In total, 10.1 ha was covered, which is exactly half of the predefined study area. GPS data and sensor data were logged synchronously at respective rates of 1 Hz and 8 Hz. The average driving speed was 7.3 km h^{-1}, resulting in an average distance of 0.25 m between two consecutive measurements along the driving line. Table 5.2 additionally gives the survey statistics for each individual survey zone.

Table 5.2 EMI survey statistics for landfill case study I, overall and for each separate survey zone. The number of data points (N) is the minimum number of remaining data points after data processing of the four coil configurations.

Zone	Area (ha)	Median driving speed	Survey time (min)	N
1	1.68	7.5	40	18 846
2	2.09	6.7	56	26 226
3	0.48	7.5	12	5 907
4	0.86	7.6	19	9 180
5	0.34	7.1	12	5 534
6	0.08	6.9	3	1 380
7	0.08	7.3	2	1 110
8	0.08	7.1	3	1 381
9	0.08	6.3	3	1 487
10	1.03	7.0	28	13 355
11	1.46	7.8	31	14 901
12	0.59	7.6	15	7 187
13	1.21	7.4	31	14 522
Total	10.1		4 h 16 min	121 016
Weighted mean		7.3		

The first step in the data processing was the manual removal of data points with anomalous positions. Particularly in zone 11 several series of data points were removed to deduplicate overlapping parts of survey lines resulting from deviation of the intended driving pattern because of the presence of trees, possibly amplified by positioning inaccuracies due to the obstruction of the GNSS receiver. Next, for each of the survey zones, the data were corrected for the offset between the sensor (transmitter-receiver coil pair midpoints) and the GNSS receiver mounted at the back of the quad bike (see the paragraph on shift correction in section 3.4.4 Data processing). A combination of a kinematic correction and the constrained method as

described in Delefortrie et al. (2016) was applied. In this case study, the optimal time lag for shift correction was particularly difficult to assess for the small survey zones 6 to 9, for which only very few, short parallel survey lines were measured (respecting the proposed inter-line spacing of 4 m). For these zones, the time lag choice was made relying on the values found for the other, larger survey zones. A similar problem arose when correcting the sensor data for measurement drift, following the procedure presented in Delefortrie, De Smedt, et al. (2014), in that small survey zones provided a poor data support to identify and accurately model drift. Also in the larger zones, the number of comparison points between the survey and calibration data sets was rather small because of the relatively coarse survey resolution. On the other hand, the influence of drift is expected to be minimal when survey duration is short, as is the case here. For zones 6 to 9, none of the measurement signals were corrected for drift. In the other zones, the drift in EC_a was observed to be limited to a few tens of millisiemens per metre. For the PRP EC_a signals, drift was consistently modelled by a zero-order function; a constant value was added to (or subtracted from) the survey data to adjust them to the average calibration data level. The drift in the IP signals was generally more variable and modelled using higher order polynomials. These observations are congruous with the results presented in Delefortrie, De Smedt, et al. (2014). The EC_a data were not standardized to a reference temperature of 25°C, because the (locally) frozen soil surface layer prohibited making reliable soil temperature measurements. Since the survey was completed within a period of three days, this didn't have considerable consequences for the interpretation of the data. Finally, the data were interpolated to a grid with 0.2 m by 0.2 m cell size using ordinary kriging (Goovaerts, 1997). Per coil configuration, the data of the different survey zones were merged into one data set. The variogram models were constructed based on classical Matheron experimental variograms.

5.2.3 **Results and discussion**

Each of the EMI signals cover a broad range of values and display a consistent spatial pattern. Figure 5.3 shows the interpolated maps of the 1 m HCP and 2 m HCP EC_a, and the 1 m HCP MS_a. To facilitate comparison the two EC_a maps are displayed using a colour scale with the same range. The actual minimum and maximum EC_a values measured were −288.6 and 487.3 mS m^{-1} for the 1 m HCP configuration, and −279.0 and 188.1 mS m^{-1} for the 2 m HCP configuration. Because the response of the upper soil layer is integrated in each of the measurement signals, the characterized

pattern most probably relates to soil property variations at shallow depth, within the upper 0.5 m to 1 m soil layer. For the largest part of the surveyed area, low electrical conductivity was observed which is conform to the natural loamy sandy soil. In addition, the decreasing trend in conductivity from north to south agrees with the trend in soil texture and natural drainage as defined in the soil map. The median EC_a is 9.5, 17.0, 16.7 and 21.2 mS m^{-1} for the 1.1 m PRP, 2.1 m PRP, 1 m HCP and 2 m HCP configurations, respectively. The increasing trend with the theoretical DOE of the coil configurations indicates soil electrical conductivity generally increases with depth. An increase in soil moisture and/or clay content is a possible explanation. The occurrence of natural soil is further substantiated by the neutral MS_a response.

In the areas where the EC_a data suggest natural soil material, some structures can be recognized which are typical of a polder landscape. In the north of survey zone 2, linear structures are outlined by slightly higher values of EC_a. These likely correspond to former ditches which are commonly characterized by soil material with higher fractions of clay and OM. This is supported by a subtle contrast in MS_a at these locations (this is hardly visible in Figure 5.3c because of the large range of the colour scale used). Moreover, the structures are connected to the area which was largely under water at the time of the survey (Figure 5.2B). In the southern part of survey zones 1 and 2, a more gradual variation of EC_a can been seen, the overall pattern of which aligns with the course of the creek that forms the southern border of the study area. Probably these variations are remnants of the palaeo-river system under influence of tidal dynamics. Furthermore, survey zone 13 shows patterns the shape of which suggests a fluvial origin.

More important in view of the research question are the sharply contrasting EC_a and MS_a values in survey zones 5, 6, 7, 10 and 11 (zone 1 indicated in Figure 5.3d, 1.1 ha). These (absolute) measurement values are much higher than for the natural soil in the environment and signify a different type of material. Together with the clear definition of the anomaly's extent, this testifies to the presence of a landfill. From its embedding in the environment, a connection with an old river branch or former wetland can be suspected. The high amplitudes of the EC_a signals indicates material with a very high electrical conductivity, such as saline sludges and certain industrial residues, or waste with a high metallic fraction. For a part of the presumed landfill zone, the EC_a measurements change from positive in the 1 m HCP configuration to negative in the 2 m HCP configuration. This phenomenon is similar to the sign change caused by a metallic object at a shallow depth and, therefore, it corroborates that the

anomaly results from highly conductive material present from a depth close to the surface. That the sign change does not occur over the entire area can point to differences in the depth or the thickness of the waste layer. A similar subdivision of the area is suggested by the MS_a data. Northeast of the first, well-defined, anomalous zone, a zone of more "diffuse" disturbance in EC_a and MS_a can be seen (zone 2 in Figure 5.3d, 1.0 ha). This area coincides with the observation of waste scattered over the terrain surface (Figure 5.2B). Different interpretations of the EMI data are conceivable. A first is that only a thin layer of waste was disposed on top of the natural soil and only waste with strongly contrasting properties stands out. A second option is that waste was not directly disposed in this area, but was spread from the actual landfill – the concentrated anomaly described above – through tillage. Third, it is possible that a comparable volume of waste is present as in the first zone and the different EMI response is then explained by a difference in waste properties. In that case, the bulk properties of the waste would be more similar to those of the natural soil. If the landfill indeed corresponds to the infilling of an old river bed, the last interpretation is the most plausible.

Lastly, a marked anomaly is shown in the south of survey zone 5. Its signature in the different EMI signals suggests it originates from a metallic object or structure, possibly above ground; yet, this could not be verified in the field.

The total landfill area estimated from the EMI survey covers 2.1 ha. Essentially, the exploratory EMI survey narrowed down the area of interest for invasive investigation to 10% of the original study area, or to 20% if only accounting for the actually surveyed area. In either way, a significant improvement of the invasive investigation efficiency can be expected. Because of concerns related to confidentiality, the company in charge of the redevelopment project contested the release of the data obtained from drillings and trench excavations, hence, the lack of validation data presented here. However, the environmental consultant confirmed in personal communication that the presence and lateral delineation as derived from the EMI survey was corroborated. Unfortunately, no information was provided on the type of material found.

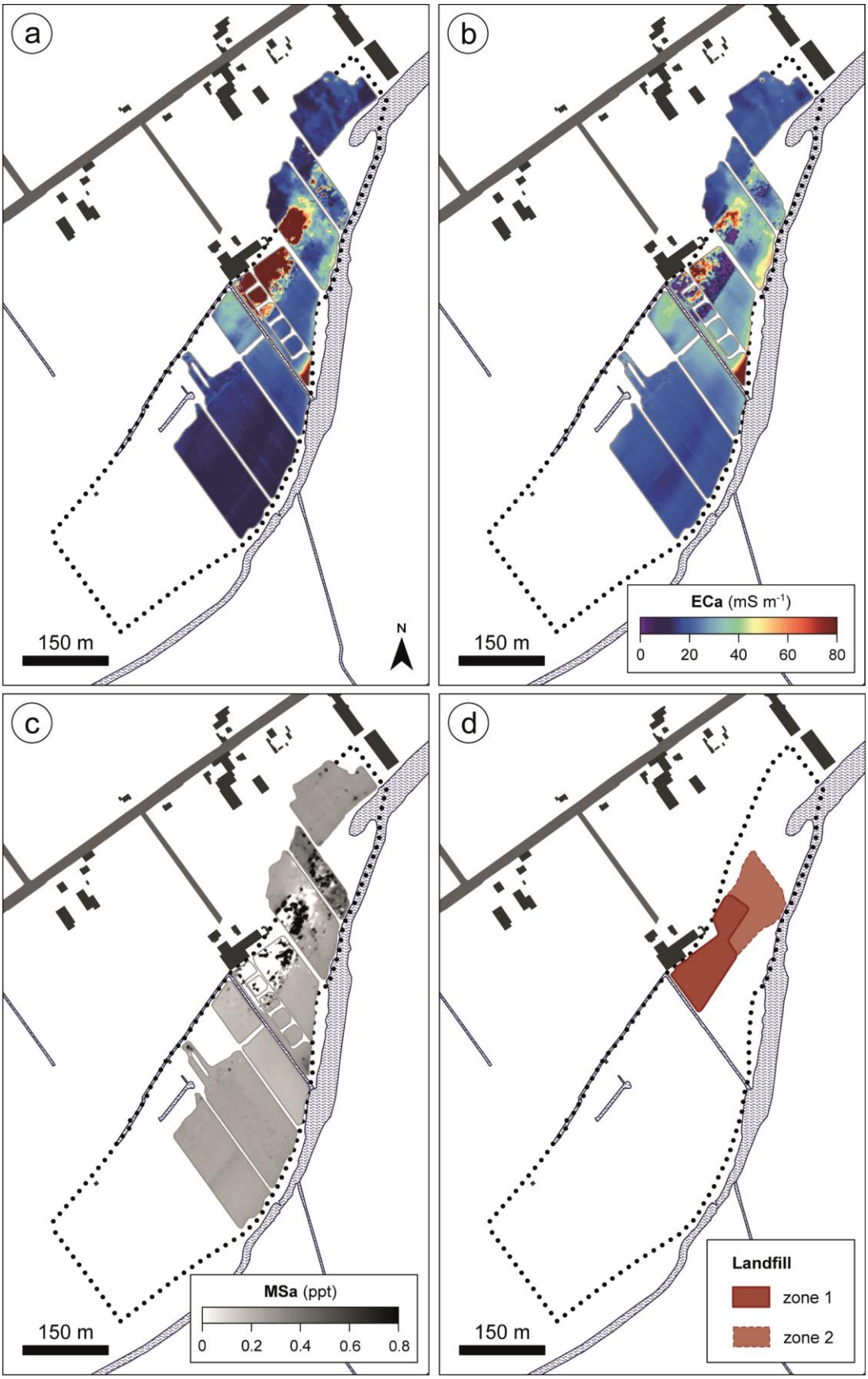

Figure 5.3 Ordinary kriging map of the 1 m HCP (a) and 2 m HCP EC_a (b), and 1 m HCP MS_a data (c) and the derived lateral delineation of a presumed landfill, including two distinct zones (d).

5.3 CASE STUDY II: Wetland landfill investigation in view of soil remediation

5.3.1 Site description and research objectives

The site under study in the second case study is part of a series of landfills constructed in the low-lying area along a river course in the province of Antwerp. At the time the area was raised with, mainly, MSW to avoid flooding. This is supported by the soil map indicating the area has a reduced, extremely wet soil of light sand-loam, with a peaty topsoil. After a major storm surge flood in 1976, an integrated flood protection plan for the Scheldt estuary, named the Sigma Plan, was established. By consequence of this plan, dykes were built along the banks of the river flanking the studied landfill site. The dyke on the northern river side, on top of which a bike road has been constructed, is visible in Figure 5.4. Today, the landfills can be recognized as areas with slightly raised elevation.

The specific landfill site considered has an area of 1.4 ha and for the most part is natural area; a limited part is residential area. Between the end of 1970 and the middle of 1973, the site was licenced as IW landfill. However, mainly construction and demolition waste (CDW) was disposed. In practice, the landfill remained operational until the spring of 1974. According to historical documents, the landfill was closed by covering the waste with a layer of sand of minimum 0.25 m thickness. Today, the site is grassland and includes several small pastures (Figure 5.4). The small pasture in the south (corresponding to survey zone 3) is used as training ring for horses and therefore recently raised with a layer of sand. Along the dividing line between the two main parcels, the site is crossed by high voltage overhead power lines, which are a possible source of electromagnetic noise. In the western pasture, surfacing blocks of concrete revealed the presence of landfilled waste. In previous soil investigations carried out by the environmental consultant between 2010 and 2012, waste was found between a depth of 0.25 m to 4.5 m. Waste materials encountered were rubble of stone and brick, concrete, metal (iron) scrap, tar, and cinder and ash. Moreover, it was demonstrated that the landfill activities had resulted in contamination of the soil with HMs and polycyclic aromatic hydrocarbons (PAHs), and of the groundwater with benzene, toluene, ethylbenzene and xylene (BTEX). Human and ecotoxicological risk assessment indicated remediation was required. For the remediation of the soil, the environmental consultant suggested the removal of the upper 1 m soil layer to replace

it with a clean "living" layer; possible waste masses at a greater depth would remain in place.

In this case study, the EMI survey aimed to support the further characterization of the landfill for the development of an adequate remediation scenario and for the evaluation of the ELFM potential of the site. This included a more detailed estimation of the volume of waste present, hence, lateral and vertical delineation of the landfill, and characterization of the contained waste. It was clear in advance, however, that a landfill mining project would not yield valuable building land, because the site is located in natural area and no revision of the land use destination is provided for.

5.3.2 **EMI survey and data processing**

The landfill site was surveyed using a DUALEM-421S sensor with a maximum theoretical DOE of 6.4 m. Therefore, the deepest EMI signals should encompass the entire depth of the landfill as observed during previous investigations. This was the reason why this sensor was preferred, despite that the correspondingly larger-sized sensor platform was less practical for manoeuvring around on the relatively small and fragmented study site. Sensor data were recorded at a rate of 8 Hz. In view of the research aim of a detailed characterization of the landfill, a cross-line survey resolution of 1 m was chosen. Position data were collected with a Leica Viva GNSS-G15 differential GPS.

The EMI survey was conducted on the 21th of September 2015 and was composed of four separate parts (Figure 5.4b). The bulging part of the study area in the north was not covered because the small pasture was practically inaccessible for the survey configuration. Similarly, the two subpastures in the northeast could not be surveyed. The part of the survey area alongside the dyke was avoided because of soggy terrain conditions. The driving pattern followed in this EMI survey was used as exemplary illustration in Chapter 3 (Figure 3.7). A combination of the standard zigzag and a block driving pattern was adopted. A distance of at least 1 m was kept between the sensor and the metal fences enclosing the different pastures to minimize interference. A larger distance from aboveground obstacles is generally recommended, particularly if they are composed of metal; yet, here the distance was kept to an absolute minimum to prevent losing too much spatial coverage. Table 5.3 gives a summary of the survey statistics. With an average driving speed of 6.4 km h^{-1}, an average in-line survey resolution of 0.20 m was achieved. The total area surveyed was 0.9 ha, corresponding to 62% of the study area.

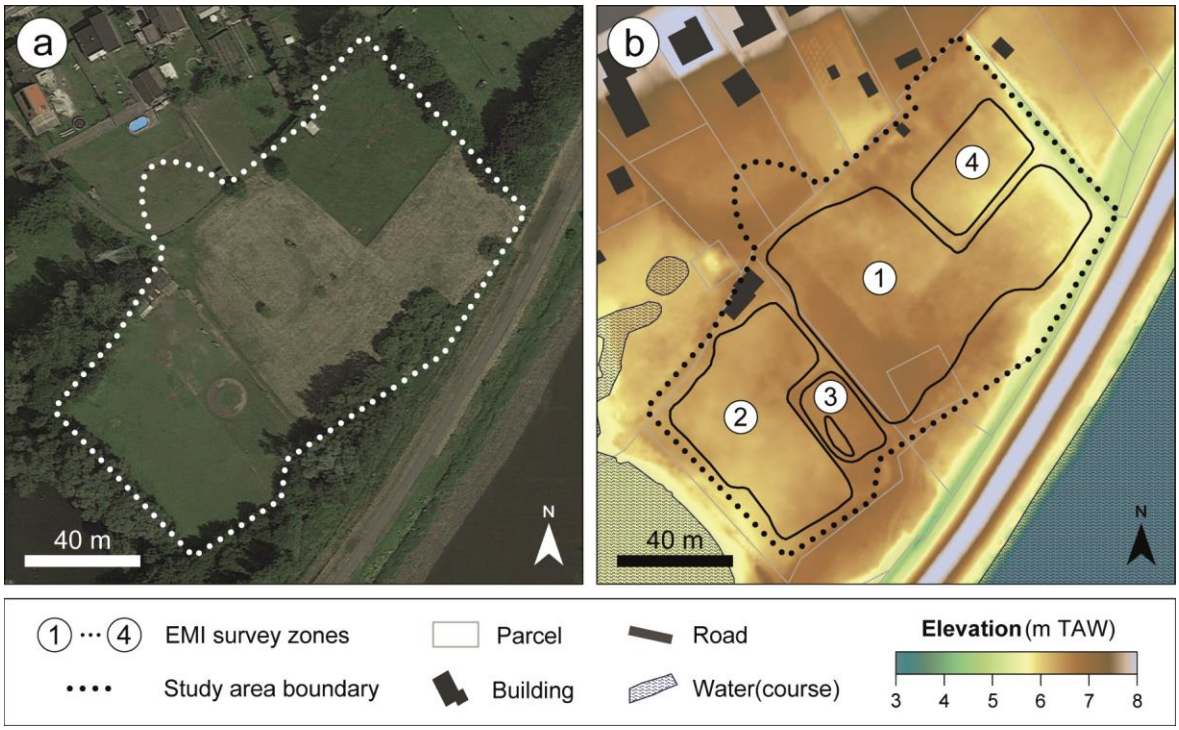

Figure 5.4 (a) Satellite image of the study area considered in landfill case II (source: Google Maps, Imagery ©2016, Aerodata International Surveys, Cnes/Spot Image, DigitalGlobe) and (b) local DTM with the elevation expressed in m TAW (AGIV, 2014), overlaid by the cadastral parcel boundaries, buildings, roads and watercourses included in the LRD (AGIV, 2016b). The four separate survey zones are outlined by black contours.

Table 5.3 EMI survey statistics for landfill case study II, overall and for each separate survey zone. The number of data points (N) is the minimum number of remaining data points after data processing of the four coil configurations.

Zone	Area (ha)	Median driving speed (km h^{-1})	Survey time (min)	N
1	0.48	6.4	62	29 414
2	0.27	6.5	30	14 308
3	0.05	7.0	7	3 220
4	0.10	6.5	13	5 955
Total	0.90		1 h 52 min	52 897
Weighted mean		6.5		

Following the conventional procedure for data processing, first the GPS data points were checked and corrected for anomalies. Particularly for the survey lines in the utmost west of the study area, pronounced aberrations were observed as RTK correction of the GPS signal that was lost when driving close to the trees surrounding the field. Subsequently, the sensor data positions were shifted to compensate for the offset between sensor and GNSS receiver. As in case study I, this correction

consisted in a combination of a kinematic correction and the constrained method as presented in Delefortrie et al. (2016). In this case, visually deciding on a proper time lag value for the correction was hampered by the abundance of local anomalies in the data (as shown in the maps in Figure 5.5) and, therefore, appeal was made to values commonly found for this sensor setup. The dense succession of local anomalies – beyond what can be successfully mitigated by filtering – also complicated the evaluation of drift in the data, as the time-series of differences between survey and calibration data generally demonstrated very noisy profiles. Furthermore, as specifically observed in survey zone 1, a part of the large deviations between survey and calibration line data were attributed to differences in influence from the metal fences delineating the survey zone. As calibration data are generally collected by driving perpendicular to the survey lines, the calibration line only closely approached the metal fences in its turns and therefore exhibited much less interference. It is important that such deviations are recognized and properly dealt with. The calibration procedure applied is designed to correct for drift – systematic variations in instrument response in time without appreciable changes above or below the soil surface and not to compensate for actual anomalies and, hence, should not be used as such. In the same way the spline fits serving as drift models could be fine-tuned to such an extent that they smooth out local anomalies, they can be turned into a source of artefacts. The drift calibration procedure is a versatile yet very powerful tool and should be handled cautiously. Modest corrections for drift were made in survey zones 1 and 2; no corrections were made for survey zones 3 and 4. After separate processing, the data of the different survey zones were combined. Per coil configuration, the data were interpolated with ordinary kriging (Goovaerts, 1997) using variogram models derived from Matheron experimental variograms. Despite the predominance of short-scale spatial variation, the experimental variograms showed a stable behavior. The cell size of the created grids was 0.1 by 0.1 m.

5.3.3 Test pit excavations

The maps produced from the EMI survey were used to select appropriate locations for test pits excavations, which aimed to support the characterization of the landfilled waste to evaluate its potential for ELFM. At the same time, the excavation results served as validation of the interpretations made from the EMI data.

5.3.4 **Results and discussion**

EMI data

The interpolated maps of EC_a for the 1.1 m PRP (DOE 0.5 m), 1 m HCP (DOE 1.6 m) and 4 m HCP (DOE 6.4 m) are shown in Figure 5.5. For large parts of the surveyed area, extreme – both positive and negative – values of EC_a and MS_a were observed, which clearly contradict the presence of natural soil material. If such anomalies coincide for the different coil configurations, they are typically indicative of metallic objects occurring at shallow depth. Large metallic objects, such as metal drums or underground storage tanks, or dense concentrations of smaller objects can result in very strong anomalies that affect each of the signals irrespective of their measurement depth. Whether the sign of the measurement values is positive or negative in the different signals depends on the size, depth and orientation of the metallic objects in relation to the respective transmitter-receiver coil combination. In the large pasture in the southwest and the small one in the northeast, discrete anomalies can hardly be distinguished, suggesting waste with a relatively high metallic fraction. Possible examples are CDW with a considerable amount of scrap metal, such as from reinforced concrete rebar, IW consisting of combustion residues as slag and ashes, or poorly sorted MSW – which is not unlikely considering the time period in which the landfill was installed. As "outcropping" concrete was observed in the southwestern pasture, the presence of CDW is highly probable. A local resident mentioned metal drums had been buried in the northeastern part of the study area, offering a plausible explanation for the strong anomalies observed over there. The southwestern corner of survey zone 1 demonstrates a smaller concentration of highly conductive anomalies. Waste is still expected, but its nature likely differs, for instance, CDW that largely consists of inert materials as (non-reinforced) concrete, mortar and brick. Apart from a few small metal anomalies, the northeastern part of survey zone 1 shows more homogeneous EMI responses. The background electrical conductivity is markedly lower than for the other parts of the survey area, particularly for the signals with the smallest DOE, which more closely matches the expectations for the natural soil in the area. Furthermore, this area corresponds with the lowest elevation, around 1 m lower than the highest elevation of the study area. However, the contrast in EMI data did not correspond with an abrupt change in elevation. This suggests that either the waste fill gradually wedges out, or the area with lower conductivity was leveled up with material mainly consisting of natural soil. Based on the lateral variations observed in the EMI data, three different zones were delineated: two landfill zones with a

different type of waste, with a combined area of approximately 8550 m², and a zone where no or only limited waste disposal had occurred (Figure 5.5d).

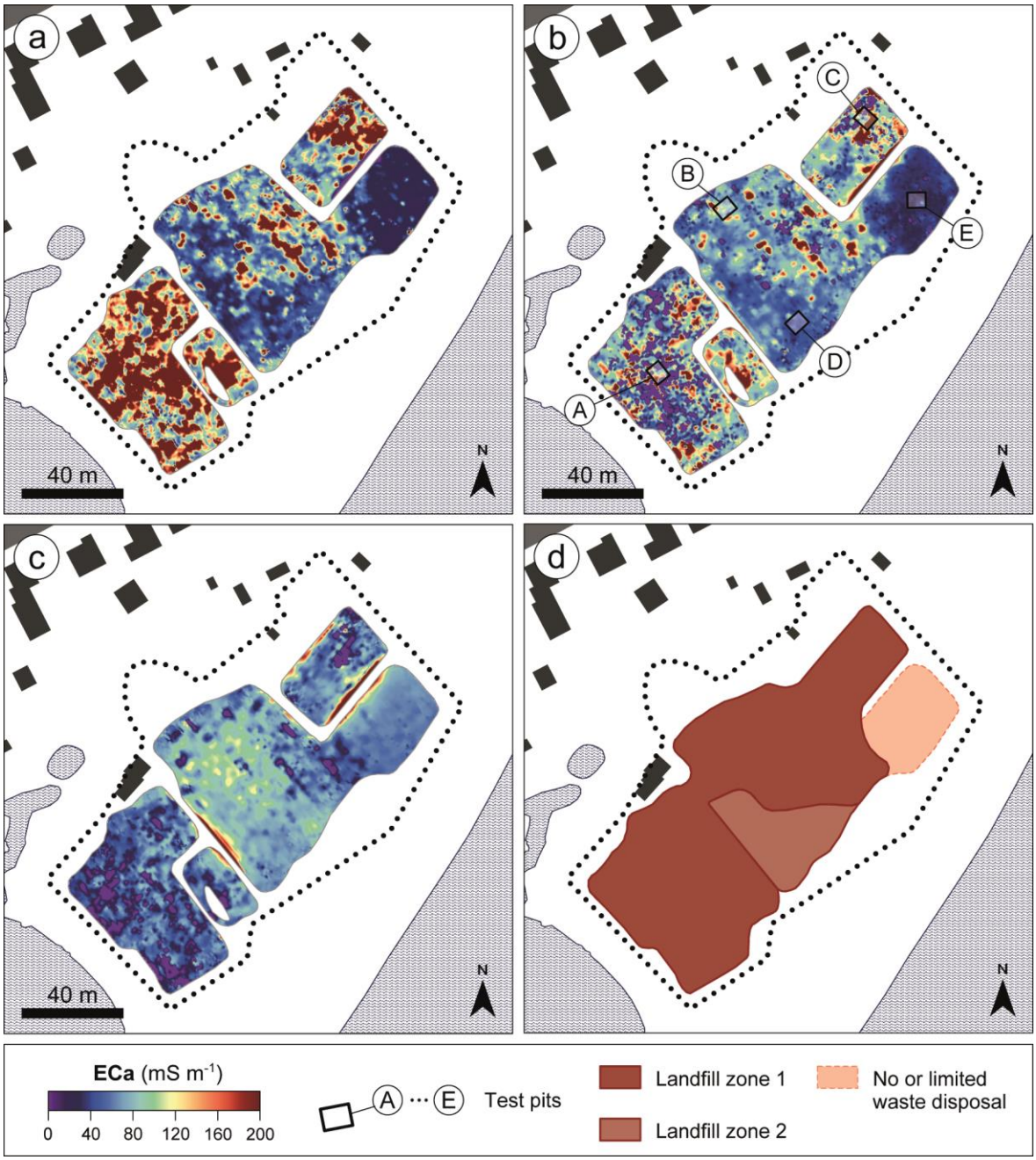

Figure 5.5 Ordinary kriging map of the 1.1 m PRP (a), 1 m HCP (b) and 4 m HCP EC_a data (c). Three zones were discriminated in the survey area: (1) a landfill zone with a predominant signature of metallic waste, (2) a landfill zone with more homogeneous waste, with a smaller metallic fraction as in the first zone, and (3) a zone with limited indications of waste disposal. On the 1 m HCP map (b), the five locations selected for test pits excavations (A–E) are indicated; note that the excavation areas are not drawn to scale.

Because of the plentiful local extremes, the EMI data are of limited use to reconstruct vertical variations in subsurface properties. The EC_a of the 4 m HCP coil configuration (Figure 5.5c), with the largest theoretical DOE, varies more smoothly

than for the other coil configurations. The contribution to this EC_a signal response of the supposedly more homogeneous natural soil underlying the waste layer possibly counterbalanced the influence of the strong waste anomalies. However, as increasing soil volumes are integrated, smoothing of variations with increasing DOE is a generally observed trend, and, in addition, the highly conductive anomalies occurring near the surface likely caused a reduced penetration depth as compared to the theoretical DOE: two arguments veiling this interpretation in some uncertainty.

Finally, attention is drawn to the anomalously high EC_a and MS_a measured directly along the boundaries between the different survey zones. This is a typical illustration of the influence of, above ground, metal fences. Note that the influence increases with the DOE of the coil configurations. The EMI were not appreciably affected by the overhead power lines.

Validation through test pit excavations

Guided by the EMI results, five locations for test pit excavations were indicated (A–E in Figure 5.5b). The excavations took place on the 30th of November and the 1st of December 2015. The test pits were about 1 m wide, 1.2 m long and 1 m deep, unless the occurring waste prevented excavation to this depth. In test pit A, a mixture of MSW and CDW was found (Figure 5.6, top). Specific materials included plastic (mainly film), textile, styrofoam, brick, tiles, concrete, wood and fiberboard, and scrap metal (wire netting, wires and cables). The topsoil layer covering the waste had a thickness of only 5 to 15 cm. In test pit B, underneath an organic topsoil layer of 10 to 15 cm thickness, a separate waste cover layer of sand seemed to be present, with a thickness varying between 10 and 20 cm. However, neither of these layers were completely free of waste, for example, pieces of wire and cable were present in the topsoil layer. Below, CDW was found which mainly existed in brick, cement, mortar and plaster. Groundwater was reached at a depth of 1.10 m. In test pit C, directly underneath the topsoil of only a few centimetres thick, a layer of ashes of 5 to 10 cm thickness was observed. Following, a layer of soil-like material mixed with coarse fragments of waste of variable nature occurred, for instance, bitumen roofing, plastic film and metal pipes. The presence of metal drums as suggested by a local resident could not be confirmed. In this pit, the groundwater level was observed at a depth of 90 cm. In test pit D, the topsoil was underlain by a layer of clay of 15 to 25 cm thickness (Figure 5.6, middle). The lower part of the clay layer had a predominant orange to orange-brown colour due to a dense pattern of rust patches. Underneath, a layer of brick was encountered and at a depth of about 50 cm an impenetrable

structure was hit, which prevented deeper excavation. The associated blue colour likely indicates a contaminant. Finally, test pit E showed a dark brown topsoil layer of 60 cm thickness that was free of waste, excepting some stones and small brick fragments (Figure 5.6, bottom). The dark grey colour and the occurrence of small pieces of glass and plastic in the upper part of the underlying layer reveal that this area was also affected by the landfill activities. However, the direct disposal of waste appears to have been very limited; the observed artefacts could have also resulted from (unintentional) lateral spreading of waste over the soil surface at that time. Test pit E was the only location where the original natural soil was observed within an excavation depth of 1 m. During excavation of the pit on the 30th of November, groundwater was reached at a depth of 90 cm; yet, overnight the groundwater level rose up to 50 cm from the surface. This higher groundwater level is consistent with the lower elevation of this area.

The observations from the excavation pits support the delineation of the three landfill zones derived from the EMI survey. In test pits A, B and C, all three located in the first landfill zone identified, relatively large pieces of scrap metal were found near the soil surface, offering an explanation for the EMI anomalies indicative of highly conductive material. Possibly, the shallow ash layer observed in test pit C also contributed to an increased conductivity (e.g. Boudreault et al., 2010; Meuser, 2010). The waste encountered in test pit D was more homogeneous in composition, which is conform to the definition of the second landfill zone. Lastly, the limited extent of the disturbance discerned in test pit E confirmed that in this zone no significant volumes of waste had been disposed.

Combining the information gained from the EMI survey and the test excavations, it is concluded that the landfill covers an area of at least 8 550 m². In the test pits where the proposed excavation depth of 1 m was achieved, waste was observed over the entire depth profile. Consequently, a remediation scenario consisting in the replacement of the contaminated upper 1 m soil layer with a clean living layer will require removing a minimum soil volume of 8 550 m³. Recuperation of the plastics and scrap metals can be an interesting prospect for an ELFM project. However, the amounts of materials that could be successfully separated and upcycled are expected to be rather small, because of the relatively small size of the landfill and the highly variable composition of the disposed waste. Hence, it can be doubted whether an ELFM project is worth the investment.

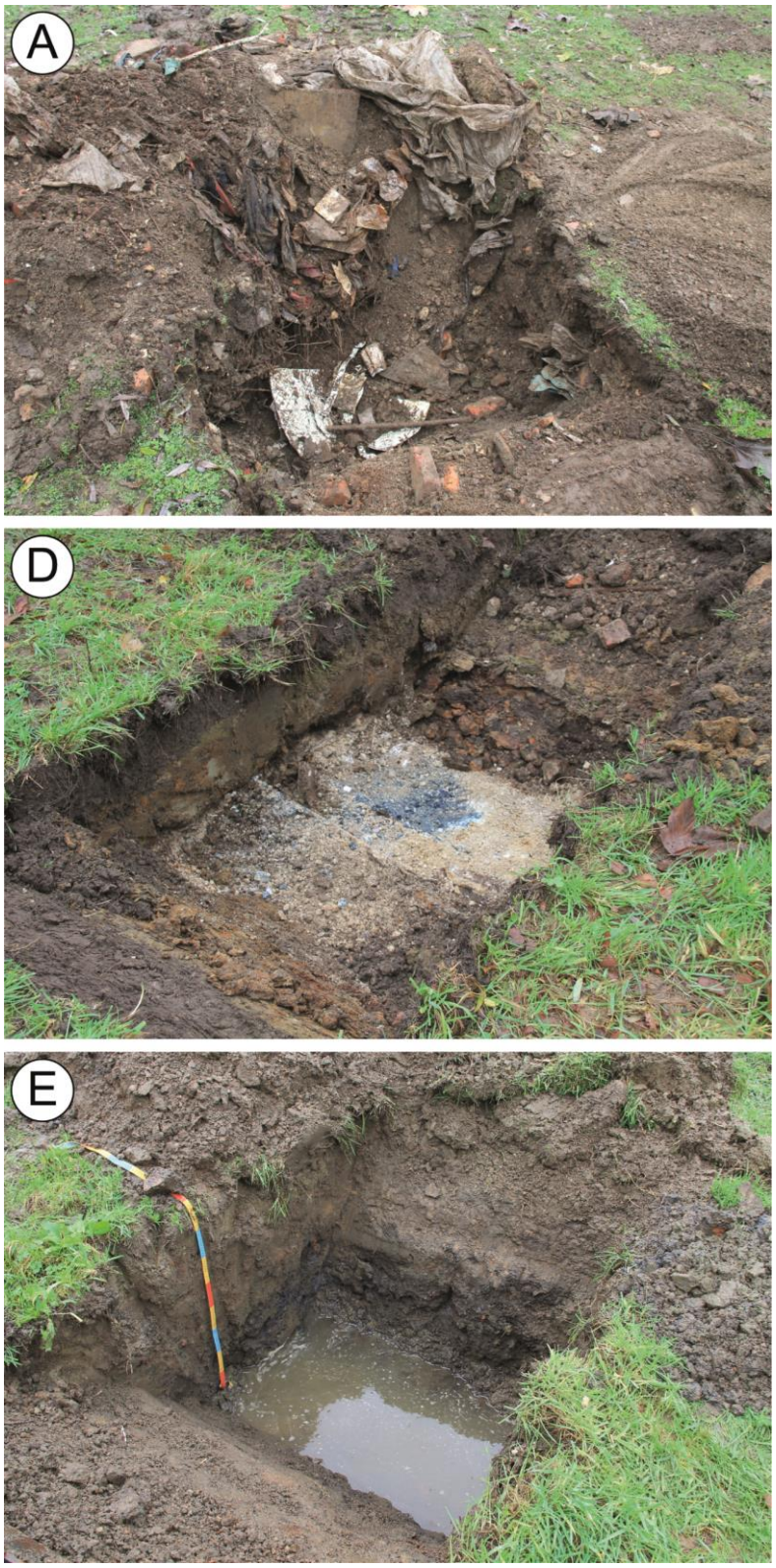

Figure 5.6 Photographs of the test pits excavations A (top), D (middle) and E (bottom), the locations of which are indicated in Figure 5.5b.

5.4 CASE STUDY III: Land-raise characterization in view of ELFM

5.4.1 Site description and research objectives

The site considered in this case study is part of a large industrial area located near the Brussels-Capital Region. Between 1950 and 1973, several parts of the industrial area were used as landfill, including both licensed and illegal activities. According to historical documents, mainly MSW was disposed. Earlier soil investigations indicated that the landfill activities have resulted in a large-scale contamination of the soil and groundwater with various contaminants (petroleum hydrocarbons, BTEX, PAHs, HMs and volatile chlorinated organic compounds [VOCls]).

A test area of circa 1.6 ha was selected for geophysical investigation through EMI surveying (Figure 5.7). This area was part of a landfill for which operation was licensed between 1964 and 1973. The license for the last two years of this period prohibited disposal of MSW, only disposal of commercial waste and bulky household refuse was permitted. No information is available on possible levelling works performed at the time of or after closure of the landfills. The area currently has an elevation that is about 4 m higher than its surroundings (Figure 5.7b), so the landfill actually involves a land-raise. It is noted that the original elevation of the area was probably even lower than that of the current surroundings, as the area used to be part of a march which was frequently flooded. This presumably was the initial incentive for the (illegal) disposal of household waste and rubble. Furthermore, borehole drillings made during previous soil investigations indicated waste was present down to a depth of over 6 m; no detailed descriptions of the waste composition were provided. Today, the site is used as a parking lot and has a surface cover of asphalt. Close to the eastern boundary of the selected survey area, the industrial site is traversed by high-voltage overhead power lines (150 kV).

The natural geology of the landfill environment comprises four layers. The upper layer occurs to a depth of 3.5 to 5 m and consists in sand of Quaternary origin. The layer below is composed of Tertiary fine sand and has a thickness of up to 8 m. Underneath, a more heterogeneous layer with a clayey-sandy texture is found. The natural soil material thus exists in both sandy and clayey sediments. The groundwater level has been reported to fluctuate around 2.5 m depth; yet this refers to the non-raised surface level. Measurements in monitoring wells, installed during earlier investigations, indicated the groundwater level was at a depth of about 6 m in the area selected for the EMI survey. Furthermore, earlier studies of the groundwater

movement direction suggested interaction between the water dynamics in the landfill and the surrounding surface and groundwater systems may be restricted.

The EMI survey was requested for by OVAM, to serve as a test case on the use of geophysical methods to characterize landfills and the waste materials they contain, with a view to providing input for decision-making on a redevelopment scenario. It was specifically asked to outline volumes of waste present. As the selected area involves a land-raise, it is assumed all material is human-transported. However, part of it may consist of non-waste, soil-like material applied to level the terrain to suit its current commercial/industrial use.

Figure 5.7 (a) Satellite image of the study area considered in landfill case III (source: Google Maps, Imagery ©2015, Aerodata International Surveys, Cnes/Spot Image, DigitalGlobe) and (b) local DTM with the elevation expressed in m TAW (AGIV, 2014), overlaid by the cadastral parcel boundaries, buildings, roads, watercourses, railways and public terrain included in the LRD (AGIV, 2016b). The surveyed area is indicated by the black dotted line.

5.4.2 **EMI survey and data processing**

The EMI survey was performed on February 10, 2015. Because waste had been observed to extend to a depth of over 6 m, the sensor with the largest DOE available was employed for the survey, a DUALEM-421S sensor. Considering the test area's use as parking lot, no limitations on manoeuvrability were imposed. Position data were recorded using a Leica Viva GNSS-G15 differential GPS. A spacing of around 1.5 m was maintained between the parallel survey lines. With the sampling rate of the

sensor set to 4 Hz, the average driving speed of 8.7 km h^{-1} resulted in an average in-line sampling distance of 0.6 m. Within the survey time of 1 h 24 min, more than 18 500 data points were measured.

Overlapping parts of the survey lines were manually deleted from the position data set. The sensor measurement positions were shifted along the driving line to compensate for their distance from the GPS antenna mounted at the back of the quad, following the constrained method presented in Delefortrie et al. (2016). As in case study II, fine-tuning of the shift distance was interfered with by local anomalies, although to a lesser extent. For the PRP coil configurations, a compromise was made on the fancifulness of local extremes and larger scale anomalies (as can be seen in Figure 5.8d), due to the asymmetric sensitivity distribution of these coil configurations (Tølbøll & Christensen, 2007). Small corrections for signal drift were made, reckoning with the magnitude of drift that can be expected for the time surveyed. The data were interpolated to a grid with 0.1 m by 0.1 m cell size through ordinary kriging. The variogram models of the different signals were derived from the Dowd's estimator of the experimental variograms (Webster & Oliver, 2007).

5.4.3 Borehole drillings

The EMI maps were used to select locations for further invasive investigation of the landfill through borehole drillings. The locations were selected so that the bulk range of the observed EMI values was covered and the observations from the collected cores could be used for validation of their interpretation. A direct push machine (Geoprobe Model 7822DT, Geoprobe, Salina, KS, United States) was used to collect continuous soil cores of approximately 5.6 cm diameter down to a depth of 8 m.

5.4.4 Results and discussion

EMI data

The interpolated maps of the EC_a data of all coil configurations and the MS_a data for the 1 m and 2 m HCP coil configurations are shown in Figure 5.8. Some statistics of the EC_a are given in Table 5.4. In the maps, numerous local anomalies of extreme EC_a and MS_a can be observed that coincide in the different signals. As described above, these are characteristic of metallic objects/structures. Some of them resulted from infrastructure installed in or on top of the surface cover layer, such as sewer grates and metal plates overlying drainage channels to reduce the bumpiness of the

surface for truck traffic. Also a linear anomaly of contrasting EC_a and MS_a was visible, the course of which connected different lighting poles; hence, it likely corresponds to an electric cable (Figure 5.8a). Furthermore, the background MS_a reveals some features that are not apparent in the EC_a. The 1 m HCP data show a well-demarcated zone of higher MS_a (Figure 5.8c). The absence of this contrast in the 2 m HCP data suggests it involves higher magnetic susceptible material that occurs in the upper 0.5 m soil layer (De Smedt, Saey, et al., 2014). Note that in this zone the asphalt is darker coloured (Figure 5.7a). Presumably, the asphalt was applied at a different time than in the south and other material was used. Alternatively, the foundation layer(s) were composed of different materials, for instance, rubble higher in brick content. In addition, the MS_a maps show linear features overlapping with the surface drainage channels. These anomalies possibly relate to the underlying subsurface drainage pipes. For example, old drainage pipes often consist of vitrified clay, which has an enhanced magnetic susceptibility.

Outside of the local anomalies discussed above, the EC_a shows distinct variations, laterally as well as vertically, i.e. between the different signals representative of different soil volumes. As can be seen in Table 5.4, the median EC_a systematically increases with the theoretical DOE of the coil configurations. This indicates the subsurface material has an increasing electrical conductivity with depth. An increasing water content is a logical contributing factor, yet, is unlikely to fully explain the magnitude of the increase observed. The low background EC_a values recorded for the 1.1 m PRP coil configuration, with the most shallow DOE (Figure 5.8), fit the expectations for an asphalt layer with a base course (and possibly subbase course) of a construction aggregate, which here likely consists in recycled construction rubble. For the coil configurations with larger DOEs, particularly as from the 4.1 m PRP coil configuration, more structured variations in EC_a are observed (Figure 5.8), suggesting (waste) materials of different nature were disposed. It is noted that the boundaries between areas of low and high electrical conductivity tend to follow straight lines, which may correspond to different landfilling phases. Generally, it is assumed that zones of low electrical conductivity are associated with volumes of rather coarse, largely inert, material such as construction and demolition debris, while zones of high electrical conductivity more likely indicate waste with a higher proportion of organic material as is typical of MSW. However, as discussed in the previous chapter, the electromagnetic signature of landfilled waste not only depends on the nature of the materials originally disposed, but also on the landfill water balance and the occurrence

and progress of processes such as settlement of the waste, and leachate and landfill gas generation (e.g. Bernstone et al., 2000; Meju, 2000). Considering the asphalt sealing and the drainage system installed in the surface layer, direct water infiltration from the surface is assumed to be limited. Nevertheless, the electrical conductivity of the zones filled with MSW probably has been enhanced by the production of leachate – with a high concentration of inorganic salts and OM – from the decomposition of the degradable fraction. Mixing of leachate with groundwater at the base of the landfilled waste volumes may have contributed to the more gradual variations of EC_a in the 4 m HCP signal (Figure 5.8f), the DOE of which approaches the depth of the groundwater level previously observed. Moreover, the existing contamination of soil and groundwater may have influenced the EMI responses acquired. For example, a recent contamination with petroleum hydrocarbons can result in a decrease in the bulk electrical conductivity, due to the insulating properties of these contaminants. On the other hand, biodegradation of petroleum hydrocarbons can cause the electrical conductivity to increase so that a contaminated zone changes into a positive anomaly (Atekwana & Atekwana, 2010). In this case, the latter idea is supported by the earlier observation of groundwater contaminated with petroleum hydrocarbons and BTEX in monitoring wells located in the high conductivity zones in the northeast and south of the survey area.

Table 5.4 Statistics of the EC_a data collected in landfill case study III. Abbreviations: N, number of data points; min, minimum; Q1, first quartile; me, median; Q3, third quartile; max, maximum.

Coil configuration	DOE (m)	N	EC_a (mS m^{-1})				
			min	Q1	me	Q3	max
1.1 m PRP	0.5	18 524	−991.8	24.4	30.2	38.7	846.2
2.1 m PRP	1.0	18 523	−372.8	32.0	37.7	45.9	510.8
1 m HCP	1.6	18 524	−2912.4	36.0	43.0	51.8	557.7
4.1 m PRP	2.0	18 510	−61.5	48.5	56.8	66.1	717.0
2 m HCP	3.2	18 522	−571.9	54.5	63.7	73.8	664.6
4 m HCP	6.4	18 508	−90.7	67.4	76.0	88.7	418.8

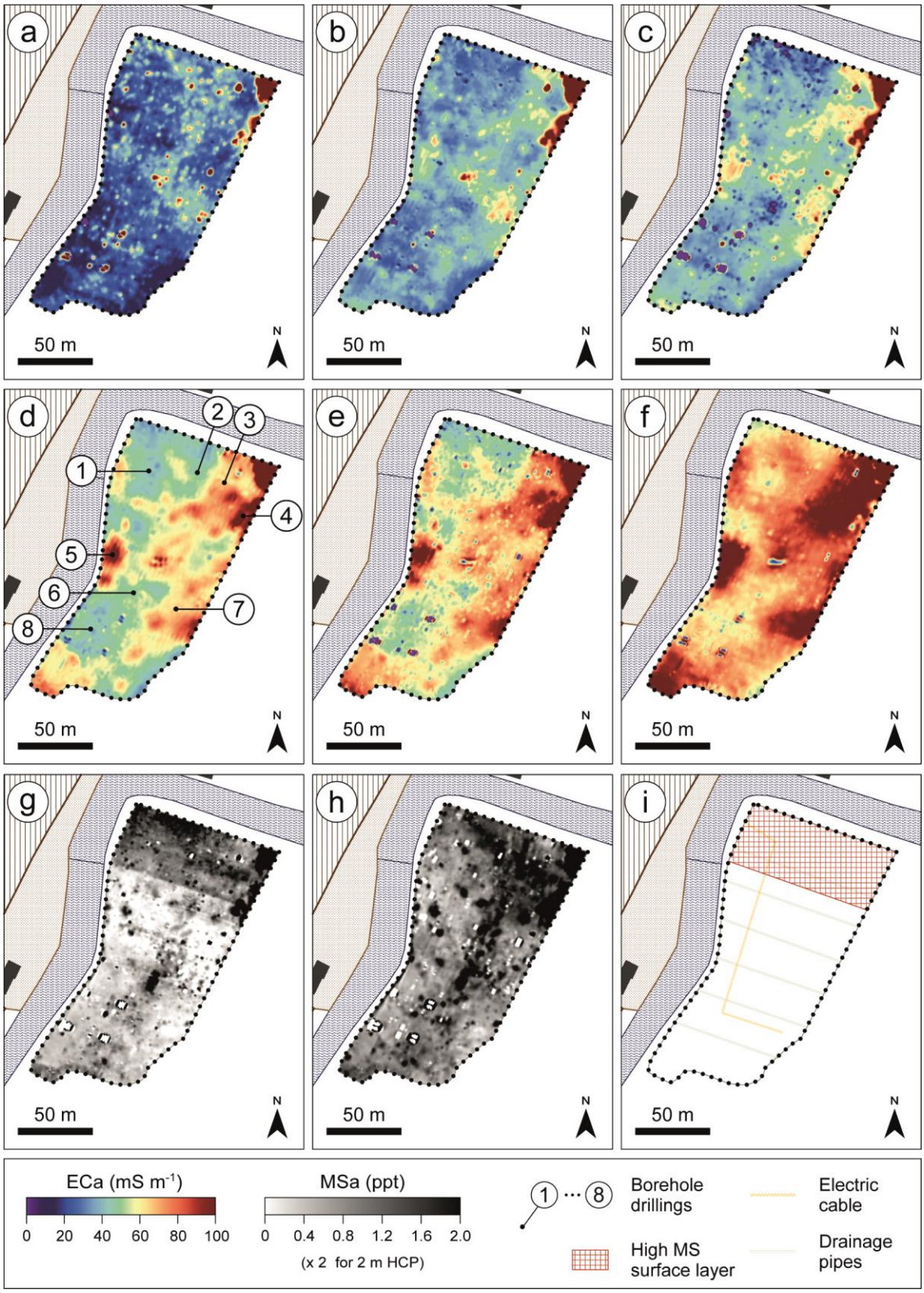

Figure 5.8 Ordinary kriging map of the 1.1 m PRP (a), 2.1 m PRP (b), 1 m HCP (c), 4.1 m PRP (d), 2 m HCP (e) and 4 m HCP EC_a data (f), and the 1 m HCP (g) and 2 m HCP MS_a data (h); on the 4.1 m PRP EC_a map, the eight locations selected for core drillings are indicated. Finally, an overview map of the principal superficial structures identified is given (i).

Validation through borehole drillings

Eight locations were selected for investigation through borehole drilling (Figure 5.8d). Unfortunately, accurate soil profile reconstruction from the collected cores turned out to be difficult. Many liners were largely empty upon retrieval, because the drilling hit coarse stones or a high water content caused the material to fall back out of the liner (Figure 5.9). In non-empty liners the material often had been strongly compressed so that the depth and thickness of the layers observed could be determined only roughly. The severe heterogeneity within the soil cores and the relatively small volumes they encompassed additionally complicated the recognition of the various technogenic substrates encountered, despite consideration of available identification keys, for instance, as provided by Meuser (2010) – a short summary of which also is included in FAO's guidelines for soil description (FAO, 2006). It is clear that there are some caveats to the adoption of the derived soil profiles as "ground truth". Yet, because the site was still actively used, excavations were not possible and borehole drillings were the best achievable option to collect validation data.

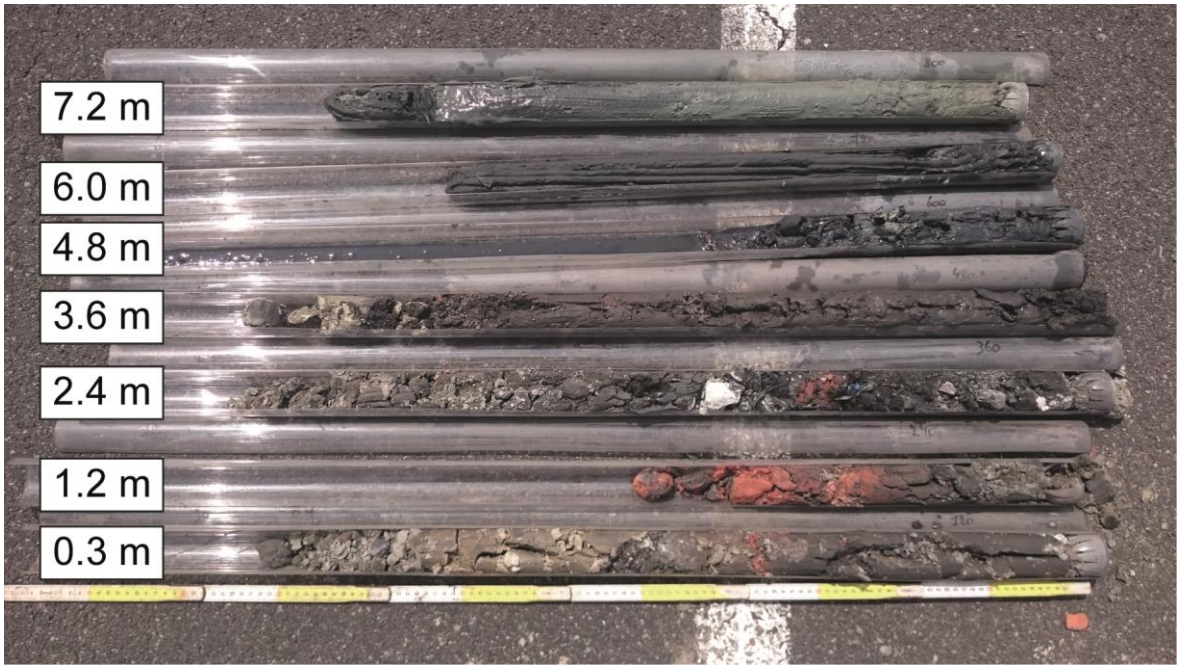

Figure 5.9 Soil cores collected at drilling location 4 down to a maximum depth of 8 m. The labels indicate the start depth of the different liners.

Simplified representations of the profile descriptions are given in Figure 5.10. The crushed stone and sand layers directly beneath the asphalt cover form the pavement foundations. The indication of a crushed stone layer at greater depth generally means the corresponding liner was empty because coarse, stony material was hit. It is possible this involves a construction aggregate such as crushed limestone; however,

slags and ashes with gravelly structure are also plausible, especially when ashes were observed at adjacent depths as well. The legend unit of MSW here refers to the presence of a mixture of two or more typical MSW components as paper and cardboard, textile and glass. Plastics and wood (here mostly fibreboard) are indicated as separate additions. Only a few isolated findings of scrap metal were made, likely because the small diameter of the liners, and therefore metal is not included in the legend in Figure 5.10. With respect to the additions, no differentiation is made for the volumetric proportion a material occupies. Note that some additions also occur as main substrate, for example, wood between 2 m and 3 m depth at location 1, and ashes around 2 m depth at location 7. The indications of odour and petroleum product are based on organoleptic observations only. Mostly, the odour perceived also was assumed to originate from a type of petroleum-derived fuel. Furthermore, the supposed lower limit of landfilled material is marked in the profile representations in Figure 5.10. Yet, they involve a large uncertainty as the soil cores from deepest liner often were incomplete.

Drilling locations 1–4 were situated in the north of the survey area according to a general trend of increasing electrical conductivity from west to east, although it is noted that the measurement values achieved at the exact location of drilling 4 were likely also influenced by a nearby metal anomaly. Location 4 corresponds to an anomaly that shows a relative sign change over the signals of different coil configurations: the anomaly is defined by increased EC_a in all signals except for the 4 m HCP coil configuration. For the EC_a signals with the most shallow measurement depths, 1.1 m PRP and 2.1 m PRP, the trend of increasing conductivity from west to east is supported by a decreasing fraction of more coarsely textures substrates such as sand and crushed stone. At greater depth, at location 1 plastics and dry wood chips were found, which are expected to show only poor electrical conductivity. At locations 2 and 3, presumably low conductive, coarse substrates remain dominant. A notable contrast is observed for location 4, where between a depth of 2 and 5 m a large part of the profile contained an addition of ashes, with considerable volumetric proportions (15–50%). This suggests the ashes may have been determinant for the higher EC_a observed for the signals with larger DOEs. They were likely also responsible for the remarkably higher (leachate) water content retained between 3.8 and 4.8 m depth, which, in its turn, further enhanced the electrical conductivity of the substrate. The DOE of the 4 m HCP coil configuration theoretically covers 70% of the measurement response, which means the subsurface volume below 6.4 m depth theoretically still

contributes for 30%. In practice, the influence of this deeper volume can be particularly significant if it corresponds to a high electrical conductivity. In this case, this means that the petroleum hydrocarbon contamination may have added to a high conductivity as well. This then implies that the contamination has already undergone biodegradation; considering the contamination can originate from the 1960s this is a reasonable assumption.

The profiles observed at locations 5–8 generally showed an even higher vertical heterogeneity than at locations 1–4 (Figure 5.10), making the integrated interpretation of the EMI data and the profile descriptions more complex. Around drilling location 5, the EC_a exhibits the strongest increase with the measurement depth of the signals and, for the 4 m HCP coil configuration, has the highest values as compared to all other drilling locations. The most shallow EC_a signal gives values that can be anticipated for an asphalt surface layer with a base course of crushed stone. The markedly higher EC_a for the 2.1 m PRP coil configuration in comparison with the 1.1 m PRP configuration can probably be attributed to the wet clay layer directly underneath the asphalt foundation. The occurrence of a second asphalt layer around 1.25 m depth "paves the way" for accumulation of water in the upper layer. Based on the substrates found at greater depth, no significantly larger electrical conductivity would be expected than at the other drilling locations, which is contradictory to the EC_a values measured. As for locations 3 and 4, this suggests the existence of a contamination has been of importance. A similar derivation can be made for drilling location 7; besides, ashes were prominently present, which were assumed to be explanatory of the high conductivity values indicated for the surroundings of drilling location 4. At location 8, the opposite is showcased: whereas the consistently higher clay content of the main substrate leads to the expectation of a higher electrical conductivity, relatively low EC_a were obtained. This is another argument for the non-negligible effect of additions in general, and ashes and (petroleum) contamination in specific.

To explain the observed zonation in MS_a, the profiles were compared with respect to the occurrence of brick and ashes, both characterized by a thermally enhanced magnetic susceptibility. At locations 1–4, the layer directly beneath the asphalt base course contained brick fragments, while this was not the case at locations 5–8. Furthermore, at the first four locations a pure brick layer of 10–20 cm thickness, occurring between 1.2 m and 2.0 m depth (not indicated in the soil profiles in Figure 5.10, but visible in the second liner in Figure 5.9), may have added to raised MS_a

values. Alternatively, the asphalt itself has a higher content of magnetic susceptible material as when coarse natural aggregates are (partly) replaced by slag; yet, this was not discernible from the asphalt cores retrieved. An explanation for the differences between the first four drilling locations, and particularly for the patterns observed in the 2 m MS_a, is less evident. Still, brick is present over larger depth intervals at locations 2 and 3 as compared to location 1. That the highest MS_a values were found near location 4 is consistent with the observation of ashes at shallow depth.

5.4.5 **Conclusion**

In this case study, the EMI survey proved an efficient technique to image subsurface variations which were linked to surface and shallow infrastructure, and differences in the nature and condition of the waste material disposed. Comparison of the geophysical data with the observations from the core drillings suggested that not only the type of main substrate – which is largely fixed from the raw waste disposal history – is an important factor in the geophysical signature of the landfill, but also the presence and distribution of contamination such as petroleum hydrocarbons or leachate – which, contrarily, is greatly determined by post-deposition landfill dynamics.

The entire investigated area can be assumed to be occupied with waste. Considering an average waste depth of approximately 6.5 m as derived from the borehole drillings, the land-raise includes a waste volume of at least more than 100 000 m^3. Mainly inert waste was found, which in the case of a landfill mining project could be recycled in the production of building materials. However, the EMI data indicated the quality of the disposed materials is strongly variable and the presence of contaminations will be a necessary point of interest if a waste-to-material scenario is envisioned.

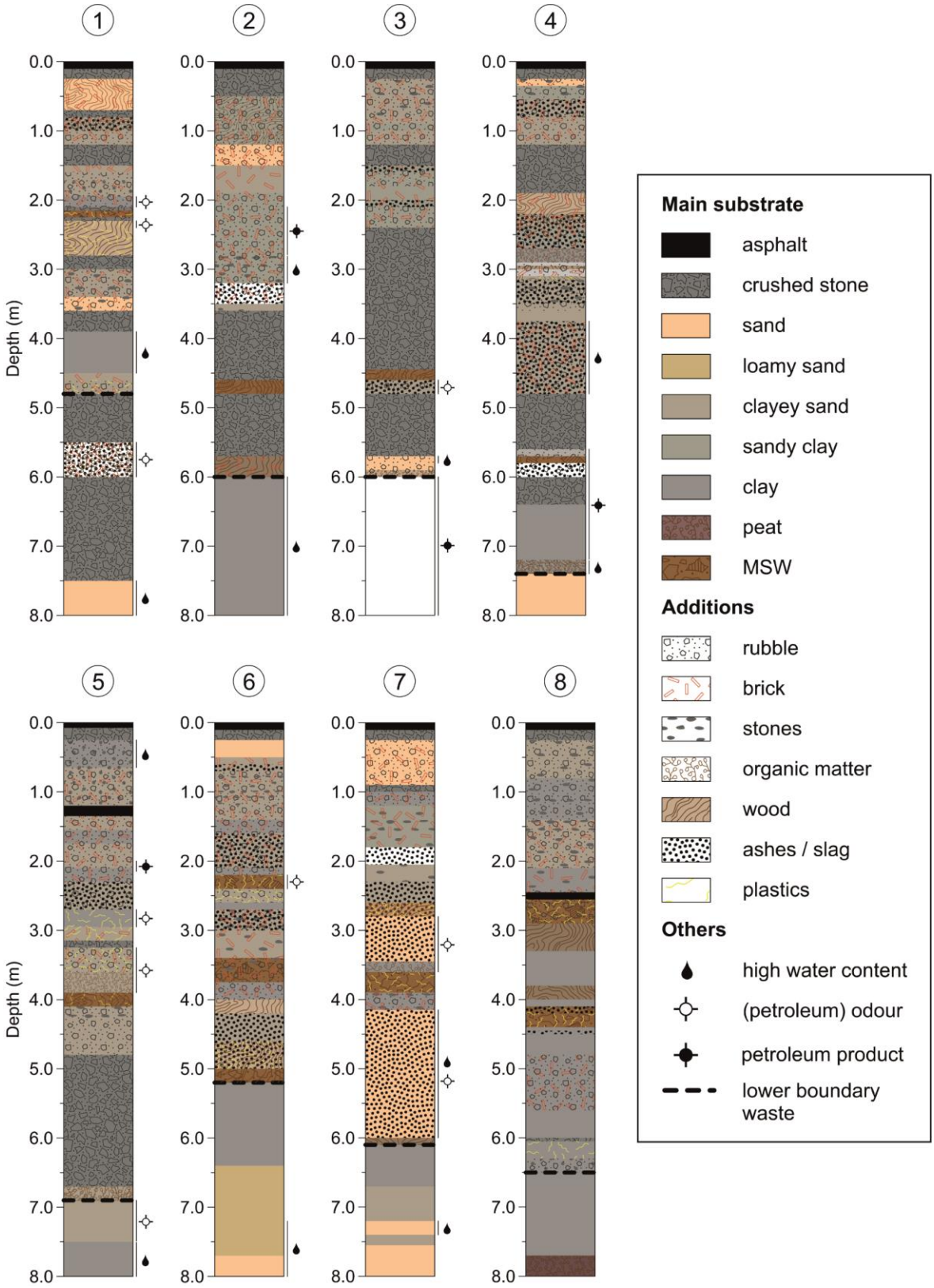

Figure 5.10 Simplified representation of the soil profiles observed at the eight borehole drilling locations indicated in Figure 5.8d.

5.5 CASE STUDY IV: Quarry landfill characterization in view of ELFM[7]

5.5.1 Site description and research objectives

This case study involves a landfill which was constructed in a former sand quarry located in the province of Flemish Brabant, near the Brussels-Capital Region. As the landfill activities resulted in soil contamination with various contaminants (cyanides, HMs, PAHs and petroleum hydrocarbons), between 1999 and 2012 already several environmental assessment studies had been conducted. These studies focused on the inventory of the existing soil contamination and provided little information on the waste that had been disposed. The EMI survey presented here was part of an additional study that specifically aimed at the evaluation of the site's potential for ELFM.

From historical documents such as land register data, environmental permits and aerial photographs, it was evident that the sand quarry consisted in two separate excavation pits with a total area of approximately 10 ha. The contours of the pits as derived from historical information are indicated in Figure 5.11. The first permit for exploitation of the quarry was granted at the end of 1958; yet, an aerial photograph from 1951 already shows activity in the western zone (southern part of survey zone 4 in Figure 5.11b). Sand and material of miscellaneous origin was used for backfilling. Although it was difficult to distinguish between actual quarry exploitation and landfilling activities on the old aerial photographs, it was suspected that backfilling with waste occurred from the end of the 1970s to the end of the 1990s, when the quarry/landfill was closed. A permit for operation of a landfill at the site could not be found and no records are available on the amounts and types of waste disposed. Yet, in the available environmental assessment reports it is suggested the landfilled waste mainly consisted in inert CDW. The historical analysis was complicated because of changes in official parcel boundaries during the active period of the quarry and discrepancies between parcel boundaries and practical land use boundaries, as also evidenced by

[7] This case study was presented at the 3rd International Symposium on Enhanced Landfill Mining, Lisbon, Portugal, 8–10 February 2016:

Van De Vijver, E., & Van Meirvenne, M. (2016). Delving into the potential of multi-receiver electromagnetic induction surveying for enhanced landfill exploration in view of ELFM. In *Proceedings of the 3rd International Symposium on Enhanced Landfill Mining* (pp. 179–191). Lisbon, Portugal.

the current situation (Figure 5.11a). This adds some uncertainty to the derived estimation of the location and (lateral) extent of the landfills and, hence, of the potential resources that could be recovered through ELFM.

As it is an objective of this study to verify the landfill boundaries supposed from historical analyses, the study area was defined more widely and also included fields outside these boundaries which could serve as reference for the geophysical response of the natural soil in the area. In total, the study area covered more than 50 administrative parcels and an almost equally large number of (both public and private) land owners and users were involved. At present, the major part of the area is used agricultural land (Figure 5.11a). The eastern zone mainly consists of grassland. The larger parcels in the western zone are divided into pastures, while the smaller parcels are being used as vegetable gardens. The field in between the two former sand pits is used as arable land. According to the regional zoning plan, most of the study area belongs to a buffer zone.[8] The remainder is residential area. The environment is characterized by a slightly undulating topography. In the eastern part of the study area, the reconstructed landscape simulates a natural look. In the western part, elevation differences are less pronounced. However, over the entire area, and particularly along (former) parcel boundaries, local abrupt changes in elevation occur, which likely relate to the former landfill activities. In the western zone (along the north-west boundary of survey zone 2), bare parts of the soil surface with a blue-grey colour revealed the presence of a cyanide contamination, which suggests the landfill also includes IW. This contamination was characterized by previous descriptive soil investigations. Furthermore, recently disposed waste (e.g., vehicle parts, tyres, plastics, construction debris) was observed along the boundaries of and within the western quarry zone, indicating the site currently remains a popular illegal dumping area.

[8] A buffer zone refers to a green corridor serving as a transition zone between areas with a conflicting use or which have to be separated from each other on behalf of a proper local environmental planning. (Koninklijk Besluit van 28 december 1972 betreffende de inrichting en de toepassing van de ontwerp-gewestplannen en de gewestplannen [Royal decree of 28 December 1972 on the establishment and application of the draft regional zoning plans and the regional zoning plans], 1972).

Figure 5.11 (a) Satellite image of the study area considered in landfill case IV (source: Google Maps, Imagery ©2015, Aerodata International Surveys, Cnes/Spot Image, DigitalGlobe) and (b) local DTM with the elevation expressed in m TAW (AGIV, 2014), overlaid by the cadastral parcel boundaries, buildings, roads included in the LRD (AGIV, 2016b), and digitized field roads and pathways. The seven separate survey zones are outlined by black contours.

According to the geological map of Belgium, two main layers are discerned in the local stratigraphy. The upper soil layer of around 1 m thickness is made up of Quaternary sand or loam. The layer below, extending to a depth of 70 m, is part of the Middle Eocene Formation of Brussels and consists of calcareous sand with concretions of calcareous sandstone. The groundwater table in the area is situated at a depth of 12–13 m.

As mentioned above, the EMI survey served to aid evaluating the landfill's potential for ELFM. The main objectives were (1) to derive the location and extent of the two landfill parts corresponding to the two former quarry pits, and (2) to map possible variations in the nature of the disposed (waste) materials.

5.5.2 **EMI survey and data processing**

The EMI survey was conducted using a DUALEM-421S sensor, with the deepest available maximum DOE of 6.4 m. In one of the previous investigations in the western zone, a deeper drilling had indicated waste was present down to 11.5 m depth. Hence, it was anticipated that the EMI data would not allow for vertical delineation of the landfill, at least not in the western part.

The fieldwork was spread over three days and, constrained by the current land use, consisted in the survey of seven separate zones (numbered in chronological order of survey in Figure 5.11b). The zone corresponding to the eastern pit of the former sand quarry was surveyed on the 2nd of December 2014. The utmost eastern parcels are used as garden area and were not covered because of the limited manoeuvrability for the mobile sensor platform. The elongated piece of land presumably north of the quarry pit, between the unpaved track and the small forest, also was included in the survey as it could represent an area of relatively undisturbed soil. In the western part of the study area, EMI surveying was performed on the 18th of February and 4rd of March 2015. Also here, a few smaller parcels were excluded due to practical reasons of accessibility. Only on the 30th of July 2015, after wheat harvesting, the study was supplemented with the survey of the arable field in between the two former quarry pits. For this field, historical analysis revealed no indications of former landfill activities. Hence, this field was considered a reference for the natural soil in the area, though it had been influenced by agricultural use.

The survey area was scanned along parallel lines that were 1.5 m apart. For the major part of the survey (zones 1–6), sensor data were recorded at a rate of 4 Hz. An average driving speed of 7.1 km h^{-1} resulted in an in-line distance between two

measurements of 0.5 m. In the arable field, less spatial variation was expected and, as an experiment, the sampling rate was set to 8 Hz. The average driving speed was nearly the same, so that the in-line resolution was halved. The survey statistics for each separate zone are given in Table 5.5. Although the eastern zone in practice also was surveyed in different parts, according to the area's composite shape, the data were merged into one survey zone (zone 1) corresponding to the common calibration line that was collected. During acquisition of the calibration line, the soil temperature at a depth of approximately 10 cm was measured using a UMP-1 BT sensor (Umwelt-Geräte-Technik GmbH, Müncheberg, Germany) near the centre of the survey zone, to enable correcting for the temperature difference among the different survey times (Table 5.5).

Table 5.5 EMI survey statistics for landfill case study IV, overall and for each separate survey zone. The number of data points (N) is the minimum number of remaining data points after data processing of the four coil configurations. Note that the sampling rate was 4 Hz in zones 1–6 and 8 Hz in zone 7.

Zone	Area (ha)	Median driving speed	Survey time	N	Topsoil temperature (°C)
1	2.41	6.7	2 h 52 min	40 609	12.05
2	0.62	7.6	49 min	10 913	8.97
3	0.52	8.1	36 min	8 016	8.07
4	1.27	6.8	1 h 36 min	21 946	9.20
5	1.20	7.2	1 h 22 min	18 601	8.36
6	0.73	7.8	49 min	11 174	8.33
7	3.16	7.1	3 h 40 min	100 145	18.23
Total	9.93		11 h 44 min	211 404	
Weighted mean		7.1			

Processing of the EMI data started with clearing the survey data sets of artefacts and redundant parts. In zone 1, the southern turns of the north-south oriented survey lines covering the reference area were trimmed to eliminate overlap with the straight, east-west oriented survey lines of the southern adjoining survey part. Furthermore, a single survey line near the south-eastern corner of zone 1 was removed, because it appeared to have suffered from interference. For the other survey zones, data removal was limited to a few overlapping survey lines. In northern part of survey zones 4 and 5, some instability was observed in the signals of the PRP coil

configurations (most clearly visible in the 4.1 m PRP configuration, Figure 5.13d). This was attributed to the rough surface conditions created from a large number of molehills, which were responsible for high-frequency changes in the pitch and roll of the sensor sled. A similar phenomenon occurred in the northern part of the arable field, where ploughing had left a very rugged surface. However, as the amplitude of this local noise was subordinate to that of more structured variations and its origin could easily by explained, the affected parts of the data were preserved in further processing.

Shift correction was again performed through the kinematic-constrained combination method proposed by Delefortrie et al. (2016). In survey zone 1, a typical time lag comprise had to be made for variations existing at different spatial scales. For the PRP coil configurations, the striping pattern arising from bidirectional surveying could not be fully eliminated (Figure 5.13). In survey zones 2 and 4–6, shift correction was hampered by the large number of strong local contrasts, part of them presumable related to metallic objects or structures. Therefore, the selection of the most appropriate time lag for shift correction relied on the choices made for survey zone 1. Furthermore, to provide full coverage of fancifully shaped survey areas, such as zones 2 and 5, the driving pattern often departs from the proposed parallel survey lines, which can additionally complicate data processing. This is particularly the case when combined with strong local anomalies; remind that the EMI response of metallic objects depends on their orientation with respect to the sensor (e.g. Everett, 2013). In survey zone 3, on the other hand, shift correction suffered from exactly the opposite: the lack of pronounced background variability provided only a poor basis to eliminate the shift between adjacent survey lines. Here, the variation induced by approaching the metal fences bordering the survey area received considerable weight in selecting the time lags. Each of these events also had to be reckoned with in correcting the data for drift in time according to Delefortrie, De Smedt, et al. (2014). Moreover, due to the composite geometry of zone 1 and the variable main driving direction over its different parts, there was a considerable deviation from a consistent (optimal perpendicular) angle between the survey and calibration lines, which had an obvious effect on their comparison for estimating possible drift. Nevertheless, apart from the generally broader range of calibration-survey differences caused by local anomalies (particularly in the northern part of the survey zone), normal drift patterns were observed. For zones 2–6, the survey time was too short to support proper drift evaluation and, particularly for zone 3, care had to be taken not to confuse the influence of metal

fences with drift (as discussed in case study II). For these zones only small corrections were made using simple, smooth spline fits. The presumed reference zone 7 showed the typical drift as expected for non-disturbed agricultural fields, such as the illustrations given in Delefortrie, De Smedt, et al. (2014). The procedure corrects for drift over the time period spent on the survey part corresponding to a separate line and, hence, implies only a relative calibration. It does not make up for possible long-term drift effects, for instance, due to different weather conditions on different survey days. This was partly compensated for by standardizing the measured EC_a values to a reference temperature of 25°C using the formula presented in Sheets and Hendrickx (1995).

For visualization, the EMI data were interpolated to a 0.1 m square grid by performing ordinary kriging. To cope with the numerous local outliers Dowd experimental variograms were preferred (Webster & Oliver, 2007). For calculation of the variogram and subsequent interpolation, the EMI signals of different survey zones were grouped based on the frequency distribution (see Figure 5.12) and the nature of the spatial variation as displayed by the point data location maps. Four groups were identified: (i) zone 1, (ii) zones 2 and 4–6, (iii) zone 3, and (iv) zone 7.

5.5.3 **Borehole drillings and trench excavations**

To verify and complement the information from the historical analysis and EMI survey, (additional) borehole drillings and test pit excavations were planned. The first were primarily oriented to determine the lateral and vertical boundaries of the landfilled waste masses, while the second were focused to the landfill's internal structure and characterization of the waste. As the surface cover layer was anticipated to be limited in thickness, the drillings for lateral delineation were conducted manually, by use of an Edelman auger. The intended maximum depth was about 3 m. The deeper drillings aiming for vertical delineation were performed with a direct push machine (similar to that used in case study II). They were continued in depth until the natural sand(stone) substrate was reached. The trenches were dug with a crawler excavator (Atlas TC 225, Atlas GmbH, Ganderkesee, Germany) and covered volumes of approximately 6.5 m in length, 2.5 m in width, and 6 m in depth. From a few typical substrates, samples were collected to analyse the electrical conductivity of a 1:5 soil:water extract (EC_e) in the laboratory using an Orion conductivity meter, model 150 (Thermo Electron Corporation, Beverly, MA, USA). In addition, the soil texture of the samples was determined according to the sieve-pipette method (International

Organization for Standardization [ISO], 2009). However, considering the expected high $CaCO_3$ content of the natural soil and the alternative nature of waste derived substrates as compared to standard soil, it was preferred not to disperse the soil aggregates by removal of $CaCO_3$ and OM. Sample preparation only included air drying and sieving to separate the coarse fraction (>2 mm). The $CaCO_3$ content is determined by mixing the soil with a known amount of H_2SO_4, followed by titration with NaOH to measure the amount of H_2SO_4 that did not react with $CaCO_3$. Also the TOC content was analysed according to the method of Walkley and Black (1934); yet, only significant results will be reported. Very coarse and/or visibly contaminated substrates were not sampled due to their poor compatibility with standard soil analysis procedures. However, the contamination-suspected substrates were sampled and analysed by order of the environmental consultant in charge.

5.5.4 **Results and discussion**

EMI data

The frequency distributions of the EC_a data are visualized by box-plots in Figure 5.12. The kriging interpolations of the EC_a of all signals and the MS_a of the 1 m and 2 m HCP coil configurations are shown in Figure 5.13. Both illustrate the large variation in electrical conductivity and magnetic susceptibility suggesting considerable variation in subsurface materials and conditions over the study area. The magnitude and spatial scale of the variations are markedly different in different parts of the area – which served as basis for the stratified interpolation of the data. In the central arable field (zone 7), the EC_a is overall low and varies in a smooth way, except for the above-mentioned high-frequency noise in the north. Disregarding the few local anomalies, the EC_a for each of the separate coil configurations has a very narrow range; the interquartile range increases with the DOE, from 1.9 mS m^{-1} for the 1.1 m PRP coil configuration to 5.5 mS m^{-1} for the 4 m HCP coil configuration (Figure 5.12). Also in terms of MS_a the field is quasi homogeneous as compared to its neighbours. Thus, the geophysical signature of this field meets the expectation for a dry, predominantly sandy soil, which justifies its use as reference for an undisturbed subsurface.

In the eastern part of the study area (zone 1), the EMI data are significantly more heterogeneous, giving a first indication of the presence of landfilled (waste) material (Figure 5.12 and 5.13). A large number of local anomalies are observed that are demonstrative of metal objects, such as pieces of rebar in construction debris. These metal anomalies are also abundant in the piece of grassland in the north, outside the

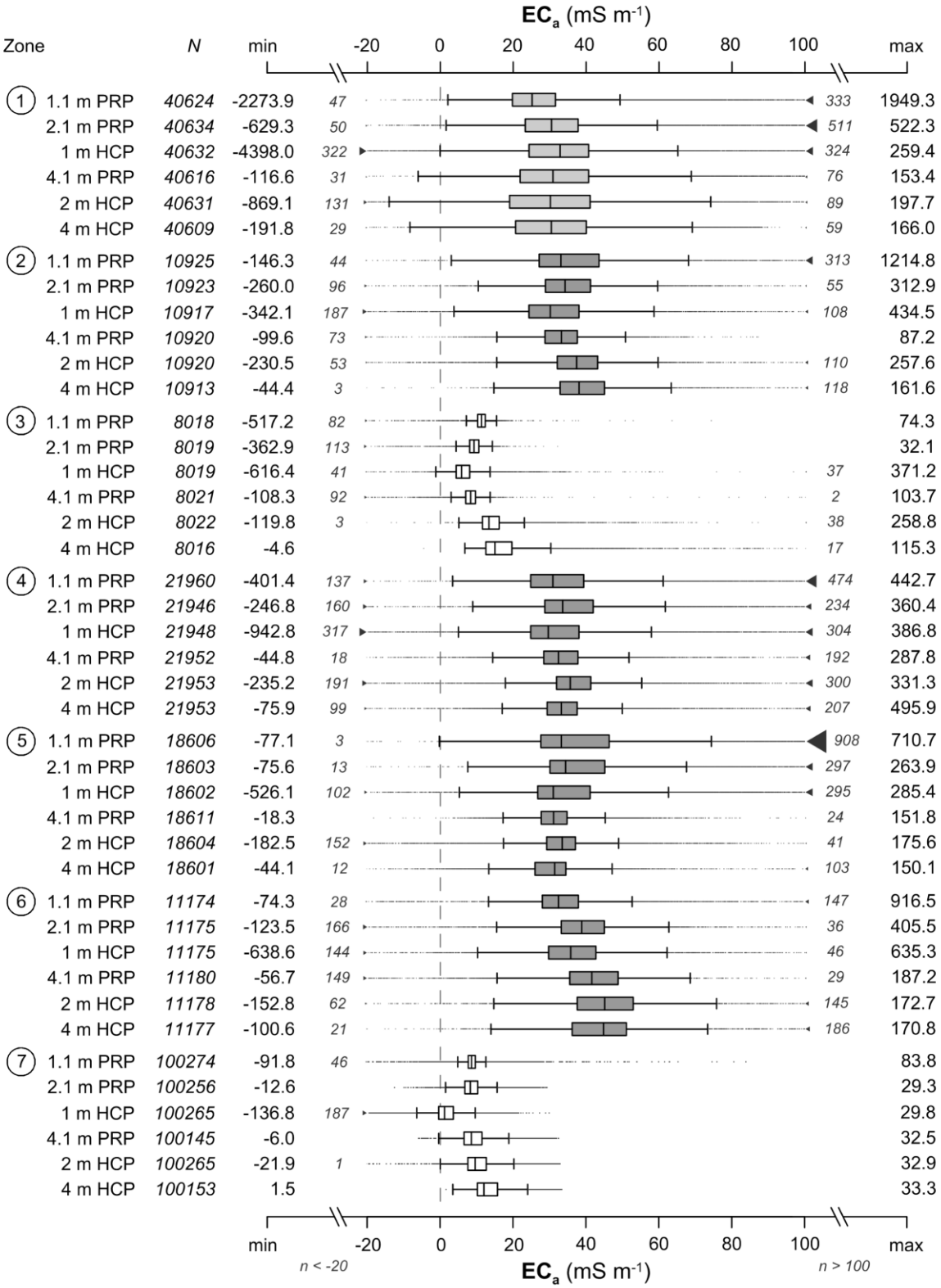

Figure 5.12 Box-plots of the EC_a data for each of the DUALEM-421S measurement signals collected in the seven separate survey zones. The whiskers correspond to the quartiles plus and minus 1.5 times the interquartile range. For each separate data set, the number of data points (N) and the minimum (min) and maximum (max) EC_a are given, and the number of data points outside the range of the EC_a axis ($n < -20$ mS m^{-1} and $n > 100$ mS m^{-1}).

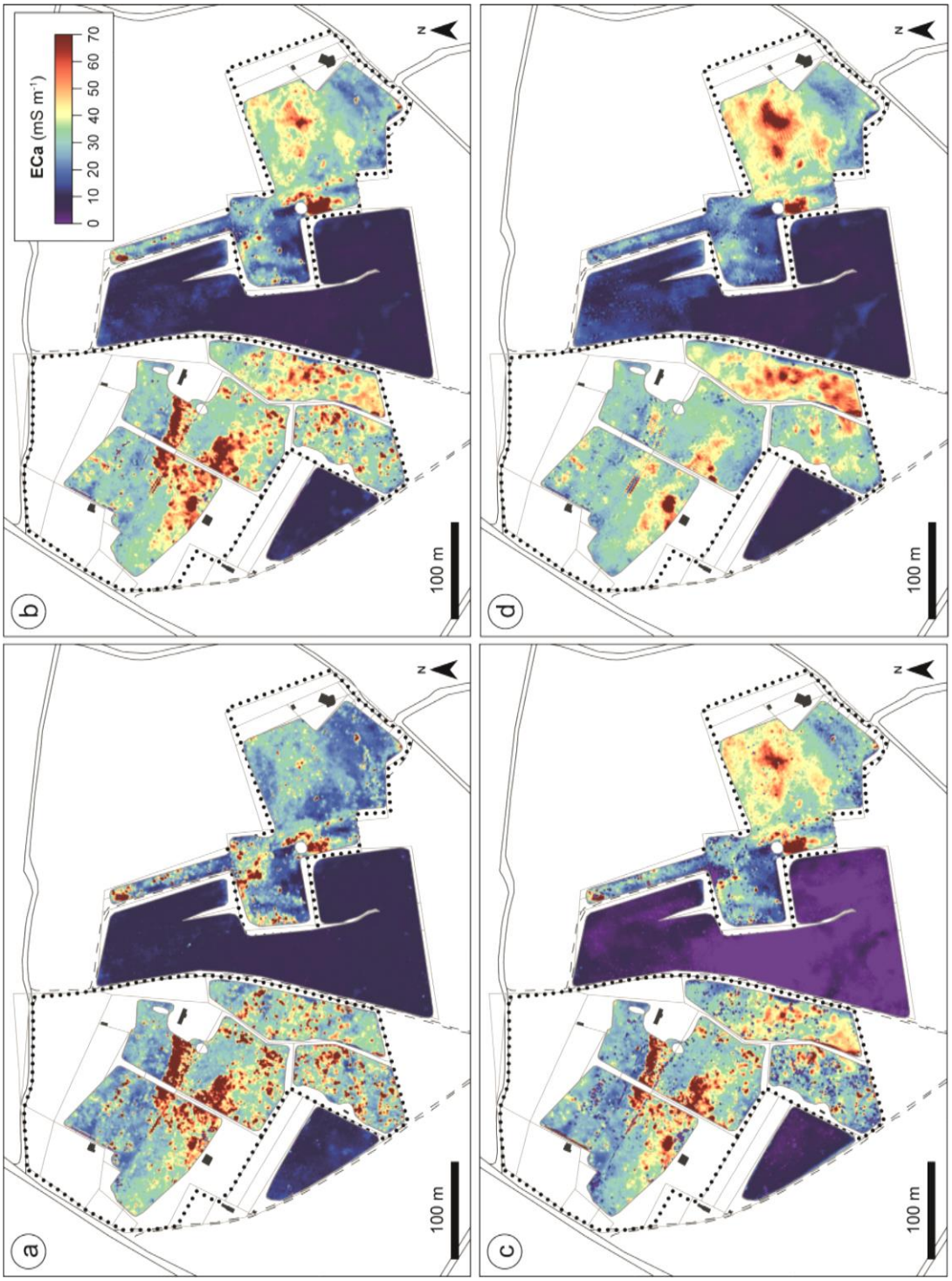

Figure 5.13 Ordinary kriging map of the 1.1 m PRP (a), 2.1 m PRP (b), 1 m HCP (c), 4.1 m PRP (d), 2 m HCP (e) and 4 m HCP EC_a data (f), and the 1 m HCP (g) and 2 m HCP MS_a data (h).

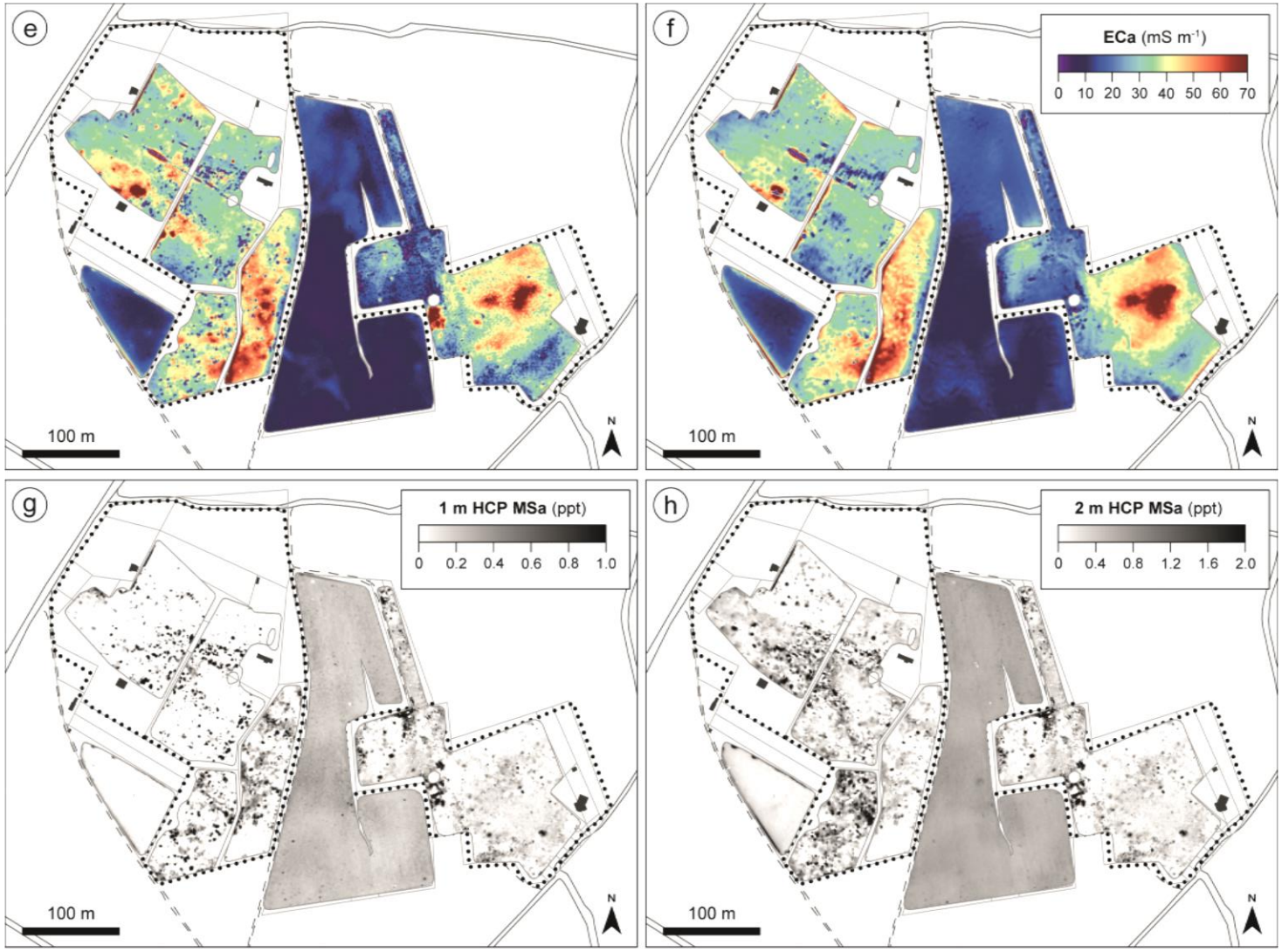

Figure 5.13 (continued) Ordinary kriging map of the 1.1 m PRP (a), 2.1 m PRP (b), 1 m HCP (c), 4.1 m PRP (d), 2 m HCP (e) and 4 m HCP EC_a data (f), and the 1 m HCP (g) and 2 m HCP MS_a data (h).

former quarry/landfill as inferred from historical data. This compromises its use as "blank" area. Possibly, this soil disturbance stems from more recent illegal waste disposal. Aside from discrete metal anomalies, confined clusters of these anomalies occur (Figure 5.14). Comparison with old aerial photographs learns that the cluster in the north, along the presumed landfill boundary, coincided with a former access road for transport of quarry sand and waste to be landfilled (which to the north extended to the still existing field road). An plausible explanation is that metal-containing construction debris was deposited to provide extra stability. Likewise, the metal cluster along the current walkway suggests construction debris was deliberately installed for traffic related to the former landfill activities, or the recent agricultural activities, although there was no terrain evidence to support this. In addition the emphatic presence of metal anomalies, the background EMI signature of the eastern landfill area is clearly different from that of the natural soil as represented by the central arable field, with the electrical conductivity and magnetic susceptibility being consistently higher. According to these background variations, three distinct landfill zones can be distinguished (Figure 5.14). In the north (subzone 1), the relatively lower electrical conductivity suggests inert materials such as (non-reinforced) concrete and brick are predominant (e.g. Boudreault et al., 2010), which would agree with the historical information. A further division of this subzone could be made as indicated by the dashed line in Figure 5.14. This probably corresponds to different phases of mining and backfilling with waste and/or corresponding temporary roads. In the east, an area with markedly higher electrical conductivity defines a second subzone. As discussed in the previous chapter, this can be explained by a higher organic waste fraction – and a correspondingly higher potential for biological waste degradation, leading to the production of leachate – as is commonly the case for MSW, or by the presence of certain types of IW that induce higher levels of TDS and thus higher salinity. Yet, the electrical conductivity values are too low to correspond to metalliferous slag or ashes. The southern part represents a third landfill zone (subzone 3), with properties that tend to be similar to those of the upper northern part (subzone 1).

The utmost south-western parcel that was surveyed (zone 3) shows a comparable geophysical signature as the arable field: a very low electrical conductivity characteristic of a dry sandy soil. This provides a confirmation of the location of the western boundary of the landfill site as assumed from historical analysis. Within the supposed boundaries of the western landfill area, the EMI data demonstrate the

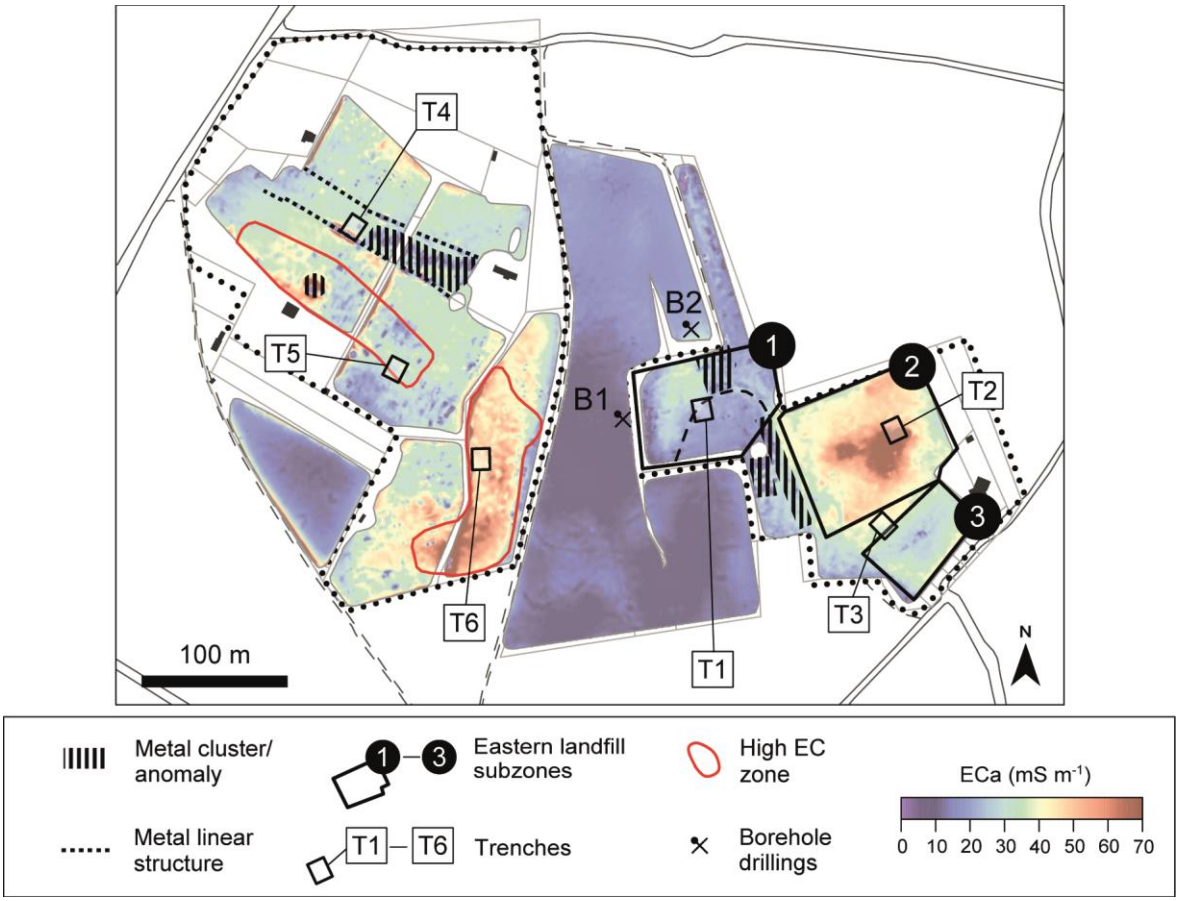

Figure 5.14 Ordinary kriging map of the 4 m HCP EC_a data with indication of the main clusters of metal anomalies, the three subzones in the eastern landfill part, and the two zones with (shallow) high-conductive material in the western part. Also the selected locations for two borehole drillings in the central reference field and for six trenches spread over the two landfill parts are given.

subsurface is even more heterogeneous than the eastern area. Particularly in the south, a large number of metal anomalies is observed. In the north, two linear structures of a metallic nature are indicated (Figure 5.14). These likely correspond to superficial remnants of fences from a former partition into pastures; that the southern structure aligns with parcel boundaries further supports this assumption. Between the linear structures, the strong responses of both EC_a and MS_a suggest another cluster of metallic objects occurring at shallow depth. The landfilled materials generally appear to have a higher electrical conductivity than the natural soil material (Figure 5.12 and 5.13). Contrary to the eastern landfill area, no clear zonation can be discerned. Yet, two zones with higher electrical conductivity can be delineated (Figure 5.14). The first is located south of and roughly runs parallel with the southern linear metal structure. A higher EC_a is observed for the EMI signals with a DOE of maximum 3.2 m (1.1 m PRP to 2 m HCP); in the deepest EC_a signal (4 m HCP) the contrast is faded. This indicates more conductive material does not occur over the entire depth

profile but only in the upper few metres. The presence of CDW or IW leading to an increased salt content is a possible explanation. A notably large metal anomaly is located in the middle of this zone (Figure 5.14). This probably pinpoints the location of a large metallic object such as a storage drum. The second high conductivity zone largely coincides with the south-eastern parcel comprised in the western landfill area (zone 6). Here, the higher values are shown in all EC_a signals except for that with the most shallow measurement depth (1.1 m PRP), which situates the responsible conductive material at a greater depth.

Validation through borehole drillings and trench excavations

The borehole drillings were carried out on the 6th of May 2015. The locations of the manual drillings were selected based on the lateral boundaries as derived from historical analysis and the EMI survey. In total, 17 manual boreholes were made, 15 of which were located in the eastern part of the study area, as this area had not been considered in previous soil investigations. Nine drillings were spread just along the outside of the presumed eastern landfill boundary to verify its shape; six covered the inside. In the western area, only two additional were made: one aiming to validate the southern boundary of the quarry/landfill pit and one located in the parcels used as vegetable garden (surrounded by survey zones 2, 3 and 5). The absence/presence of waste in the observed soil profiles corroborated the assumed boundaries of the two landfill zones. Figure 5.15 gives the soil profiles of two borehole drillings (B1 and B2) located in the central arable field, representing the local natural soil. Their exact locations are indicated in Figure 5.14. Both profiles evidence a loamy sandy topsoil and a sandy subsoil, which is also supported by the clay content determined for the four samples taken at these locations. The electrical conductivity was generally low in the arable field; yet, the EC_a values are, relatively, far lower (~0 mS m^{-1}) near the location of B1 than around B2. This can be attributed to the higher degree of cementation as revealed by the presence of sandstone. On the contrary, both samples from B1 had a higher EC_e than the samples from B2. Soil extracts were derived from the <2 mm fraction and the significantly higher $CaCO_3$ content at B1 (over 30% at 1.6–2.6 m depth) produced a higher solution electrical conductivity.

Five mechanical drillings served to make an estimation of the landfill depth. Two drillings were made in the eastern zone, one in landfill subzone 1 and one in subzone 2. The first drilling was interrupted at a depth of 3.8 m due to the presence of impenetrable material. In the second the natural substrate was reached at a depth of 17.3 m. Accounting for the variation in elevation, the average depth of the eastern

landfill zone was estimated at around 15 m. The three drillings in the western zone were located in survey zones 4 and 5. In these respective zones, waste was observed down to depths of 11.4 m and 13.2 m, with an average of 12.3 m.

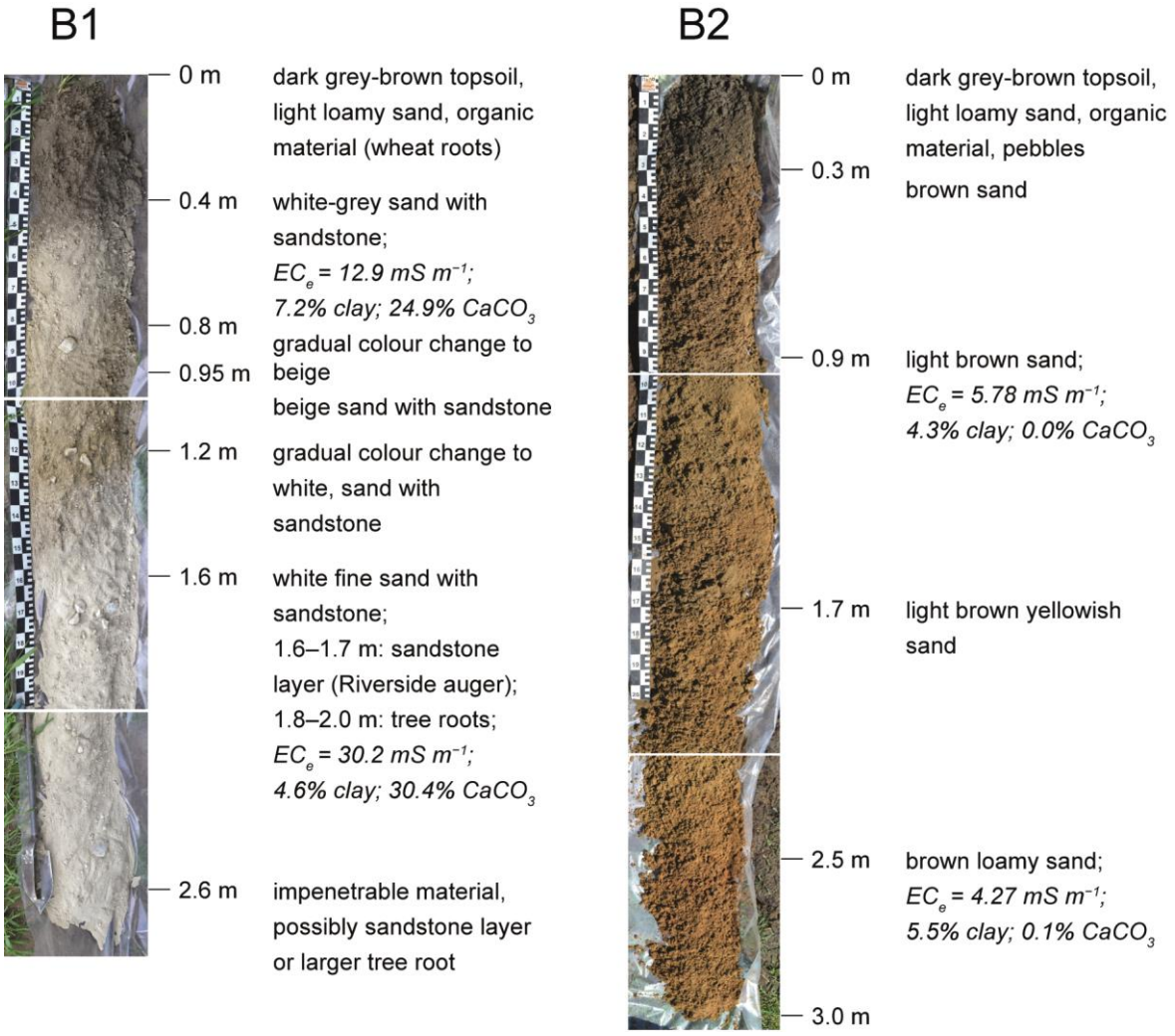

Figure 5.15 Description of soil profiles observed at two manual drilling locations indicated in Figure 5.14, including the laboratory analysis results of EC_e, clay content and $CaCO_3$ content of four selected samples.

Trench excavations were conducted on the 23rd of April 2015. Six locations were selected to validate the contrasts observed in the EMI data (Figure 5.14). Illustrated descriptions of the observed profiles are given in Figures 5.16, 5.17 and 5.18. The descriptions are aligned with a scaled depth axis; there might be some discrepancy between the (apparent) depth in the descriptions and in the photographs, due to the perspective in the latter.

The first trench (T1) was dug in the subzone characterized by low conductivity (subzone 1). The upper layer consisted in sand-loam and had a thickness of about 0.6 m. Underneath a layer of white calcareous sand was found, which closely resembled

the naturally occurring material as observed in the subsoil at borehole drilling B1 (Figure 5.15). Between 1.2–4.0 m depth, a layer of chiefly inert construction debris was observed. A considerable part of the debris was relatively fine-grained, although also very large pieces of (reinforced) concrete (>1 m diameter) and brick wall fragments were included. This type of coarse material probably explains why the mechanical drilling in this zone had to be stopped prematurely. Underneath the waste layer, white sand was again observed. From around 5 m depth, a bluish black colour of the sandy material and a smell of heating oil suggested contamination with a petroleum product. As the excavation was terminated at 5.9 m depth, the (vertical) spread of the contamination could not be accurately verified; yet, from the concentration pattern of the staining it was suspected the contamination had a limited extent. The contamination was confirmed by laboratory analysis of a sample taken by the environmental consultant: the total petroleum hydrocarbon (TPH, C10–C40), ethylbenzene and xylene concentrations exceeded the respective soil sanitation thresholds.[9] For both sand layers, the similarity with the natural soil material was supported by texture analysis. This indicated that the sand exploited in the quarry also was used as (intermediate) waste cover material. The sequence of sandy layers and inert construction debris is consistent with the generally low EC_a values observed in this subzone, while some large pieces of reinforced concrete provided an explanation for the local metal anomalies. For the uncontaminated sandy layers, the low conductivity also is evidenced by the laboratory measurements of EC_e. The sample taken from the contaminated layer, however, had a remarkably high EC_e. Considering its texture is comparable to that of the above-lying sandy layers, it can be concluded that the contaminants had a significant contribution to the electrical conductivity of the soil extract. The contaminated volume likely was too small to have a visible effect on the EMI sensor data, also because the contamination occurred at a relatively large depth. Notwithstanding the construction debris contained an important proportion of brick, low MS_a were observed. This can be attributed to the low sensitivity of the MS_a signals for larger depths.

The second trench (T2) targeted the landfill subzone with the highest background electrical conductivity (subzone 2). Again, a topsoil of sand-loam was observed, although its thickness was more than twice as large as at T1. The dark coloured layer

[9] In agricultural area, the soil remediation thresholds for TPH is 900 mg per kg dry matter (DM), for ethylbenzene 1.8 mg (kg DM)$^{-1}$, and for xylene 2.7 mg (kg DM)$^{-1}$ (VLAREBO, 2008).

of organic material below, densely interwoven with tree roots, probably represents a former topsoil, which along with its covering vegetation was truncated for the installation of the current surface layer. Underneath, a clay layer of 15–20 cm thickness overlaid a waste layer, which filled the remainder of the excavated profile. As presumed from the EMI data, the waste was of a different nature as observed in subzone 1. Its dark colour and the odour it released suggested biodegradation of organic material has been occurring. Together with the presence of plastic, textile and paper, this evidences a municipal origin of the waste. Yet, brick and stony debris also represented a considerable waste portion. The larger thickness of the sand-loam surface layer, the conductive layers of organic material and clay, and the higher OM content of the waste, which probably had been subjected to biodegradation resulting in the production of highly conductive leachate, all added to a higher electrical conductivity as compared to the first landfill subzone occupied with electrically inert materials of both natural and technogenic origin. However, the conductivity values measured were substantially lower than those generally observed in previous geophysical investigations of "pure" MSW (partly) saturated with leachate (e.g. Abdulrahman et al., 2016; Bellezoni et al., 2014) –note that these studies made use of ERT instead of EMI. In this landfill part, the generation of leachate was tempered by the mixed waste composition of MSW and construction debris. Furthermore, considering the waste deposition dates from a few decades ago, the upper landfill layers, which were primarily measured by the EMI survey, might have reached a more mature biodegradation stage already, in which the generated leachate has already migrated to larger depths. From the MS_a data, or more correctly from the IP data, it seems the waste is associated with higher values of magnetic susceptibility as well. While this may be plausible due to, for instance, the complexation of iron by the organic material and the production of ferromagnetic minerals from bacterial activity – the underlying mechanisms of which are still poorly understood, it cannot be excluded that the IP response was (additionally) enhanced because the true electrical conductivity exceeded the LIN limits. For the 4 m HCP coil configuration the LIN limit is as low as 15 mS m^{-1} (Dualem Inc., 2013).

The third trench (T3) was located at the interface between landfill subzones 2 and 3. Here, the sand-loam surface layer had a thickness of 2.3 m. This was consistent with the higher elevation of subzone 3 as compared to subzone 2. Presumably, a thicker cover layer was installed in view of the reclamation of the corresponding parcels as building area. At greater depth, the northern and southern side of the

trench showed different material, which confirmed the interpretations made from the EMI data. In the north, the waste material found was similar to that found in T2. A sample taken from this substrate affirmed its higher conductivity. The TOC content was 1.6%; although still low in absolute terms, it was the highest of all samples analysed. Between the sand-loam and the waste, a layer of grey material was observed. Although this was not verified in the field, this likely is a (clayey) waste cover layer as the one present at T2, albeit of greater thickness. In the south, the fill mainly consisted in inert construction debris such as brick and mortar, explaining the similarity between the geophysical signatures of subzones 1 and 3. In subzone 3, the slightly higher values measured by the most shallow coil configurations can be attributed to the greater thickness of the sand-loam surface layer.

Trench 4 (T4) was situated north-west of the metal cluster crossing the boundary between survey zone 4 and 5 and intersected the southern linear metal structure (Figure 5.14). An explanation for this linear anomaly was found at a mere depth of 0.1 m: a narrow band of sheep wire (approximately 10 cm in height) remained from a former fence. The EMI anomaly resulting from this wire stretched over a width of several metres, showcasing the overwhelming influence superficial conductors can have. At a slightly greater depth in the sand-loam surface layer, a steel drum of about 200 L was exposed, responsible of one of the metal anomalies observed in the area. From a depth of 1 m, a sandy layer occurred which included a few large pieces of construction waste. Underneath, the predominance of natural soil materials was substituted with a substrate of construction debris. Inert materials such as brick and mortar were the major component, but also wood and plastic were present. The deepest part of the trench was characterized by a similar waste substrate. The layer of white sand at 3.0–3.5 m depth probably represented an intermediate waste cover layer. Overall, the preponderance of inert construction debris matches the low background EC_a near the trench. It can be expected that the landfill part extending north of the linear metal anomaly also principally consists in a mixture of inert waste and natural soil material.

Trench 5 (T5) was excavated in survey zone 5, overlapping the southern edge of the high-conductivity area stretching out over survey zone 4 and 5. Below the usual sand-loam topsoil, with a comparable thickness as in T4, a mixed waste layer was found. In the southern part of the trench CDW was predominant, but in the north organic waste also had an important share, as illustrated by the photograph in Figure 5.18. A remarkable amount of water was seeping out of the layer on the northern side.

Between 1.45 m and 1.6 m depth, a layer of grey material occurred, the strong cementation of which suggesting a high $CaCO_3$ content (Meuser, 2010). Together with the silty to sandy texture of the material, the determination key of Meuser (2010) led to its identification as fly ash. The lack of glass and metal residues suggested an origin of coal combustion. The impervious nature of this layer and, the 10 cm thick clay layer underneath, explained the accumulation of water in the waste layer above. On the north side of the trench, layers of construction debris further alternated with (dark) grey layers of ashes. These layers wedged out to the south of the trench, where a larger proportion of soil-like material was present from a depth of about 2 m. At 4.4–4.9 m depth, waste with an intense blue colour was observed (not visible in photograph in Figure 5.18 due to collapse of material from above-lying layers), which indicated the presence of cyanides; this was afterwards confirmed by laboratory analysis by order of the environmental consultant. Based on the combined occurrence of cyanides and ashes, it could be suspected these were cyanide complexes derived from gas purification as performed at gasworks (manufactured gas plants; Hatheway, 2002). At the bottom of the trench, the waste again mainly consisted in construction debris. Although the blue colour seemed to fade with depth, it was not possible to make an accurate vertical delineation of the cyanide contamination. The variety and complex spatial organisation of the waste found makes it difficult to link the excavation results with the EMI data. The difference in waste type and water saturation in the uppermost waste layer is considered a main factor in the relatively strong EC_a contrast between the northern and southern part of the trench observed in the most shallow measurements signals. The interpretation of the contribution of the ash layers underneath is more tricky. As discussed in the previous chapter, the (extract) EC of (fly) ashes is strongly variable; yet, it was concluded that ashes have the capacity to show high EC because of their generally high TOC content and CEC. Also in case studies II and III, ashes were assumed to have contributed to a higher EC_a. Here, a high conductivity of the ash layers disagrees with the disappearance of the EC_a contrast in the deepest signal (4 m HCP). The dry conditions of the ashes, also due to the impermeable nature of the above-lying layers, provide a plausible explanation. The effect of the cyanide contamination is unclear: or its electric properties did not significantly differ from the surrounding materials, or its volume was too small to have a significant contribution to the measurements of the 4 m HCP coil configuration. Finally, the sixth trench (T6) aimed to uncover the landfill depositions at the origin of the EMI signature observed in survey zone 6. The sand-loam surface layer of 1.2 m

T1

0 m — yellowish brown sand-loam, pebbles
EC_e = 13.0 mS m^{-1}; 14.1% clay; 7.4% $CaCO_3$

0.6 m — white-beige to yellow-brown sand with sandstone, brick fragments (5–10 cm diameter);
EC_e = 12.9 mS m^{-1}; 4.6% clay; 11.3% $CaCO_3$

1.2 m — waste: largely inert construction debris, including brick, concrete, ceramic tiles, metal rebar

4.0 m — white sand;
EC_e = 17.8 mS m^{-1}; 2.5% clay; 10.2% $CaCO_3$

5.0 m — white sand, yellow-orange oxidation stains, bluish black stain with petroleum odour;
EC_e = 255 mS m^{-1}; 9.7% clay; 12.1% $CaCO_3$

5.9 m

T2

0 m — yellowish brown sand-loam, pebbles;
EC_e = 11.0 mS m^{-1};
16.0% clay; 1.15% $CaCO_3$

1.3 m — very dark brown to black organic material, tree roots

1.45 m — light grey clay

1.6 m — dark brown predominantly soil-like material

1.75 m — waste: brick

1.85 m — waste: plastic, textile, paper, brick and stone debris, metal pipes;
odour of decomposing material

6.2 m

Figure 5.16 Descriptions of the profiles observed in trenches T1 (north side) and T2 (south side), the locations of which are indicated in Figure 5.14. The laboratory analysis results of EC_e, clay content and $CaCO_3$ content are also included.

T3

0 m — brown to yellowish brown sand-loam, pebbles;
EC_e = 7.2 mS m^{-1}; 14.3% clay; 0.4% $CaCO_3$

	NORTHERN SIDE	SOUTHERN SIDE
2.3 m	grey (cover) material	waste: grey, cemented construction debris including mortar and brick
2.9 m	waste: dark grey to black, organic material (tree roots), textile, plastic; odour of decomposing material; EC_e = 170 mS m^{-1}; 7.7% clay; 3.8% $CaCO_3$	waste: largely inert construction debris, including brick, mortar, concrete, gypsum, wood, metal rebar

6.2 m

T4

0 m — brown to yellowish brown loamy sand, pebbles; 0.1 m: sheep wire; 0.8 m: metal drum;
EC_e = 7.2 mS m^{-1}; 14.3% clay; 0.4% $CaCO_3$

1.0 m — white sand, large pieces of concrete (>50 cm diameter), metal rod

2.0 m — construction and demolition waste: brick, stone debris, (reinforced) concrete, wood, plastic, metal rods

3.0 m — white sand

3.5 m — construction and demolition waste: brick

4.0 m — construction and demolition waste: brick, stone debris, iron wire, glass, plastic, large piece of concrete (1 m diameter)

6.3 m

Figure 5.17 Descriptions of the profiles observed in trenches T3 (east side on photo) and T4 (south side), the locations of which are indicated in Figure 5.14.

T5

0 m — brown to yellowish brown sand-loam, pebbles; EC_e = 12.2 mS m^{-1}; 12.4% clay; 2.1% $CaCO_3$

0.8 m — waste: brick, stone debris, wood; black decomposing organic material; water seepage (north side)

1.45 m — waste: grey cemented material, presumably fly ash

1.6 m — light grey clay

1.7 m — construction and demolition waste: stone debris, tiles, metal scrap, plastic

3.1 m — waste: dark grey to black, silty to sandy material, presumably fly ash

4.0 m — waste: grey-brown mixture of construction debris and soil-like material

4.4 m — waste: intense blue material, likely cyanides

4.9 m — construction and demolition waste: stone debris, brick, tiles, insulating material

6.0 m

T6

0 m — brown to dark brown sand-loam, few brick fragments, black particles (possibly coal); EC_e = 29.2 mS m^{-1}; 13.9% clay; 0.8% $CaCO_3$

1.2 m — brown sand-loam, few brick and stone fragments

2.0 m — grey clay (discontinuous)

2.5 m — waste: alternating depositions of ashes and construction debris; odour of burnt material

4.1 m — waste: bright white to light grey, cemented material; EC_e = 768 mS m^{-1}; 59.9% $CaCO_3$

4.5 m — waste: dark grey to black, ashes and (partly) burnt material; plastic, textile, paper, wood, metal scrap; petroleum odour; EC_e = 228 mS m^{-1}; 6.1% clay; 15.9% $CaCO_3$

5.9 m

Figure 5.18 Descriptions of the profiles observed in trenches T5 (north side) and T6 (north side), the locations of which are indicated in Figure 5.14.

thickness was darker coloured than at the other trenches. Also the TOC content of 1.1% was relatively high; in the other topsoil layers TOC content only varied between less than 0.1% (T3) and 0.6% (T2). Note that in the photograph of T6 shown in Figure 5.18 the black colour of the upper layer in the north-western corner (left) is due to contamination with material from larger depth. The second layer was composed of very similar material, but slightly more brick and stone fragments occurred. In the north-eastern part of the trench clay was found between 2.0 m and 2.5 m depth; in the south-western part, this layer had a smaller thickness or was even absent. The 2.5–4.1 m depth interval consisted in alternating depositions of ashes and construction debris. Next, a 40 cm thick layer of whitish material was observed, a sample of which demonstrated a $CaCO_3$ content of nearly 60% and an EC_e of as much as 768 mS m^{-1}. The remaining part of the trench was characterized by a very dark coloured waste substrate, including sandy textured, combustion residues as well as coarse municipal and construction waste. Laboratory analysis by order of the environmental consultant confirmed that the petroleum smell of the substrate corresponded with a petroleum hydrocarbon contamination. Also the HMs copper and nickel exceeded the soil remediation threshold.[10] The exact composition of this substrate could not be determined based on visual observations, but laboratory analysis indicated it represented highly conductive material (EC_e = 228 mS m^{-1}). Like T5, T6 contained a complex combination of CDW, IW and MSW and the connection with the EMI results is less straightforward. Yet, in terms of electrical conductivity the depth profile of T6 could generally be divided in two parts. The upper two metres of soil consisted in low conductive material, which agrees with the EC_a observations for the 1.1 m and 2.1 m PRP, and 1 m HCP coil configurations. Note that the trench escaped from superficial metal anomalies. The 4.1 m PRP measurements, with a theoretical DOE of 2.0 m, appeared to have already "sensed" the deeper more conductive materials, of which the 0.5 m thick clay layer is the first. Although EC_e values often are overestimations of the bulk EC in the field, here the high conductivity measured in the laboratory is in agreement with the higher EC_a of the 4 m HCP signal, with the largest measurement depth.

[10] The soil remediation thresholds for copper and nickel are 186 mg (kg DM)$^{-1}$ and 93 mg (kg DM)$^{-1}$ (VLAREBO, 2008).

5.5.5 **Conclusion**

The high-resolution EMI survey produced detailed maps of subsurface variations in electrical conductivity and magnetic susceptibility indicative of variations in material composition. The strong contrasts between the reference areas of natural soil and the suspected quarry/landfill areas accorded with the location of the latter's boundaries as derived from historical information. Even in zones meeting the assumption of low conductive construction debris, the electromagnetic response was still clearly different from the apparently very low conductive natural sandy soil, in terms of both the values measures and their spatial variability. Due to limited accessibility, the EMI survey could only cover a part of the quarry/landfill boundaries. However, it is reasonable to extrapolate the validity of the historical data to non-surveyed parts. Furthermore, the boundaries were corroborated through borehole drillings. Also within the two landfill areas large variations in EMI data were observed, which contradicted the mono-deposition of inert CDW. Over the two landfill parts, several areas were identified that evidenced a large number of, presumable shallow, metallic objects/structures. The eastern part encompassed three distinct zones: two where inert construction debris was expected and one suggesting more conductive MSW or possibly IW. The EMI maps suggested a more complex landfill history for the western part. Six locations were selected, three in each landfill part, to provide ground truth for the observed EMI contrasts. In the eastern part, the findings from the trench excavations confirmed the three distinguished zones, proving the use of the EMI survey to support volume estimations of the different waste substrates present. The trenches in the western provided important feedback to make more sound interpretations from the EMI data in terms of the more complex combination of waste. The consistency between the series of EMI maps, particularly of EC_a, and the profiles observed in the trenches strengthens the potential use of the EMI data to reconstruct vertical subsurface variations as well. The design of a conceptual landfill model should rely on more advanced processing of the dataset including inverse modelling.

The interest of an ELFM scenario, involving the actual mining of the site, essentially is in the conversion of waste to material, with secondary resources for the building industry as main product. Considering the limited volume of MSW, mostly intermixed with construction debris and presumably already in an advanced state of decomposition, the waste-to-energy option is less relevant. The large size of the site and its close location the road network are arguments in favour of ELFM. However, the possible profit of material recuperation should be balanced against the costs of

again disrupting the green buffer area and the currently ongoing processes of natural development. The urgency of remediating the existing contaminations with petroleum hydrocarbons, HMs and cyanides is a key decision factor. To make a well-founded estimation of the added value ELFM can offer, additional investigation of the contamination-associated risks is recommended.

5.6 Overall discussion and conclusions

5.6.1 Practical implementation: context conditions

Before discussing the constraints posed by the physical environments of landfills sites, we first want to spend a few words on some organisational aspects of landfill investigation projects. As in the case studies here presented, commonly parties of different capacities are involved. OVAM is involved as governmental body responsible for the management of information databases on contaminated sites and landfills in Flanders. One or more environmental consultants act as soil remediation experts and guarantee the quality of the investigations to perform a reliable environmental risk assessment. Last but not least, land owners and users, and local residents play a role. Flanders is characterized by a fragmented landscape (e.g. De Decker, 2011; see also Chapter 2). Particularly in residential areas and their surroundings under private use, parcel sizes are generally small and often even further subdivided into smaller units of land use, for instance, for pasture. Hence, even for small study areas, a number of land owners and/or users is involved, as illustrated in case study II, and this number easily multiplies as the size of the study area increases, as seen in case studies I and IV. Obviously, this does not facilitate the organisation of field work. In addition, the presence of a landfill – often dating from before the current proprietors/residents – and the threatening prospect of remediation measures can make these cases into sensitive situations. Land owners and users might be sceptical or even suspicious about (additional) geophysical investigations, although also many of them are curious about the mysterious ways of the yellow tube dragged along the terrain. Experience learns that most of them become a sympathetic public if properly informed, about the practical implications of the survey as well as on the use of the data. The main message here is that communication between the different parties involved can be a determining factor to the success of the project and spending the necessary time to achieve mutual understanding usually is worth the investment.

The conditions for practical implementation of the survey methodology relating to the physical environment of a site mainly arise from the useful and safe operation of the mobile survey platform. The quad-bike-based platform has a length of approximately 7.5 m or 9.5 m depending on the EMI instrument used. The geometry of the survey area, referring to both its dimensions and shape, is an important criterion to evaluate the practical feasibility of an EMI survey using the set-up here presented. As mentioned above, survey areas are commonly small in the urban and semi-urban landscapes of Flanders. As a rough guideline, a minimum surface area of 1000 m² is required to justify the application of a mobile survey configuration. The larger the available area, the more elegant the application (see also the discussion on survey efficiency below). For areas smaller than 1000 m², data acquisition in on-the-go mode, by carrying the sensor or by manually moving a sensor-carrier sled or cart, likely will be more time-efficient. This surface area relates to the area that is actually accessible for survey, under guarantee of safe operation conditions. Any enclosed areas covered with shrubs or tree vegetation, or infrastructure, such as fences, has to be excluded. Furthermore, it is recommended to maintain a perimeter of a few metres around aboveground obstacles, to avoid interference with the electromagnetic field transmitted by the sensor – which is particularly important in the case of metal structures/objects, and to prevent obstruction of the GPS signal – in the case of obstacles that exceed the height of the GPS antenna mounted at the back of the quad bike, such as trees and buildings. Also uneven terrain surfaces with abrupt elevation changes or steep slopes imply risks for damaging the survey equipment and for the safety of the quad driver. Furthermore, if such terrain conditions do not restrain from performing the survey, they may introduce operational noise, as was observed for the roughly ploughed arable field in case study IV, a problem which has been described in previous studies as well (e.g. Dabas et al., 2016). The survey configuration is compatible with bare soil and soil under grassy/herbaceous vegetation, as well as with technogenic surface covers such as asphalt or concrete. The smooth surface provided by the last even expedites the survey speed. However, the presence of dense reinforcement in such surface covers renders the sensor data, so to speak, senseless, as the sensor response will be dominated by these superficial metal structures and therefore will no longer be informative of the soil underneath. Similar problems may arise when measuring in the vicinity of sources of electromagnetic fields, such as high voltage power cables. Many authors have warned for the abundant sources of so-called cultural noise in urban and industrial environments (e.g. Everett, 2013; Meju,

2000; Reynolds, 2011). However, the influence of static sources such as metal fences is usually limited to a few meters and can easily be avoided by survey design, or can be abstracted from data interpretation. In case studies II and III, the overhead power lines presented a source of dynamic noise; yet, no significant effect was perceived, which likely also is due to the high signal-to-noise ratio. To address these practical considerations, it is good practice to conduct a proper pre-survey inquiry of the area to be surveyed, through consultation of historical information and records of utility infrastructure and, if possible, by thorough terrain inspection during a site visit in the direct run-up to the survey, so that the conditions are representative for the actual survey time.

5.6.2 **EMI survey parameters: efficiency versus resolution**

In the presented case studies, the EMI sensor instrument was chosen based on, firstly, the desirable investigation depth, which is implied by the study objectives and any *a priori* available information on the vertical extent of the landfill, and, secondly, the geometrical constraints of the survey area with respect to manoeuvrability of the mobile sensor platform. Also the cross-line resolution was adapted to the study objectives: a coarser resolution (4 m, case I) was deemed sufficient for waste detection, while a finer resolution (1.0–1.5 m, cases II–IV) was applied when aiming for material characterization. The in-line measurement resolution is determined by the sampling rate and the driving speed, the latter of which depends on the surface roughness and on the geometry of the survey area. A small and/or fancifully shaped area requires more turning, reducing the average driving speed, as will be clearly demonstrated in the next paragraph.

Survey efficiency

The survey parameters can be evaluated in terms of the survey efficiency, expressed as the area surveyed per time. For the different survey zones included in the four presented case studies, the survey efficiency is plotted in function of the distance between survey lines (~cross-line resolution), the surface area of the survey zone and the compactness of the shape of the survey zone (Figure 5.19). The last is

quantified using the *normalized perimeter index*.[11] Obviously, the survey efficiency generally increases with an increasing distance between the survey lines, on average with the same factor. Yet, Figure 5.19a illustrates that there can be considerable variation depending on other parameters and the variation shows to be greater for greater between-line distance. For instance, the survey efficiency for the non-composite area surveyed in the case study III, at a between-line distance of 1.5 m, is slightly larger than that for one of the small zones included in case study I, in which a between-line distance of 4 m was applied. This can be explained by the asphalt surface cover in case study III allowing to reach higher driving speeds. As already mentioned above, the proportion of straight driving lines is usually greater for larger survey areas, so more surface area can be surveyed per time. The effect of surface area seems to be more significant for smaller areas, hence, the rule of thumb that an area should at least be 1000 m² to consider a mobile survey. Despite their larger surface area, survey zone 2 in case I and, zones 1 and 7 in case IV did not show larger survey efficiency, which can be attributed to their irregular shape. The same holds for the overall survey efficiency for the total, composite survey areas in cases I, II and IV. On the other hand, the effect of the compactness of a survey area is subordinate to its surface area and to the cross-line resolution adopted. For example, the survey efficiency is low for the pretty compact survey zones 6–9 in case I, because their size is particularly small in relation to the coarse cross-line survey resolution. It is concluded that, using the proposed survey methodology, the survey efficiency will always be largely dependent on the characteristics of the survey area, irrespective of the survey parameters chosen. If the minimum surface area criterion is met and terrain conditions are fairly smooth, it can reasonably be assumed that the survey efficiency will be close to 1 hectare per hour.

Note that the survey efficiency as here discussed refers to the time of actual surveying. The time necessary to set up the mobile survey configuration and for moving between separate survey zones is not included. Particularly the latter can consume a considerable amount of field time and provides an important argument for proper planning of the survey in advance.

[11] The *normalized perimeter index* is the ratio of the perimeter of the equal area circle and the perimeter of the shape, with the equal area circle a circle with an area equal to that of the shape. The higher the normalized perimeter index, the more compact the shape; a circle corresponds to a value of 1.

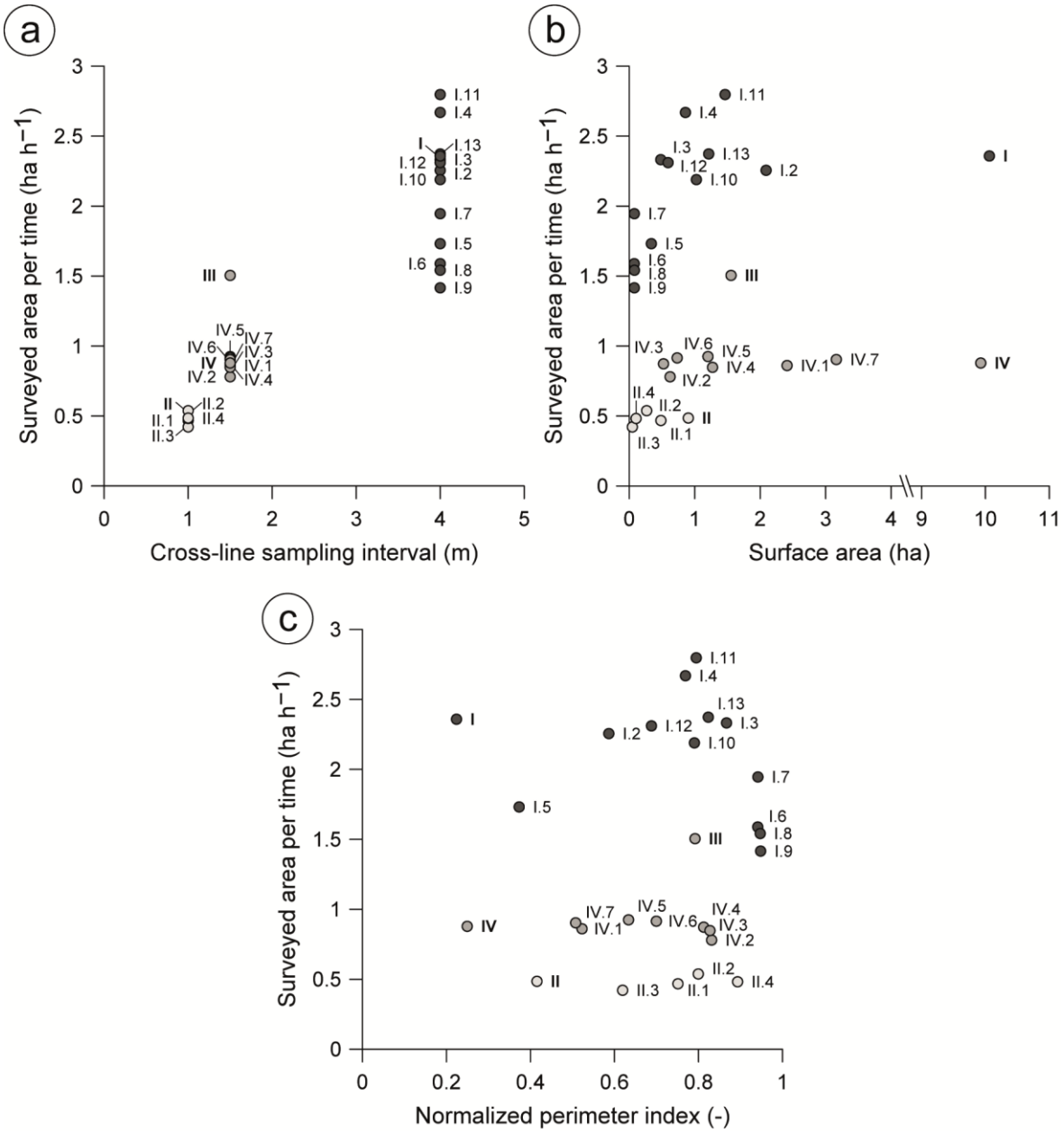

Figure 5.19 Survey efficiency, expressed as surveyed surface area per time (ha h−1), for all separate survey zones and for the total (composite) survey area covered in the four presented case studies plotted in function of cross-line sampling interval (m), surface area (ha) and compactness, quantified by the normalized perimeter index, of the surveyed area. The grey tone symbol fill corresponds to the cross-line sampling interval; the symbol labels indicate the case study (Roman numerals) and the survey part.

Survey resolution

The sampling density, the number of measurement points per area, determines the overall survey resolution. It depends on the data sampling rate, the driving speed and the distance between survey lines. In the presented case studies, the sensor data rate was set to either 4 Hz or 8 Hz, in line with previous studies using a mobile survey platform (Beamish, 2011; Delefortrie, De Smedt, et al., 2014). The sampling density varied between about 12 000 and 17 500 data points per hectare if the data rate was

8 Hz (respectively for the survey area in case III and zone 2 in case IV), and between about 10 000 and 67 000 data point per hectare if the data rate was 4 Hz (for zone 11 in case I and zone 3 in case II). This corresponded to in-line between-measurement distances in the order of 0.50–0.65 m and 0.20–0.25 m. For a certain data sampling rate, sampling density is inversely related to survey efficiency, and survey design seems to pose a trade-off between them. The cross-line resolution has to be decided based on the minimum size of contrast that needs to be resolvable in view of the research question. The driving speed is largely determined by the field conditions: on arable or grassland, 6.5 km h^{-1} to 7.5 km h^{-1} can be reached; on a smooth (technogenic) surface pavements, the speed can easily be pushed up to 8.5 km h^{-1}. This leaves the sampling rate as tuning factor for the sampling density, or more specifically the in-line sampling distance. For the specific DUALEM-21S and DUALEM-421S instruments used in this work the maximum data rates are respectively 8 Hz and 10 Hz. Recent advances in sensor electronics have raised the sampling rate up to 50 Hz. To make a useful decision on the sampling rate, several considerations have to be taken into account. At the same survey speed, a higher sampling rate proportionally increases the spatial sampling resolution. On the other hand, maintaining the sampling resolution, higher sampling rates allow for higher survey speeds, so that larger areas can be surveyed at the same time interval; yet, as discussed above, this might be impeded by the field conditions. A decrease of the data sampling interval, corresponding to a decrease of the signal integration time, can negatively affect data quality (e.g. Beamish, 2011; Delefortrie, De Smedt, et al., 2014), which becomes more relevant for coil configurations that integrate larger subsurface volumes, such as the 4-m arrays of the DUALEM-421S sensor. Data instability due to surface roughness was encountered in the arable reference field in case study IV, which could have been avoided, or at least reduced, by using a sampling rate of 4 Hz instead of 8 Hz. This kind of noise did not show in case study II, in which the DUALEM-42S sensor was operated at the same higher rate, however, in this case the signal-to-noise ratio was considerably higher, largely because of metal anomalies were plentiful. Furthermore, particularly if subsequent measurements are made at a distance smaller than the transmitter-receiver coil separation, a significant overlap can be expected between the subsurface volumes supporting the measurements corresponding to an overlap in information. Finally, the production of larger data sets inevitably leads to longer processing times. A large discrepancy between in-line and cross-line sampling density also might introduce artefacts in interpolated maps,

requiring more advanced geostatistical methods to remedy. The sampling density of ≥10 000 data points per hectare, at a minimum data rate of 4 Hz, appeared sufficient to adequately address the survey objectives. The mobile survey configuration provided that no exceptional effort was required to achieve this number. There is no pressing incentive for a further increase, on the contrary, less even may be more.

5.6.3 **EMI data processing: cautious customization**

Besides different survey parameters, the different case studies faced similar challenges with respect to the EMI data processing. More extensive data cleaning was required if the site geometry and/or aboveground obstacles entangled the purposed survey pattern. An insufficient number of parallel survey lines obscured the visual evaluation of the optimal time lag for correcting the spatial offset between position and sensor data. However, the time lag appears to be fairly consistent, so it is justified to maintain the value derived from a properly aligned survey part. Furthermore, deviations from the systematic survey pattern contribute to inconsistency in the comparison of survey and calibration data to correct for drift and short survey times may hamper the identification of a trend. On another note, shallow metallic objects/structures demonstrated to play havoc with both shift and drift correction, due to their introduction of extreme short-scale variability. Especially when they are so densely distributed that they can no longer be recognized as discrete anomalies, it becomes impossible to neutralize their influence by relatively simple data filtering. Case study II presented an example of severe metal cluttering. The main tenet is not to add trends or other artefacts through bold application of drift correction. Small survey areas corresponding to short survey times also reassure that drift not yet had an appreciable effect, particularly with respect to the EC_a data. Nonetheless, it is recommended to adopt a minimum uncertainty level (at least 1 mS m^{-1}) in the absolute interpretation of the EC_a measurements. The random, extreme short-scale variability arising from metal anomalies also affects data interpolation. It was shown that, in interpolation through kriging, this can be coped with by deploying the Dowd robust estimator of the variogram instead of the classical estimator of Matheron. It is noted that an abundancy of metal objects is an obstacle for advanced processing of the data. For instance, there currently is no readily available solution to elegantly deal with this type of interference in inverse modelling. In general, sufficient attention should be devoted to the irregularities that may be contained in EMI data sets derived

from these specific environments and impetuous routine application of standard data processing is discouraged.

5.6.4 **EMI data interpretation: make-or-break contrasts**

In general, the high-resolution EMI surveys provided detailed images of subsurface variations in electrical conductivity and magnetic susceptibility, allowing to deduce the location and lateral extent of waste depositions. Even if the waste materials were expected to show similar intrinsic properties as the naturally occurring materials, such as the inert construction debris and the calcareous sand in case study IV, there usually are differences in bulk properties due the differences in the deposition of the substrates and their subsequent development in time. In addition, natural and anthropogenic depositions typically contrast in spatial heterogeneity. The latter commonly display a higher short-scale variability, which mostly includes the presence of local metal anomalies, giving away their non-natural origin. It is evident that accurate determination of the landfill location and lateral extent is conditional to the of inclusion the actual landfill boundaries in the EMI survey.

If the depth of the waste was larger or approximately equal to the maximum DOE of the EMI sensor, vertical delineation of the landfill (obviously) was impossible. However, also when the interface between waste and natural material was within the depth range of the EMI measurements, as in case study II, it proved difficult to resolve. Several reasons can be given. First, it is possible that waste and host materials show insufficient contrast in geophysical properties. For instance, when both constitute porous soil media, saturation of the soil pores with the same fluid (water or leachate) can strongly reduce the contrast in bulk properties. In addition, there are restrictions inherent to the measuring technique applied. The depth resolution of EMI generally decreases with increasing depth: for the DUALEM-421S, five EC_a measurement signals are concentrated within the upper three metres of soil; only one measurements signal (4 m HCP) covers the next three metres. Moreover, a high concentration of metallic objects complicates the interpretation of the data in function of their depth sensitivity and obscures the contribution of surrounding, less conductive, soil materials. Nevertheless, the availability of multiple signals with different depth sensitivities proved informative of vertical variations in material composition. Provided the influence of metal interferences is limited or can be removed through filtering, more advanced processing of the data through inverse modelling promises to improve the reconstruction of vertical variations in subsurface properties.

Observed variations in EMI data could be related to variations in nature of the (waste) materials, allowing to define zones with a different landfill history. It was demonstrated that EC_a and MS_a data can provide complementary information. However, due to the ambiguity on the depth sensitivity and independence of the MS_a response, for interpretation in terms of material characterization the focus remained on the EC_a. Interpretations were usually conditioned to expectations on the type of wastes disposed, emphasizing thorough desk study of available historical documents is equally relevant in preparation of geophysical studies as for conventional soil investigations. Furthermore, the discrimination of different landfill zones largely relied on relative contrasts in measurement values. As anticipated from the broad range of electrical conductivities and magnetic susceptibilities (mono-types of) wastes can show, the EMI data cannot provide a unique solution to material characterization; yet, the possibilities are strongly narrowed down. Decisive answers can only be filled in by invasive investigations, which afterwards can be used to improve the translation of the EMI maps into additional information input to a conceptual landfill model. The abundancy of metal objects can be problematic for the characterization of their host waste substrate and, from this respect, near-surface geophysicists may be correct in denoting them as cultural noise. In recent years considerable progress has been made on the discrimination of discrete metal anomalies, which is mainly advertised for the detection of UXO detection. Both analytical and experimental approaches have been presented (e.g. Benavides & Everett, 2005, 2007; Saey, Van Meirvenne, Dewilde, et al., 2011). However, the crux of these methods lies in the successful separation of target and background, which is compromised if different metal objects are so close together that they produce a joint, composite anomaly. Considering the interest in the metallic waste fraction for material recovery, the development of suitable routines allowing to use EMI data to make estimates on the metal content of the waste provides a compelling topic for future research. In this context, an important role is to be reserved for the IP response, which is known to be more sensitive to buried metal objects (e.g. Marchetti & Settimi, 2011). More detailed analysis of the raw QP and IP output components likely holds significant unlocked potential for improving material characterization in general. For instance, combined analysis of the QP and IP responses has been used to derive improved, robust estimates of EC_a that are also valid outside the condition of LIN (Guillemoteau et al., 2015).

In a final remark on the EMI data interpretation, we come back to the discussion on the value of very small sample intervals. Whereas there are clear advantages for

lateral delineation of the landfill (zone) boundaries, the use of a very high survey resolution for material characterization is debatable. In the case of both very low and very high spatial variability of the subsurface electrical conductivity and magnetic susceptibility, a high sampling density does not necessarily add to a facilitated solution of the posed research questions. With the proposed methodology, the relevance of high resolution surveying can only be properly evaluated *a posteriori*. Therefore, it could be worth investing in upgrading the survey platform in order to provide real-time visualisation and analysis of the collected data, so that the survey parameters can be fine-tuned to the required data quality during field surveying.

5.6.5 Borehole drillings and trench excavations: advanced sampling strategy design

In each of the presented case studies, the EMI maps served as basis for the design of an invasive investigation campaign. The sample locations were chosen as to cover observed variations in electrical conductivity and magnetic susceptibility. Although not tested against alternative sampling design strategies, it is reasonable to assume this corresponded to an improvement in representativeness of the invasive observations. The structure of spatial variability in the EMI data can be used as guide to decide on the size of the sample, in terms of the number of sampling locations and the individual sample volumes. When the landfill exists in a few relatively homogeneous zones, such as the eastern landfill part in case study IV, a small number of localized observations is sufficient to make an extrapolated interpretation for the entire landfill. The necessary individual sample volume mainly depends on the magnitude of the short-scale variability. If high, small sample volumes as provided by borehole drillings can be difficult to relate the EMI measurements, not only because of the discrepancy in volume support between sampling and sensing observations, but also because small sample volumes can impede the correct identification of waste materials and the accurate estimation of their vertical extent. This issue was clearly demonstrated in case study III. Furthermore, if the EMI data suggest the presence of rather coarse, hard materials such as those comprised in construction debris, the collection of small sample volumes using conventional soil drilling equipment is highly prone to practical problems as well. The EMI data can thus provide input for both the conceptual and practical design of an invasive sampling campaign.

Previous studies on the characterization of landfills in view of landfill mining, in which only conventional investigation methods were used, indicated larger sampling

volumes are required for the samples to be reliable (e.g. Kaartinen et al., 2013). Yet, if at all allowed and possible, the collection of samples at landfill, and particularly of large sample volumes, cannot be taken for granted. Specialized drilling equipment, for instance a hydraulic piling rig in auger mode operation, allowing to make larger-diameter boreholes (in the order of 1 m, as demonstrated in Kaartinen et al., 2013), are to be preferred above conventional soil drilling equipment; however, specialized equipment often is not readily available, except at an excessive cost. In addition, some substrates may be resistant to any sampling tool, for instance, Jones et al. (2013) describe metal containing slag to be impenetrable for a cactus grab crane. This underlines the value of a preliminary geophysical survey as a guide to limiting the number of samples to a minimum.

Even if borehole drillings or trench excavations can be performed without problems, the determination of separate waste materials and the proportions in which they are present can be far from obvious, especially for complex inter-mixtures of different waste types. Matching the interpretation of EMI data with invasive observations can be considered an iterative process. As mentioned above, waste substrates do not have unique geophysical signatures and there are mostly different possibilities that fit the EMI measurements. Ideally, invasive observations should then allow to select the correct option. However, if the material identification from invasive observations is ambiguous, the measured values of electrical conductivity and magnetic susceptibility can be used to select the most plausible solution. Theoretically, the minimum sample volume required for adequate interpretation of the EMI measurements is determined by the sensitivity distribution of the corresponding coil configuration. For the DUALEM-421S 4 m HCP configuration, this would be a sample of roughly 6 m × 6 m × 6 m = 216 m³, while for the 1.1 m PRP configuration the size is limited to 1 m × 1 m × 1 m = 1 m³. In practice, the necessary sample size will have to be evaluated in function of the specific research objectives. Considering the detailed mapping of the local material composition is generally not an aim in itself, very small-scale invasive observations might be deemed irrelevant. Yet, such small-scale observations can improve our knowledge on the geophysical properties of waste materials and advance our understanding of the 3D response of complex subsurface compositions as registered by geophysical sensors.

5.6.6 EMI for ELFM: current status and the way forward

High-resolution surveying with a multi-receiver EMI sensor proved ideally suited for reconnaissance surveying in the initial stage of landfill exploration in view of ELFM. Accurate information can be provided on the location and lateral extent of the landfill and the boundaries of possible zones with a distinct landfill history. Detailed images of the subsurface heterogeneity are obtained, which are indicative of the heterogeneity in waste composition. Both represent important criteria to evaluate the suitability of a landfill site for ELFM. The EMI maps can serve as guide for the design of a targeted, and hence more efficient, invasive sampling campaign.

For the mapping of lateral subsurface variations, mobile EMI surveying is more time-efficient than ERT. Therefore, EMI definitely is a worthy geophysical surrogate if relatively shallow landfill characterization is sufficient, for instance, if the envisioned land remediation and reclamation strategy only involves the removal and replacement of the top landfill layer. The lack of information on the deeper landfill layers could be (partly) compensated for by invasive investigations. Alternatively, supplemental geophysical investigations with larger measurement depths – as ERT – could be considered. However, the results of these would probably also require validation with invasive investigations.

To conclude, a few future research prospects are highlighted to advance the use of EMI for landfill characterization. First, new data processing routines are required to adequately resolve the influence of strong local anomalies as produced by metallic objects. This is a crucial intermediate step to allow for the meaningful application of more advanced data processing through inverse modelling and, hence, the reconstruction of a conceptual landfill model. Second, a more systematic approach should be established for the use of EMI data in the design of an invasive sampling strategy, in order to facilitate the integration of the information they provide. Last, the combination and fusion of data from EMI and related geophysical methods such as ERT and time-domain electromagnetic induction provides an interesting topic for further research, which is relevant to addressing the limited depth resolution of EMI as well as to improving material characterization.

5.7 Acknowledgements

These case studies were performed in collaboration with the OVAM and the environmental consultants ABO NV and Saneco BVBA. We would like to thank each of these parties for the open exchange of site information and the collaboration in the

organisation of invasive site investigations. We also thank Valentijn Van Parys, Bram Vandekerckhove and Nicolas Note for their help in performing the EMI surveys.

Chapter 6
Investigating a petroleum hydrocarbon contaminated site through EMI and GPR

The content of this chapter is based on:

> Van De Vijver, E**.**, Van Meirvenne, M., Vandenhaute, L., Delefortrie, S., De Smedt, P., Saey, T., & Seuntjens, P. (2015). Urban soil exploration through multi-receiver electromagnetic induction and stepped-frequency ground penetrating radar. *Environmental Science: Processes & Impacts*, 17(7), 1271–1281.

6.1 **Introduction**

In a world with accelerating urbanization, urban soil management is of continuously growing importance (e.g. De Kimpe & Morel, 2000; Lehmann & Stahr, 2007). Meuser (2010) defines 'urban soils' as 'soils in urban and suburban areas consisting of anthropogenic deposits with natural (mineral, organic) and technogenic materials, formed and modified by cutting, filling, mixing, intrusion of liquids and gases, sealing and contamination' (p. 5). This definition argues one of the most important motives behind urban soil investigation as well as the challenges involved in doing this. As urban soils may be contaminated, they often become the subject of

environmental assessments setting out the management strategy towards the future land use destination (Norra & Stüben, 2003). Whereas identifying soil contamination can be considered the main aim of contaminated site assessment, characterizing the host soil matrix is also critical to understanding contaminant migration and distribution (Redman, 2009). Conventional soil investigation, commonly including soil coring, soil sampling and well monitoring, is expensive and usually only provides information from a limited number of observation points. Furthermore, these are small localized measurements the location of which can be biased depending on the a priori available site information and the expertise of the professionals involved. Therefore, the typically large spatial heterogeneity of urban soils can affect the reliability and representativeness of conventional soil survey results. Non-invasive geophysical techniques allow rapid collection of high-resolution data, enabling narrowing of the spatial information gaps between invasive observations. In this paper, we focus on EMI and GPR. Both techniques have an established reputation for the indirect mapping of spatial variations in 'natural' soil properties such as soil texture, soil moisture and OM content as evidenced by numerous studies in the field of precision agriculture (e.g. Adamchuk et al., 2004; Corwin & Lesch, 2005a). The suitability of EMI and GPR for identifying physical artefacts such as building remains, ditches and remoulded or refilled soil material and investigating their surrounding soil context has been demonstrated in a number of recent studies in landscape archaeology (e.g. Verdonck et al., 2009; De Smedt, Van Meirvenne, et al., 2013; Saey et al., 2013). The detection of petroleum hydrocarbons and their interactions with their host soil environment is an important example of the chemical counterpart of this problem. In the search for a non-invasive solution, several authors have studied the electrical properties (electrical conductivity and dielectric permittivity) of hydrocarbon contaminated soils. Mainly focusing on the application of GPR, these properties have been theoretically estimated, often using laboratory measurements as calibration (e.g. Carcione et al., 2003; Cassidy, 2007), and have been measured under laboratory and controlled field conditions (e.g. Brewster et al., 1995; Daniels et al., 1995; Santamarina & Fam, 1997). Fewer studies have been conducted on the use of EMI for detecting hydrocarbon contamination (e.g. Jin et al., 2008; Martinelli et al., 2012). However, recognizing the complexity of this geophysical problem and the advantage of a multi-sensor approach, most uncontrolled field studies have used a combination of EMI and GPR and possibly other techniques (e.g. Atekwana et al., 2000; Guy et al., 2000). Because the concentration and composition of a petroleum hydrocarbon

contamination and the bio-physicochemical conditions of its soil environment vary in space and time, the electrical response of hydrocarbon contaminated soils is very complex. Petroleum hydrocarbons commonly have a very low intrinsic conductivity (0.0001 to 0.001 mS m−1 to Carcione et al., 2003) and thus initially reduce the soil electrical conductivity when displacing water in the pore space. Due to physico-chemical changes of the contaminated environment induced by biodegradation processes, with time the geophysical response generally changes from being less conductive to more conductive. The time required for this change to occur varies and exceptions have been reported (e.g. de la Vega et al., 2003), but the usual behaviour is that hydrocarbon contaminated soil volumes eventually present anomalously high conductivity.(Redman, 2009; Sauck, 2000; Werkema et al., 2003; Atekwana & Atekwana, 2010) In any case urban soils provide inter- esting environments to explore the combination of EMI and GPR as they encompass various soil variations of natural and anthropogenic origins. However, the application of both EMI and GPR to address the integral problem of urban soil investigation remains poorly studied. Following the trend towards denser 3D surveying (Auken et al., 2006), we have used a motorized setup of a multi-receiver EMI sensor and a stepped-frequency GPR system operating with an antenna array. Our objective was to investigate the potential contribution of these state-of-the-art soil sensors to urban soil investigation, including detection and identification of physical and chemical anomalies.

6.2 Materials and methods

6.2.1 Study site

The study site is located in an urban area of West-Flanders, Belgium. It consists of a former garage with petrol station and storage of accident-involved vehicles (Figure 6.1) that was active from 1976 to 2012. An environmental assessment was carried out between 2008 and 2012, in which soil information was collected from borings and groundwater monitoring wells at the locations indicated in Figure 6.1. These locations were clustered around the location of two underground storage tanks for diesel and gasoline, while large other parts of the study site were only sparsely covered. Based on the soil borings, soil texture was described as sandy for the first two meters below the surface and as loamy sandy between two and three meters. The groundwater table was situated at a depth between 2 and 2.5 m. Based on the laboratory analyses of soil and groundwater samples, contamination with petroleum hydrocarbons and

BTEX was found. Figure 6.1 shows the spatial extent of the soil contamination with petroleum hydrocarbons as defined by testing the total petroleum hydrocarbon TPH (C10–C40) concentration against the thresholds provided by the Flemish soil remediation legislation (VLAREBO, 2008). To obtain useful soil data from EMI and GPR, the survey area has to be exempt, as much as possible, of surface or above-ground metallic structures. Therefore, our survey area was limited to a 1050 m^2 part of the car parking area covered with limestone gravel, where the vehicles had already been removed (Figure 6.1).

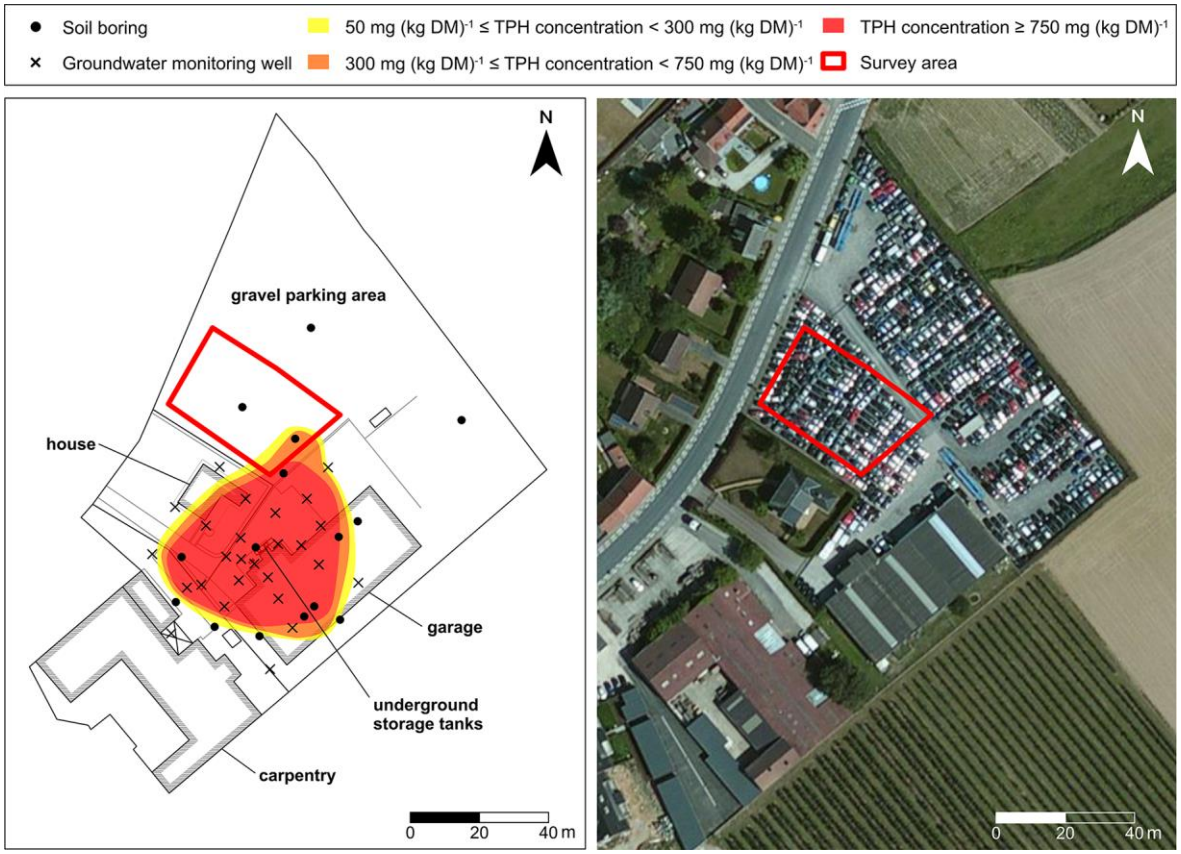

Figure 6.1 Outline map of the study site with indication of the invasive investigation locations of the environmental assessment carried out between 2008 and 2012 and the consequent delineation of the soil contamination with petroleum hydrocarbons according to the TPH concentration thresholds provided by the Flemish soil remediation legislation (background value 50 mg (kg DM)$^{-1}$, target value 300 mg (kg DM)$^{-1}$ and soil remediation threshold 750 mg (kg DM)$^{-1}$) (left); aerial photograph of the study site in 2012 which still shows stored vehicles at the parking area (right).

6.2.2 **EMI survey**

The EC_a of the soil was surveyed using a frequency-domain EMI sensor. We refer to Keller and Frischknecht (1966) for a detailed theoretical description of the application of EMI techniques to measuring soil EC_a; McNeill (1980) gives a more practical summary for operation under conditions of low induction number, which were

adopted here. In this study, a DUALEM-21S sensor (DUALEM Inc., Milton, Canada) was used. This multi-receiver EMI sensor has an operating frequency of 9 kHz and contains four coil configurations: one transmitter coil paired with four receiver coils at spacings of 1 m, 1.1 m, 2 m and 2.1 m. The 1 m and 2 m transmitter–receiver pairs have a horizontal coplanar orientation (1 m HCP and 2 m HCP), while the 1.1 m and 2.1 m pairs have a PRP orientation (1.1 m PRP and 2.1 m PRP). Due to a different transmitter–receiver spacing and orientation, the four coil configurations have a different depth sensitivity for measuring the soil EC_a (Keller & Frischknecht, 1966; McNeill, 1980). To link the four EC_a responses to the respective soil volumes they represent, the DOE has been conventionally defined as the depth where 70% of the cumulative response is obtained from the soil volume above this depth. For the 1.1 m and 2.1 m PRP, 1 m HCP and 2 m HCP coil configurations the DOE is 0.5 m, 1.0 m, 1.6 m and 3.2 m, respectively (Saey, Simpson, et al., 2009). The multi-receiver EMI sensor thus provides simultaneous EC_a measurements representative of these four different soil volumes.

The EMI sensor was mounted in a sled pulled by an all terrain vehicle. A Leica Viva GNSSG15 differential GPS (Leica Geosystems, Heerbrugg, Switzerland) was used to georeference the measurements with a pass-to-pass accuracy of less than 0.1 m. The area was surveyed along parallel lines 0.9 m apart and, with a sampling rate of 8 Hz and a driving speed around 8 km h^{-1}, the in-line distance between two measurements was circa 0.25 m. Afterwards, the measurement coordinates were corrected for the spatial offset between the GPS antenna and the centre of the transmitter–receiver coil pairs of the EMI sensor (Simpson, 2008). The measured EC_a values were standardized to a reference temperature of 25°C using the formula presented in Sheets and Hendrickx (1995). To map the EC_a data, they were interpolated to a grid with 0.1 m cell size using ordinary point kriging (Goovaerts, 1997). Additionally, the four EC_a measurements were combined into the ‘fused electromagnetic metal prediction’ (FEMP) as developed by Saey, Van Meirvenne, Dewilde, et al. (2011) to investigate the presence of subsurface metallic structures. To remove the influence from background EC_a variations and to focus on local anomalies, the EC_a measurements were ‘detrended’ by subtracting the moving average within a circular window with a radius of 4 m. The FEMP was then calculated as the following linear combination of the residual EC_a values (Saey, Van Meirvenne, Dewilde, et al., 2011):

$$\mathrm{FEMP} = 2.05 \cdot \Delta EC_{a,\ 1.1\ m\ PRP} - 1 \cdot \Delta EC_{a,\ 2.1\ m\ PRP} - 0.82 \cdot \Delta EC_{a,\ 1\ m\ HCP} - 1.89 \cdot \Delta EC_{a,\ 2\ m\ HCP}$$

which provides a measure of the probability of the occurrence of a metallic object.

6.2.3 **GPR survey**

In this study, GPR data were collected using a SFCW system (GeoScope-GS3F, 3d- Radar AS, Trondheim, Norway). This system produces a wave- form consisting of a sequence of sine waves with linearly increasing frequencies within the range of 100 to 3000 MHz. While a conventional impulse GPR requires a centre frequency to be chosen beforehand, as a trade-off between the desired penetration depth and vertical resolution, the wide frequency bandwidth adopted by a SFCW system offers an optimal resolution for each achievable penetration depth. Furthermore, a SFCW system focuses energy in one single frequency at a time and the phase and amplitude of the reflected signal are recorded for each discrete frequency step which anticipates an improved penetration depth and SNR (Koppenjan, 2009). As the data are recorded in the frequency domain, an inverse Fourier transform needs to be applied to visualize the data in time-domain profiles. The SFCW system operates with an array of multiple fixed-offset antenna pairs that can collect data quasi-simultaneously, expediting full spatial coverage of the survey area. Here, a V1213 antenna array was used including 13 transmitter–receiver combinations at a uniform spacing of 0.075 m, providing a total scan width of 0.975 m. Similar to the EMI survey, the GPR system was used in a motorized configuration with real-time georeferencing (Trimble AgGPS 332 GPS receiver with OmniSTAR correction, Trimble Navigation Ltd, Sunnyvale, California). The antenna array was mounted on a trailer, with the GPS antenna on top of its centre. To achieve full-area coverage, the driving pattern ensured a minimal overlap of 0.1 m between two adjacent scans. The inline distance between two measurements was fixed at 0.05 m and was controlled by an odometer integrated within one of the trailer wheels. The acquisition frequency range of the SFCW system was adjusted to 100–1500 MHz and was stepped in intervals of 2 MHz with a 2 ms duration of each frequency step.

Post-acquisition data processing started with an interference suppression in the frequency domain: for each measurement location, the frequency spectrum of the received signal was analyzed and frequencies with outlying power were suppressed. Afterward, the data were converted to the time domain through an inverse fast Fourier

transform. A Kaiser window with a beta value of 6 was applied, while the recorded frequency bandwidth was narrowed to 150–800 MHz to reduce both low- and high-frequency noise. Time zero was estimated as the average two- way travel time where the highest magnitude occurred, and was assumed identical over the survey area. Through a horizontal high-pass filter, 90% of the background was removed, 10% was preserved to avoid the complete removal of possible reflections from horizontal soil contrasts. An additional horizontal filter the window size of which increased with depth further improved the SNR. Prior to visualization, the originally overlapping scans with horizontal measurement resolution of 7.5 cm by 5 cm were subsampled to a 10 cm square grid using a nearest-neighbour interpolation in which priority increased according to the "centrality" of the transmitter–receiver pair in the antenna array. This procedure thus suppressed the sampling of GPR traces from outer antenna pairs as they are generally more susceptible to interference. Finally, for the trace subsample, the median magnitude was equalized in depth using AGC (Cassidy, 2009b) The resulting 3D data volume was then visualized in a selection of relevant vertical and horizontal slices.

6.2.4 **Soil borings and sample analysis**

Because of the scarce soil borings in the survey area, the survey results led us to select an additional number of locations (areas of 1 m by 1 m) for boring investigation. Depending on the observed EC_a and/or GPR contrast and the local field conditions, different means of invasive investigation were deployed.

Soil profile description

After removing the gravel cover with a spade, a gouge auger was used to investigate the soil profile in successive 0.5 m depth intervals. The investigation depth was limited by the groundwater table or by impenetrable material. In the profile description, the soil horizons and their composing materials were identified, with special attention for human-induced soil features (e.g. compaction) and technogenic materials (e.g. brick fragments, concrete debris).

6.2.5 **EC-probe measurements**

At each location where the soil profile was described, a second sequence of gouge-auger borings was made to investigate the vertical electrical conductivity variation through EC-probe measurements (14.01 EC- probe, Eijkelkamp Agrisearch Equipment, Giesbeek, The Netherlands). The probe contains four ring-shaped

electrodes, spaced 0.025 m apart, that measure the soil resistivity based on the Wenner method (Rhoades & van Schilgaarde, 1976) The measured resistivity is representative of an 80 cm^3 elliptical volume around the probe. An additional sensor in the EC-probe's cone recorded the soil temperature. The soil resistivity was then converted to electrical conductivity (EC_p), for a reference temperature of 25°C. EC_p measurements were made for each 0.1 m depth interval down to the groundwater table.

6.2.6 Soil texture analysis

Using an Edelman hand auger, borings down to 2 m depth were made and for each depth interval of 0.2 m a soil sample was taken. The samples were analyzed following the conventional sieve–pipette method (ISO, 2009) resulting in three textural fractions: clay (0–2 mm), silt (2–50 mm) and sand (50–2000 mm).

6.2.7 TPH concentration analysis

A mixed sample per soil horizon (as identified in the soil profile) was taken for laboratory analysis of the TPH concentration. This analysis was preceded by the spectrophotometric determination of the OM content. The TPH concentration was determined by gas chromatography with a flame ionization detector (ISO, 1999) The limit of detection (LOD) for this procedure was 20 mg per kg dry matter (DM).

6.3 Results and discussion

6.3.1 EC_a data

The four EC_a maps are shown in Figure 6.2a. The median EC_a is 15.1 mS m^{-1}, 20.3 mS m^{-1}, 22.4 mS m^{-1} and 27.6 mS m^{-1} for the 1.1 m PRP, 2.1 m PRP, 1 m HCP and 2 m HCP coil configurations, respectively. As the median EC_a increases with an increasing DOE of the coil configurations, the EC_a generally increases with depth. All four EC_a signals have an extremely high variance due to both negative and positive extreme values; the coefficient of variation (CV) varies between 92% for the 1 m HCP coil configuration and 201% for the 1.1 m PRP coil configuration. The majority of the extreme EC_a values spatially coincide in the four EC_a maps. This is a typical indication for metallic objects as is confirmed by the FEMP map (Figure 6.2b) (Saey, Van Meirvenne, Dewilde, et al., 2011). A marked group of these ‘metal anomalies’ is seen in the western corner of the study area (anomaly A, Figure 6.2c). The strip of extreme

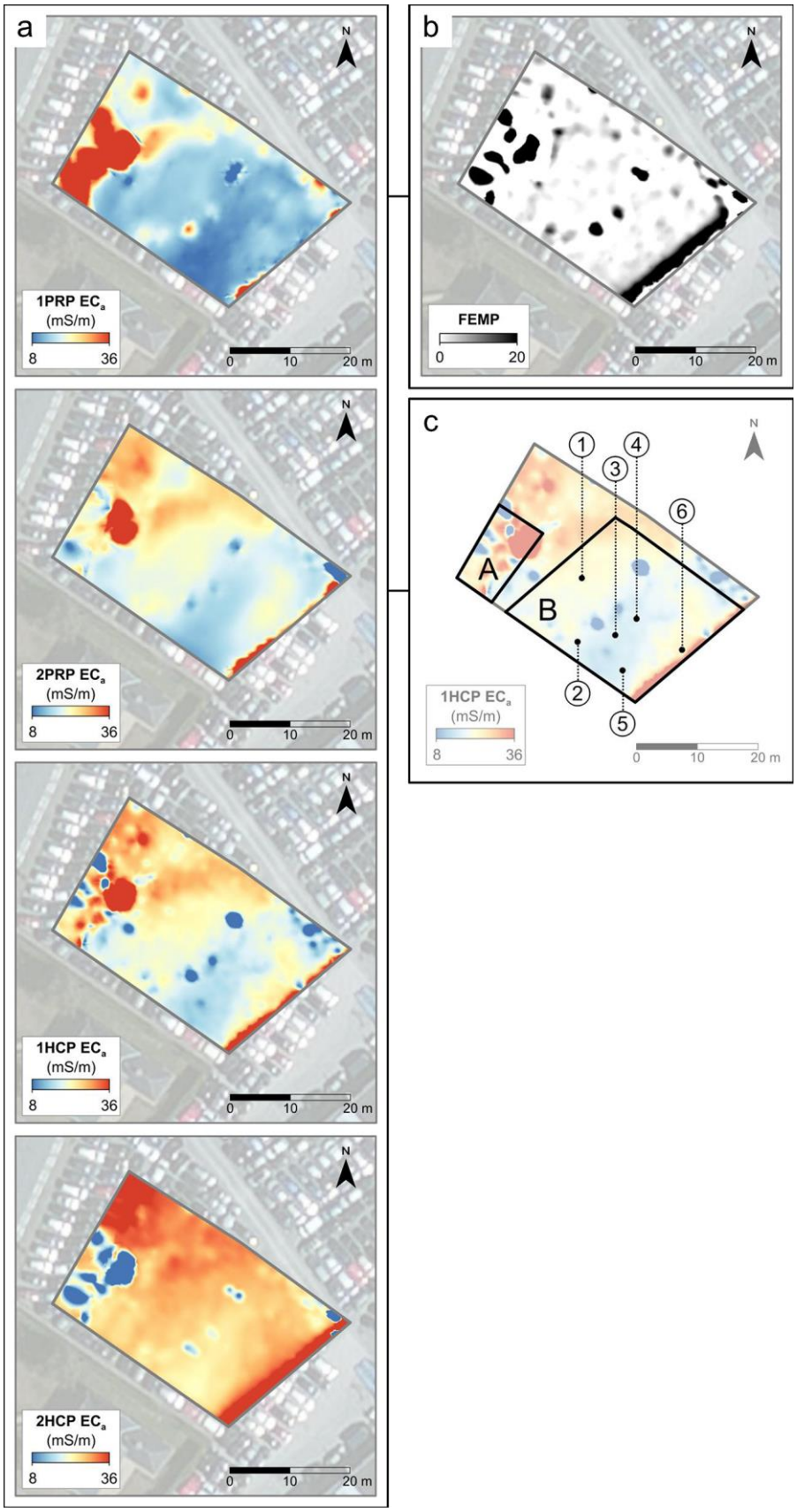

Figure 6.2 (a) EC_a maps for the four coil configurations of the EMI sensor; measurement values outside the colour scale were assigned the same colour as the scale limits; (b) FEMP map; (c) 1 m HCP EC_a map with indication of anomalies A and B, and the locations selected for additional boring investigation of anomaly B.

EC_a values at the southeastern edge of the survey area is explained by the metal-reinforced concrete pavement adjoining it. Excluding the extremes, the EC_a measurements are generally in line with the expected values for a sandy to loamy sandy soil (e.g. Saey, Van Meirvenne, et al., 2009). However, in the southern part of the survey area a zone with lower conductivity (anomaly B, Figure 6.2c) is observed. This zone consistently appears on all four EC_a maps suggesting correspondence to a soil contrast occurring at a shallow depth, i.e. within about the upper 1 m soil layer.

6.3.2 **GPR data**

Considering the depth at which the AGC gain factor reaches its maximum as an indicator of the depth at which noise becomes dominant, the penetration depth of the GPR signal is approximately 38.3 ns or 1.50 m. The conversion of depth expressed in two-way travel time to depth expressed in meters is based on a time zero of 2.83 ns and a RDP of 12.62. The origin of this RDP value will be explained below. The horizontal variation of the GPR reflection strength is considerably high (CV ≥ 65%) within the depth interval from 7.3 ns (or 0.19 m) to 24.9 ns (or 0.93 m), as illustrated in Figure 6.3 and 6.4. Two features have clearly added to this high signal variation. The first is the high-reflective area in the western corner of the survey area, corresponding to anomaly A defined above. While the spatially exaggerated response of EMI to metallic structures hampered the delineation of this anomaly, the horizontal GPR slices clearly depict its rectangular boundaries (Figure 6.3). The vertical profiles allow for a more precise demarcation of the anomaly's vertical extent: for 0 m to 5 m along transect EF strong horizontal reflections are observed starting from the ground surface down to approximately 17 ns (or 0.6 m) depth (Figure 6.4). From a depth of about 13 ns (or 0.4 m) downwards in Figure 6.3, the horizontal slices display a second notable contrast in reflection strength at the location of anomaly B in the EC_a data. Vertical GPR profiles, such as the one shown in Figure 6.4, demonstrate that this contrast is part of a slightly dipping interface, with a larger extent than possibly expected from the horizontal slices. In Figure 6.4 the interface appears to extend as far as anomaly A. Yet, the lateral increase in reflection strength correlates with the lower conductivity observed in the EC_a maps: the lower the electrical conductivity, the weaker the GPR signal attenuation and thus the stronger the reflections generated from a given soil contrast. Finally, note that the locations where the EC_a data indicated isolated metallic objects generally did not correspond to marked anomalies in the horizontal GPR

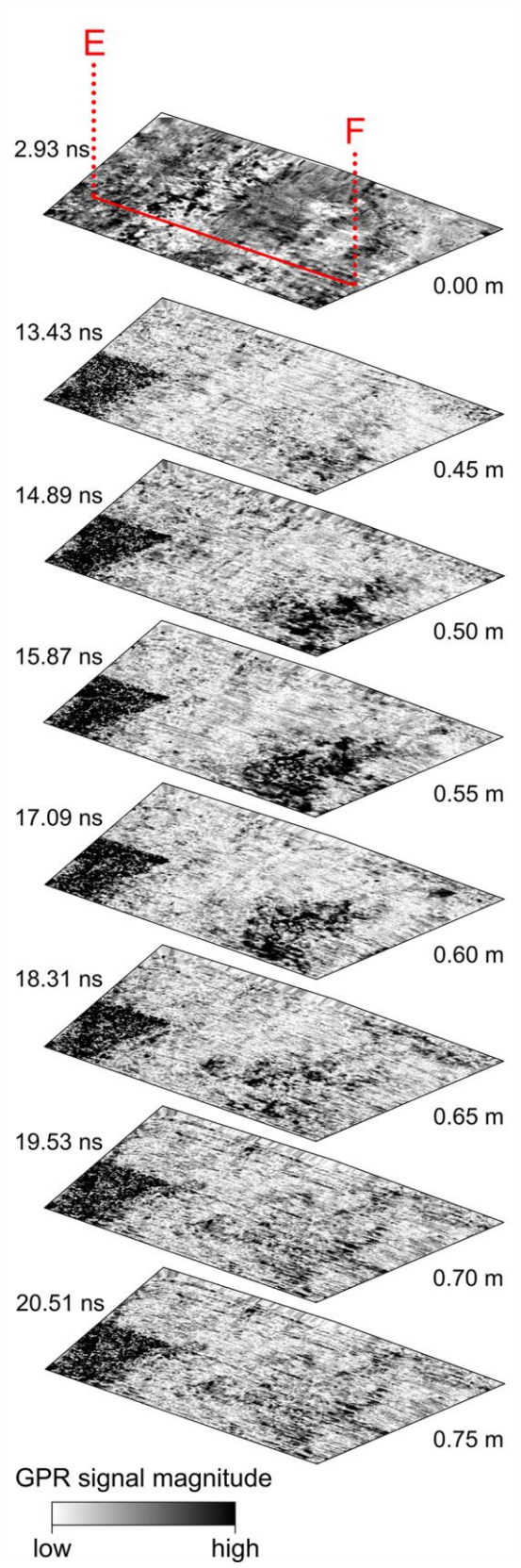

Figure 6.3 Horizontal GPR slices mapping the signal magnitude at the indicated depths. The depth is expressed both in two-way travel time (left) and in meters (right); the conversion between these units is based on a RDP of 12.62 and a time zero of 2.83 ns. The greyscale contrast has been optimised for each slice separately. On the upper slice, transect EF is indicated, the vertical GPR profile of which is shown in Figure 6.4.

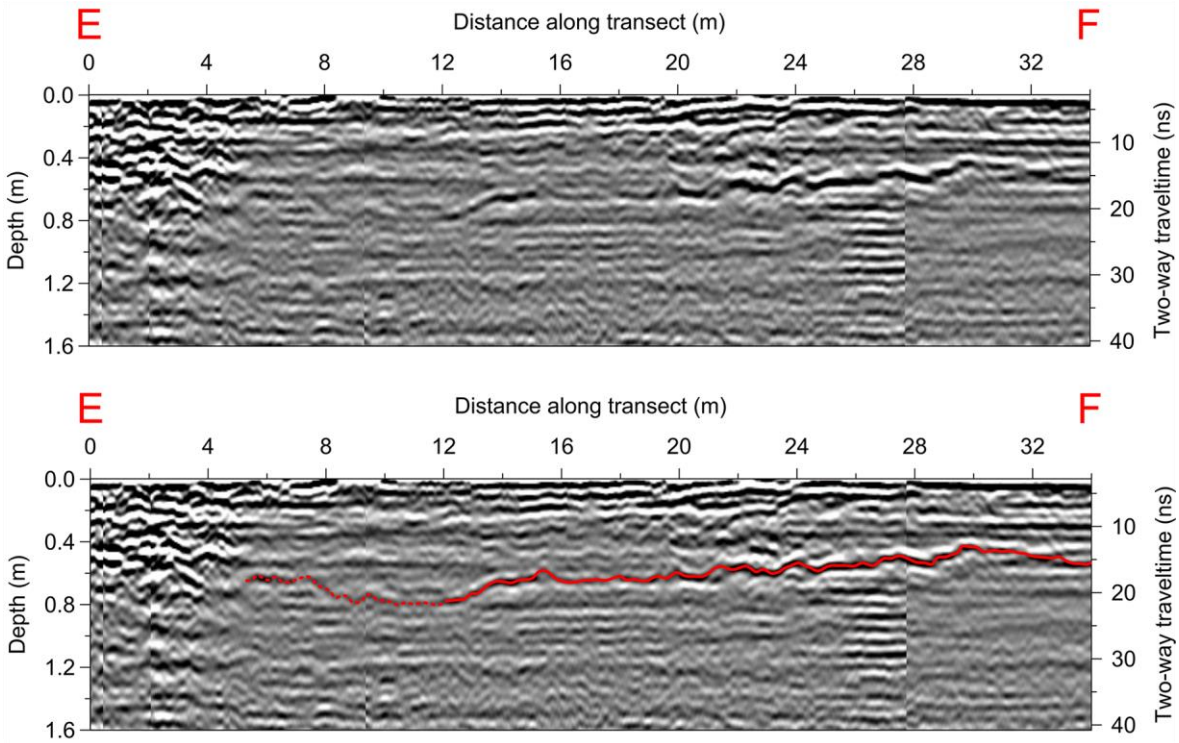

Figure. 6.4 Vertical GPR profile showing the real part of the GPR response as a function of depth along transect EF, without (top) and with (bottom) indication of the contrasting interface.

slices, demonstrating that these metallic objects generally have relatively small dimensions.

6.3.3 **Soil borings and sample analysis**

An overview of the boring results at the six locations indicated in Figure 6.2c is given in Figure 6.5. Beneath the 5 to 10 cm thick gravel cover, the observed soil profiles could roughly be divided into three layers (Figure 6.5a). First, a rather heterogeneous, brown to yellowish brown topsoil layer was seen. Particularly at location 1, the topsoil contained clear anthropogenic traces such as small brick fragments and rust patches. At all six locations, the bottom of the topsoil was delimited by an abrupt change to a layer with distinctly higher bulk density and contrasting grey to nearly black colour. In addition to the anthropogenic traces encountered within the topsoil, this layer included tiny coal fragments and a petrochemical smell was perceived at its corresponding depth at locations 1 and 3. At locations 4 and 5 the contrasting layer had an abrupt lower boundary, while at the other locations a gradual change into a fairly homogeneous subsoil with light grey to yellowish brown colour was observed. The subsoil suggested a dominant natural origin. In terms of the EC_p, the six locations also demonstrated a comparable vertical profile (Figure 6.5b). The topsoil clearly has a

lower conductivity and an average jump of about 7 mS m−1 is observed near the upper boundary of the contrasting soil layer.

Together with the soil profile observations, this links the transition from the topsoil to the contrasting soil layer to the interface observed in the GPR data. Consequently, the transition depths observed from the soil profiles were used to estimate the average RDP of the topsoil, which, together with the earlier estimated time zero, was then used to convert the GPR two-way travel time into depth in meters. Despite the stringent assumption of a constant topsoil RDP, Figure 6.5a and b evidence a close correspondence between the estimated depth of the GPR interface and the depth of the contrasting layer as observed in the soil profiles and the EC_p measurements. Despite the similar within-profile EC_p trend, the absolute EC_p measurements differ between the different locations. Whereas locations 1 and 6 show a relative constant topsoil EC_p of about 11 mS m^{-1}, at locations 2 to 5 the topsoil EC_p shows an additional dip. Below the topsoil, the between-profile differences are less pronounced. Soil texture analysis was only performed for locations 1, 4 and 6. With an overall average of 7.6% clay, 30.2% silt and 62.2% sand, the soil texture is classified as light sandy loam (Belgian soil texture triangle), which roughly confirms the data provided by the environmental assessment. As illustrated in Figure 6.5c, variations in the clay fraction are small both within and between the profiles and do not seem to correlate with the soil layering or the EC_p measurements. The OM content is generally low, varying between 0.5% DM and 1.7% DM. Particularly locations 2, 3 and 6 demonstrate a slightly higher OM content for the contrasting soil layer (Figure 6.5c). The depth-weighted average of the OM content is highest at locations 1 and 6 (1.5 and 1.0% DM), although the difference with locations 3 and 4 (0.98 and 0.91% DM) is very small. Each of the analyzed samples has a TPH concentration far below the soil remediation threshold and target value and only for one sample (location 2, 0.5–0.7 m depth) the background value is exceeded (Figure 6.5c). In contrast to locations 2 to 5, the TPH concentration hardly exceeds the LOD at locations 1 and 6. Excepting location 3, the profiles show the highest TPH concentration for the contrasting soil layer.

6.3.4 **Combined interpretation of the EC_a, GPR and borehole data**

Anomaly A was clearly delineated by sharp lateral and vertical contrasts in the GPR data. The significant scatter in the GPR signal in this area suggests the presence of coarse debris such as concrete rubble or bricks (e.g. Boudreault et al.,

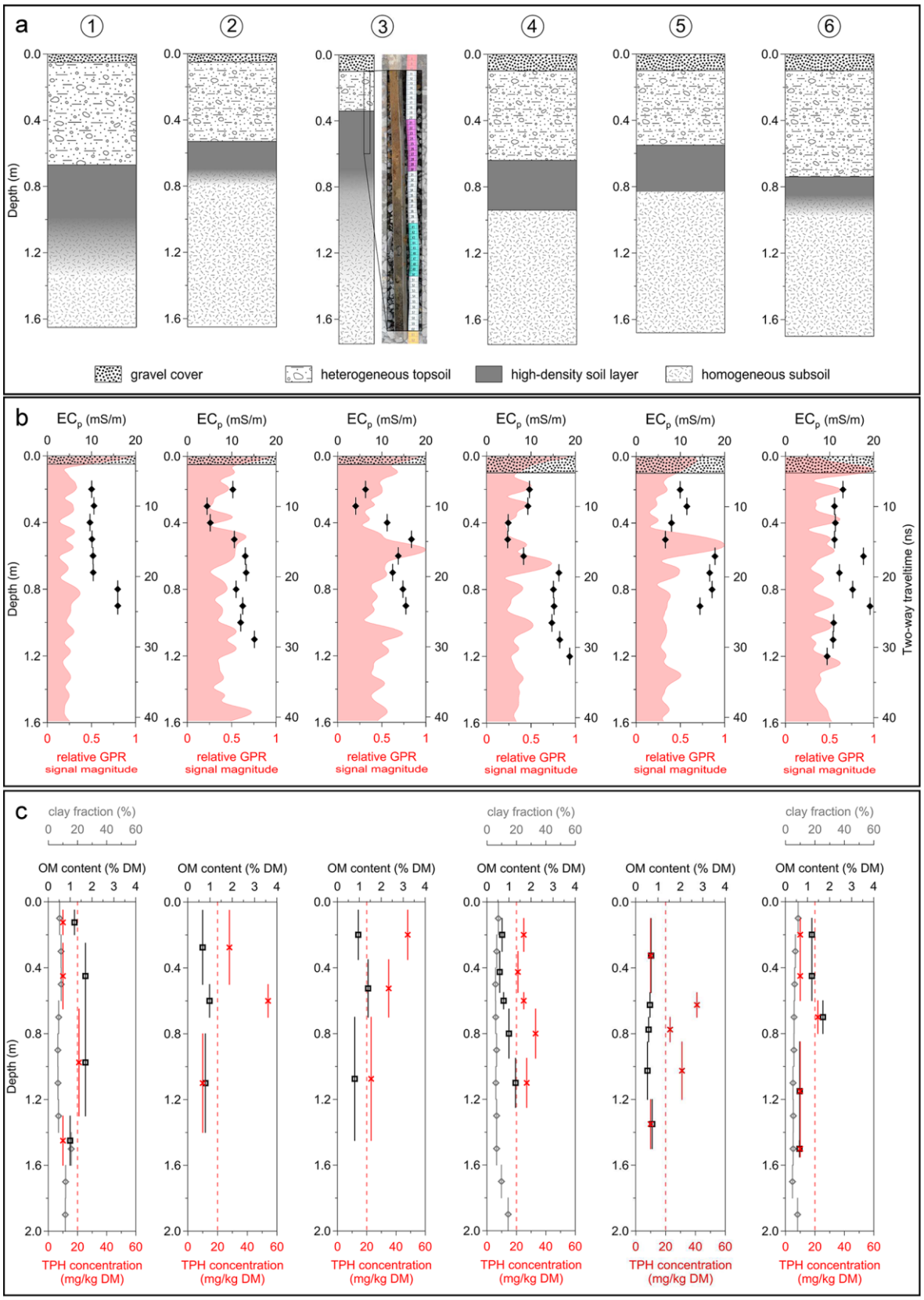

Figure 6.5 (a) Schematic representation of the soil profiles at the six locations indicated in Figure 6.2c showing four different soil layers in the upper 1.75 m of soil, with an illustration of the actual observation for 10–60 cm depth at location 3; (b) EC_p (top axis) as a function of depth (◆; vertical lines indicate the depth intervals for which the measurements are representative) and the local GPR signal magnitude (bottom axis) as a function of depth

Figure 6.5. (continued) divided by the local maximum magnitude (relative); the depth is expressed both in meters (left axis) and in two-way travel time (right axis) (c) clay fraction (upper top axis, ◇), OM content (lower top axis, □) and TPH concentration (bottom axis, ×) as a function of depth; the vertical dashed line indicates the LOD (20 mg kg^{-1} DM) for the TPH concentration; TPH analysis results below the LOD are represented by a concentration of 10 mg kg^{-1} DM.

2010). The shape and dimensions of the anomaly point to remains of a building or comparable structure. The presence of metals as indicated by the EC_a data further adds to this assumption given that old foundations and demolition debris often contain metallic objects such as reinforcing steel bars. The assumption was confirmed by surface building debris and by two soil borings encountering impenetrable material immediately beneath the gravel cover (Figure 6.6). A massive, probably reinforced, concrete structure and a brick layer of approximately 0.5 m thickness were encountered. We note that the location of the brick layer did not show the typical low-conductive signature of this material in the EC_a data, (Boudreault et al., 2010; Simpson et al., 2008; Simpson, Van Meirvenne, et al., 2009) which is likely explained by nearby metallic objects dominating the EMI sensor output. An aerial photograph of the site taken in 1986 relates the northeastern and southeastern edges of anomaly with a former fence (Figure 6.6). In November 1985, the site owner filed a request for an expansion of the existing garage. Probably the former building and its surrounding aboveground infrastructure were demolished shortly after the aerial photograph had been taken and the demolition debris used to level the area in preparation to the construction of the parking area. The discrete metallic objects scattered over the site likely relate to the former storage of accident-involved vehicles and garage activities. Anomaly B is not clearly delineated by the geophysical data, suggesting that this anomaly originates from a more gradual change of soil properties. In the GPR data, this anomaly appeared as a more reflective part of a shallow contrasting interface occurring over a major part of the survey area. Boring investigation allowed linking this interface with an abrupt transition from the topsoil to a highly disturbed layer with considerably higher bulk density. The EC_p measurements showed that the interface not only corresponded to a contrast in RDP, but also with a change in electrical conductivity. In the absence of a significant change in soil texture, the increase in conductivity can likely be attributed to the increased bulk density of the contrasting soil layer, thereby suggesting an effect of soil compaction (e.g. André et al., 2012; Islam et al., 2014a). Additionally, the slightly higher OM content may have further contributed to a higher conductivity (e.g. Omonode & Vyn, 2006; Saey, Van Meirvenne, et al.,

2009). The many anthropogenic disturbances observed for the contrasting soil layer, including its suggested higher compaction, along with its slightly higher OM content and its wide lateral extent indicated by the GPR profiles argue that its upper limit represents a former living surface. Starting from this idea, the GPR reflections defining the bottom of the debris fill in the western corner of the survey area probably coincide with this surface. This hypothesis is further supported by the aerial photograph taken in 1986 (Figure 6.6). In any case, the reorganization of the site after 1986 partly explains the heterogeneous appearance of the current topsoil. Through the EC_a and EC_p measurements, the main explanation for the lateral conductivity variability could be related to a variation of the properties of the current topsoil. While clay and OM content are two key 'natural' factors explaining spatial EC_a variations (e.g. Kühn et al., 2009; Saey, Van Meirvenne, et al., 2009), in this case neither property showed significant lateral variation. Although the observed subtle variations of these properties have contributed to the resulting sensor measurements, these do not fully explain the observed conductivity contrast. This suggests that the observed lateral contrast may also have a predominantly anthropogenic cause. Here, TPH concentration is the only property that showed a distinct difference between the boring locations as the LOD was only clearly exceeded at the locations within the low conductive zone. A decrease in electrical conductivity of the upper vadose zone due to the presence of a hydrocarbon contamination has been reported before (e.g. DeRyck et al., 1993) and has been suggested to relate to vapor effects.(Atekwana & Atekwana, 2010). A negative correlation between TPH concentration and electrical conductivity generally relies on the assumption that the effect of biodegradation is negligible. Even so, considering previous research (e.g. Daniels et al., 1995; Sauck, 2000; Carcione et al., 2003), it is questionable whether TPH concentrations lower than 50 mg (kg DM)−1 (equivalent to a hydrocarbon saturation lower than about 0.0001) are able to cause a conductivity decrease of several millisiemens per meter.

In this respect, it is more plausible that the slightly elevated TPH concentration is a proxy for a more complex physic-chemical soil disturbance that could not be fully defined by the limited number of properties that were analyzed on the boring samples. Regarding the within-profile coincidence of the highest TPH concentration and the highest conductivity, we propose two hypotheses. The first assumes that each of the observed hydrocarbon concentrations, irrespective of the depth at which they are observed, corresponds to a relatively fresh and, hence, non-degraded contamination. In this case, the higher OM content and soil bulk density have dominated the GPR

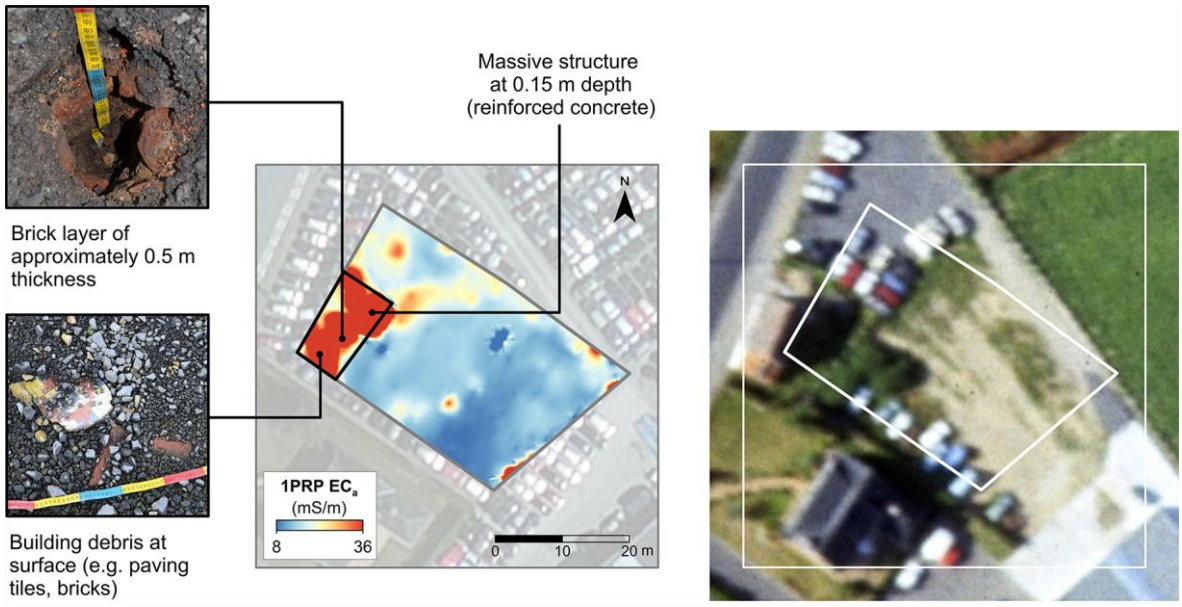

Figure 6.6 Field verification of the interpretation of anomaly A (Figure 2c) as the fill with demolition debris (left) and aerial photograph of the site taken in 1986 showing the former building and aboveground infrastructure near the location of anomaly A (source: Department of Archaeology, Ghent University, J. Semey) (right)

and EC_p measurements beneath the topsoil, but may have caused a higher retention of petroleum hydrocarbons in the contrasting soil layer (Fine et al., 1997; Yang et al., 2013) The second hypothesis assumes that the hydrocarbon concentrations observed in the contrasting soil layer relate to an older contamination event than those observed in the topsoil and that, with time, biodegradation processes have added to an increase in the electrical conductivity of this layer. Which of the two hypotheses is true cannot be determined with absolute certainty because no direct information on the occurrence of biodegradation was available. Yet, for locations 1, 2, 4 and 5, the composition of the hydrocarbon mixture showed smaller fractions of hydrocarbons in the C10 to C20 range in the contrasting soil layer as compared to the topsoil. Considering that the biodegradable fraction of petroleum hydrocarbons mainly consists of C12–C20 hydrocarbons (e.g. Minai-Tehrani et al., 2015), this may be an indication in favour of the second hypothesis. The contamination of the contrasting layer possibly even dates from before the site was reorganized at the end of the 1980s and in that case may also have a different lateral extent than the topsoil contamination.

6.4 Conclusions

Our case study demonstrated the use of combining multi-receiver EMI and stepped-frequency GPR to pinpoint locations of anthropogenic soil disturbances, particularly of those having affected physical soil properties. The identification of a soil layer with considerably higher bulk density exemplified the methodology's potential to improve insight into the upper soil stratification, which in turn could aid the understanding of the local soilforming processes. Furthermore, the sharp delineation of the building remains illustrated the high accuracy that can be achieved in spatially characterizing structures of technogenic material. Since such physical soil contrasts locally can have a strong influence on the distribution and dispersion of contaminants, they can represent important targets in the investigation of contaminated urban soils. The demonstrated correspondence between a zone of remarkably lower electrical conductivity and slightly elevated TPH concentrations suggests the potential of the sensor combination to detect specific chemical soil disturbances too. However, further investigation should aim at the expansion of the presented methodology to other conditions of contamination with petroleum hydrocarbons, including a wider range of concentrations and biodegradation stages. This case study proves the advantage of the sensors to rapidly screen urban soils for geophysical anomalies, but also indicates that interpretation of these anomalies in terms of anthropogenic disturbances might not always be straightforward. This can be complicated further when metallic objects are prevalent in the studied urban environment. Specifically EMI is very sensitive to such local high conductors causing the geophysical signature of the soil material directly surrounding them to be compromised. Yet, the guaranteed detection of metallic objects may be an advantage in case they represent major targets in the site's investigation. In any case, the detailed 3D soil information provided by the sensor combination offers a sound guide for the initial sampling design of invasive investigation. The so-designed boring investigation can serve as ground truth and can aid in selecting the relevant geophysical anomalies for more in-depth investigation. Generally, we conclude that the proposed methodology is particularly valuable in an exploratory phase of urban soil assessment, to direct future (invasive) investigation and to support the intra- and extrapolation of information derived therefrom.

6.5 **Acknowledgements**

The authors would like to thank Gert Moerenhout and Sven Van Daele from the Soil Remediation Fund for Petrol Stations (BOFAS) for introducing this case study and for providing all the earlier collected site information. We also thank the owner–occupiers for their kind hospitality during our visits and Valentijn Van Parys for his help with the EMI and GPR surveys.

Chapter 7
Combining EMI and GPR for industrial site investigation

The content of this chapter is based on:

> Van De Vijver, E., Van Meirvenne, M., Saey, T., Delefortrie, S., De Smedt, P., De Pue, J., & Seuntjens, P. (2015). Combining multi-receiver electromagnetic induction and stepped frequency ground penetrating radar for industrial site investigation. *European Journal of Soil Science*, 66(4), 688–696

7.1 Introduction

Industrial sites present a challenge to the conventional way of characterizing soil and groundwater properties because of their complex history of land use. The subsurface of these sites is typically characterized by very heterogeneous properties, which are often related to physical disturbance and contamination. Characterization of such heterogeneous soil based on a limited number of discrete observations from borings, monitoring wells and trenches can lead to results that are unreliable or unrepresentative of the industrial site. Proximal soil sensors can measure soil properties in a non-invasive way, making them efficient in recording spatially comprehensive soil data (Viscarra Rossel et al., 2011). However, because the output signal of most sensors is affected by more than one soil property, single-sensor measurements are often inadequate for discriminating between all contributing effects (Adamchuk et al., 2004). This is particularly relevant to industrial sites where the characteristics of the soil can be more complex because of anthropogenic

disturbances, which calls for an approach that combines multi-sensor measurements to improve the discrimination between the variation of different subsurface properties.

Two prime proximal sensing methods for industrial site investigation are EMI and GPR. Electromagnetic induction provides measurements of both EC_a and MS_a. Measurements of EC_a are suitable for environmental problems such as locating underground contamination sources, mapping spills and tracing groundwater contaminants, whereas MS_a measurements can be used for the detection of discrete metallic objects such as underground storage tanks (Fitterman & Labson, 2005). Ground penetrating radar uses electromagnetic waves to map changes in soil electromagnetic properties and responds primarily to contrasts in RDP and electrical conductivity. Therefore, it is useful for various applications: (i) for locating buried structures and utility services such as pipes and cables (Yelf, 2007), (ii) for exploring the variation in soil properties such as water content, soluble salts concentration, clay content, OM content and bulk density, and for detecting soil interfaces corresponding to abrupt changes in these properties (Doolittle & Butnor, 2009) and (iii) for mapping inorganic or organic chemical contamination (Redman, 2009). There are few studies that use both these sensing techniques to investigate anthropogenic soil disturbance at industrial sites (Bermejo et al., 1997; Marchetti et al., 2002; Boudreault et al., 2010). However, those that exist, confirm that EMI and GPR can provide an effective combination for the investigation of industrial sites.

Recently, there have been rapid advances in sensor technologies that facilitate the collection of soil data. For EMI, the state-of-the-art sensors are multi-receiver (Simpson, Van Meirvenne, et al., 2009; Saey, Van Meirvenne, Dewilde, et al., 2011; Triantafilis et al., 2011) or multi-frequency (Martinelli & Osella, 2010) instruments that enable the simultaneous sensing of multiple depths. This not only increases the possibilities to infer variation in depth in soil properties, but also offers a greater potential for detection and discrimination of localized soil disturbances. The GPR technology developed towards more effective coverage of 3D space with the introduction of antenna arrays (Novo et al., 2012) and multi-frequency systems (Eide and Hjelmstad, 2002). The latest sensor designs integrated with differential GPS positioning enable rapid and efficient mobile surveys with horizontal sampling resolutions in the decimetre to centimetre range. Data from these sensors can support more comprehensive analysis of soil volumes that opens up new prospects for combining data from different sensors. Despite the promising results of earlier

investigations with EMI and GPR, the potential of such an advanced sensor combination has not been examined for industrial site investigation.

This chapter presents a case study that demonstrates the use of multi-receiver EMI and stepped frequency GPR coupled with an antenna array, both in a mobile platform, to survey an industrial site. Our aims were to use this combination of sensors to describe the 3D organization of the soil and to characterize specific subsurface anomalies that relate to anthropogenic soil disturbance.

7.2 Materials and methods

7.2.1 Study site

The study is at a former gasworks site, which is a classic example of a complex industrial environment (Hatheway, 2002). The 36-ha site is in a seaport area of Belgium. Between 1995 and 2000, the site was subjected to a series of environmental assessments as part of a soil remediation project. The assessment report includes general site information obtained through a desk study as well as more detailed soil information from borings and monitoring wells. The soil was reported to consist of two distinct layers: over the entire industrial site the top natural layer of soil consists of polder clay that has been raised by a sandy embankment layer of one to two metres in thickness. The embankment layer is strongly heterogeneous with coarse sand and gravel alternating with intercalations of clay, peat and debris. The groundwater level fluctuates between 0.5 and 2 m below the surface. The assessment report gave contradictory information about salinity of the groundwater. However, its situation next to a brackish water canal and its classification on the salinity map of Vandenbohede et al. (2010) support the likelihood that saline groundwater is present. Based on the *a priori* information and the need for access with a quad bike, we selected a 3400 m² area for our multi-sensor survey. This area had a sodium tripolyphosphate (STPP) production unit that operated from 1952 to 1987 (Figure 1a). The STPP unit has been demolished, and the study area is now a mown grass area free of any industrial activity, except for an above-ground transport pipe (Figure 1b). The surrounding buildings (two to three storeys high) are still used for industrial purposes.

7.2.2 The EMI survey

The instrument used for the EMI survey was a multi-receiver frequency domain EMI sensor (DUALEM-21S, DUALEM Inc., Milton, Canada). The quadrature-phase

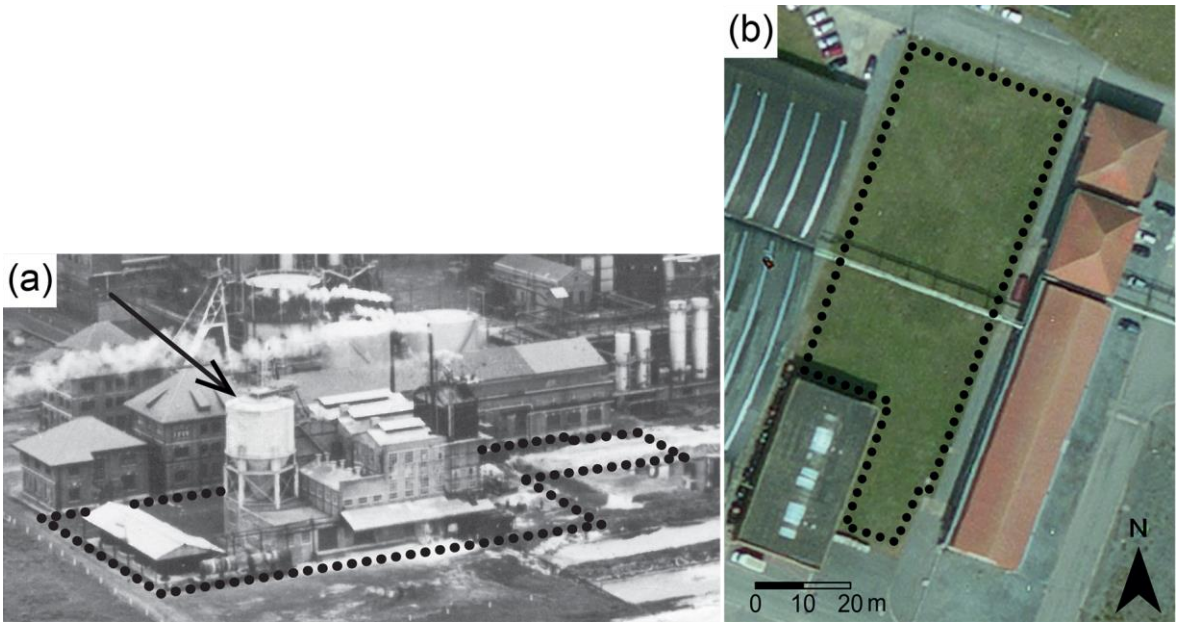

Figure7.1 Aerial photographs of the STPP production unit in 1959 (a) and the study site in its present state (b). In both photographs the boundary of the selected study area is indicated by the red line. The arrow indicates the silo of the STPP production.

and in-phase signal responses of the EMI sensor are representative of the EC_a and the MS_a of the soil (Keller & Frischknecht, 1966; McNeill, 1980). The support of these EC_a and MS_a measurements depends on the coil configuration from which they are generated. The DUALEM-21S sensor contains one transmitter coil and four receiver coils at spacings of 1 m, 1.1 m, 2 m and 2.1 m. For the 1-m and 2-m transmitter-receiver pairs, both coils have horizontal windings that form horizontal co-planar (HCP) arrays. The other pairs form PRP arrays as the receiver coils have vertical windings. Each of the four coil configurations results in a different soil volume represented in the EC_a and the MS_a measurements. The ECa measurements for the 1.1 m PRP, 2.1 m PRP, 1 m HCP and 2 m HCP configuration are representative of soil volumes to depths of 0.5 m, 1.0 m, 1.6 m and 3.2 m, respectively (Saey, Simpson, et al., 2009). The MS_a response for the PRP configurations is often unstable in field conditions (De Smedt, Saey, et al., 2014) and was disregarded in this study. For the HCP configurations, the MS_a measurements correspond to soil volumes to depths of 1 m and 1.5 m (De Smedt, Saey, et al., 2014).

The sensor was used in mobile configuration by fixing it in a sledge behind a quad bike (Figure 7.2A). A differential GPS, with its antenna mounted on the back of the quad bike, was used to georeference the sensor measurements in real-time with an accuracy of about 10 cm. The area was surveyed along parallel lines 90 cm apart. The distance between any two measurements along the lines was maintained at

around 25 cm (Figure 7.2B) through a sampling frequency of 8 Hz and a driving speed of approximately 7 km hour^{-1}.

Figure 7.2 Mobile EMI survey configuration with the DUALEM-21S sensor mounted in a sledge behind a quad bike (A) and a schematic representation of the sampling pattern (the illustration here includes three parallel survey lines) (B).

7.2.3 **Processing of the EMI data**

The mobile set-up of the EMI sensor with GPS georeferencing requires some specific processing steps. First, the measured GPS coordinates were corrected for the spatial offset between the GPS antenna and the centre of the transmitter-receiver coil pairs of the EMI sensor in MATLAB 7.13 R2011b (The MathWorks Inc., Natick, USA). This correction procedure, first described in Simpson et al. (2008), comprises a backwards shift of the recorded locations along the driving line (i.e. along the direction defined by previous GPS measurements in time) by a user-defined offset distance. Then, the measurement locations were mapped with ArcMap version 9.2 (ESRI, Redlands, USA). Measurements at locations that deviated from the lines, i.e. that related to places where the GPS satellite visibility was too weak for accurate georeferencing, were removed from the data set. Next, the sensor measurements were corrected for drift in time using measurements from a reference line that was driven prior to the EMI survey, that crossed all the parallel driving lines anticipated for the survey. By comparing the recorded EC_a and the MS_a values of the survey measurements with those of neighbouring reference measurements, the drift in time was identified and corrected for (Simpson, Van Meirvenne, et al., 2009). Then, for the EC_a and MS_a data sets of all four coil configurations the main summary statistics were calculated. Finally, to map the results the measurements were interpolated to a grid with a 0.1 m cell size by ordinary punctual kriging (Goovaerts, 1997) with the software Surfer version 10 (Golden Software Inc., Golden, Colorado).

7.2.4 **The GPR survey**

The basic configuration of surface GPR uses a transmitter antenna that emits electromagnetic energy into the ground and a receiver antenna that detects reflected and scattered energy. Reflections are generally generated from contrasts in RDP. The strength of the reflection, represented by the magnitude of the GPR signal, is proportional to the degree of contrast that was encountered, while the time delay between emission of the electromagnetic wave and detection of a returning reflection (the so-called two-way travel time) is proportional to the depth at which the contrast is located. The most common GPR systems are impulse GPRs in which a time-domain pulse is transmitted and the reflected energy is received as function of time. In this study, however, we used a GeoScope GS3F system (3d-Radar AS, Trondheim, Norway), a SFCW GPR that can generate waveforms from 50 to 3000 MHz. The transmission of a continuous wave over such a wide frequency bandwidth overcomes the trade-off between penetration depth and resolution, which is inherent in impulse GPR systems. It provides the best resolution for each achievable measurement depth. Furthermore, because the transmitting frequency is stepped in linear increments, energy is focused on one single frequency at a time. This implies a more efficient way to emit energy into the ground anticipating an improved SNR and penetration depth (Koppenjan, 2009). The stepped frequency system operates with an electronically scanned array of air-coupled antennae, where the combination of sequential transmitting-receiving antenna pairs allows the quasi-simultaneous of multiple survey lines (channels) at high speed. The air-coupling of the antennae facilitates the use of motorized conveyance, but this is at the expense of a part of the potential gain in SNR of the stepped frequency technology as more energy will be reflected at the air-ground interface. Here, a V1213 antenna array was used which covers a scan width of 97.5 cm using 13 channels with a uniform spacing of 7.5 cm.

The GeoScope was installed on the back of a quad bike as illustrated in Figure 7.3A. The antenna array was mounted on a trailer with its lowest point 5 cm above the ground surface. Similar to the EMI survey, the GPR survey platform provided real-time georeferencing using a differential GPS. Here the GPS antenna was positioned on the centre of the GPR antenna array to avoid spatial offset in the inline direction. The cross-line offsets between the GPS antenna and the different GPR antenna pairs in the antenna array were automatically accounted for by the GeoScope system. To achieve complete cover of the survey area, the driving pattern ensured a minimal overlap of 10 cm of two adjacent scans. In the inline direction, the measurement

interval was controlled by an odometer integrated in one of the trailer wheels. The interval distance was set to 5 cm, so that within an individual scan track a horizontal resolution of 7.5 cm by 5 cm was obtained (Figure 7.3). Measurements were made over a frequency bandwidth of 50 to 1500 MHz in steps of 2 MHz, with a 2-μs duration of each step. The recorded data were stored in the frequency domain.

Figure 7.3 Mobile GPR survey configuration with the V1213 antenna array mounted on a trailer pulled by a quad bike (A) and a schematic representation of the horizontal sampling pattern within a single scan track (B).

7.2.5 **Processing of GPR data**

The literature provides a large number of references devoted to the processing of GPR data (Annan, 1999, 2001; Cassidy, 2009b). The majority of these papers focus on the processing methods of time-domain GPR systems, but many processing steps are applicable to frequency-domain GPR systems. The recent paper by Sala and Linford (2012) provides a detailed description of the specific processing steps required for SFCW GPR data.

In our study, the first processing steps were performed with the 3DR-Examiner software (3d-Radar AS, Trondheim, Norway), which is specific for processing data from 3d-Radar GPR systems. First, we removed scan segments that were redundant or inaccurately positioned because of a loss of the GPS signal. We then converted the frequency domain data to time domain through an inverse fast Fourier transform (Cooley & Tukey, 1965). We used a Kaiser window with a beta value of 6 (Harris, 1978) and limited the frequency bandwidth to 200–800 MHz to reduce both low- and high-frequency noise. A background removal based on a high-pass frequency filter was applied to eliminate horizontal banding in the vertical GPR profiles. We improved further the SNR with a horizontal filter with the filter size computed as a function of depth. To facilitate subsequent analysis and visualization, the measurement locations were subsampled to a 0.1 m by 0.1 m grid by a nearest-neighbour interpolation (so-

called 'stitching' function in 3DR-Examiner that stitches individual scan tracks together). Re-sampling to this coarser horizontal resolution reduced the total file size by more than 70% (from 5.7 GB to 1.6 GB). Next, we calculated the mean and the standard deviation of the GPR signal magnitude for each depth from the re-sampled data set in MATLAB. Because of signal attenuation and spreading losses, the magnitude of the GPR signal generally decreases with depth. As signal attenuation increases with increasing electrical conductivity, the rate at which the magnitude of the GPR signal decreases with depth is indicative of the soil electrical conductivity. Note that so far the processing steps have operated in the time domain and 'depth' above refers to depth in two-way travel time. For realistic interpretation, the depth in two-way travel time was converted to depth in metres which requires an estimate of the so-called ‘time zero’ (the two-way travel time corresponding to the air-ground interface) and the average GPR wave velocity in the soil, which is directly related to the RDP of the soil. Time zero was assumed constant over the survey area and was estimated as the average two-way travel time where the largest GPR signal magnitude occurred (3DR-Examiner software). For simplicity, the RDP of the soil was also assumed to be constant and was derived from the literature as a typical RDP value for a wet sandy and potentially saline soil (Cassidy, 2009a). Prior to visualization, an AGC was applied to compensate for the decrease in reflection strength (Cassidy, 2009b). The more the GPR signal is attenuated, the larger the gain factor that is required for this compensation. As a result, the gain factor can be related to signal attenuation and thus soil electrical conductivity. Because the 3DR-Examiner software does not support AGC, we implemented the gain function in MATLAB. Finally, the 3D data set was visualized in a series of horizontal slices by mapping the average GPR signal magnitude within 10-cm depth intervals. Visualization was performed in Surfer with the same grid as for the EMI maps.

7.2.6 **Combined interpretation of EMI and GPR**

First, we examine the results of both surveys separately based on the calculated statistics and the interpolated maps of the EC_a, MS_a and GPR data. We then combine the derived information to evaluate the joint insight that the sensors can provide to the general 3D organization of the soil. The potential of the sensor combination to detect and characterize localized soil disturbances was investigated by using a selection of anomalies with different signatures in the different sensor maps. The combined

interpretation was verified with information from the earlier environmental assessments.

7.3 Results and discussion

7.3.1 The EMI results

A statistical summary of the processed EMI data is given in Table 7.1. Each of the output signals covers a wide range of values because of both positive and negative extreme values. The median EC_a varied from 101 mS m^{-1} for the 1.1 m PRP configuration to 262 mS m^{-1} for the 2 m HCP configuration. The order of the coil configurations according to the median EC_a is as follows: 1.1 m PRP < 2.1 m PRP < 1 m HCP < 2 m HCP. This order corresponds with increasing measurement depth of the coil configurations indicating an increase in soil conductivity with depth. However, the large values of the median EC_a, especially that for the 2 m HCP configuration, suggest very conductive conditions. Under such conditions, EC_a measurements might be under-estimates of the true conductivity, the depth of the soil volume of which they are representative might be reduced and EC_a and MS_a might become interdependent (Callegary et al., 2007; Beamish, 2011). This interdependence might explain the large median MS_a values that were observed. Nevertheless, the EMI measurements are still useful for observing horizontal and vertical variation in EC_a and MS_a (Delefortrie, Saey, et al., 2014). The variance was extremely large for all measurement signals: the

Table 7.1 Summary statistics of the EC_a and MS_a for the considered coil configurations of the DUALEM-21S sensor. Abbreviations: N, number of data points; m, mean; me, median; min, minimum; max, maximum; var, variance; std, standard deviation; skew, skewness.

	EC_a (mS m^{-1})				MS_a (msu SI)	
	1.1 m PRP	2.1 m PRP	1.1 m HCP	2.1 m HCP	1 m HCP	2 m HCP
N	19452	19453	19451	19451	19451	19451
m	162	235	231	280	0.00455	0.0220
me	101	180	199	262	0.00410	0.0219
min	-320	-1469	-3324	-2704	-0.656	-0.675
max	3309	3278	1892	1642	0.220	0.406
var	56743	36157	49904	37479	0.000543	0.003350
std	238	190	223	194	0.0233	0.0579
skew	8.10	2.52	-5.14	-2.41	-14.63	-6.45

CV varied between 69% and 147%, which is about five to ten times larger than for an average arable field in northern Belgium (Vitharana et al., 2006; Van Meirvenne et al., 2013). This indicates considerable variation in the EC_a and MS_a of the soil. Because the variance is generally sensitive to extreme values, in this case, no reliable inferences about relative changes in soil variability in depth can be made from the change in variance in function with measurement depth of the different coil configurations.

Kriging interpolation of the EMI data results in six detailed images of the site's subsurface (Figure 7.4). Each map reveals a complex pattern of very variable EC_a and MS_a values that illustrates the considerable heterogeneity of the soil in terms of the materials that comprise it. Many of the spatial outliers in EC_a and MS_a suggest an anthropogenic origin because of their linear or circular shapes, or their regular spatial

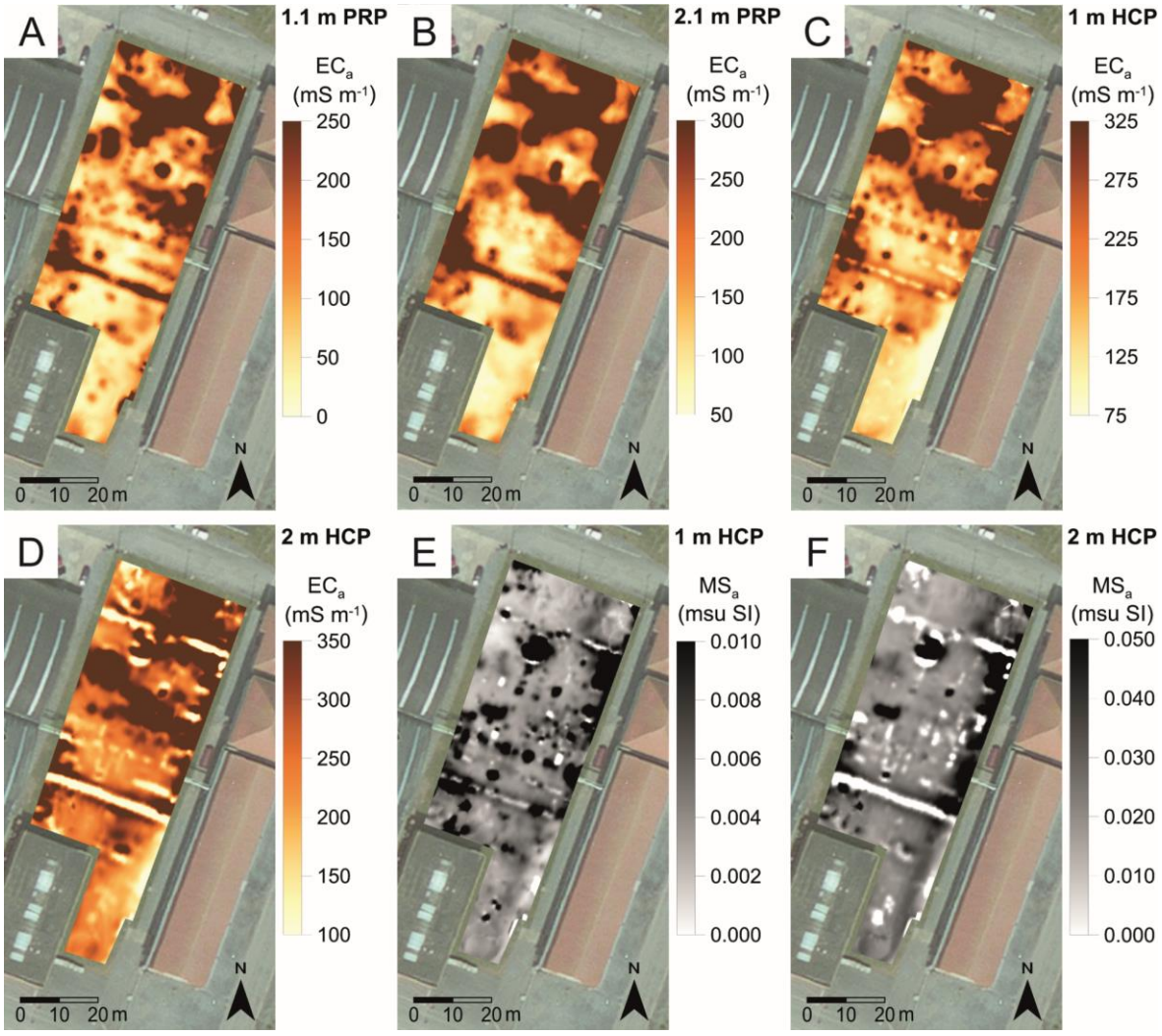

Figure 7.4 Results of the EMI survey using a DUALEM-21S sensor: interpolated EC_a data for the 1.1 m PRP (A), 2.1 m PRP (B), 1 m HCP (C) and 2 m HCP (D) coil configurations, and interpolated MS_a data for the 1 m HCP (E) and 2 m HCP (F) configurations.

arrangement. Most of these anomalies show strong responses (either positive or negative) for both EC_a and MS_a simultaneously, which typically indicates the presence of metallic objects. The EC_a maps also show large values between the local anomalies, which is consistent with the large median values of the data sets. These values are uncommonly large (Saey, Van Meirvenne, et al., 2009) for non-saline soil in northern Belgium, suggesting some degree of salinization.

7.3.2 The GPR results

In Figure 7.5A the mean and standard deviation envelope of the magnitude of the GPR signal, before AGC, is plotted as a function of depth. The conversion of depth in two-way travel time to depth in metres is based on a time zero of 2.197 ns and a RDP of 20. From its maximum at the air-ground interface (time zero) to a depth of about 0.9 m (or 30 ns), the mean magnitude of the GPR signal decreased exponentially with depth and then levels off around its minimum value. Logically, the AGC function (Figure 7.5B) shows the opposite behaviour. The gain factor increased exponentially with depth and reaches 90% of its maximum value at 0.8 m (or 26 ns) below surface level. Both plots thus indicate strong signal attenuation in the upper 0.8 m of the soil, suggesting that this shallow soil layer has a large electrical conductivity. The gain factor reached its maximum at around 1.3 m depth and then decreased with depth, indicating that noise starts to dominate. Hence, we estimate that the GPR signal was lost at a depth of approximately 1.3 m. Figure 7.6 shows the 10-cm thick horizontal slices to a depth of 1.5 m. The increasing noise level in the successive images confirms the inferences already noted concerning the SNR as a function of depth. Clear contrasts in reflection strength were discernible only in the upper slices. Confined areas with locally increased reflection strength are likely to represent buried structures such as the area indicated by the black circle in Figure 7.6. The large 3D variation in the magnitude of the GPR signal is further evidence of the considerable spatial heterogeneity of the upper 1 m of the soil.

7.3.3 Combined interpretation of EMI and GPR

The sensor maps show the extreme heterogeneity of the embankment layer in 3D space and indicate the abundance of non-natural, and often metallic, objects in the soil. Notwithstanding that the general increase in soil conductivity with depth is consistent with the transition from a sandy to a clayey layer, it is difficult to reconstruct this stratification of the soil using only the sensor results. The reason for this is

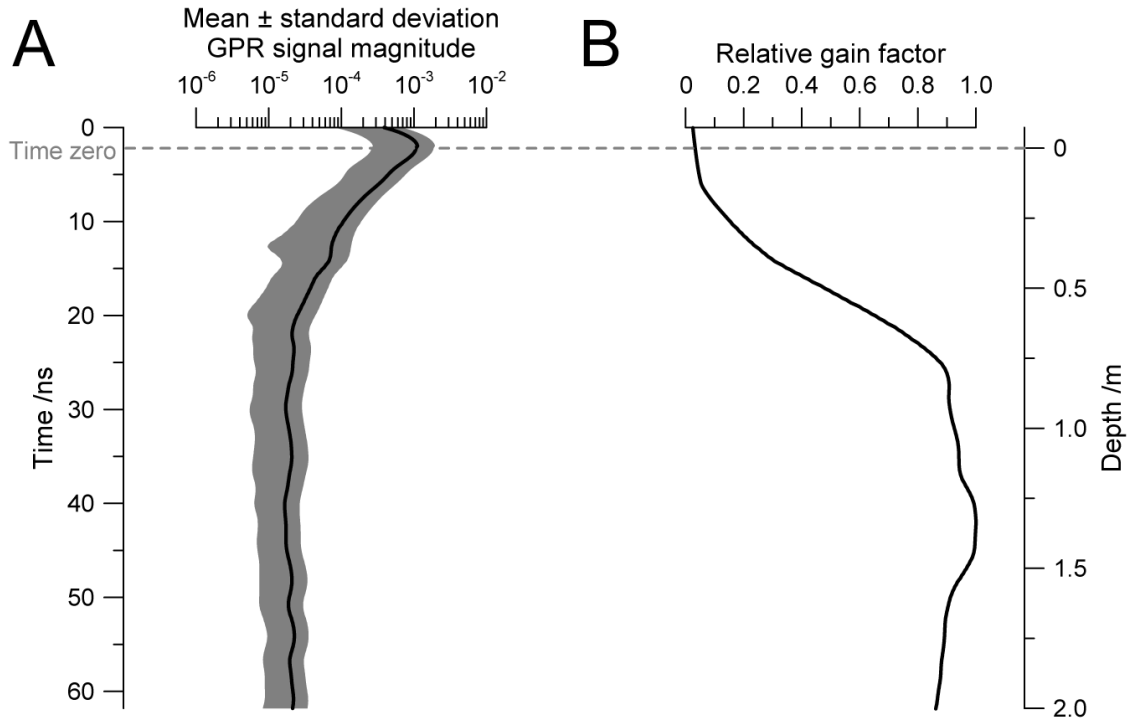

Figure 7.5 Mean (black line) and standard deviation envelope (grey shaded area) of the magnitude of the GPR signal before AGC (A) and the relative gain factor (the absolute gain factor divided by the maximum absolute gain factor in the considered depth interval) applied during AGC (B), both in function of depth. The depth is expressed in two-way travel time (left) and in metres (right); the conversion between these units is based on a RDP of 20 and a time zero of 2.197 ns. Note the logarithmic scale used to express the magnitude mean and standard deviation envelope.

twofold: (i) the spatial density of local soil disturbance is too great to make reliable inferences about background variation in the electromagnetic properties of the soil and (ii) the sensor measurements seem to be affected by salinization. The latter is consistent with our rationale about groundwater salinity. For EMI, this means we cannot use established relationships between EC_a and soil texture (Saey, Van Meirvenne, et al., 2009) on the one hand, and between EC_a and depth-to-clay on the other (Saey, Van Meirvenne, De Smedt, et al., 2011), as both are only valid in non-saline conditions. For GPR, the saline conditions were probably the main reason for the small penetration depth, which was insufficient for GPR to provide additional information about stratification of the soil compared to EMI. Other studies that used a similar stepped frequency GPR also report a small penetration depth in non-saline conditions (Linford et al., 2010). Furthermore, the industrial site studied seems to form a noisy environment for GPR, but it is difficult to confirm the specific cause. Apart from the effect of salinization specific for this site, the extent of soil disturbance is a more

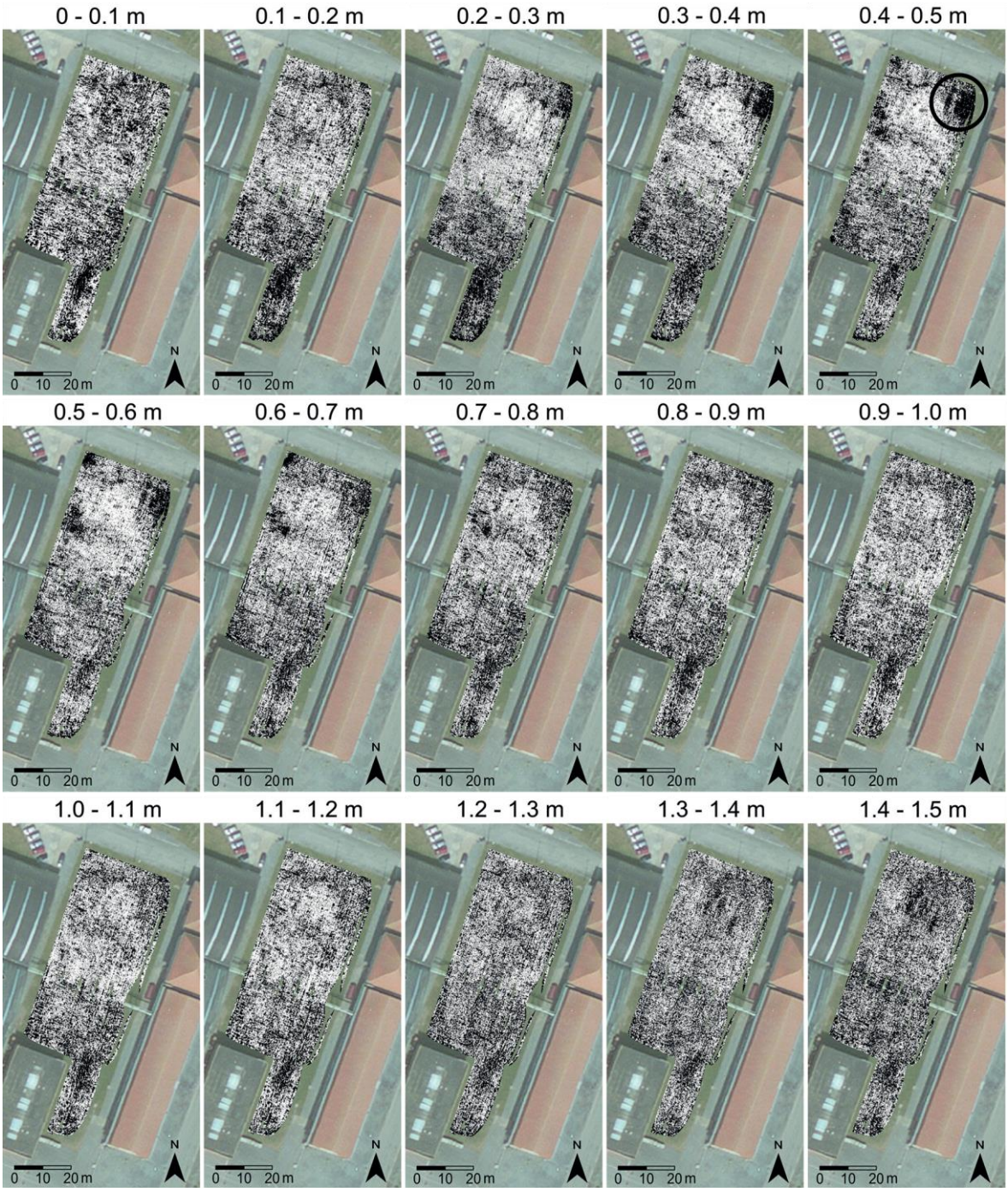

Figure 7.6 Horizontal slices of GPR data from 0 to 1.5 m depth, integrated over 10-cm depth intervals. The greyscale (white to black) represents the signal magnitude or reflection strength (weak to strong). The contrast has been optimised for each slice separately. The black circle in the 0.4–0.5-m slice indicates a confined area with locally increased reflection strength suggesting the presence of a buried structure.

representative general characteristic of industrial sites. This case study suggests that for industrial sites EMI and GPR are of limited value for mapping soil stratification or the properties of individual layers such as soil texture, which is a typical application in pedology, precision agriculture and geoarchaeology, for example (Doolittle & Collins,

1995; Vitharana et al., 2006; Saey, Van Meirvenne, De Smedt, et al., 2011). However, as industrial site investigation is usually carried out within the scope of a remediation or redevelopment project, the main focus is often on specific problems such as contamination and buried infrastructure rather than on background soil properties. Consequently, we evaluate the sensor combination in terms of the ability to detect and identify specific anthropogenic soil disturbances by discussing three types of anomalies.

Anomaly 1: utility services

The first anomaly is a linear one with extreme values of EC_a and MS_a for each of the coil configurations (Figure 7.7a): a typical indication of a metal pipe or an electric cable. As shown also in Saey, Van Meirvenne, Dewilde, et al. (2011), and Martinelli and Osella (2010), the EMI's sensitivity to strong conductors guarantees the detection of such subsurface structures, but it can lead to spatially exaggerated anomalies in the EMI maps. In the 1.1 m PRP EC_a map the width of the linear anomaly is 3 m or more, which hampers estimation of the true dimensions of the detected structure. Furthermore, the EMI measurements do not enable the depth at which the structure occurs to be estimated because the validity of the depth responses of the EMI signals is compromised by the large actual conductivity of metallic objects. The GPR measurements confirm that the EMI anomaly is caused by a buried structure because a thin line of strong reflection appears in the horizontal slice for 0.5–0.6 m depth. In this GPR slice, the width of the anomaly is much smaller than in the EMI maps with more realistic dimensions for metallic pipes or cables. The GPR can locate metallic structures more accurately in 3D space by showing their actual dimensions in the horizontal plane and their positions on a depth scale. Despite the prevalence of noise, the sensor achieves considerable detail in this because of its compatibility with near centimetre-scale horizontal measurement resolution and the wide frequency range of the GPR signal. Comparison with a utility services map suggests that the anomaly corresponds to a cable. However, the EMI and GPR maps do not show an anomaly where the cable is in the utility services map, indicating that the location of the cable was incorrectly documented. This example thus demonstrates the capacity of the sensor combination for the accurate location of buried utility services.

Anomaly 2: buried structures

The second selected anomaly (Figure 7.7b) concerns a regular pattern of dots defined by large values of EC_a and MS_a. The pattern is visible in each of the EMI

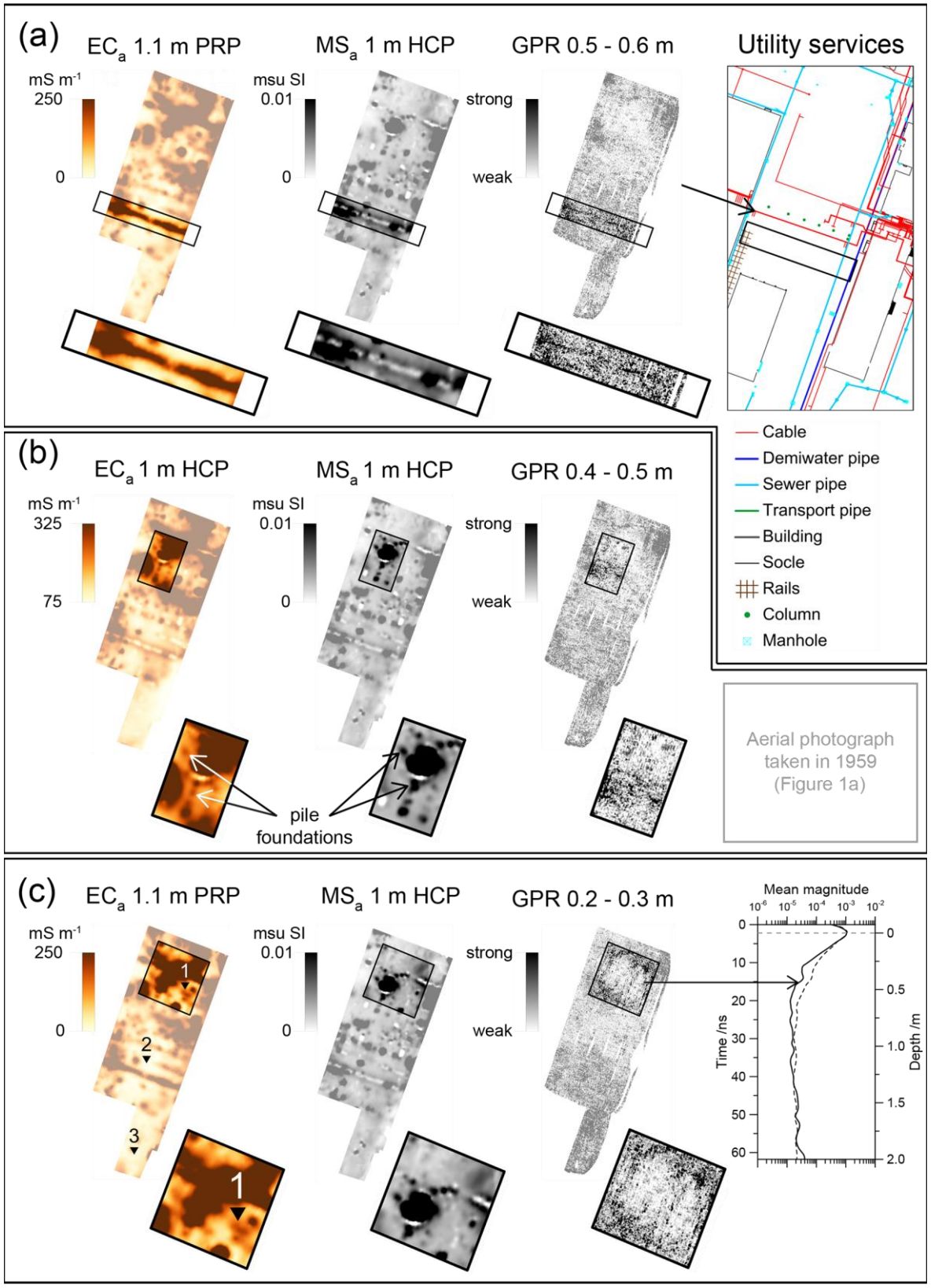

Figure 7.7 (a) Anomaly 1 highlighted on the 1.1 m PRP EC_a map, on the 1 m HCP MS_a map and on the horizontal GPR slice for depth interval 0.5–0.6 m, and comparison with a utility services map of the site. The black arrow indicates the presumably mis-represented cable causing the anomaly at the location of the black rectangle. (b) Anomaly 2 on the 1 m HCP EC_a and 1 m HCP MS_a maps and on the horizontal GPR slice for depth interval 0.4–0.5 m.

Figure 7.7 (continued) (c) Anomaly 3 on the 1.1 m PRP EC_a map, on the 1 m HCP MS_a map and on the horizontal GPR slice for depth interval 0.2–0.3 m; comparison of the mean signal magnitude in function of depth for a subsample of GPR traces contained in anomaly 3 (blue line) and the entire study area (black line). The three point locations (▼) on the 1PRP EC_a map indicate sample locations of soil extract conductivity measurements.

maps, but is most sharply outlined in the 1 m HCP output signals. The aerial photograph shown in Figure 7.1a indicates a correspondence between the dots arranged in circle and the silo piles of the former STPP unit (red arrow), suggesting that the anomaly results from the remains of reinforced foundations. Without prior knowledge of the EMI data, the reflections from these structures might be difficult to distinguish from background noise in the horizontal GPR slices. Inside the circle of pile foundations, large values of EC_a and MS_a that coincide suggest the presence of another larger, circular, structure containing metal (Figure 7.7b). The GPR data contradicts this suggestion because the generally small magnitude of the GPR signal at this location gives no indication of a large buried structure. This example shows the complementarity of the EMI and GPR sensors for detecting buried structures. If the lateral dimensions of a structure that contains metal are too small to cause a clear GPR anomaly, the dense simultaneous EC_a and MS_a measurements still ensure a large detection potential, together with a strong potential for discrimination between closed-spaced structures. In contrast, in specific cases a serried arrangement of metal structures can disturb an induced electromagnetic field so that EMI gives a false indication of another metal structure, which can then be rectified by GPR.

Anomaly 3: contamination

The last anomaly, highlighted in Figure 7.7c, is identified as a weak reflecting area in the shallow GPR slices, which is confirmed by a stronger signal attenuation than average (Figure 7.7c, right). A possible explanation is that former STPP production activities led to salt contamination resulting in locally increased conductivity. Laboratory analysis of electrical conductivity on soil extracts of samples from the three locations indicated in Figure 7.7c (left) support this explanation. For the upper 0.8 m of soil, soil extract conductivity reaches 170 mS m^{-1} at location 1, whereas at locations 2 and 3, respectively, values of only 15 mS m^{-1} and 39 mS m^{-1} occurred. The EMI maps cannot give a reliable confirmation since the anomaly from each of the EC_a signals is compromised by the proximity of metal objects. Although the GPR's speciality is the detection and location of buried structures, this example illustrates that it can provide valuable information about the nature of soil materials as well. This can be particularly

useful for applications such as the detection of contamination on industrial sites with a high density of metal structures.

7.4 Conclusions

This study is a novel contribution to proximal soil sensing through the combination of multi-receiver EMI and stepped frequency GPR for the investigation of industrial sites. The fine-resolution sensor data enabled detailed subsurface maps to be generated that showed the extreme subsurface heterogeneity that can occur on industrial sites, including various anthropogenic disturbances. These localized anthropogenic disturbances complicate the interpretation of the sensor measurements with regard to background soil properties such as soil texture and soil stratification. In our case study, however, interpretation was further compromised by the effect of salinization. Anomalies detected included utility services, building foundations and contamination; each of them represented typical targets in industrial site investigation. The characterization of these targets was possible only by the combination of the multiple EMI signals and 3D GPR data demonstrating the added value of this advanced sensor combination compared to their earlier generation counterparts. Consequently, we conclude that the combination of multi-receiver EMI and stepped frequency GPR with antenna array shows promise for industrial site investigation.

7.5 Acknowledgements

We would like to thank the company owners and environmental coordinator for granting access to the industrial site and openly exchanging existing site information. We also thank Valentijn Van Parys for sharing his technical skills and capabilities during the field work.

Chapter 8
General conclusions and future prospects

8.1 EMI and GPR in urban and industrial environments: do they deliver?

The overall objective of this work was to evaluate the use of proximal geophysical sensors to investigate the soil in urban and industrial environments. The focus was on two types of electromagnetic sensors: EMI and GPR. In this final chapter, a summary is given of the most important conclusions made with respect to the following aspects: the practical implementation of the proposed survey methodology, the direct information provided by the collected data, its integration with conventional invasive observations, and the general relevance of the achieved results to support site (re)development. Afterwards, a few suggestions are made for the future development of the proposed geophysical survey methodology.

8.1.1 Practical implementation of mobile surveys

'Success is a science; if you have the conditions, you get the result.' – Oscar Wilde

For both EMI and GPR, a mobile survey configuration was presented enabling the rapid collection of high-resolution data. The survey configuration has been previously used mainly in agricultural and archaeological soil investigations. The boundary conditions to the application of EMI and GPR surveys with motorized conveyance in urban and industrial environments are essentially the same as in rural environments.

However, urban and industrial areas typically show a highly-fragmented land use. Wide open areas are scarce and, as illustrated in the analysis of the land cover map in Chapter 2, the types of surface covers are diverse. Rough terrain conditions, such as left after excavation works, can make an area inaccessible for the survey set-up, whichwas the reason for the restricted survey area at the industrial site studied in Chapter 7. The survey configuration is compatible with soil surfaces covered with grassy or herbaceous vegetation, or with pavement such as asphalt or concrete. Yet, the latter should be free from reinforcement, which was a limiting factor to the survey area at the former garage and gasoline station considered in Chapter 6. Also above-ground metal structures, such as metal fences, should be avoided to prevent interference with the sensor measurements. Accounting for these additional physical constraints, the suitable survey area can be strongly reduced and have a complex geometry. In Chapter 5, an analysis of the EMI survey efficiency was made, which indicated the surface area and the geometry of the survey area dominate over the survey resolution in determining the survey efficiency that can be reached. A minimum surface area of about 1000 m² is required for mobile surveying to be relevant. Provided this condition is fulfilled, for EMI a survey speed of about 1 ha per hour can be anticipated. Although not specifically analysed for GPR, the same minimum required surface area can be assumed. However, due to the point-based – or, more correctly, cone-based – support of the GPR measurements, full spatial coverage requires practically every inch of the terrain to be scanned. Whereas mobile EMI surveying becomes more graceful for larger survey areas, GPR surveying becomes rather more tedious, particularly for non-ideal terrain conditions. Moreover, the quality of the GPR data is much more sensitive to the conditions of the soil surface. In case of highly conductive circumstances, rapid attenuation of the GPR signal will strongly limit the measurement depth. By virtue of its higher robustness, EMI is preferred for a first reconnaissance survey. The EMI results can then be used to select specific areas where more detailed characterization of the shallow subsurface through GPR is relevant. Finally, the abundance of extraneous sources of EM fields (e.g. power lines) in urban and industrial areas has often raised concerns about quality data collection. Yet, in the presented case studies it was demonstrated that the presence of such sources of cultural noise is not necessarily problematic. For the EMI data sets, the measured subsurface contrasts commonly resulted in high SNRs and no appreciable effect of extraneous noise was observed. The industrial site visited in Chapter 7 seemed to present a noisy environment for GPR, but it was difficult to confirm a

specific cause. Furthermore, coherent noise can generally be easily removed through filtering. When considering the planning of an EMI and/or GPR survey, the first step should be to make a realistic, *a priori* evaluation of the prevailing site conditions to decide on the usefulness of the survey. Terrain inspection is preferentially complemented with any available information from administrative, historical and technical documents, in order to get a complete picture of the boundary conditions to be respected in the design of the survey (see also paragraph 8.1.4 and Figure 8.1, preliminary “desk” study). Rashly taking the survey equipment to the field without any preparation and hoping for the best is likely to result only in waste of time.

8.1.2 Independent EMI and GPR data analysis: what information can be expected?

High-resolution surveying with EMI and GPR provides detailed images of subsurface variations in electric conductivity, magnetic susceptibility and contrasts in relative dielectric permittivity. The detection of specific structures and phenomena depends on their ability to produce resolvable contrasts in terms of these geophysical properties and the strength of their contrasts relative to interacting effects. Obviously, the detectability also depends on the depth of the targets relative to the depth sensitivity of the geophysical measurement signals.

- At the different landfill sites considered in Chapter 5, the geophysical properties of the anthropogenic depositions, and their spatial variability, clearly contrasted with the natural soil. Therefore, the EMI data enabled the accurate derivation of the location and lateral extent of the landfills. Furthermore, within individual landfills, relative variations in measurement values allowed to discriminate zones with different waste substrates. Shallow metal objects result in dominant local anomalies in both the EC_a and MS_a signals and, if they are plentiful, they obscure the signature of the surrounding soil material. Nevertheless, the spatial density of metal anomalies can also be informative of differences in waste type, as was illustrated in case study II of Chapter 5. Changing patterns over EMI signals with a different depth sensitivity are generally indicative of vertical variations in subsurface properties. However, many metal objects in combination with a decrease in measurement resolution in depth often impeded reliable reconstruction of these variations. Hence, even when the interface between waste and host materials was within the theoretical DOE of the EMI measurements, it proved difficult to distinguish.

- The high sensitivity of EMI to strong conductors, on the other hand, has the advantage of a guaranteed detection of utility infrastructure such as metal pipes and electric cables, and remnants of reinforced foundations, as these produce clearly recognizable anomalies. This was demonstrated for the industrial site investigated in Chapter 7. If these structures occur within a depth of about 1 m, supplementary measurements with GPR can provide more realistic information on the dimensions of the structures and allow to position them on a depth scale, adding to an improved identification.
- In the presented case studies, chemical contamination such as with waste leachate and petroleum hydrocarbons was suggested to have contributed as well to variations in the soil electrical conductivity. However, the nature and dynamics of chemical contamination, in interaction with a solid phase matrix that is typically highly heterogeneous in itself, are usually very complex and the unambiguous discrimination and identification of chemical contamination based on only geophysical sensor data is not straightforward. Particularly for official soil contamination assessment, direct quantitative observations of contaminant concentrations remain necessary to decide on the need for soil remediation.

It was confirmed that the detection, discrimination and identification of specific structures or phenomena benefits from high-resolution data collection and from the combination of different measurement signals. The simultaneous collection of multiple signals representative of the electrical conductivity and magnetic susceptibility of different soil volumes is a major advantage of multi-receiver EMI. The GPR data demonstrated to provide complementary information to the EMI data. However, despite the wide frequency bandwidth offered by the SFCW system, the penetration depth of the GPR signals showed to be rather limited, maximum about 1.5 m. Hence, a GPR survey with the here presented system is only relevant when the targets of interest are expected to be within this depth range.

Because many subsurface structures and phenomena have a non-unique geophysical signature, the successful determination of the origin of measured contrasts often also relies on constraining the possibilities to the physical reality of the environment. The consultation of historical or technical documents is therefore equally relevant in preparation of a geophysical study as for conventional soil investigations (see also paragraph 8.1.4 and Figure 8.1, feedforward from desk study results to the interpretation of geophysical survey data). However, as confirmed by the case studies presented in this work, these documents are often only poorly detailed and their

reliability can be questioned. In this respect, the geophysical survey results can be useful to verify and possibly correct and complete the information derived from existing documentation (Figure 8.1, feedback from geophysical survey to desk study). Nevertheless, the soil in urban and industrial environments generally encompasses a multitude of interacting processes and, even with record information on the local soil development, resolving their relative contribution to geophysical measurements remains challenging. Whereas the results achieved in the presented case studies evidence that confident interpretations can be made, absolute certainty can only be achieved through validation with observations from conventional soil sampling (see also Figure 8.1, feedback from conventional survey results to the interpretation of geophysical survey data).

8.1.3 Guidance to invasive sampling strategy design

The spatially exhaustive data provided by EMI and GPR surveys can serve as a guide for the design of invasive sampling campaigns (see Figure 8.1, feedforward from geophysical survey results to conventional survey design). The sample size and locations can be targeted to actual contrasts in physical-chemical properties of the subsurface, which directly increases the reliability and representativeness of the sample. In addition, advice can be gained on the suitability of different types of sampling equipment. When the geophysical data suggest the presence of hard, technogenic substrates such as construction debris, small-diameter borehole drillings are likely to be practically infeasible. Larger sample volumes as obtained from trench or test pit excavations are also more appropriate if the subsurface demonstrates large small-scale variability. Especially when the samples are intended to provide quantitative data for the calibration of the geophysical measurements, the determination of the sampling volumes should account for the physical basis of the sensor measurements and the "nugget effect" of their spatial variation.

8.1.4 Relevance to support site (re)development

The main motivation behind this research was to investigate the use of proximal geophysical sensing to soil investigation in view of environmental site assessment and the design of an appropriate (re)development strategy. The key to succesfull site assessment is in accurate site characterization, which is represented in a conceptual site model. Standard procedures for site assessment generally include preliminary desk study and intrusive soil investigation as compulsory parts. Based on the

achieved research results, it is concluded that a geophysical survey perfectly fits in as an intermediate step (Figure 8.1). As argued in the previous paragraphs, the success of a geophysical survey relies on the integration of its results with information from archive documents and data from conventional soil observations, evidencing the complementary advantage for the "side" of the geophysical survey. But what added value can this additional step offer to site investigation? High-resolution geophysical data provide a spatially comprehensive view on variations in soil properties. Besides the direct input to a conceptual site model, a geophysical survey also indirectly contributes to improved site characterization through interaction with information from the conventional steps (Figure 8.1). Feedback can be provided to the output of the desk study. Feedforward to invasive surveying primarily consists in the optimization of the sampling design, in terms of time and cost efficiency as well as reliability and

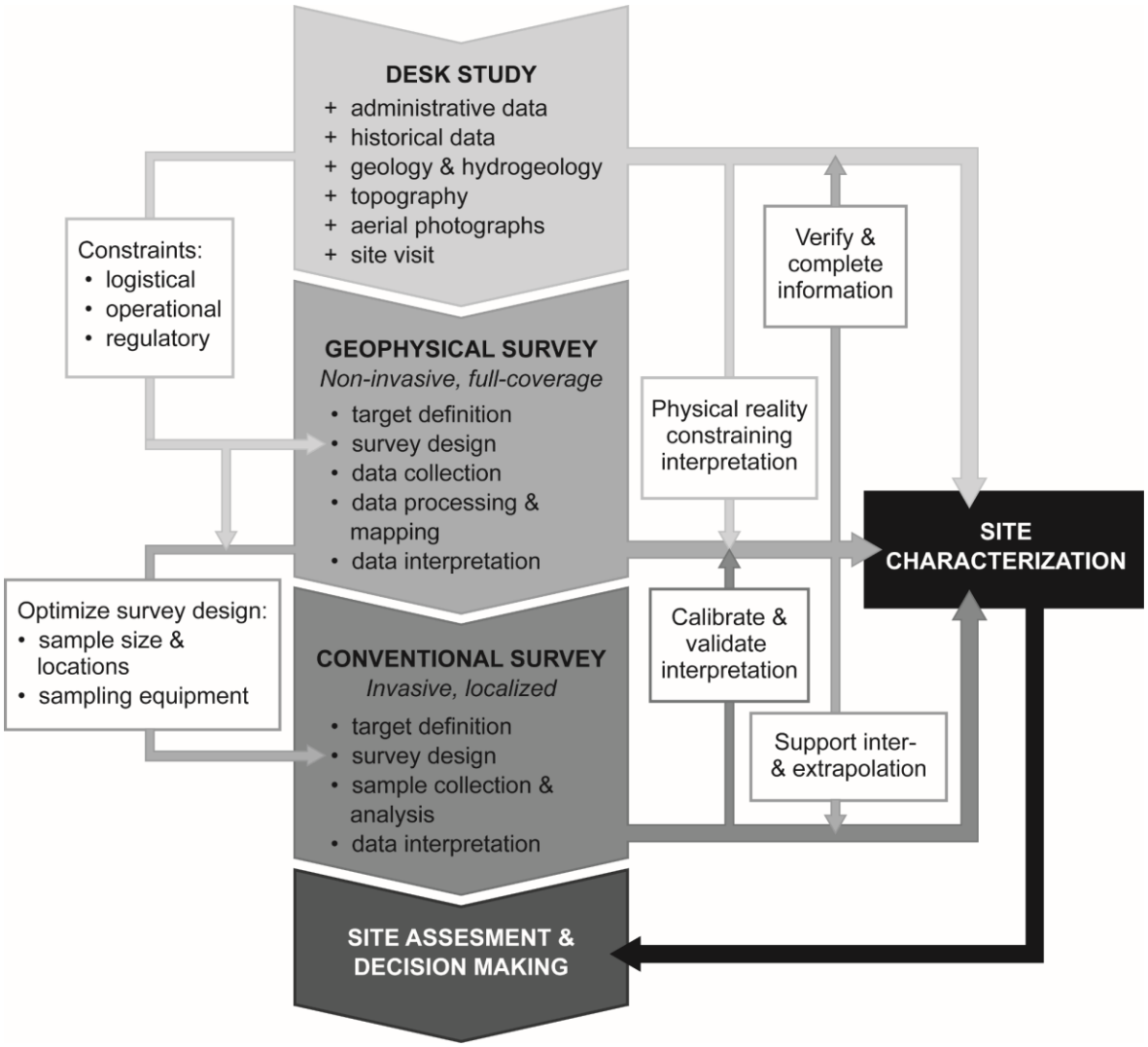

Figure 8.1 The integration of geophysical surveying into a standard procedure for environmental site assessment

representativeness of the results. Secondarily, if the data from invasive observations can be matched with the pattern in the geophysical data, the inter- and extrapolation of the localized information they provide can be performed with a higher confidence. The incorporation of site exploration through geophysical surveying thus improves the overall efficiency of site characterization while reducing the uncertainty, which could present an important step in a Triad analogue evolution towards expedited site characterization (US EPA, Office of Solid Waste and Emergency Response, 2003).

It is unlikely geophysical investigations will ever completely replace invasive investigations. They should rather be regarded as a different, complementary source of information. The conventional approach to site investigation is tailored to risk assessment. Geophysical surveying, on the other hand, provides a rapid means to gain an integrated view of the "nature" of the subsurface. In this respect, supplemental information is provided to evaluate the relevance of further, more detailed, site characterization and the urgency – or better, opportunity – of site redevelopment. For instance, for landfill investigations to evaluate the potential for ELFM, a geophysical survey allows to estimate the lateral extent of the landfill and gives an indication of the type of waste contained, which represent important criteria to decide on the relevance of an ELFM scenario as a whole. Therefore, geophysical techniques could also provide valuable input to the prioritization of landfill sites according to their ELFM potential.

8.2 The way forward

'If you can find a path with no obstacles, it probably doesn't lead anywhere.'
– Frank A. Clark

8.2.1 Optimizing survey efficiency: can less data be more?

Motorized surveys with proximal geophysical sensors proved to be efficient means for spatially dense data collection. However, the choice of survey parameters, in relation to the intended survey resolution, generally is arbitrary and depends on the experience of the surveyor. Furthermore, the quality of collected datasets with respect to proposed research objectives is hard to benchmark. Whereas it seems tempting to continue striving for an increased sampling speed in balance with sampling density, it can be questioned whether this truly entails improvement. With the currently achieved data densities, the time required for proper post-acquisition data processing is often

considerable larger than the time spent in the field. In addition, as mentioned in the discussion on the survey efficiency of EMI in Chapter 5, a high survey resolution may be superfluous if the spatial heterogeneity is either very high or very low. A detailed study of the influence of different survey parameters (e.g. sampling rate or interval, and driving speed) on the raw data quality, for different terrain conditions, presents an interesting topic for future research. The development of a methodology to evaluate the achieved data quality with respect to the survey objectives would provide a more objective guide to decide on the survey parameters. In addition, survey efficiency would benefit from extending the mobile survey configuration with a platform that enables robust analysis of the collected data quality in the field.

8.2.2 **Dreaming of ultimate calibration**

The interpretations made from the EMI data mainly relied on relative contrasts observed. Notwithstanding valuable information could be derived, more advanced quantitative characterization of subsurface materials is currently hampered by the suboptimal "calibration" of the data. Calibration here broadly refers to the absolute measurement values achieved after data processing as well as the adopted definition of the soil volumes they represent. Operation under conditions of LIN was consistently assumed, while the true conductivity presumably was often too high. As a consequence, no account was taken of possible deviations from the linear relationship between the QP output component and EC_a, interdependence between the EC_a and MS_a signals, and a reduced measurement depth of the signals. Furthermore, the applied procedures to correct for the spatial offset between sensor and position data, and to compensate for signal drift were pushed to their limits by the abundance of strong local heterogeneities. To improve the estimations of EC_a and MS_a, and ultimately of true electrical conductivity and magnetic susceptibility, two complementary paths of future research are suggested. In a more theoretical approach, the start of data processing should be taken back to the raw measurements of the QP and IP components to improve our understanding of their interaction in response to media with complex 3D heterogeneity. However, in order to produce practical measures of soil electrical conductivity and magnetic susceptibility, any theoretical calculation will at same point probably have to rely on simplifications based on arbitrary assumptions. A more pragmatic approach should focus on the development of calibration procedures that are more robust to 3D heterogeneity, for instance, through standardization of the measured values to data from related

geophysical methods that are less sensitive to small-scale variations. Probably, success will only be reached by integration of theoretical and pragmatic approaches. On a parallel track, continued efforts to study the intrinsic properties of the various materials encountered in urban soil are indispensable. Without improved knowledge on these properties, an improved absolute calibration of the sensor data cannot be validated.

8.2.3 **Consolidating the research grounds**

'Science and everyday life cannot and should not be separated.' – Rosalind Franklin

As illustrated in the very first figure of this work, Figure 1.1, the investigation of urban soil using geophysical sensors is at the interface of multiple disciplines including but not limited to soil science, (hydro)geology, geophysics, geotechnical and civil engineering, environmental, social and economic impact assessment, and archaeology. From literature review it was clear that among these disciplines a diverse methodology and vocabulary to study similar concepts. To expedite unravelling complex urban soil environments, the importance of intensified interaction between these fields of expertise, relying on the establishment of a common communication language, cannot be overemphasized. In addition, and even more important, the topic evidently transcends the boundaries of academic science. The further development of the researched geophysical survey methodology should occur in direct interaction with the different stakeholders involved in urban (re)development. Actually the opposite is practically impossible: urban and industrial sites are the only full-scale experimental sites available. Outreach and communication should aim at uniting the stakeholders' interests to create a broader support for the implementation of geophysical surveys into the daily practice of urban (re)development and for the acknowledgement of the valuable input they can provide for decision support tools on the future management of urban and industrial areas.

References

Abdu, H., Robinson, D. A., & Jones, S. B. (2007). Comparing Bulk Soil Electrical Conductivity Determination Using the DUALEM-1S and EM38-DD Electromagnetic Induction Instruments. *Soil Science Society of America Journal*, 71(1), 189–196.

Abdulrahman, A., Nawawi, M., Saad, R., Abu-Rizaiza, A. S., Yusoff, M. S., Khalil, A. E., & Ishola, K. S. (2016). Characterization of active and closed landfill sites using 2D resistivity/IP imaging: case studies in Penang, Malaysia. *Environmental Earth Sciences*, 75, 347.

Abudeif, A. M. (2015). Integrated electrical tomography and hydro-chemical analysis for environmental assessment of El-Dair waste disposal site, west of Sohag city, Egypt. *Environmental Earth Sciences*, 74(7), 5859–5874.

Adamchuk, V. I., Hummel, J. W., Morgan, M. T., & Upadhyaya, S. K. (2004). On-the-go soil sensors for precision agriculture. *Computers and Electronics in Agriculture*, 44(1), 71–91.

Agentschap voor Geografische Informatie Vlaanderen. (2002). *Bodemgebruiksbestand, opname 2001* [Land use file, survey 2002; Data file]. Retrieved from http://www.geopunt.be/download?container=bodemgebruik-2001&title=Bodemgebruiksbestand,%20opname%202001

Agentschap voor Geografische Informatie Vlaanderen. (2003). *Voorlopig referentiebestand gemeentegrenzen, toestand 22/05/2003* [Temporary reference file municipal boundaries, situation 22/05/2003; Data file]. Retrieved from http://www.geopunt.be/download?container=referentiebestand-gemeenten\VoorlopigRefBestandGemeentegrenzen_2003-05-22&title=Voorlopig%20referentiebestand%20gemeentegrenzen,%20toestand%2022/05/2003

Agentschap voor Geografische Informatie Vlaanderen. (2013). *Orthofotomozaïek, middenschalig, zomeropnamen, 2012, Vlaanderen* [Orthophoto mosaic, middle-scale, summer survey, 2012; Data file]. Retrieved from http://www.geopunt.be/download?container=omz12vl&title=Orthofotomoza%C3%AFek,%20middenschalig,%20zomeropnamen,%202012,%20Vlaanderen

Agentschap voor Geografische Informatie Vlaanderen. (2014). *Digitaal Hoogtemodel Vlaanderen II, DTM, raster, 1 m, versie 2014.01* [Digital Elevation Model Flanders, DTM, raster, 1 m, version 2014.01; Data file]. Retrieved from http://www.geopunt.be/download?container=dhm-vlaanderen-ii-dtm-raster-1m&title=Digitaal%20Hoogtemodel%20Vlaanderen%20II,%20DTM,%20raster,%201m

Agentschap voor Geografische Informatie Vlaanderen. (2016a). *Bodembedekkingskaart (BBK), 1m resolutie, opname 2012* [Land cover map, 1m resolution, survey 2012; Data file]. Retrieved from http://www.geopunt.be/download?container=bodembedekkingsbestanden2012\BBK1_12&title=Bodembedekkingskaart%20(BBK%29,%201m%20resolutie,%20opname%202012

Agentschap voor Geografische Informatie Vlaanderen. (2016b). *Grootschalig Referentiebestand, toestand 2016-09-16* [Large-scale Reference Database, situation 2016-09-16; Data file]. Retrieved from https://download.agiv.be/Producten/Detail?id=1&title=GRBgis/

Ahmad, A., Zhang, Y., & Nichols, S. (2011). Review and evaluation of remote sensing methods for soil-moisture estimation. *SPIE Reviews*, 2(1), 1–18.

André, F., van Leeuwen, C., Saussez, S., Van Durmen, R., Bogaert, P., Moghadas, D., de Rességuier, L., Delvaux, B., Vereecken, H., & Lambot, S. (2012). High-resolution imaging of a vineyard in south of France using ground-penetrating radar, electromagnetic induction and electrical resistivity tomography. *Journal of Applied Geophysics*, 78, 113–122.

Annan, A. P. (1999). *Practical Processing of GPR Data.* Mississauga, ON, Canada: Sensors & Software Inc.

Annan, A. P. (2001). *Ground Penetrating Radar Workshop Notes.* Mississauga, ON, Canada: Sensors & Software Inc.

Annan, A. P. (2009). Electromagnetic principles of Ground Penetrating Radar. In Jol. H. M. (Ed.), *Ground Penetrating Radar Theory and Applications* (pp. 4–40). Amsterdam, The Netherlands: Elsevier Science.

Antrop, M. (2004). Landscape change and the urbanization process in Europe. *Landscape and Urban Planning*, 67(1–4), 9–26.

Atekwana, E. A., Sauck, W. A., & Werkema, D. D. (2000). Investigations of geoelectrical signatures at a hydrocarbon contaminated site. *Journal of Applied Geophysics*, 44(2–3), 167–180.

Atekwana, E. A., & Atekwana, E. A. (2010). Geophysical Signatures of Microbial Activity at Hydrocarbon Contaminated Sites: A Review. *Surveys in Geophysics*, 31, 247–283.

Auken, E., Pellerin, L., Christensen, N. B., & Sørensen, K. (2006). A survey of current trends in near-surface electrical and electromagnetic methods. *Geophysics*, 71(5), G249–G260.

Avery, B. W. (1980). *Soil classification for England and Wales. Soil Survey Technical Monograph No. 14.* Harpenden, United Kingdom: Lawes Agricultural Trust.

Ayolabi, E. A., Epelle, E. S., Lucas, O. B., & Ojo, A. (2015). Geophysical and geochemical site investigation of eastern part of Lagos metropolis, southwestern Nigeria. *Arabian Journal of Geosciences*, 8(9), 7445–7453.

Ayolabi, E. A., Oluwatosin, L. B., & Ifekwuna C. D. (2015). Integrated geophysical and physicochemical assessment of Olushoshun sanitary landfill site, southwest Nigeria. *Arabian Journal of Geosciences*, 8(6), 4101–4115.

Bavec, Š., & Gosar, M. (2016). Speciation, mobility and bioaccessibility of Hg in the polluted urban soil of Idrija (Slovenia). *Geoderma*, 273, 115–130.

Beamish, D. (2011). Low induction number, ground conductivity meters: A correction procedure in the absence of magnetic effects. *Journal of Applied Geophysics*, 75(2), 244–253.

Bellezoni, R. A., Cristiano, K. I., Elis, V. R., da Silva Paganini, W., & Hamada, J. (2014). Small-scale landfills: impacts on groundwater and soil. *Environmental Earth Sciences*, 71(5), 2429–2439.

Belmonte-Jiménez, S. I., Bortolotti-Villalobos, A., Campos-Enríquez, J. Ó., Pérez-Flores, M. A., Delgado-Rodríguez, O., & Ladrón de Guevara-Torres, M. A. (2014). Electromagnetic methods application for characterizing a site contaminated by leachates. *Revista Internacional de Contaminación Ambiental*, 30(3), 317–329.

Benavides, A., & Everett, M. E. (2005). Target signal enhancement in near-surface controlled-source electromagnetic data. *Geophysics*, 70(3), G59–G67.

Benavides, A., & Everett, M. E. (2007). Non-linear inversion of controlled source multi-receiver electromagnetic induction data for unexploded ordnance using a continuation method. *Journal of Applied Geophysics*, 61(3–4), 243–253.

Bermejo, J. L., Sauck, W. A., & Atekwana, E. A. (1997). Geophysical Discovery of a New LNAPL Plume at the Former Wurtsmith AFB, Oscoda, Michigan. *Groundwater Monitoring & Remediation*, 17(4), 131–137.

Bernstone, C., Dahlin, T., Ohlsson, T., & Hogland, W. (2000). DC-resistivity mapping of internal landfill structures: two pre-excavation surveys. *Environmental Geology*, 39(3–4), 360–371.

Beyer, L., Kahle, P., Kretschmer, H., & Wu, Q. (2001). Soil organic matter composition of man-impacted urban sites in North Germany. *Journal of Plant Nutrition and Soil Science*, 164(4), 359–364.

Blum, W. E. H. (2005). Functions of soil for society and the environment. *Reviews in Environmental Science and Bio/Technology*, 4(3), 75–79.

Bosmans, A., Vanderreydt, I., Geysen, D, & Helsen, L. (2013). The crucial role of Waste-to-Energy technologies in enhanced landfill mining: a technology review. *Journal of Cleaner Production*, 55, 10–23.

Boudreault, J.-P., Dubé, J.-S., Chouteau, M., Winiarski, T., & Hardy, É. (2010). Geophysical characterization of contaminated urban fills. *Engineering Geology*, 116(3–4), 196–206.

Brewster, M. L., Annan, A. P., Greenhouse, J. P., Kueper, B. H., Olhoeft, G. R., Redman, J. D., & Sander, K. A. (1995). Observed migration of a controlled DNAPL release by geophysical methods. *Ground Water*, 33(6), 977–987.

Butler, D. K. (2005). What is Near-Surface Geophysics? In D. K. Butler (Ed.), *Near-Surface Geophysics, Investigations in Geophysics No. 13* (pp. 1–6). Tulsa, OK: Society of Exploration Geophysicists.

Callegary, J. B., Ferré, T. P. A., & Groom, R. W. (2007). Vertical spatial sensitivity and exploration depth of low-induction-number electromagnetic induction instruments. *Vadose Zone*, 6(1), 158–167.

Callegary, J. B., Ferré, T. P. A., & Groom, R. W. (2012). Three-Dimensional Sensitivity Distribution and Sample Volume of Low-Induction-Number Electromagnetic-Induction Instruments. *Soil Science Society of America Journal*, 76(1), 85–91.

Campbell, J. B., & Wynne, R. H. (2011). *Introduction to Remote Sensing. Fifth edition.* New York, NY: The Guilford Press.

Carcione, J. M., Seriani, G., & Gei, D. (2003). Acoustic and electromagnetic properties of soils saturated with salt water and NAPL. *Journal of Applied Geophysics*, 52(4), 177–191.

Cartwright, K., & McComas, M. R. (1968). Surveys in the vicinity of sanitary landfills in northeastern Illinois. *Ground Water*, 6(5), 23–30.

Cassidy, N. J. (2007). Evaluating LNAPL contamination using GPR signal attenuation analysis and dielectric property measurements: Practical implications for hydrological studies. *Journal of Contaminant Hydrology*, 94, 49–75.

Cassidy, N. J. (2009a). Electrical and Magnetic Properties of Rocks, Soils and Fluids. In H. M. Jol (Ed.), *Ground Penetrating Radar Theory and Applications* (pp. 41–72). Amsterdam, The Netherlands: Elsevier Science.

Cassidy, N. J. (2009b). Ground penetrating radar data processing, modelling and analysis. In H. M. Jol (Ed.), *Ground Penetrating Radar Theory and Applications* (pp. 141–176). Amsterdam, The Netherlands: Elsevier Science.

Christiansen, A. V., & Auken, E. (2012). A global measure for depth of investigation. *Geophysics*, 77(4), WB171–WB177.

Çinar, H., Altundaş, S., Ersoy, E., Bak, K., & Bayrak, N. (2016). Application of two geophysical methods to characterize a former waste disposal site of the Trabzon-Moloz district in Turkey. *Environmental Earth Sciences*, 75, 52.

Clark, D. A. (1997). Magnetic petrophysics and magnetic petrology: aids to geological interpretation of magnetic surveys. *AGSO Journal of Australian Geology & Geophysics*, 17(2), 83–103.

Clément, R., Descloitres, M., Günther, T. Oxarango, L., Morra, C., Laurent, J.-P., & Gourc, J.-P. (2010). Improvement of electrical resistivity tomography for leachate injection monitoring. *Waste Management*, 30(3), 452–464.

Conyers, L. B. (2004). *Ground-Penetrating Radar for Archaeology*. Geophysical Methods for Archaeology. Langham, United Kingdom: AltaMira Press.

Cooley, J. W., & Tukey, J. W. (1965). An algorithm for the machine calculation of complex Fourier series. *Mathematics of Computation*, 19(90), 297–301.

Corwin, D. L., & Lesch, S. M. (2005a). Apparent soil electrical conductivity measurements in agriculture. *Computers and Electronics in Agriculture*, 46(1–3), 11–43.

Corwin, D. L., & Lesch, S. M. (2005b). Characterizing soil spatial variability with apparent soil electrical conductivity. I. Survey protocols. *Computers and Electronics in Agriculture*, 46(1–3), 103–133.

Council Directive 1999/31/EC of 26 April 1999 on the landfill of waste. *Official Journal of the European Communities* L 182, 16.7.1999, pp. 1–19.

Dabas, M., Anest, A., Thiesson, J., & Tabbagh, A. (2016). Slingram EMI Devices for Characterizing Resistive Features Using Apparent Conductivity Measurements: check of the DualEM-421S Instrument and Field Tests. *Archaeological Prospection*, 23(3), 165–180.

Dahlén, L., & Lagerkvist, A. (2008). Methods for household waste composition studies. *Waste Management*, 28(7), 1100–1112.

Daniels, J. J., Roberts, R., & Vendl, M. (1995). Ground penetrating radar for the detection of liquid contaminants. *Journal of Applied Geophysics*, 33(1–3), 195–207.

Databank Ondergrond Vlaanderen. (2015). *WRB Soil Units 40k: Bodemkaart van het Vlaamse Gewest volgens het internationale bodemclassificatiesysteem World Reference Base op schaal 1:40.000* [WRB Soil Units 40k: Soil map of the Flemish Region according to the international soil classification system World Reference Base at scale 1:40.000]. Data file managed by the Flemish Government, Department of the Environment, Nature and Energy, Division of Land and Soil Protection, Subsoil, and Natural Resources. Retrieved from https://www.milieuinfo.be/dms/d/a/workspace/SpacesStore/8c951464-8ee2-4609-9cc3-170620f6a306/wrb_40k.zip

De Carlo, L., Perri, M. T., Caputo, M. C., Deiana, R., Vurro, M., & Cassiani, G. (2013). Characterization of a dismissed landfill via electrical resistivity tomography and mise-à-la-masse method. *Journal of Applied Geophysics*, 98, 1–10.

De Decker, P. (2011). Understanding housing sprawl: the case of Flanders, Belgium. *Environment and Planning A*, 43(7), 1634–1654.

De Kimpe, C. R., & Morel, J.-L. (2000). Urban soil management: a growing concern. *Soil Science*, 165(1), 31–40.

de la Vega, M., Osella, A., & Lascano, E. (2003). Joint inversion of Wenner and dipole-dipole data to study a gasoline contaminated soil. *Journal of Applied Geophysics*, 54(1), 97–109.

Delbecque, N., & Verdoodt, A. (2016). Spatial patterns of heavy metal contamination by urbanization. *Journal of Environmental Quality*, 45(1), 9–17.

Delefortrie, S., De Smedt, P., Saey, T., Van De Vijver, E., & Van Meirvenne, M. (2014). An efficient calibration procedure for correction of drift in EMI survey data. *Journal of Applied Geophysics*, 110, 115–125.

Delefortrie, S., Saey, T., Van De Vijver, E., De Smedt, P., Missiaen, T., Demerre, I., & Van Meirvenne, M. (2014). Frequency domain electromagnetic induction survey in the intertidal zone: Limitations of low-induction-number and depth of exploration. *Journal of Applied Geophysics*, 100, 14–22.

Delefortrie, S., Saey, T., De Pue, J., Van De Vijver, E., De Smedt, P., & Van Meirvenne, M. (2016). Evaluating corrections for a horizontal offset between sensor and position data for surveys on land. *Precision Agriculture*, 17(3), 349–364.

De Pue, J., Cornelis, W., & Van Meirvenne, M. (2016). Accounting for Surface Refraction in Velocity Semblance Analysis With Air-Coupled GPR. *IEEE Journal of Selected Topics in Applied Earth Observations and Remote Sensing*, 9(1), 60–73.v

DeRyck, S. M., Redman, J. D., & Annan, A. P. (1993). Geophysical monitoring of a controlled kerosene spill. In *Proceedings of the Symposium on the Application of Geophysics to Engineering and Environmental Problems (SAGEEP), Wheat Ridge, CO, April 18–22, 1993* (pp. 5–19). Denver, CO: Environmental and Engineering Geophysical Society.

De Smedt, P., Saey, T., Lehouck, A., Stichelbaut, B., Meerschman, E., Islam, M. M., Van De Vijver, E., & Van Meirvenne, M. (2013). Exploring the potential of multi-receiver EMI survey for geoarchaeological prospection: A 90 ha dataset. *Geoderma*, 199, 30–36.

De Smedt, P., Van Meirvenne, M., Herremans, D., De Reu, J., Saey, T., Meerschman, E., Crombé, P., & De Clercq, W. (2013). The 3-D reconstruction of medieval wetland reclamation through electromagnetic induction survey. *Scientific Reports*, 3(1517), 1–5.

De Smedt, P., Saey, T., Meerschman, E., De Reu, J., De Clercq, W., & Van Meirvenne, M. (2014). Comparing Apparent Magnetic Susceptibility Measurements of a Multi-receiver EMI Sensor with Topsoil and Profile Magnetic Susceptibility Data over Weak Magnetic Anomalies. *Archaeological Prospection*, 21(2), 103–112.

De Smedt, P., Van Meirvenne, M., Saey, T., Baldwan, E., Gaffney, C., & Gaffney, V. (2014). Unveiling the prehistoric landscape at Stonehenge through multi-receiver EMI. *Journal of Archaeological Science*, 50, 16–23.

De Vos, J. (2015). The influence of land use and mobility policy on travel behavior: A comparative case study of Flanders and the Netherlands. *The Journal of Transport and Land Use*, 8(1), 171–190.

Doolittle, J. A., & Collins, M.E. (1995). Use of soil information to determine application of ground penetrating radar. *Journal of Applied Geophysics*, 33(1), 101–108.

Doolittle, J. A., & Butnor, J. R. (2009). Soils, Peatlands, and Biomonitoring. In H. M. Jol (Ed.), *Ground Penetrating Radar Theory and Applications* (pp. 179–202). Amsterdam, The Netherlands: Elsevier Science.

Doolittle, J. A., & Brevik, E. C. (2014). The use of electromagnetic induction techniques in soils studies. *Geoderma*, 223–225, 33–45.

Dondeyne, S., Van Ranst, E., & Deckers, J. (2012). *Converting the legend of the Soil Map of Belgium to the World Reference Base for Soil Resources. Case studies of the Flemish Region*. Study by order of the Flemish Government, Department of the Environment, Nature and Energy, at KU Leuven and Ghent University, Belgium.

Dondeyne, S., Van Ranst, E., & Deckers, S. (2013). *The soil map of the Flemish region converted to a World Reference Base legend: the inland regions.* Study by order of the Flemish Government, Department of the Environment, Nature and Energy, at KU Leuven and Ghent University, Belgium.

Dondeyne, S., Vanierschot, L., Langohr, R., Van Ranst, E., & Deckers, J. (2014). *The soil map of the Flemish region converted to the 3rd edition of the World Reference Base for soil resources*. Study by order of the Flemish Government, Department of the Environment, Nature and Energy, at KU Leuven and Ghent University, Belgium.

Dorendorf, J., Eschenbach, A., Schmidt, K., & Jensen, K. (2015). Both tree and soil carbon need to be quantified for carbon assessments of cities. *Urban Forestry & Urban Greening*, 14(3), 447–455.

Dowd, P. A. (1984). The variogram and kriging: robust and resistant estimators. In. G. Verly, M. David, A. G. Journel, & A. Marechal (Eds.), *Geostatistics for Natural Resources Characterization*. Dordrecht, Holland: D. Reidel Publishing Company.

Dualem Inc. (2013). *DUALEM-421S User's Manual*. Milton, ON, Canada: Author.

Dudal, R. (2005). The sixth factor of soil formation. *Eurasian Soil Science*, 38, S60–S65.

Dudal, R., Deckers, J., Van Orshoven, J., & Van Ranst, E. (2005). Soil survey in Belgium and its applications. In R. J. A. Jones, B. Houšková, P. Bullock, & L. Montanarella (Eds.), *Soil Resources of Europe* (2nd ed., pp. 63–91). European Soil Bureau Research Report No. 9, EUR 20559 EN. Luxembourg, Luxembourg: Office for Official publications of the European Communities.Edjabou, M. E., Jensen, M. B., Götze, R., Pivnenko, K., Petersen, C., Scheutz, C., & Astrup, T. F. (2015). Municipal solid waste composition: Sampling methodology, statistical analyses, and case study evaluation. *Waste Management*, 36, 12–23.

Eide, E. S., & Hjelmstad, J. F. (2002). 3D utility mapping using electronically scanned antenna array. In S. Koppenjan, & H. Lee (Eds.), *Proceedings of the Ninth International Conference on Ground Penetrating Radar, Santa Barbara, CA, April 29–May 2, 2002*. Proceedings of SPIE, Volume 4758, pp. 192–196. International Society for Optics and Photonics, Bellingham, WA.

El-Fadel, M., Shazbak, S., Saliby, E., & Leckie, J. (1999). Comparative assessment of settlement models for municipal solid waste landfill applications. *Waste Management & Research*, 17(5), 347–368.

European Committee for Standardization. (2002). *Characterization of Waste – Leaching – Compliance test for leaching of granular materials and sludge – Part 4: One-stage batch test at a liquid to solids ratio of 10 L/kg for materials with a particle size below 10 mm (with or without size reduction)* (EN 12457-4). Brussels, Belgium: Author.

European Enhanced Landfill Mining Consortium. (2015). *Data launched on the landfill situation in the EU-28.* Retrieved from https://www.eurelco.org/infographic

European Environment Agency. (2016). *Corine Land Cover (CLC) 2012, Version 18.5.1* [Data file]. Retrieved from http://www.eea.europa.eu/data-and-maps/data/clc-2012-raster/

European Parliament and Council Directive 94/62/EC of 20 December 1994 on packaging and packaging waste. *Official Journal of the European Communities* L 365, 31.12.94, pp. 10–23.

Eurostat (2017). *Municipal waste statistics* [Data file]. Retrieved from http://ec.europa.eu/eurostat/statistics-explained/images/2/2e/MW_25_01_2017.xlsx

Evans, M. E., & Heller, F. (2003). *Environmental Magnetism: Principles and Applications of Enviromagnetics.* San Diego, CA: Academic Press.

Everett, M. E. (2013). *Near-Surface Applied Geophysics*. New York, NY: Cambridge University Press.

Fackler, W. C. (2002). Chapter 39. Materials in electronic packaging. In M. Kutz (Ed.), *Handbook of Materials Selection* (pp. 1223–1254). New York, NY: John Wiley & Sons, Inc.

Fine, P., Graber, E. R., & Yaron, B. (1997). Soil interactions with petroleum hydrocarbons: Abiotic processes. *Soil Technology*, 10(2), 133–153.

Fischer, C. (2011). The development and achievements of EU waste policy. *Journal of Material Cycles and Waste Management*, 13(1), 2–9.

Fitterman, D.V., & Labson, V.F. (2005). Electromagnetic induction methods for environmental problems. In D. K. Butler (Ed.), *Near-Surface Geophysics, Investigations in Geophysics No. 13* (pp. 295–349). Tulsa, OK: Society of Exploration Geophysicists.

Food and Agriculture Organization of the United Nations. (2006). *Guidelines for soil description*. Rome, Italy: Author.

Food and Agriculture Organization of the United Nations, & Intergovernmental Technical Panel on Soils. (2015). *Status of the World's Soil Resources (SWSR) – Main report*. Rome, Italy: Author.

Food and Agriculture Organization of the United Nations (2016). *Soil survey*. Retrieved from http://www.fao.org/soils-portal/soil-survey/en/

FPS Economy, SMEs, Self-employed and Energy (2016a). *Land use. Belgium, regions and municipalities (1834–2015)* [Data file]. Retrieved from http://statbel.fgov.be/nl/modules/publications/statistiques/environnement/downloadbare_bestanden/bodemgebruik.jsp

FPS Economy, SMEs, Self-employed and Energy (2016b). *Population – Population statistics 2010–2016* [Data file]. Retrieved from http://statbel.fgov.be/nl/modules/publications/statistiques/bevolking/bevolking_-_cijfers_bevolking_2010_-_2012.jsp

Frischknecht, F. C., Labson, V. F., Spies, B. R., and Anderson, W. L. (1991). In M. N. Nabighian, *Electromagnetic methods in applied geophysics, Volume 2, Application, Parts A and B* (pp. 105–270). Investigations in Geophysics No. 3. Tulsa, OK: Society of Exploration Geophysicists.

Goovaerts, P. (1997). *Geostatistics for Natural Resources Evaluation*, New York, NY: Oxford University Press.

Gottfried, T., Auerswald, K., & Ostler, U. (2012). Kinematic correction for a spatial offset between sensor and position data. *Computers and Electronics in Agriculture*, 84, 76–84.

Greinert, A. (2015). The heterogeneity of urban soils in the light of their properties. *Journal of Soils and Sediments*, 15(8), 1725–1737.

Grejner-Brzezinska, D. A. (2008). Integration of the Global Position System (GPS) into Agricultural Geophysics. In B. J. Allred, J. J. Daniels, & M. R. Ehsani (Eds.), *Handbook of Agricultural Geophysics*. Boca Raton, FL: CRC Press, Taylor & Francis Group.

Grimm, N. B., Grove, J. M., Pickett, S. T. A., & Redman, C. L. (2000). Integrated approaches to long-term studies of urban ecological systems. *BioScience*, 50(7), 571–584.

Guillemoteau, J., Sailhac, P., Boulanger, C., & Trules, J. (2015). Inversion of ground constant offset loop-loop electromagnetic data for a large range of induction numbers. *Geophysics*, 80(1), E11–E21.

Guy, E. D., Daniels, J. J., Holt, J., & Radzevicius, S. J. (2000). Electromagnetic Induction and GPR Measurements for Creosote Contaminant Investigation. *Journal of Environmental & Engineering Geophysics*, 5(2), 11–19.

Harris, F. J. (1978). On the use of windows for harmonic analysis with the discrete Fourier transform. *Proceedings of the IEEE*, 66, 51–83.

Hatheway, A. W. (2002). Geoenvironmental protocol for site and waste characterization of former manufactured gas plants; worldwide remediation challenge in semi-volatile organic wastes. *Engineering Geology*, 64, 317–338.

Henderson, R. J. (1992). Urban Geophysics – A Review. *Exploration Geophysics*, 23, 531–542.

Hogland, W., Marques, M., & Nimmermark, S. (2004). Landfill mining and waste characterization: a strategy for remediation of contaminated sites. *Journal of Material Cycles and Waste Management*, 6(2), 119–124.

Howard, J. L., & Orlicki, K. M. (2015). Effects of anthropogenic particles on the chemical and geophysical properties of urban soils, Detroit, Michigan. *Soil Science*, 180(4–5), 154–166.

Howard, J. L., Orlicki, K. M., & LeTarte, S. M. (2016). Evaluation of some proximal proximal sensing methods in urbanized terrain, Detroit, Michigan, USA. *Catena*, 143, 145–158.

Hull, R. M., Krogmann, U., & Strom, P. F. (2005). Composition and Characteristics of Excavated Materials from a New Jersey Landfill. *Journal of Environmental Engineering*, 131(3), 478–490.

Huot, H., Simonnot, M. O., Watteau, F., Marion, P., Yvon, J., De Donato, P., & Morel, J. L. (2014). Early transformation and transfer processes in a Technosol developing on iron industry deposits. *European Journal of Soil Science*, 65(4), 470–484.

Huot, H., Simonnot, M. O., & Morel, J. L. (2015). Pedogenetic Trends in Soils Formed in Technogenic Parent Materials. *Soil Science*, 180(4–5), 182–192.

International Organization for Standardization. (1999). *Water Quality - Determination of hydrocarbon oil index - Part 4: Method using solvent extraction and gas chromatography.* (ISO Standard No. 9377-4).

International Organization for Standardization. (2009). *Soil quality – Determination of particle size distribution in mineral soil material – Method by sieving and sedimentation* (ISO Standard No. 11277).

International Union of Soil Science Working Group WRB. (2006). *World reference base for soil resources 2006. A framework for international classification, correlation and communication*. World Soil Resources Reports No. 103. Rome, Italy: Food and Agriculture Organization of the United Nations.

International Union of Soil Science Working Group WRB. (2015). *World Reference Base for Soil Resources 2014, update 2015. International soil classification system for naming soils and creating legends for soil maps*. World Soil Resources Reports No. 106. Rome, Italy: Food and Agriculture Organization of the United Nations.

Islam, M. M., Meerschman, E., Saey, T., De Smedt, P., Van De Vijver, E., Delefortrie, S., & Van Meirvenne, M. (2014). Characterizing Compaction Variability with an Electromagnetic Induction Sensor in a Puddled Paddy Rice Field. *Soil Science Society of America Journal*, 78(2), 579–588.

Islam, M. M., Saey, T., De Smedt, P., Van De Vijver, E., Delefortrie, S., & Van Meirvenne, M. (2014). Modeling within field variation of the compaction layer in a paddy rice field using a proximal sensing system. *Soil Use and Management*, 30(1), 99–108.

Jenny, H. (1994). *Factors of soil formation: a system of quantitative pedology*. New York, NY: Dover Publications, Inc.

Jin, S., Fallgren, P., Cooper, J., Morris, J., & Urynowicz, M. (2008). Assessment of diesel contamination in groundwater using electromagnetic induction geophysical techniques. *Journal of Environmental Science and Health, Part A*, 43(6), 584–588.

Jodeiri Shokri, B., Doulati Ardejani, F., & Moradzadeh, A. (2016). Mapping the flow pathways and contaminants transportation around a coal washing plant using the VLF-EM, Geo-electrical and IP techniques—A case study, NE Iran, *Environmental Earth Sciences*, 75(1), 62.

Joffe, J. S. (1936). *Pedology*. New Brunswick, NJ: Rutgers University Press.

Johnson, C. C., Demetriades, A., Locutura, J., & Ottesen, R. T. (Eds.) (2011). *Mapping the Chemical Environment of Urban Areas*. Chichester, United Kingdom: John Wiley & Sons, Ltd.

Jol, H. (Ed.). (2009). *Ground Penetrating Radar: Theory and Applications*. Amsterdam, The Netherlands: Elsevier Science.

Jones, A., Panagos, P., Barcelo, S., Bouraoui, F., Bosco, C., Dewitte, O., … Yigini, Y. (2012). *The State of Soil in Europe*. EUR 25186 EN. Reference Report by the Joint Research Centre of the European Commission. Luxembourg, Luxembourg: Publications Office of the European Union.

Jones, P. T., Geysen, D., Tielemans, Y., Van Passel, S., Pontikes, Y., Blanpain, B., Quaghebeur, M., & Hoekstra, N. (2013). Enhanced Landfill Mining in view of multiple resource recovery: a critical review. *Journal of Cleaner Production*, 55, 45–55.

Kaartinen, T., Sormunen, K., & Rintala, J. (2013). Case study on sampling, processing and characterization of landfilled municipal solid waste in the view of landfill mining. *Journal of Cleaner Production*, 55, 56–66.

Keller, G. V., & Frischknecht, F. C. (1966). *Electrical Methods in Geophysical Prospecting* (1st ed.). Oxford, United Kingdom: Pergamon Press Inc.

Koppenjan, S. (2009). Ground Penetrating Radar Systems and Design. In H. M. Jol (Ed.), *Ground Penetrating Radar Theory and Applications* (pp. 73–97). Amsterdam, The Netherlands: Elsevier Science.

Krook, J., Svensson, N., & Eklund, M. (2012). Landfill mining: A critical review of two decades of research. *Waste Management*, 32(3), 513–520.

Kühn, J., Brenning, A., Wehrhan, M., Koszinski, S., & Sommer, M. (2009). Interpretation of electrical conductivity patterns by soil properties and geological maps for precision agriculture. *Precision Agriculture*, 10(6), 490–507.

Kulessa, B., Chiarulli, B., McCarthy, P., Haney, S., & Jones, K. (2006). Large-scale geophysical reconstruction of man-made ground at former industrial iron-furnace plantations. *Geophysics*, 71(3), B55–B61.

Lal, R. (2007). Soil Science and the Carbon Civilization. *Soil Science Society of America Journal*, 71(5), 1425–1437.

Landau, H., Chen, X., Klose, S., Leandro, R., & Vollath, U. (2009). Trimble's RTK and DGPS solutions in comparison with precise point positioning. In M. G. Sideris (Ed.), *Observing our Changing Earth*. *Proceedings of the 2007 IAG General Assembly, Perugia, Italy, July 2–13, 2007* (pp. 709–718). Berlin, Germany: Springer.

Lehmann, A. (2006). Technosols and other proposals on urban soils for the WRB (World Reference Base for Soil Resources). *International Agrophysics*, 20(2), 129–134.

Lehmann, A., & Stahr, K. (2007). Nature and Significance of Anthropogenic Urban Soils. *Journal of Soils and Sediments*, 7(4), 247–260.

Lindsay, J. D., Scheelar, M. D., & Twardy, A. G. (1973). Soil survey for urban development. *Geoderma*, 10(1–2), 35–45.

Linford, N., Linford, P., Martin, L., & Payne, A. (2010). Stepped Frequency Ground-penetrating Radar Survey with a Multi-element Array Antenna: Results from Field Application on Archaeological Sites. *Archaeological Prospection*, 17(3), 187-198.

Liu, L., & Chan, L. S. (2007). Sustainable urban development and geophysics. *Journal of Geophysics and Engineering*, 4(3), 243–244.

Lou, X. W., Archer, L. A., & Yang, Z. (2008). Hollow Micro-/Nanostructures: Synthesis and Applications. *Advanced Materials*, 20(21), 3987–4019.

Marchetti, M., Cafarella, L., Di Mauro, D., & Zirizzotti, A. (2002). Ground magnetometric surveys and integrated geophysical methods for solid buried waste detection: a case study. *Annals of Geophysics*, 45(3/4), 563–573.

Marchetti, M., & Settimi, A. (2011). Integrated geophysical measurements on a test site for detection of buried steel drums. *Annals of Geophysics*, 54(1), 105–114.

Martinelli, H.P., & Osella, A.M. (2010). Small-loop electromagnetic induction for environmental studies at industrial plants. *Journal of Geophysics and Engineering*, 7(1), 91–104.

Martinelli, H. P., Robledo, F. E., Osella, A. M., & de la Vega, M. (2012). Assessment of the distortions caused by a pipe and an excavation in the electric and electromagnetic responses of a hydrocarbon-contaminated soil. *Journal of Applied Geophysics*, 77, 21-29.

Matheron, G. (1965). *Les Variables Régionalisées et leur Estimation* [Regionalized Variables and their estimation]. Paris, France: Masson.

McNeill, J. D. (1980). *Electromagnetic Terrain Conductivity Measurement at Low Induction Numbers.* Technical Note TN-6. Geonics Limited, Mississauga, ON, Canada.

McNeill, J. D., & Bosnar, M. (1999). *Application of "Dipole-Dipole" Electromagnetic Systems for Geological Depth Sounding*. Technical Note TN-31. Geonics Limited, Mississauga, ON, Canada.

Meju, M. A. (2000). Geoelectrical investigation of old/abandoned, covered landfill sites in urban areas: model development with a genetic diagnosis approach. *Journal of Applied Geophysics*, 44(2–3), 115–150.

Meuser, H. (2010). *Contaminated Urban Soils. Environmental Pollution Volume 18*. New York, NY: Springer.

Miller, R. (2013). Introduction to this special section: Urban geophysics. *The Leading Edge*, 32(3), 248–249.

Minai-Tehrani, D., Rohanifar, P., & Azami, S. (2015). Assessment of bioremediation of aliphatic, aromatic, resin, and asphaltene fractions of oil-sludge-contaminated soil. *International Journal of Environmental Science and Technology.* 12(4), 1253–1260.

Minsley, B. J., Smith, B. D., Hammack, R., Sams, J. I., & Veloski, G. (2012). Calibration and filtering strategies for frequency domain electromagnetic data. *Journal of Applied Geophysics*, 80, 56–66.

Mücher, C. A., Hennekens, S. M., Bunce, R. G. H., Schaminée, J. H. J., & Schaepman, M. E. (2009). Modelling the spatial distribution of Natura 2000 habitats across Europe. *Landscape and Urban Planning*, 92(2), 148–159.

Nabighian, M. N. (1987). *Electromagnetic methods in applied geophysics, Volume 1, Theory*. Investigations in Geophysics No. 3. Tulsa, OK: Society of Exploration Geophysicists.

Nabighian, M. N. (Ed.). (1991). *Electromagnetic methods in applied geophysics, Volume 2, Application, Parts A and B*. Investigations in Geophysics No. 3. Tulsa, OK: Society of Exploration Geophysicists.

Nachtergaele, F. (2005). The "soils" to be classified in the World Reference Base for Soil Resources. *Eurasian Soil Science*, 38(1), 13–19.

Norra, S., & Stüben, D. (2003). Urban soils. *Journal of Soils and Sediments*, 3(4), 230–233.

Novo, A., Dabas, M., & Morelli, G. (2012). The STREAM X multichannel GPR system: first test at Vieil-Evreux (France) and comparison with other geophysical data. *Archaeological Prospection*, 19(3), 179–189.

Omonode, R. A., & Vyn, T. J. (2006). Spatial dependence and relationships of electrical conductivity to soil organic matter, phosphorus, and potassium. *Soil Science*, 171(3), 223–238.

Ondova, M., Stevulova, N., & Estokova, A. (2012). The study of the properties of fly ash based concrete composites with various chemical admixtures. *Procedia Engineering*, 42, 1863–1872.

OVAM. (2015). *Duurzaam voorraadbeheer van stortplaatsen in Vlaanderen* [Sustainable resource management of landfills in Flanders]. Retrieved from http://www.ovam.be/duurzaam-voorraadbeheer-van-stortplaatsen-in-vlaanderen-0

OVAM. (2017a). *Grondeninformatieregister* [Land Information Register]. Retrieved from http://www.ovam.be/gir

OVAM. (2017b). *Standaardprocedure Beschrijvend Bodemonderzoek* [Standard Procedure Descriptive Soil Examination]. Mechelen, Belgium: Author. Retrieved from https://www.ovam.be/sites/default/files/atoms/files/Standaardprocedure_Beschrijvend_Bodemonderzoek%2C_versie%20jan%202017.pdf

Panagos, P., van Liedekerke, M., Yigini, Y., & Montanarella, L. (2013). Contaminated Sites in Europe: Review of the Current Situation Based on Data Collected through a European Network. *Journal of Environmental and Public Health*, 2013(158764), 1–11.

Pataki, D. E., Alig, R. J., Fung, A. S., Golubiewski, N. E., Kennedy, C. A., McPherson, E. G., Nowak, D. J., Pouyat, R. V., & Romero Lankao, R. (2006). Urban ecosystems and the North American carbon cycle. *Global Change Biology*, 12(11), 2092–2102.

Pazzi, V., Tapete, D., Cappuccini, L., & Fanti, R. (2016). An electric and electromagnetic geophysical approach for subsurface investigation of anthropogenic mounds in an urban environment. *Geomorphology*, 273, 335–347.

Pedrera-Parilla, A., Van De Vijver, E., Van Meirvenne, M., Espejo-Pérez, Giráldez, J. V., & Verlinden, K. (2016). Apparent electrical conductivity measurements in an olive orchard under wet and dry soil conditions: significance for clay and soil water content mapping. Precision Agriculture, 17(5), 531–545.

Pellerin, L. (2002). Applications of Electrical and Electromagnetic Methods for Environmental and Geotechnical Investigations. *Surveys in Geophysics*, 23(2–3), 101–132.

Pettry, D. E., & Coleman, C. S. (1973). Two decades of urban soil interpretations in Fairfax County, Virginia. *Geoderma*, 10, 27–34.

Pichtel, J. (2014). *Waste Management Practices. Municipal, Hazardous, and Industrial* (2nd ed.). Boca Raton, FL: CRC Press, Taylor & Francis Group.

Pouyat, R. V., Yesilonis, I. D., & Nowak, D. J. (2006). Carbon Storage by Urban Soils in the United States. *Journal of Environmental Quality*, 35, 1566–1575.

Prechthai, T., Padmasri, M., & Visvanathan, C. (2008). Quality assessment of mined MSW from an open dumpsite for recycling potential. *Resources, Conservation and Recycling*, 53(1–2), 70–78.

Prokof'eva, T. V., Gerasimova, M. I., Bezuglova, O. S., Bakhmatova, K. A., Gol'eva, A. A., Gorbov, S. N., Zharikova, E. A., Matinyan, N. N., Nakvasina, E. N., & Sivtseva, N. E. (2014). Inclusion of soils and soil-like bodies of urban territories into the Russian soil classification system. *Eurasian Soil Science*, 47(10), 959–967.

Purves, D. (1967). Contamination of Urban Garden Soils with Copper, Boron, and Lead. *Plant and Soil*, XXVI(2), 380–381.

Quaghebeur, M., Laenen, B., Geysen, D., Nielsen, P., Pontikes, Y., Van Gerven, T., & Spooren, J. (2013). Characterization of landfilled materials: screening of the enhanced landfill mining potential. *Journal of Cleaner Production*, 55, 72–83.

Rawlins, B. G., Harris, J., Price, S., & Bartlett, M. (2015). A review of climate change impacts on urban soil functions with examples and policy insights from England, UK. *Soil Use and Management*, 31(S1), 46–61.

Redman, J. D. (2009). Contaminant Mapping. In H.M. Jol (Ed.), *Ground Penetrating Radar: Theory and Applications* (pp. 247–269). Amsterdam, The Netherlands: Elsevier Science.

Rehman, F., Abuelnaga, H. S. O., Harbi, H. M., Cheema, T., & Atef, A. H. (2016). Using a combined electrical resistivity imaging and induced polarization techniques with the chemical analysis in determining of groundwater pollution at Al Misk Lake, Eastern Jeddah, Saudi Arabia. *Arabian Journal of Geosciences*, 9, 286.

Reynolds, J. M. (2011). *An Introduction to Applied and Environmental Geophysics* (2nd ed.). Chichester, England: John Wiley & Sons, Ltd.

Rhoades, J. D., & van Schilfgaarde, J. (1976). An Electrical Conductivity Probe for Determining Soil Salinity. *Soil Science Society of America Journal*, 40(5), 647–651.

Rhoades, J. D., Chanduvi, F., & Lesch, S. (1999). *Soil salinity assessment. Methods and interpretation of electrical conductivity measurements. FAO Irrigation and Drainage Paper #57.* Rome, Italy: Food and Agriculture Organization of the United Nations.

Robinson, D. A., Lebron, I., Lesch, S. M., & Shouse, P. (2004). Minimizing drift in electrical conductivity measurements in high temperature environments using the EM-38. *Soil Science Society of America Journal*, 68(2), 339–345.

Rossiter, D. G. (2007). Classification of Urban and Industrial Soils in the World Reference Base for Soil Resources. *Journal of Soils and Sediments*, 7(2), 96–100.

Rowell, D. L. (1994). *Soil Science: Methods and Applications.* London, UK: Routledge, Taylor & Francis Group.

Rucker, D. F., Loke, M. H., Levitt, M. T., & Noonan, G. E. (2010). Electrical-resistivity characterization of an industrial site using long electrodes. *Geophysics*, 75(4), WA95–WA104.

Saey, T., Simpson, D., Vermeersch, H., Cockx, L., & Van Meirvenne, M. (2009). Comparing the EM38DD and DUALEM-21S Sensors for Depth-to-Clay Mapping. *Soil Science Society of America Journal*, 73(1), 7–12.

Saey, T., Van Meirvenne, M., Vermeersch, H., Ameloot, N., & Cockx, L. (2009). A pedotransfer function to evaluate the soil profile textural heterogeneity using proximally sensed apparent electrical conductivity. *Geoderma*, 150, 389–395.

Saey, T., Van Meirvenne, M., De Smedt, P., Cockx, L, Meerschman, E., Islam M. M., & Meeuws, F. (2011). Mapping depth-to-clay using fitted multiple depth response curves of a proximal EMI sensor. *Geoderma*, 162(1–2), 151–158.

Saey, T., Van Meirvenne, M., Dewilde, M., Wyffels, F., De Smedt, P., Meerschman, E., Islam, M. M., Meeuws, F., & Cockx, L. (2011). Combining multiple signals of an electromagnetic induction sensor to prospect land for metal objects. *Near Surface Geophysics*, 9(4), 309–317.

Saey, T., Van Meirvenne, M., De Smedt, P., Neubauer, W., Trinks, I., Verhoeven, G., & Seren, S. (2013). Integrating multi-receiver electromagnetic induction measurements into the interpretation of the soil landscape around the school of gladiators at Carnuntum. *European Journal of Soil Science*, 64(5), 716–727.

Saey, T., Van Meirvenne, M., De Smedt, P., Stichelbaut, B., Delefortrie, S., Baldwin, E., & Gaffney, V. (2015). Combining EMI and GPR for non-invasive soil sensing at the Stonehenge World Heritage Site: the reconstruction of a WW1 practice trench. *European Journal of Soil Science*, 66(1), 166–178.

Sala, J., & Linford, N. (2012). Processing stepped frequency continuous wave GPR systems to obtain maximum value from archaeological data sets. *Near Surface Geophysics*, 10(1), 3–10.

Santamarina, J. C., & Fam, M. (1997). Dielectric permittivity of soils mixed with organic and inorganic fluids (0.02 GHz to 1.30 GHz). *Journal of Environmental & Engineering Geophysics*, 2(1), 37–52.

Sauck, W. A. (2000). A model for the resistivity structure of LNAPL plumes and their environs in sandy sediments. *Journal of Applied Geophysics*, 44(2–3), 151–165.

Savage, G. M., Golueke, C. G., & von Stein, E. L. (1993). Landfill mining: past and present. *Biocycle*, 34(5), 58–61.

Scharenbroch, B. C., Lloyd, J. E., & Johnson-Maynard, J. L. (2005). Distinguishing urban soils with physical, chemical and biological properties. *Pedobiologia*, 49(1), 283–296.

Schmidt, A. (2007). Archaeology, magnetic methods. In D. Gubbins & E. Herrero-Bervera (Eds.), *Encyclopedia of Geomagnetism and Paleomagnetism* (pp. 23–31). New York, NY: Springer.

Scull, P., Franklin, J., Chadwick, O. A., & McArthur, D. (2003). Predictive soil mapping: a review. *Progress in Physical Geography*, 27(2), 171–197.

Senft, F. (1847). *Lehrbuch der Gebirgs- und Bodenkunde*. Jeny, Germany: Mauke.

Shah, A. A., Hasan, F., Hameed, A., & Ahmed, S. (2008). Biological degradation of plastics: A comprehensive review. *Biotechnology Advances*, 26(3), 246–265.

Sheets, K. R., & Hendrickx, J. M. H. (1995). Noninvasive soil water content measurement using electromagnetic induction. *Water Resources Research*, 31(10), 2401–2409.

Simpson, D., Lehouck, A., Van Meirvenne, M., Bourgeois, J., Thoen, E., & Vervloet, J. (2008). Geoarchaeological prospection of a medieval manor in the Dutch polders using an electromagnetic induction sensor in combination with soil augerings. *Geoarchaeology: An International Journal*, 23(2), 305–319.

Simpson, D., Lehouck, A., Verdonck, L., Vermeersch, H., Van Meirvenne, M., Bourgeois, J., Thoen, E., & Docter, R. (2009). Comparison between electromagnetic induction and fluxgate gradiometer measurements on the buried remains of a 17th century castle. *Journal of Applied Geophysics*, 68, 294–300.

Simpson, D., Van Meirvenne, M., Saey, T., Vermeersch, H., Bourgeois, J., Lehouck, A., Cockx, L., & Vitharana, U. W. A. (2009). Evaluating the Multiple Coil Configurations of the EM38DD and DUALEM-21S Sensors to Detect Archaeological Anomalies. *Archaeological Prospection*, 16(2), 91–102.

Simpson, D., Van Meirvenne, M., Lück, E. L., Rühlmann, J. R., Saey, T., & Bourgeois, J. (2010). Sensitivity of multi-coil frequency domain electromagnetic induction sensors to map soil magnetic susceptibility. *European Journal of Soil Science*, 61(4), 469–478.

Sleutel, S., Van De Vijver, E., Moeskops, B., Bouckaert, L., Ameloot, N., De Bolle, S., Van Meirvenne, M., & De Neve, S. (2011). *Onderbouwing van een methodiek voor de systematische monitoring van koolstofvoorraden in landbouwbodems* [Developing a methodology for the systematic monitoring of carbon stock in agricultural soils]. Study by order of the Flemish Government, Department of the Environment, Nature and Energy at the Department of Soil Management, Ghent University, Belgium.

Sudduth, K. A., Drummond, S. T., & Kitchen, N. R. (2001). Accuracy issues in electromagnetic induction sensing of soil electrical conductivity for precision agriculture. *Computers and Electronic in Agriculture*, 31(3), 239–264.

Tabbagh, A. (1986a). Applications and advantages of the Slingram electromagnetic method for archaeological prospecting. *Geophysics*, 51(3), 576–584.

Tabbagh, A. (1986b). What is the best coil orientation in the Slingram electromagnetic prospecting method? *Archaeometry*, 28(2), 185–196.

Teixidó, T. (2011). The Surface Geophysical Methods: a useful Tool for the Engineer. *Procedia Engineering*, 46, 89–96.

Tezkan, B. (1999). A review of environmental applications of quasi-stationary electromagnetic techniques. *Surveys in Geophysics*, 20(3–4), 279–308.

Tølbøll, R. J., & Christensen, N. B. (2007). Sensitivity functions of frequency-domain magnetic dipole-dipole systems. *Geophysics*, 72(2), F45–F56.

Triantafilis, J., Roe, J. A. E., & Monteiro Santos, F. A. (2011). Detecting a leachate plume in an aeolian sand landscape using a DUALEM-421 induction probe to measure electrical conductivity followed by inversion modelling. *Soil Use and Management*, 27(3), 357–366.

Triantafilis, J., Ribeiro, J., Page, D., & Monteiro Santos, F. A. (2013). Inferring the Location of Preferential Flow Paths of a Leachate Plume by Using a DUALEM-421 and a Quasi-Three-Dimensional Inversion Model. *Vadose Zone Journal*, 12(2), 117–125.

United Nations, Department of Economic and Social Affairs, Population Division. (2015). *World Urbanization Prospects: The 2014 Revision, (ST/ESA/SER.A/366).* New York, NY: United Nations.

Våland, P. A. (n.d.). *Penetration with Step Frequency Ground Penetrating Radar*. Trondheim, Norway: 3d-Radar AS.

Vandenbohede, A., Courtens, C., Lebbe, L. & De Breuck, W. (2010). Fresh-salt water distribution in the central Belgian coastal plain: an update. *Geologica Belgica*, 11, 163-169.

Van De Vijver, E., De Pue, J., Cornelis, W., & Van Meirvenne, M. (2015). Comparison of air-launched and ground-coupled configurations of SFCW GPR in time, frequency and wavelet domain. In: *Geophysical Research Abstracts*, Vol. 17, EGU2015-10038, 2015. EGU General Assembly 2015, Vienna, Austria, 12-17 April 2015.

Van De Vijver, E., Van Meirvenne, M., Saey, T., Delefortrie, S., De Smedt, P., De Pue, J., & Seuntjens, P. (2015). Combining multi-receiver electromagnetic induction and stepped frequency ground penetrating radar for industrial site investigation. *European Journal of Soil Science*, 66(4), 688–696.

Van De Vijver, E., Van Meirvenne, M., Vandenhaute, L., Delefortrie, S., De Smedt, P., Saey, T., & Seuntjens, P. (2015). Urban soil exploration through multi-receiver electromagnetic induction and stepped-frequency ground penetrating radar. *Environmental Science: Processes & Impacts*, 17(7), 1271–1281.

Van De Vijver, E., & Van Meirvenne, M. (2016). Delving into the potential of multi-receiver electromagnetic induction surveying for enhanced landfill exploration in view of ELFM. In: *Proceedings of the 3rd International Symposium on Enhanced Landfill Mining* (pp. 175–187). Lisbon, Portugal.

Van De Vreken, P., Beckers, V., Jacxsens, P., Van Meirvenne, M., & Van Orshoven, J. (2011). *Historiek van de bodemdatabank AARDEWERK-Vlaanderen-2010* [Historical overview of the soil database AARDEWERK-Vlaanderen-2010]. Study by order of the Flemish Government, Department of the Environment, Nature and Energy, at KU Leuven and Ghent University, Belgium.

van Liedekerke, M., Prokop, G., Rabl-Berger, S., Kibblewhite, M. & Louwagie, G. (2014). *Progress in the management of contaminated sites in Europe*. EUR 26376 EN. Reference Report by the Joint Research Centre of the European Commission. Luxembourg, Luxembourg: Publications Office of the European Union.

Van Meirvenne, M., Islam, M.M., De Smedt, P., Meerschman, E., Van De Vijver, E., & Saey T. (2013). Key variables for the identification of soil management classes in the aeolian landscapes of north-west Europe. *Geoderma*, 199, 99-105.

Van Orshoven, J., Maes, J., Vereecken, H., Feyen, J., & Dudal, R. (1988). A structured database of Belgian soil profile data. *Pedologie*, XXXVIII, 191–206.

Vargemezis, G., Tsourlos, P., Giannopoulos, A., and Trilyrakis, P. (2015). 3D electrical resistivity tomography technique for the investigation of a construction and demolotion waste landfill site. *Studia Geophysica et Geodaetica*, 59(3), 461–476.

Vaudelet, P., Schmutz, M., Pessel, M., Franceschi, M., Guérin, R., Atteia, O., Blondel, A., Ngomseu, C., Galaup, S., Rejiba, F., & Bégassat, P. (2011). Mapping of contaminant plumes with geoelectrical methods. A case study in urban context. *Journal of Applied Geophysics*, 75(4), 738–751.

Verdonck, L., Simpson, D., Cornelis, W. M., Plyson, A., Bourgeois, J., Docter R., & Van Meirvenne, M. (2009). Ground-penetrating Radar Survey over Bronze Age Circular Monuments on a Sandy Soil, Complemented with Electromagnetic Induction and Fluxgate Gradiometer Data. *Archaeological Prospection*, 16(3), 193-202.

Verma, S. K., & Sharma, S. P. (2011). Urban Geophysics Preface. *Physics and Chemistry of the Earth*, 36(16), 1209–1210.

Viscarra Rossel, R. A., McBratney, A., & Minasny, B. (Eds.). (2010). *Proximal Soil Sensing*. Progress in Soil Science. New York, NY: Springer.

Viscarra Rossel, R. A., Adamchuk, V. I., Sudduth, K. A., McKenzie, N. J., & Lobsey, C. (2011). Proximal Soil Sensing: An Effective Approach for Soil Measurements in Space and Time. In D. L. Sparks (Ed.), *Advances in Agronomy, Vol. 113* (pp. 237–282). Burlington, MA: Academic Press.

Vitharana, U.W.A., Van Meirvenne, M., Cockx, L. & Bourgeois, J. (2006). Identifying potential management zones in a layered soil using several sources of ancillary information. *Soil Use & Management*, 22(4), 405-413.

VLAREBO 2008, Besluit van de Vlaamse Regering houdende vaststelling van het Vlaams reglement betreffende de bodemsanering en de bodembescherming [Order of the Flemish Government establishing the Flemish regulation on soil remediation and soil protection], 14 December 2007, 2008. Retrieved from https://navigator.emis.vito.be/mijn-navigator?woId=22989

Wait, J. R. (1962). A note on the electromagnetic response of stratified earth. *Geophysics*, 27(3), 382–385.

Walkley, A., & Black, I. A. (1934). An examination of the Degtjareff method for determining soil organic matter, and a proposed modification of the chromic titration method. *Soil Science*, 37(1), 29-38.

Wang, T.-P., Chen, C.-C., Tong, L.-T., Chang, P.-Y., Chen, Y.-C., Dong, T.-H., Liu, H.-C., Lin, C.-P., Yang, K.-H., Ho, C.-J., & Cheng, S.-N. (2015). Applying FDEM, ERT and GPR at a site with soil contamination: A case study. *Journal of Applied Geophysics*, 121, 21–30.

Wapler, M. C., Leupold, J., Dragonu, I., von Elverfeld, D., Zaitsev, M., & Wallrabe, U. (2014). Magnetic properties of materials for MR engineering, micro-MR and beyond. *Journal of Magnetic Resonance*, 242, 233–242.

Webster, R. (2015). Technological developments for spatial prediction of soil properties, and Danie Krige's influence on it. *The Journal of The Southern African Institute of Mining and Metallurgy*, 115(2), 165–172.

Webster, R., & Lark, M. (2013). *Field Sampling for Environmental Science and Management*. Oxon, United Kingdom: Routledge.

Webster, R., & Oliver, M. A. (2007). *Geostatistics for Environmental Scientists. Second Edition.* Chichester, United Kingdom: John Wiley & Sons Ltd.

Werkema Jr., D. D., Atekwana, E. A., Endres, A. L., Sauck W. A., & Cassidy D. P. (2003). Investigating the geoelectrical response of hydrocarbon contamination undergoing biodegradation. *Geophysical Research Letters*. 30(12), 1647.

Whiteley, R. J., & Jewell, C. (1992). Geophysical Techniques in Contaminated Lands Assessment – Do they Deliver? *Exploration Geophysics*, 23(4), 557–565.

Wijesekara, S. S. R. M. D. H. R., Mayakaduwa, S. S., Siriwardana, A. R., de Silva, N., Basnayake, B. F. A., Kawamoto, K., & Vithanage, M. (2014). Fate and transport of pollutants through a municipal solid waste landfill leachate in Sri Lanka. *Environmental Earth Sciences*, 72(5), 1707–1719.

Wille, E. (2016). Sustainable stock management and landfills: introduction to Enhanced Landfill Management & Mining (ELFM²). In *Proceedings of the 3rd International Symposium on Enhanced Landfill Mining* (pp. 30–49). Lisbon, Portugal. Retrieved from https://docs.wixstatic.com/ugd/f593b3_ae93c5832fc84b32a4259099817a1aa9.pdf

Wilson, R. C., Freeland, R. S., Wilkerson, J. B., & Hart, W. E. (2005). Interpolation and Data Collection Error Sources for Electromagnetic Induction-Soil Electrical Conductivity Mapping. *Applied Engineering in Agriculture*, 21(2), 277–283.

Xin, L., Chu, J., Wang, J.-Y., Yin, K., Tong, H.-H., Chia, C. Y. H., & Noh, O. A. M. (2015). Geophysical methods for the investigation of a closed dumping ground. *Geomechanics and Engineering*, 8(5), 727–739.

Yang, M., Yang, Y. S., Du, X., Cao, Y. & Lei, Y. (2013). Fate and Transport of Petroleum Hydrocarbons in Vadose Zone: Compound-specific Natural Attenuation. *Water, Air, & Soil Pollution*, 224(3), 1439.

Yamanaka, M., Hachimura, T., & Hasegawa, S. (2015). Distribution of landfill by geophysical exploration methods at illegal industrial wastes disposal site. *International Journal of GEOMATE*, 9(17), 1342–1347.

Yelf, R. J. (2007). Application of Ground Penetrating Radar to Civil and Geotechnical Engineering. *Electromagnetic Phenomena*, 7(1), 102–117.

Yin, K., Tong, H. H., Noh, O., Wang, J.-Y., & Giannis, A. (2015). Mapping Refuse Profile in Singapore Old Dumping Ground through Electrical Resistivity, S-Wave Velocity and Geotechnical Monitoring. *Bulletin of Environmental Contamination and Toxicology*, 94(3), 275–281.

Zanetti, M., & Godio, A. (2006). Recovery of foundry sands and iron fractions from an industrial waste landfill. *Resources, Conservation and Recycling*, 48(4), 396–411.

Curriculum vitae

Personal information

Name	Ellen Van De Vijver
Date of birth	23 January 1987
Nationality	Belgian
Address	Statiestraat 25 / 201, 1740 Ternat, Belgium
Phone	+32 (0)478 57 67 39
E-mail	ervdevij.vandevijver@ugent.be

Education

1998–2004	Secondary school, Science-Mathematics, Sint-Pietersinstituut, Ghent, Belgium
2004–2008	Bachelor in Bioscience Engineering: Environmental Technology, Ghent University, Belgium
2008–2010	Master in Bioscience Engineering: Environmental Technology, Ghent University, Belgium
2009–2014	Specific Teacher's Training: Bioscience Engineering Ghent University, Belgium
2010–2017	Doctoral Training Programme, Doctoral School of (Bioscience) Engineering, Ghent University, Belgium

Transferable skills courses followed:

- Advanced Academic English: Writing Skills (2011)
- Authentic Networking (2013)
- Fostering Responsible Conduct of Research (2015)

Specialist course followed:

- 1st MAC International Workshop on Archaeological Geophysics, Ullastret, Spain (2012)

Professional experience

2010–2017 Teaching assistant / Doctoral researcher,
Department of Soil Management, Faculty of Bioscience Engineering, Ghent University, Belgium

Teaching experience

2010–2015 Land Information Systems (Master Physical Land Resources) – *PC exercises*

2010–present Geostatistics (Master Bioscience Engineering) – *PC exercises, lectures (2016–2017)*

Mathematics 3 and (geo)statistics – Part (geo)statistics (Bachelor Geology, Bachelor Geography) – *PC exercises, lectures (2016–2017)*

2011–2012 Contaminant Transport in Soils (Master Environmental Sanitation) – *laboratory practicals*

2011–present Contamination and remediation of soils / Environmental technology: soil and waste (Master Bioscience Engineering) – *class exercises*

2012–present Inventory techniques for soil and water (Bachelor Bioscience Engineering) – *PC exercises, lectures (2016–2017)*

2013–2015 Earth Sciences – Exercise 'Norm and mode' (Bachelor Bioscience Engineering) – *class exercises*

Tutoring of Master thesis projects

2010–2011 Nele Boon. Geostatistical analysis of the concentration of heavy metals in the soil around the metallurgical sites of Olen, Balen en Overpelt. Master Statistical Data Analysis.

2011–2012 Mervin Manalili. Comparison of Ground Penetrating Radar and Time Domain Reflectometry in measuring water content of a sandy soil. Master Physical Land Resources.

2012–2013 Laura Vandenhaute. The delineation of soil pollution with mobile sensors. Master Bioscience Engineering.

2013–2014 Simon Petit. Potential of mobile soil sensors to characterize contamination with mineral oil. Master Bioscience Engineering.

2014–2015 Kimberley Desplenter. Mobile proximal soil sensors for characterization of a landfill in the context of Enhanced Landfill Mining. Master Bioscience Engineering.

2015–2016 Elise Audenaert. Use of geophysical soil sensors for the characterization of landfills in the context of Enhanced Landfill Mining. Master Bioscience Engineering.

2016–2017 Laura Moens. Characterization of landfills in the context of Enhanced Landfill Mining (ELFM). Master Bioscience Engineering.

Hanne Meurisse. Optimization of bioremediation in biobeds: effect of heating and aeration. Master Bioscience Engineering.

Faculty committee memberships

2010–present Education Quality Control Committee, Assisting Academic Staff representative

2015–present Study Programme Committee Land and Water Management, Assisting Academic Staff representative

Scientific organisation memberships

2013–present COST Action TU1208 Civil Engineering Applications of Ground Penetrating Radar, Member Working Group 'Combined use of GPR and other non-destructive methods'

2014–present European Consortium on Enhanced Landfill Mining (EURELCO), UGent representative

2015–present COST Action 15115 Mining the European Anthroposphere (MINEA), Management Committee Substitute Member

Scientific publications

Artikels

A1

22. Saey, T., Verhegge, J., De Smedt, P., Smetryns, M., Note, N., **Van De Vijver, E.**, Laloo, P., Van Meirvenne, M., & Delefortrie, S. (2016). Integrating cone penetration testing into the 1D inversion of multi-receiver EMI data to reconstruct a complex stratigraphic landscape. *Catena*, 147, 356–371.
21. Pedrera-Parilla, A., **Van De Vijver, E.**, Van Meirvenne, M., Espejo-Pérez, A.J., Giráldez, J.V., & Vanderlinden, K. (2016). Apparent electrical conductivity measurements in an olive orchard under wet and dry soil conditions: significance for clay and soil water content mapping. *Precision Agriculture*, 17(5), 531–545.
20. Delefortrie, S., Saey, T., De Pue, J., **Van De Vijver, E.**, De Smedt, P., & Van Meirvenne, M. (2016). Evaluating corrections for a horizontal offset between sensor and position data for surveys on land. *Precision Agriculture*, 17(3), 349–364.
19. **Van De Vijver, E.**, Van Meirvenne, M., Vandenhaute, L., Delefortrie, S., De Smedt, P., Saey, T., & Seuntjens, P. (2015). Urban soil exploration through multi-receiver electromagnetic induction and stepped-frequency ground penetrating radar. *Environmental Science: Processes & Impacts*, 17(7), 1271–1281.
18. **Van De Vijver, E.**, Van Meirvenne, M., Saey, T., Delefortrie, S., De Smedt, P., De Pue, J., & Seuntjens, P. (2015). Combining multi-receiver electromagnetic induction and stepped frequency ground penetrating radar for industrial site investigation. *European Journal of Soil Science*, 66(4), 688–698.
17. Saey, T., De Smedt, P., Delefortrie, S., **Van De Vijver, E.**, & Van Meirvenne, M. (2015). Comparing one- and two-dimensional EMI conductivity inverse modeling procedures for characterizing a two-layered soil. *Geoderma*, 241–242, 12–23.
16. Delefortrie, S., De Smedt, P., Saey, T., **Van De Vijver, E.**, & Van Meirvenne, M. (2014). An efficient calibration procedure for correction of drift in EMI survey data. *Journal of Applied Geophysics*, 110, 115–125.
15. Saey, T., Van Meirvenne, M., De Pue, J., **Van De Vijver, E.**, & Delefortrie, S. (2014). Reconstructing mole tunnels using frequency-domain ground penetrating radar. *Applied Soil Ecology*, 80, 77–83.

14. Islam, M. M., Meerschman, E., Saey, T., De Smedt, P., **Van De Vijver, E.**, Delefortrie, S., & Van Meirvenne, M. (2014). Characterizing compaction variability with an electromagnetic induction sensor in a puddled paddy rice field. *Soil Science Society of America Journal*, 78(2), 579–588.
13. Islam, M. M., Saey, T., De Smedt, P., **Van De Vijver, E.**, Delefortrie, S., & Van Meirvenne, M. (2014). Modeling within field variation of the compaction layer in a paddy rice field using a proximal soil sensing system. *Soil Use and Management*, 30(1), 99–108.
12. Delefortrie, S., Saey, T., **Van De Vijver, E.**, De Smedt, P., Missiaen, T., Demerre, I., & Van Meirvenne, M. (2014). Frequency domain electromagnetic induction survey in the intertidal zone: Limitations of low-induction-number and depth of exploration. *Journal of Applied Geophysics*, 100, 14–22.
11. Meerschman, E., Van Meirvenne, M., Mariethoz, G., Islam, M. M., De Smedt, P., **Van De Vijver, E.**, & Saey, T. (2014). Using bivariate multiple-point statistics and proximal soil sensor data to map fossil ice-wedge polygons. *Geoderma*, 213, 571–577.
10. Meerschman, E., Van Meirvenne, M**., Van De Vijver, E.**, De Smedt, P., Islam, M. M., & Saey, T. (2013). Mapping complex soil patterns with multiple-point geostatistics. *European Journal of Soil Science*, 64, 183–191.
9. Van Meirvenne, M., Islam, M. M., De Smedt, P., Meerschman, E., Meeuws, F., **Van De Vijver, E.**, & Saey, T. (2013). Key variables for the identification of soil management classes in the aeolian landscapes of north-west Europe. *Geoderma*, 199, 99–105.
8. Boets, P., Thas, O., **Van De Vijver, E.**, Lock, K., Töpke, K., De Cooman, W., Janssen, C., & Goethals, P. (2013). Relating taxonomy-based traits of macroinvertebrates with river sediment quality based on basic and zero-inflated Poisson models. *Ecological Informatics*, 18, 49–60.
7. De Smedt, P., Saey, T., Lehouck, A., Stichelbaut, B., Meerschman, E., Islam, M. M., **Van De Vijver, E.**, & Van Meirvenne, M. (2012). Exploring the potential of multi-receiver EMI survey for geoarchaeological prospection: a 90 ha dataset. *Geoderma*, 199, 30–36.

6. Saey, T., De Smedt, P., Islam, M. M., Meerschman, E., **Van De Vijver, E.**, Lehouck, A., & Van Meirvenne, M. (2012). Depth slicing of multi-receiver EMI measurements to enhance the delineation of contrasting subsoil features. *Geoderma*, 189–190, 514–521.
5. Saey, T., Islam, M. M., De Smedt, P., Meerschman, E., **Van De Vijver, E.**, Lehouck, A., & Van Meirvenne, M. (2012). Using a multi-receiver survey of apparent electrical conductivity to reconstruct a Holocene tidal channel in a polder area. *Catena*, 95, 104–111.
4. Saey, T., De Smedt, P., Meerschman, E., Islam, M. M., Meeuws, F., **Van de Vijver, E.**, Lehouck, A., & Van Meirvenne, M. (2012). Electrical conductivity depth modelling with a multireceiver EMI sensor for prospecting archaeological features. *Archaeological Prospection*, 19 (1), 21–30.
3. Islam, M. M., Meerschman, E., Saey, T., De Smedt, P., **Van De Vijver, E.**, & Van Meirvenne, M. (2011). Comparing apparent electrical conductivity measurements on a paddy field under flooded and drained conditions. *Precision Agriculture*, 13, 384–392.
2. Islam, M. M., Saey, T., Meerschman, E., De Smedt, P., Meeuws, F., **Van De Vijver, E.**, & Van Meirvenne, M. (2011). Delineating water management zones in a paddy rice field using a floating soil sensing system. *Agricultural Water Management*, 102 (1), 8–12.
1. Meerschman, E., Van Meirvenne, M., De Smedt, P., Saey, T., Islam, M. M., Meeuws, F., **Van De Vijver, E.,** & Ghysels, G. (2011). Imaging a polygonal network of ice-wedge casts with an electromagnetic induction sensor. *Soil Science Society of America Journal*, 75 (6), 2095–2100.

<u>Conference proceedings</u>

P1

1. Van Meirvenne, M., **Van De Vijver, E.**, Vandenhaute, L., & Seuntjens, P. (2014). Investigating soil pollution with the aid of EMI and GPR measurements. In: *15th International Conference on Ground Penetrating Radar (GPR 2014)*, Brussels, Belgium, 30 June–4 July 2014, pp. 1006–1010.

C1

2. **Van De Vijver, E.**, & Van Meirvenne, M. (2016). Delving into the potential of multi-receiver electromagnetic induction surveying for enhanced landfill exploration in view of ELFM. In: Proceedings of the Third International Academic Symposium on Enhanced Landfill Mining, Lisboa, Portugal, 8–10 February 2016, pp. 175–187.
1. **Van De Vijver, E.**, Van Meirvenne, M., & Seuntjens, P. (2015). On the use of apparent electrical conductivity survey data to investigate the biodegradation of petroleum hydrocarbons in a landfarm. In: *Proceedings of the 4th Global Workshop on Proximal Soil Sensing 2015*, Zhejiang University, Hangzhou, China, 12–15 May 2015, pp. 77–82.

C3

15. **Van De Vijver, E.**, & Van Meirvenne, M. (2017). Proximal landfill sensing: new research grounds for high-resolution electromagnetic induction surveys. In: *Abstract Book Pedometrics 2017*, Wageningen, The Netherlands, 26 June–1 July 2017, p. 243.
14. Delefortrie, S., De Pue, J., **Van De Vijver, E.**, & Van Meirvenne, M. (2015). An evaluation of spatial offset corrections between sensor and position data for land-based, motorized surveys. In: *Proceedings of the 4th Global Workshop on Proximal Soil Sensing 2015*, Zhejiang University, Hangzhou, China, 12–15 May 2015, p. 102.
13. Schneidewind, U., Thornton, S., **Van De Vijver, E.**, Joris, I., & Seuntjens, P. (2015). Spatial variability of streambed hydraulic conductivity of a lowland river. In: Geophysical Research Abstracts, Vol. 17, EGU2015-5363-1, 2015. EGU General Assembly 2015, Vienna, Austria, 12–17 April 2015.
12. **Van De Vijver, E.**, De Pue, J., Cornelis, W., & Van Meirvenne, M. (2015). Comparison of air-launched and ground-coupled configurations of SFCW GPR in time, frequency and wavelet domain. In: *Geophysical Research Abstracts*, Vol. 17, EGU2015-10038, 2015. EGU General Assembly 2015, Vienna, Austria, 12–17 April 2015.
11. **Van De Vijver, E.**, Van Meirvenne, M., & Seuntjens, P. (2015). Investigating bioremediation of petroleum hydrocarbons through landfarming using apparent electrical conductivity measurements. In: *Geophysical Research Abstracts*, Vol. 17, EGU2015-9304, 2015. EGU General Assembly 2015, Vienna, Austria, 12–17 April 2015.

10. De Pue, J., **Van De Vijver, E.**, Cornelis, W., & Van Meirvenne, M. (2014). Comparison of pulse and SFCW GPR in time, frequency and wavelet domain. In: *Geophysical Research Abstracts*, Vol. 16, EGU2014-16072-3, 2014. EGU General Assembly 2014, Vienna, Austria, 27 April–2 May 2014.
9. **Van De Vijver, E.**, Van Meirvenne, M., Saey, T., De Smedt, P., Delefortrie, S., & Seuntjens, P. (2014). Combining ground penetrating radar and electromagnetic induction for industrial site characterization. In: *Geophysical Research Abstracts*, Vol. 16, EGU2014-1886-1, 2014. EGU General Assembly 2014, Vienna, Austria, 27 April–2 May 2014.
8. De Smedt, P., **Van De Vijver, E.**, Saey, T., & Van Meirvenne, M. (2014). Reconstructing the prehistoric landscape of Stonehenge (UK) through multi-receiver EMI survey. In: *Proceedings from the 27th Annual Symposium on the Application of Geophysics to Engineering & Environmental Problems (SAGEEP)*, Boston, Massachusetts, United States, 16–20 March 2014, p. 54.
7. **Van De Vijver, E.**, Van Meirvenne, M., & Seuntjens, P. (2014). Urban soil exploration using electromagnetic induction and ground penetrating radar. In: *Proceedings from the 27th Annual Symposium on the Application of Geophysics to Engineering & Environmental Problems (SAGEEP)*, Boston, Massachusetts, United States, 16–20 March 2014, p. 140.
6. **Van De Vijver, E.**, Saey, T., De Smedt, P., Meerschman, E., Delefortrie, S., Seuntjens, P., & Van Meirvenne, M. 2013. Combining electromagnetic induction and ground penetrating radar for industrial site characterization. In: Gebbers, R., Lück, E. & Rühlmann, J. (Eds.), *Proceedings of the 3rd Global Workshop on Proximal Soil Sensing 2013*, Leibniz-Institute for Agricultural Engineering Potsdam-Bornim, Potsdam, Germany, pp. 193–195.
5. Van Meirvenne, M., Saey, T., De Smedt, P., **Van De Vijver, E.**, Islam, M. M., Delefortrie, S., & Meerschman, E. (2013). Proximal sensing for soil functions. In: Gebbers, R., Lück, E. & Rühlmann, J. (Eds.), *Proceedings of the 3rd Global Workshop on Proximal Soil Sensing 2013*, Leibniz-Institute for Agricultural Engineering Potsdam-Bornim, Potsdam, Germany, p. 106.

4. Pedrera, A., **Van De Vijver, E.**, Vanderlinden, K., Martos-Rosillo S., Van Meirvenne, M., Espejo-Pérez, A.J., Taguas, E.V., & Giráldez, J.V. (2013). Effectiveness of apparent electrical conductivity surveys at varying soil water contents for assessing soil and water dynamics across a rainfed mountain olive orchard in SW Spain. In: *Geophysical Research Abstracts*, Vol. 15, EGU2013-1008-2, 2013. EGU General Assembly 2013, Vienna, Austria, 7–12 April 2013.
3. Meerschman, E., **Van De Vijver, E.**, Mariethoz, G., & Van Meirvenne, M. 2012. Using bivariate multiple-point statistics for the processing of proximal soil sensor data. In: Gómez-Hernández, J.J. (Ed.), *Proceedings of geoENV2012, IX Conference on Geostatistics for Environmental Applications*, Valencia, Spain, 19–21 September 2012, pp. 219–220. Poster presentation.
2. Islam, M. M., Van Meirvenne, M., Loonstra, E., Meerschman, E., De Smedt, P., Meeuws, F., **Van De Vijver, E.**, & Saey, T. (2011). Key properties for delineating soil management zones. In: Adamchuk, V.I. & Viscarra Rossel, R.A. (Eds.), *Proceeding of the Second Global Workshop on Proximal Soil Sensing*, McGill University, Montreal, Canada, pp. 52–55.
1. **Van De Vijver, E.**, Saey, T., De Smedt, P., Islam, M. M., Meeuws, F., & Van Meirvenne, M. (2011). Proximal soil sensing for soil inventory and monitoring. In: Engelen, M., Van Keer, I., Boënne, W., Bronders, J., Seuntjens, P., Bonroy, J. & Cornelis, W. (Eds.), *Book of abstracts of Symposium 'In-situ Environmental Monitoring and Policy. The Application of Sensors and Passive Samplers'*, Ghent, Belgium, 26–27 May 2011.

Scientific activities

International conferences and symposia

7. Third International Academic Symposium on Enhanced Landfill Mining, Lisboa, Portugal, 8–10 February 2016. *Oral presentation.*
6. 4th Global Workshop on Proximal Soil Sensing, Zhejiang University, Hangzhou, China, 12–15 May 2015. *Oral presentation.*
5. European Geosciences Union General Assembly 2015, Vienna, Austria, 12–17 April 2015. *Two oral presentations and poster.*
4. 27th Annual Symposium on the Application of Geophysics to Engineering & Environmental Problems (SAGEEP), Boston, Massachusetts, USA, 16–20 March 2014. *Two oral presentations.*

3. 3rd Global Workshop on Proximal Soil Sensing, Leibniz-Institute for Agricultural Engineering Potsdam-Bornim, Potsdam, Germany, 26–29 May 2013. *Oral presentation.*
2. GeoENV2012, IX Conference on Geostatistics for Environmental Applications, Valencia, Spain, 19–21 September 2012, pp. 219–220. *Poster presentation.*
1. In-situ Environmental Monitoring and Policy. The Application of Sensors and Passive Samplers', Ghent, Belgium, 26–27 May 2011. *Oral presentation.*

National conferences and symposia

1. 'Innovatieve prospectiemethoden bij vernieuwend concept', Duurzaam voorraadbeheer van stortplaatsen, OVAM, Brussels, Belgium, 24 May 2016. *Invited oral presentation*.

Invited lectures at universities and scholarly institutions

2. 'Stortplaatsen en geofysisch onderzoek. Kader en beleidsaspecten. De weg naar duurzame sanering en management bij stedelijke herontwikkeling', CES&T Inspiring afternoon: 'inspiration through collaboration', Ghent University, Ghent, Belgium, 17 March 2017. Invited oral co-presentation with Eddy Wille (OVAM).
1. 'Geophysical exploration techniques for ELFM', MSCA ETN NEW-MINE Kick-off event workshop, Novotel Leuven Centrum, Leuven, Belgium, 8 February 2017. *Invited lecture.*

Scientific services

Scientific committee memberships

Scientific Committee Member Pedometrics 2017, Wageningen, The Netherlands, 26 June–1 July

Activities as peer reviewer

- Biosystems Engineering
- Geoderma
- Sensors
- Waste Management & Research